The University Of Sheffield.

Impedance Spectroscopy of Solid Oxide Cells and YSZ Electrolytes: Methodology and Characterisation

By:

Alison Rachel Thompson

A thesis submitted in partial fulfilment of the requirements for the degree of Doctor of Philosophy

Supervisor:

Prof. Derek C. Sinclair

Department of Chemical and Biological Engineering

Faculty of Engineering

The University of Sheffield

March 2019

TABLE OF CONTENTS

ABSTRACT

Anthropogenic CO_2 emissions are contributing to global warming through the greenhouse effect. If left unabated, this will cause significant climate change. Decarbonisation of the energy supply will reduce CO_2 emissions significantly. Fuel cell/electrolyser systems, such as solid oxide cells (SOCs) can play a part, both in energy storage and in carbon utilisation. SOCs consist of fuel and oxygen electrodes, and a solid electrolyte. Impedance spectroscopy (IS) can be used to separate its electrical response into individual processes for characterisation. The resulting immittance data can be represented in the following formalisms: impedance, Z*, admittance, Y*, permittivity, ε* and electric modulus, M*. In this work, immittance spectra were recorded for a variety of samples: commercial SOCs (NextCell, FuelCellMaterials^{TM}), YSZ (yttria stabilised zirconia) single crystals and YSZ ceramics sintered at temperatures ranging between 1275 and 1450 ^{o}C. YSZ is a typical electrolyte material used in SOCs.

SOC immittance spectra for commercial SOCs, measured at 850 ^{o}C, were influenced at high frequency due to a large contribution from jig inductance. Data were corrected for this unwanted contribution by using an inductor L_s in parallel with a resistor R_0 in the equivalent circuit. L_s was estimated from Kramers-Kronig transform calculations because corrections from closed-circuit experiments were unreliable. The resulting spectra plotted in the form of Z* plots contained two broad arcs, each thought to represent multiple processes. However, despite analysis using Analysis of Differences in Impedance Spectra (ADIS) and Distribution of Relaxation Times (DRT), the number of processes present remained unclear and it was not possible to attribute the features to any specific process(es).

IS results from 8mol% YSZ single crystals, measured between 150 and 325 ^{o}C, exhibited a bulk response at high to mid frequency and electrode effects at mid to low frequencies, due to charge transfer and diffusion. In ε' spectroscopic plots, the bulk response exhibited two features: a high frequency plateau at ε' ~ 30, and a lower frequency plateau (visible mainly as a point of inflection in ε') at ~90-100. At lower frequencies, the ε' spectra were dominated by the electrode response.

Bulk YSZ data from the single crystals were fitted using a combination of resistor(s) (*R*), capacitor(s) (*C*) and a constant phase element (*Q*). Four circuits were compared to investigate which one gave i) the best fit in all four formalisms, and ii) the most reasonable physical trends in parameters with temperature. Circuits A, B and C have been used previously in literature to describe bulk YSZ, whereas circuit D is newly proposed in this work. Circuit A consisted of an *R* and a *Q* element in parallel. Circuit B contained an additional parallel capacitor, giving an *RQC* element, which results in a high frequency plateau in ε'. Circuit C combines an *RQC* element in parallel with a series R_d-C_d element, in which R_d and C_d represent local dipole interactions. Circuit D is also based on an *RQC* element, with an additional capacitance C_q in series with *Q*, which results in a low frequency plateau in ε', equal to the sum of the two capacitors. All equivalent circuits tested gave accurate values of bulk (ionic) conductivity (σ =1/*R*), which obeyed an Arrhenius law with an activation of ~1.03 eV, but did not all

give accurate values of relative permittivity ε_r, expected to be temperature independent with a value of ~ 30. Circuit A gave a poor fitting in all formalisms except Z*. Circuits B and C fitted reasonably well in all formalisms but gave inaccurate fits of low frequency data in ε'. Circuit D gave both the best fit and the most reasonable physical parameter trends; in particular, ε_r was stable with temperature at ~30. C_q decreased moderately with increasing temperature, from 72 (a.u.) at 175 ^{o}C, to 57 at 325 ^{o}C. This additional capacitance indicates there is a distribution of characteristic frequencies for the bulk response, which decreases with increasing temperature. The origin of this is proposed to be associated with localised heterogeneity in the bulk, due to micro-clusters of oxygen vacancies. This response may be more general in functional oxides where local structure plays an important role in the electrical properties and not specific only to YSZ. Further investigation requires work on single crystals, not ceramics; the presence of grain boundaries obscures the low frequency ε' bulk plateau as described in the next paragraph.

In the immittance spectra of YSZ ceramics, measured between 175 and 325 ^{o}C, there was a bulk response at high frequency and a grain boundary response at mid frequency. Data were fitted using a parallel *RQC* element and a parallel *RQ* element connected together in series, representing the bulk and grain boundary responses, respectively. There was no need to include C_q in the bulk element as the low frequency plateau was swamped by the grain boundary response. The grain boundary response was most prominent for samples sintered at the lowest temperature investigated (1275 ^{o}C), which were also the most porous samples (66%). The highest density achieved was 96% for ceramics sintered at 1450 ^{o}C. In contrast to the electro-active grain boundaries, porosity was not represented as an individual response but instead affected the magnitude of the whole spectrum. The bulk conductivity increased with the relative density of the ceramics and, at 300^{o}C, gave values of 3.1×10^{-6} and 8.2×10^{-6} S/cm for densities of 66 and 96%, respectively. The relative permittivity almost doubled, from 16 to 29, as the density increased by ~ 30% towards full theoretical density.

ACKNOWLEDGEMENTS

Thanks to the EPSRC and the Department of Chemical and Biological Engineering for funding. Thanks to Rachael Rothman for giving me this opportunity and for involving me in the 4CU project. Thanks to Corinne Howse, our project manager, and to all those in SP5: Ali, Ann, Chris, Denis, Jen, Kay and Tom for sharing your fuel cell knowledge with me. Special thanks to Jen Manerova for all your help and support, both in and out of the lab. I really value your friendship. Thanks also to Mogens Mogensen for the suggestion to investigate single crystals.

Many, many thanks to Derek Sinclair: you have been an incredible supervisor and I have really enjoyed working with you. I am so grateful for the care and guidance you have given me and all the time you have invested in me. Your knowledge on impedance and electro-ceramics has been invaluable. You are smart, kind and an excellent role model. You always believed in me and you brought out the best in me.

Thanks to the Functional Materials group, especially to Fan Yang for carrying out XRD on the YSZ starting powder and making the YSZ pellets that are characterised in Chapter 5. I am grateful too for your help in the lab, particularly with the SEM. Thanks also to Richard Veazey for carrying out glancing angle XRD on the YSZ single crystal sample and to Andrew Mould for guidance in the lab. Thanks to Julian Dean for introducing me to finite element modelling, giving me access to ElCer and for including me in EM&M group meetings. Thanks to both Julian and to Will Zimmerman for providing access to COMSOL.

Thank you to my officemates past and present, in particular: Ana, Steve, Tom, Silvia, Karen, Jen, Justin, Elle and Gareth for all the shared lunchtimes and cups of tea.

Thanks to the incredible people at St Tim's, Crookes, most particularly to the Leake family. There are no words sufficient to describe the depth of kindness and hospitality you have shown me.

To my wonderful housemate, Eleanor: your fun and craziness have lifted my spirits; thanks for all the laughter and companionship we have shared.

Thanks to my Dad, David, for introducing me to the world of engineering, Matlab and PhDs. Thank you for your encouragement and for taking an active interest in my research. I really appreciate you making the time to read through my thesis and provide helpful feedback. Thank you also to the rest of my family: my Mum and my sisters, Fiona and Sandy, for your moral support and for tolerating engineering talk at the dinner table when we are all back home!

Ultimately, thanks to God for being with me always and giving me the strength to persevere. "*For from him and through him and for him are all things. To him be the glory forever! Amen*" (Romans 11:36)

LIST OF ACRONYMS

ADIS	Analysis of Differences in Impedance Spectra
ASR	Area Specific Resistance
BLM	Brickwork Layer Model
CCS	Carbon Capture and Storage
CCUS	Carbon Capture, Usage and Storage
CDU	Carbon dioxide utilisation
CHP	Combined Heat and Power
CNLS	Complex Non-linear Least Squares
CPE	Constant Phase Element
DFT	Discrete Fourier Transform
DRT	Distribution of Relaxation Times
EC	Equivalent Circuit
FEM	Finite Element Method
FLW	Finite Length Warburg
FSW	Finite Space Warburg
FT	Fourier Transform
FWHM	Full Width Half Maximum
GA-XRD	Glancing Angle X-Ray Diffraction
GDC	Gadolinia Doped Ceria
GHG	Greenhouse gas
iFT	inverse Fourier Transform
IS	Impedance Spectroscopy
ISCD	Inorganic Crystal Structure Database
KK	Kramers-Kronig
LSCF	Lanthanum Strontium Cobalt Ferrite
LSGM	Lanthanum Gallate doped with Strontium and Magnesium
LSM	Lanthanum Strontium Manganite
OCV	Open Circuit Voltage
PRD	Partial Radial Distribution
RWGS	Reverse Water Gas Shift
ScSZ	Scandia Stabilised Zirconia
SEM	Scanning Electron Microscopy
SOC	Solid Oxide Cell
TPB	Triple Phase Boundary
XRD	X-Ray Diffraction
YSZ	Yttria Stabilised Zirconia

LIST OF SYMBOLS

Symbol	Meaning	Units
A	Electrode area perpendicular to electric current	cm^2
a	Lattice parameter	Å
C	Capacitance; Capacitor	F
C_0	Vacuum capacitance of sample	F
c	Fraction of occupied sites	-
$\mathcal{D}_{\text{eff}}$	Effective diffusion coefficient	cm^2/s
d	Thickness	cm
E_{act}	Activation energy	eV
F	Faraday constant	C/mol
f	Frequency	Hz
f^{o}	Characteristic frequency	Hz
G	Gibbs free energy	J/mol
g	Scaling term in DRT; partial radial distribution function	-
gf	Geometric factor	cm^{-1}, cm^{-2}
h,k,l	Miller indices	-
I	Current	A
i	Current density	A/cm^2
j	Square root of -1	-
k	Reaction rate; Boltzmann constant	s^{-1}; J/K
L	Inductance, Inductor	H
M	Electric Modulus, number of *RC* elements used in KK	-
N	Number of measured data points	-
n	Exponential coefficient in the constant phase element	-
P	Model parameter (Warburg element)	-
p	Partial pressure; volume fraction of pores	Pa; -
Q	Constant phase element	N/A
R	Resistance; resistor; universal gas constant	Ω; J/mol K
s	sech(y); sum of the error	
T	Temperature; Time period of wave; Sampling interval (DRT)	K, s, -
t	Time; thickness	s; cm
V	Voltage, Potential	V
V_m	Molar volume	$Å^3$
W	Model parameter (Warburg element)	-
w	Hanning window function, weighting factor	-
X	Generic immittance formalism (either Z,Y,M or ε)	(various)
x	Vacancy concentration	mol

Y	Admittance	S
Y_0	Proportional factor for the constant phase element	S
Z	Impedance	Ω
α_D	Dielectric polarisability	$Å^3$
γ	scaling factor (in DRT)	-
Δ	Residual	-
ΔH_A	Enthalpy of association	J/mol
ΔH_m	Migration enthalpy	J/mol
$\Delta \dot{Z}'$	Change in the derivative of the real component of the impedance with respect to the natural logarithm of frequency	Ω
ε	Permittivity	F/cm
ε_0	Permittivity of free space	F/cm
ε'_∞	High frequency plateau of the permittivity	-
ε_r	Relative permittivity	-
η	Overpotential or polarisation	V
θ	Phase difference; angle	rad
λ	Wavelength of X-rays	Å
μ	Optimisation parameter	-
σ	(Ionic) conductivity	S/cm
τ	Time constant or relaxation time	s
ϕ	Phase angle	rad
χ^2	Chi-squared (sum of the residuals)	-
ω	Angular frequency ($2\pi f$)	rad/s
ω_0	Characteristic frequency of a process ($1/\tau$)	rad/s

Subscripts

b	Bulk
c	Critical
ct	Charge transfer
d	Dipole
f	Free n
gb	Grain boundary
hf	High frequency
i	Counter
Im	Imaginary component
k	Counter (in original domain)
m	Effective medium
n	Counter (in Fourier domain)

N	Nernst
OC	Open circuit
p	Parallel
pol	Polarisation
Re	Real component
s	Series
tot	Total
x	Fixed n
Ω	Ohmic

Superscripts

'	Real component
''	Imaginary component
*	Complex number
~	Fourier domain
^	KK-transformed data

CHAPTER 1: INTRODUCTION

1.1 BACKGROUND

1.1.1 THE ROLE OF GREENHOUSE GASES IN CLIMATE CHANGE

The motivation for this work is based on the need to reduce anthropogenic greenhouse gas emissions to mitigate climate change. The Earth receives electromagnetic radiation from the Sun and acts as a blackbody emitter with the peak wavelength emitted in the infrared region (Trogler, 1995). The atmosphere of the Earth predominantly consists of oxygen and nitrogen, which are both transparent to infrared radiation. However, some trace gases that are present are infrared-active; they absorb infrared radiation and then re-radiate it, which warms the Earth (DECC, 2014). These infrared-active gases are termed *greenhouse gases* (GHGs) and play an important role in the determination of the Earth's temperature. Without them, there would be about a 30 ^{o}C decrease in surface temperature (The Geological Society, 2010). The largest GHG contributor is water vapour, which accounts for 80% of this temperature difference (Trogler, 1995). Its atmospheric concentration is maintained by the natural water cycle and scales with increasing surface temperature (Raval and Ramanathan, 1989). The next largest GHG contributor is carbon dioxide (CO_2). It is clear from geological records, such as ice sheets and fossil tree rings, that there is a correlation between the amount of CO_2 in the atmosphere and the fluctuation in the Earth's temperature (The Geological Society, 2010). Since the industrial revolution, anthropogenic (i.e. caused by human activity) emissions of CO_2 have increased dramatically (Boden et al., 2017), see Figure 1.1. CO_2 lasts in the atmosphere for around 50 to 200 years (Trogler, 1995), and so far has caused an increase in atmospheric levels from around 280 parts per million (ppm) in pre-industrial times (Riebeek and Simmon, 2011) to 405 ppm in 2017 (Hartfield et al., 2018). The carbon cycle can no longer be balanced naturally (North, 2014). Other anthropogenic GHG emissions include methane, nitrous oxide (N_2O) and fluorinated gases (EPA, 2017). These are all more infrared-active than CO_2 but are present in smaller concentrations and hence contribute less to the overall GHG effect (Trogler, 1995).

Since the 1850s, the global surface temperature has increased by around 1.0 ^{o}C (IPCC, 2018), and for the last three decades, each decade has been warmer than any recorded previously (Met Office, 2018a). This cannot be attributed to any recognisable natural geological cause (The Geological Society, 2010). Instead, there is overwhelming evidence that the temperature increase is due to human activity (Met Office, 2018b, IPCC, 2018); in particular, due to the burning of fossil fuels (EPA, 2017).

The effects of global warming have already been observed (IPCC, 2018). Present consequences include more frequent and more intense extreme weather events, such as heat waves, droughts, storms, floods and forest fires (Hartfield et al., 2018). This could lead to food and water shortages, and pressure for human migration. In addition, global warming will result in a rise in sea level from melting ice sheets and expansion of the water already present, due to warming of the oceans (The Geological Society, 2010). This will damage coastal habitats and cause flooding (Met Office, 2016). If global warming continues, there is also the possibility of major alterations to the Earth's climate, such as rapid thawing of artic permafrost (DECC, 2014). This would release GHGs that were previously locked away and cause a rapid increase in atmospheric concentrations (Met Office, 2018b).

In order to prevent unsafe interference with the climate system, the global temperature rise should be limited to below 2 ^{o}C until at least 2500 (Met Office, 2016). However, climate models (Met Office, 2016) predict a 4 ^{o}C rise above preindustrial levels by 2100 if global emissions continue at the current rate. Therefore, a reduction of GHG concentrations in the atmosphere is necessary in order to achieve this.

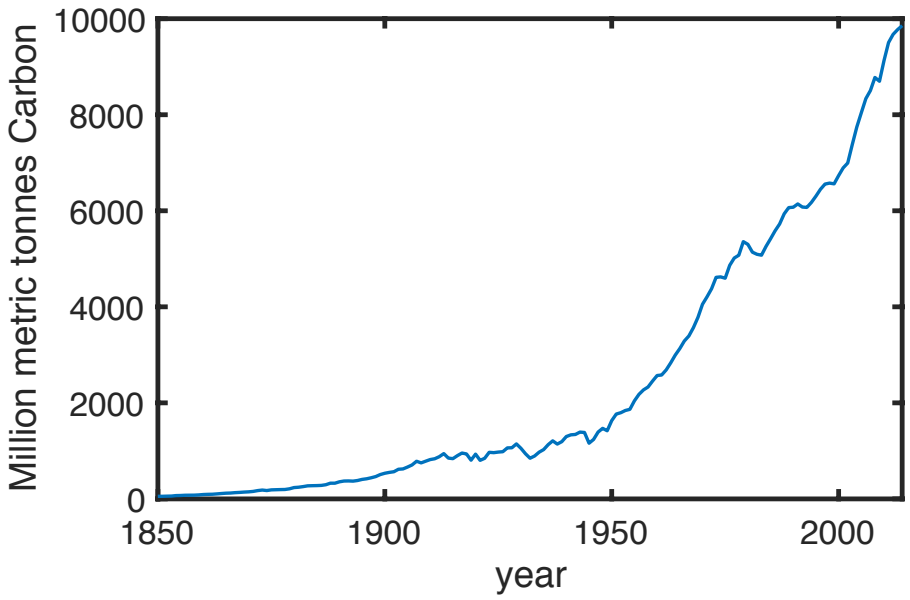

Figure 1.1: Global carbon emissions from fossil fuel consumption and cement production between 1850 and 2014. Data taken from Boden et al. (2017).

1.1.2 CLIMATE CHANGE POLICY

The need to reduce anthropogenic greenhouse gas emissions has been recognised in government policy. In the UK, the Climate Change Act (2008) was passed, which set out targets to reduce UK GHG emissions by at least 80%, compared with 1990 levels, by 2050. It provided a system for carbon budgeting, with interim targets every five years. Internationally, in 2015, the UK was one of 195 countries to pledge in the Paris

Agreement (2015) to stretch national targets with the aim of limiting the rise in temperature above pre-industrial levels to well below 2 ^{o}C and making efforts to limit it to an increase of 1.5 ^{o}C. They aim to reduce global GHG emissions and set the goal to reach a balance of sources and sinks of anthropogenic GHGs by 2050. In addition, in 2017, the UK government produced its Clean Growth Strategy (BEIS, 2017), which aims to cut greenhouse gas emissions whilst simultaneously growing national income, for example from the commercialisation of green technologies.

In 2017, anthropogenic greenhouse gas emissions in the UK were 456 million tonnes of carbon dioxide equivalent per year ($MtCO_2e$/year), which is 57% of the value from 1990 (BEIS, 2018). A further decrease in emissions is hence necessary to meet the 2050 targets. There are various strategies in operation to reduce CO_2 emissions across a range of industries; carbon dioxide accounted for 80% of the emissions in 2017 (BEIS, 2018). Two are described below: the use of energy storage to facilitate the use of renewable energy technologies on a larger scale, and reduction in CO_2 emissions by carbon capture, usage and storage. The use of fuel cells/electrolysers in each application is also explored.

1.1.3 The need for flexible energy storage

There has already been a significant decrease in UK GHG emissions from the energy supply sector, from 278 $MtCO_2e$ in 1990 to 120 $MtCO_2e$ in 2016 (BEIS, 2018), accounting for 26% of the total emissions in 2016. This is mainly attributed to a change in fuel mix in electricity generation. Coal consumption, in particular, has decreased dramatically, and accounted for only 9.0% of the electricity generated in 2016. There has been an increase in renewable energy production; it made up 24.5% of the UK's electricity in 2016 and 29.3% in 2017 (BEIS, 2018). However, the intermittency of renewable energy sources, such as solar or wind power, limits the extent to which these sources can be utilised.

The electrical frequency of the UK National Grid needs to be maintained at 50 Hz (National Grid, 2019), by a continuous match of electricity supply to demand. For intermittent energy sources to supply a larger proportion of the grid's energy, increased energy storage is crucial; the storage capacity needed is thought to be around 20-30% of the annual load (Becker et al., 2014). Existing storage methods tend to rely on specific geographic locations, for example hydroelectric storage, and are not easily scalable. There has been an increased interest in batteries for short-term energy storage (Dunn et al., 2011); however, due to self-discharge they are less suitable for longer-term storage (Aneke and Wang, 2016). In contrast, a reversible fuel cell/electrolyser system facilitates an external supply of chemical energy, enabling it to be operated continuously, when required; this makes it a promising intermediate/long term energy storage option (Jensen et al., 2015). An example is illustrated in Figure 1.2. When there is a surplus of energy supply, it can be used to

power the electrolysis of water and carbon dioxide, to produce hydrogen and carbon monoxide, which have a higher chemical energy. Then, when grid demand is high, the system can be used in reverse as a fuel cell, which produces electrical energy by converting the stored products back to carbon dioxide and water.

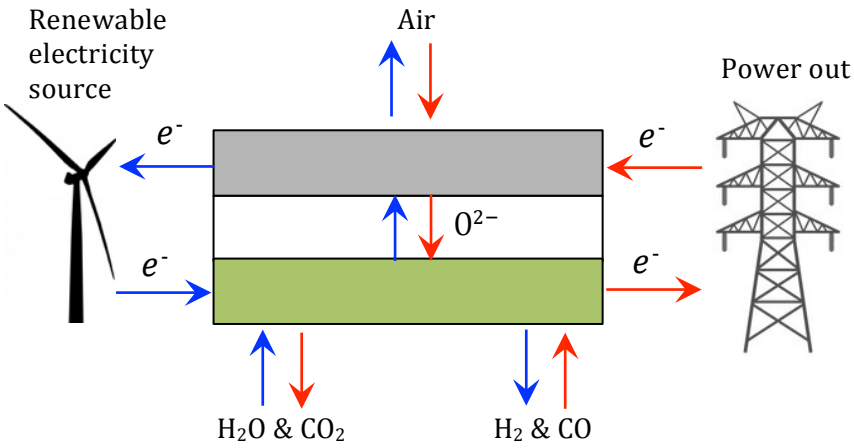

Figure 1.2: Schematic of an electricity storage system. When the grid power supply is larger than the required demands, surplus electricity can be used to power electrolysis (blue arrows). When extra power supply is needed to balance the grid, the system can be run in fuel cell mode (red arrows), generating power. Diagram adapted from Jensen et al. (2015).

1.1.4 CARBON CAPTURE, USAGE AND STORAGE (CCUS)

To meet the targets in the Climate Change Act, the Committee on Climate Change estimated that the UK needs to store around 60-180 $MtCO_2$/year by 2050 (Macdonald-Smith, 2017). In conjunction with the Clean Growth Strategy, the CCUS council (HM Government, 2017) was set up to advise the government on the development of Carbon Capture, Usage and Storage (CCUS). The concept is illustrated in Figure 1.3. Carbon dioxide can be captured from combustion plants and compressed. It can then be transported and stored permanently in geological sites such as old oil wells underground (Boot-Handford et al., 2014), termed carbon capture and storage (CCS). Alternatively, after compression, carbon dioxide can be used as a feedstock to create products, for example, fuels, or chemicals, such as urea and methanol (Markewitz et al., 2012). This is termed carbon dioxide utilisation (CDU).

According to an IChemE Energy Centre publication (2018), in April 2018, there were 37 CCS projects worldwide, which collectively store a total of 51 Mt CO_2/year; 18 are operational and the rest are still in the development stage. The amount of carbon utilized is around 200 Mt CO_2/year (IChemE Energy Centre, 2018), which is about four times the amount stored. However, CCS is expected to be the main player in the sequestration of CO_2 as CDU does not necessarily achieve long-term storage; roughly 75% of the products from CDU release CO_2 during usage (IChemE Energy Centre, 2018), for example the burning of fuel. However, there is also the possibility of

capturing CO_2 from the atmosphere (Styring et al., 2014); hence a synthetic carbon cycle can be achieved, which is sustainable.

An example of CDU is the electrolysis of carbon dioxide and water to obtain syngas (a mixture of carbon monoxide and hydrogen) (Stoots et al., 2009, Ebbesen et al., 2009). This can then be used to create synthetic fuels, for example by the Fischer-Tropsch process (Graves et al., 2011b).

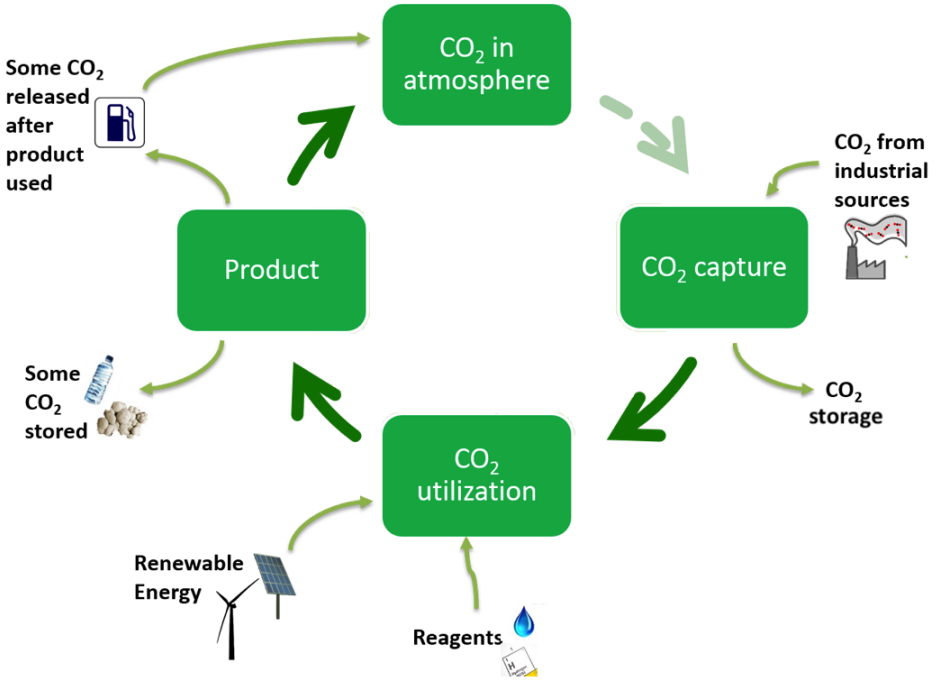

Figure 1.3: Synthetic carbon cycle, illustrating the role of carbon capture, usage and storage in creating a sustainable carbon industry. Adapted from CO2Chem (2014).

1.1.5 Solid oxide cells (SOCs)

It was mentioned in the previous sub-sections that fuel cell/electrolyser technologies can be used both for CDU and for flexible energy storage. There are a number of types of fuel cells. They operate at different temperatures and are used in different applications. Solid Oxide Cells (SOCs) operate at high temperature, in the region 750-900 ^{o}C, and are favoured in large stationary applications due to their high efficiencies (Ebbesen et al., 2014). An example of a low temperature system is the Proton Exchange Membrane (PEM) fuel cell, which operates at around 80 ^{o}C and is used for example in city buses (Steele and Heinzel, 2001).

Considerable progress has been made in SOC technology in the last couple of decades, starting at the lab scale and progressing through prototypes to the pre-commercial and, in some cases, commercial stage (Blum et al., 2005, Steele and Heinzel, 2001). Lab tests on individual cells have included looking to optimise the reliability and longevity of the cell (Hauch, 2007, Weber et al., 2015, Tietz et al., 2013), attempting to increase the conductivity of the cell at lower temperatures

(Mahato et al., 2015, Fergus, 2006), seeking to decrease the cost of the cell components (Ebbesen et al., 2014), aiming to mitigate the effects of impurities from input gases (Schuler et al., 2011) and attempting to determine suitable sealant materials to avoid contamination (Weil, 2006, Lessing, 2007). A single cell has a power output in the order of Watts (Fuel Cell Materials, 2017). By combining cells to create “stacks”, a higher power output can be achieved.

One of the methods used to test SOCs is Impedance Spectroscopy (IS) (Mogensen and Hendriksen, 2003). It enables the electrical response of an SOC to be separated into individual processes, which can be used, for example to compare materials, and geometries, as well as for degradation studies, investigating the change in spectra over time. IS is explored in more detail in Section 2.2.

In the last few years, there have been an increasing number of demonstrations of fuel cell technology, particularly in combined-heat-and-power (CHP) applications. This is where electricity and heat are produced from a single source of fuel, hydrogen or natural gas in this instance, and is also termed co-generation. The demonstrators span a range of sizes, from residential-scale “micro-CHP” systems such as the 1 kW SteelGen system by Ceres Power (Ceres Power, 2016), to larger units such as those demonstrated in the ComSos project (Hydrogen Europe, 2018); namely, 12 kW units by SOLID power, 25 kW system by Sunfire and 60 kW units by Convion.

There is some commercial fuel cell technology currently available such as the off-grid power generators by Bloom Energy (Bloom Energy, 2019). These are modular, see Figure 1.4. Each server module is made up of multiple stacks and can be combined in various configurations to produce power systems with outputs between 0.2 and 100 MW. To the author’s knowledge, the only SOC electrolyser commercially available at present is eCOS^{TM} (Haldor Topsoe, 2017), which is marketed as a carbon monoxide generator. As further research into electrolysis is carried out, more systems are likely to become commercialised.

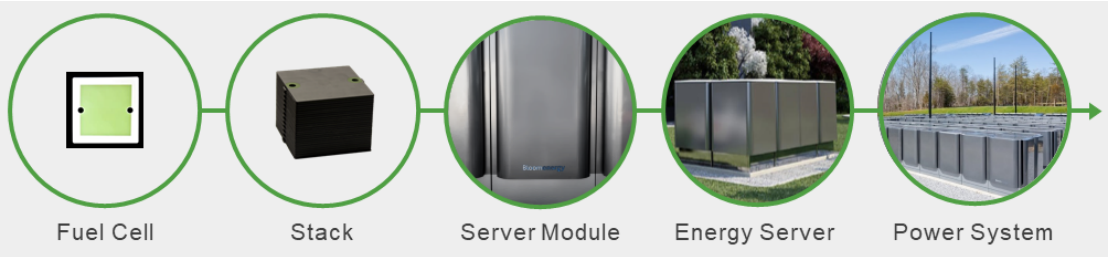

Figure 1.4: Modular design of the off-grid power generators by Bloom Energy (2019).

1.2 OVERVIEW OF THE THESIS

1.2.1 OVERALL AIMS AND THESIS STRUCTURE

The overall aim of this work is to determine the extent to which impedance spectroscopy (IS) can be used to characterise solid oxide cells (SOCs) and their individual components, and to improve methodology so that greater accuracy in the results can be obtained. The structure of the thesis is outlined below.

In Chapter 2, theory is presented regarding SOCs and impedance spectroscopy is introduced as a method of electrical characterisation. Different techniques seen in the literature are explored to analyse IS data: namely, Analysis of Differences in Impedance Spectra (ADIS) and Distribution of Relaxation Times (DRT). In addition, the theory of Kramers-Kronig transforms is explored, to aid in determining the reliability of IS data, and the need for jig correction is considered, to correct for artefacts.

The theory presented in Chapter 2 is built upon in Chapter 3. First, experiments are carried out to obtain IS data for a commercial SOC. Next, the reliability of the results is considered. The need to account for jig inductance is stressed and a methodology is devised for this. In addition, the corrected IS results are analysed using ADIS and DRT to investigate the effect of the input gas composition on the impedance response of the SOC.

The following two chapters are on yttria stabilised zirconia (YSZ), a typical electrolyte material in SOCs, and impedance spectroscopy is again undertaken. Chapter 4 investigates YSZ single crystals and the reliability of extracting the bulk material parameters, conductivity and permittivity, using different electrical equivalent circuits (ECs). A new equivalent circuit is proposed. In Chapter 5, the focus shifts to YSZ ceramics and the effects that grain boundaries have on the visibility of the bulk response. Ceramics sintered at a range of temperatures are studied, which results in a range of sample porosities and grain sizes.

General conclusions and suggestions for future work are presented in Chapter 6. This is followed by appendices and references.

1.2.2 AIMS OF EACH CHAPTER

The aims of each experimental chapter are as follows:

Chapter 3:

- to devise a methodology for determining:
    - the suitability of impedance spectroscopy (IS) data for equivalent circuit fitting

- the number of processes occurring in an SOC, to aid with characterisation of the fuel cell.

Chapter 4:

- to establish a means for relevant equivalent circuit (EC) fitting of immittance data from yttria stabilised zirconia (YSZ) single crystals, to obtain the following bulk parameters and their temperature dependence:
  - ionic conductivity, σ
  - activation energy, E_{act}
  - relative permittivity, ε_r
- to determine whether or not the presence of dipoles in YSZ can be confirmed from immittance data and subsequent EC fitting.

Chapter 5:

- to determine the effect of porosity on the immittance response of polycrystalline YSZ
- to separate the grain boundary response from the bulk response.

1.2.3 ORIGINAL CONTRIBUTIONS

The original research contributions in this thesis are as follows:

- An equivalent circuit (EC) was devised to describe the bulk response of YSZ, based on spectra from YSZ single crystals, which accounted for plateaus at both high and low frequency, and non-ideal behaviour at mid frequency.
- It is proposed that the low frequency plateau is due to the presence of local electrical heterogeneity in the bulk from local clusters of oxygen vacancies.
- The low frequency bulk plateau is not observed in YSZ ceramics as it is veiled by the grain boundary response. This was the case for all sintering temperatures investigated.
- Although ECs reported in literature for bulk YSZ (circuits A, B and C in chapter 4) were suitable for the determination of resistances, in this work, they were shown to be unsuitable for the determination of relative permittivity, ε_r. The trends reported in literature for ε_r versus measuring temperature by Perry et al. (2011) was shown to be an artefact of the fitting method.
- For full SOCs, jig inductance was shown to have a large impact on the IS results and jig correction was only possible in part. A methodology for jig correction was devised.

CHAPTER 2: IMPEDANCE SPECTROSCOPY OF SOLID OXIDE CELLS: THEORY & LITERATURE

This chapter provides an introduction to solid oxide cells and to impedance spectroscopy, before giving a more thorough review of the relevant literature.

2.1 SOLID OXIDE ELECTROLYSIS

Solid oxide cells (SOCs) can be operated in both fuel cell and electrolysis modes. In fuel cell mode electrochemical reactions cause a current to be drawn across the cell, supplying electrons, whereas in electrolysis mode an applied current drives the reactions in the opposite direction (Elder et al., 2014).

SOCs consist of a solid electrolyte sandwiched between two electrodes: one fuel-side and one oxygen-side. Gases flow continuously on both sides of the cell. In H_2O electrolysis, steam flows past the fuel electrode and is converted to hydrogen and oxide ions, *via* an electrochemical reaction, due to an applied current (see Figure 2.1a). This occurs at Triple Phase Boundaries (TPBs), where the gaseous, electron-conducting and oxide ion-conducting phases all meet. The oxide ions travel through the electrolyte to the other electrode, due to the difference in oxygen partial pressure in the cell. The overall cell reaction is given by:

$$2H_2O_{(g)} \rightarrow 2H_{2(g)} + O_{2(g)} \quad [2.1]$$

CO_2 electrolysis is also possible by replacing H_2O with CO_2 (Figure 2.1b). In this case the products are carbon monoxide and oxygen.

$$2CO_{2(g)} \rightarrow 2CO_{(g)} + O_{2(g)} \quad [2.2]$$

In addition, steam and carbon dioxide can be added together, known as co-electrolysis (Figure 2.1c). This gives both carbon monoxide and hydrogen as products; the mixture, called syngas, can be used to synthesise hydrocarbons. The overall cell reaction is given by:

$$H_2O_{(g)} + CO_{2(g)} \rightarrow CO_{(g)} + H_{2(g)} + O_{2(g)} \quad [2.3]$$

As well as the electrochemical reactions occurring, the reverse water gas shift (RWGS) chemical equilibrium reaction also occurs:

$$CO_{2(g)} + H_{2(g)} \rightleftharpoons CO_{(g)} + H_2O_{(g)} \quad [2.4]$$

The direction of this reaction depends on the cell operating conditions and shifts to the right as temperature increases.

Solid Oxide Cells are named after the type of electrolyte material used: solid oxides, typically yttria stabilised zirconia (YSZ). YSZ is a good oxygen ion conductor at high temperatures; the cell must be operated at high enough temperatures for suitably

low resistances to be obtained, generally between 700 and 850 °C. YSZ has high mechanical and high-temperature stability, adding to its suitability (Elder et al., 2014). Other possibilities for electrolyte materials include lanthanum gallate doped with strontium and magnesium (LSGM) or gadolinium-doped ceria (GDC). As some electrical conduction can occur in GDC, it is typically combined with a thin layer of YSZ, to ensure there is no electrical pathway between the electrodes through the electrolyte (Elder et al., 2014, Shri Prakash et al., 2018). The following discussion is based on electrolysis mode.

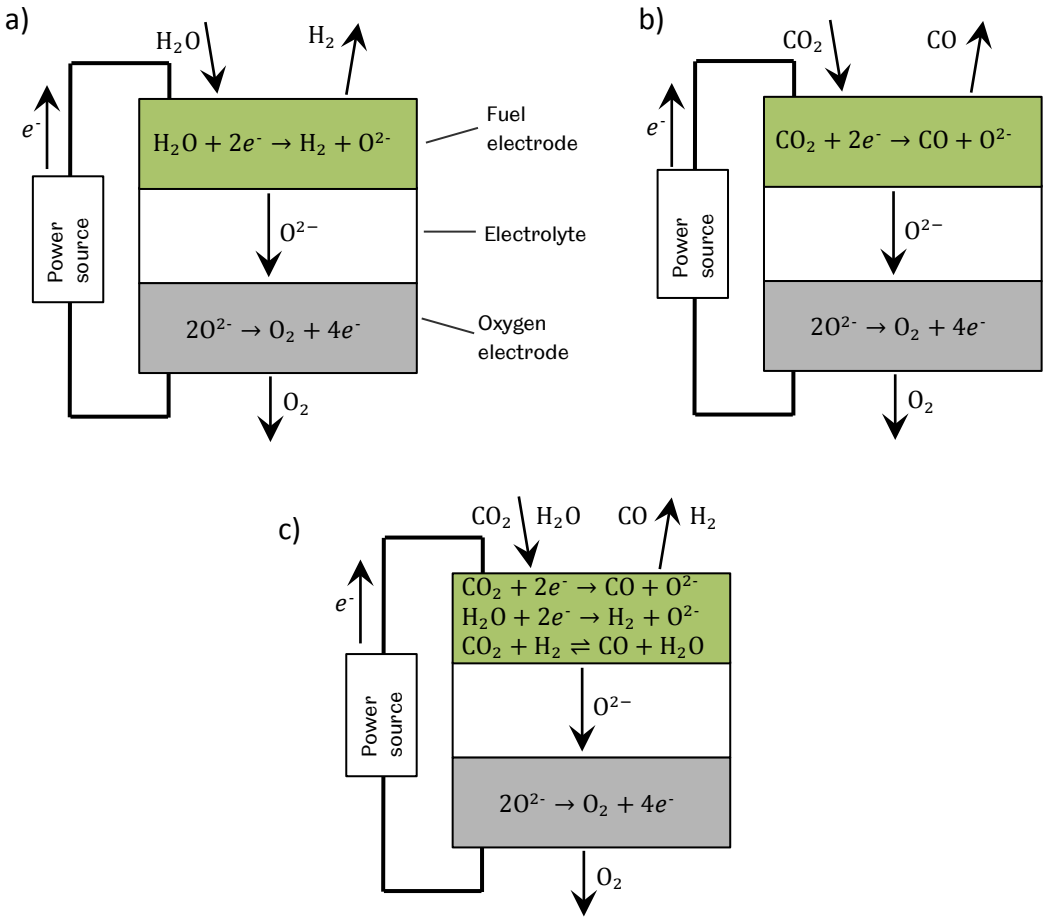

Figure 2.1: Schematic of a solid oxide cell undergoing electrolysis with the following fuels: a) water, b) carbon dioxide and c) water and carbon dioxide co-electrolysis.

The electrodes need to be designed to facilitate the interaction of electronic, ionic and gas phases at TPBs. Typically, the fuel electrode is made of Ni-YSZ: a ceramic-metal composite. Ni is a good electronic conductor, as well as an efficient catalyst, while YSZ is a good oxygen ion conductor. The electrode is porous, to allow the supply of gases. The oxygen electrode must be stable at high oxygen partial pressure and needs to catalyse the formation of oxygen from oxide ions (Elder et al., 2014). Oxygen electrodes are either composites of electronic or ionic conductors, such as lanthanum strontium manganite (LSM) mixed with YSZ (Wilson et al., 2009), or

mixed ionic-electronic conductors, for example: lanthanum ferrite doped with strontium and cobalt (LSCF) (Ebbesen et al., 2014).

At zero current, the cell has a finite voltage across it. The theoretical value is equal to the Nernst potential V_N. This outlines the deviation from the ideal standard potential E^0, calculated at standard state conditions, due to variations for example in temperature and partial pressure. For example, for H_2O electrolysis (Pilatowsky et al., 2011):

$$V_N = E^0 + \frac{RT}{nF} \ln\left(\frac{p_{H_2O}}{p_{H_2} p_{O_2}^{1/2}}\right) \quad [2.5]$$

Here, R is the universal gas constant, T is the temperature in Kelvin, n is the number of electrons transferred per molecule of oxygen, F is the Faraday constant and p_i represents the partial pressure of species i.

The measured value of the voltage, termed the open circuit voltage (OCV), tends to be slightly lower than V_N, for example, due to gaseous or electronic leaks (Ebbesen et al., 2009, Elder et al., 2014).

When a current flows through the cell, the change in cell voltage is called the overpotential or polarisation, η:

$$V = V_{OC} + \eta \quad [2.6]$$

The overpotential is positive for electrolysis and negative for fuel cell mode. It varies with current, as illustrated in Figure 2.2, and has several components contributing to it: ohmic loss, diffusion polarisation, conversion polarisation and activation polarisation. These are described below.

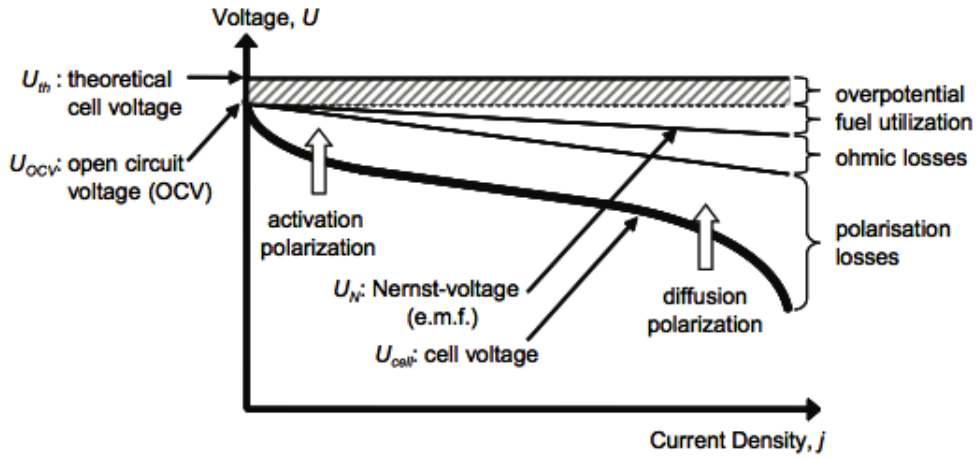

Figure 2.2: Overall polarisation and the contributions of different polarisation mechanisms in a fuel cell as a function of current density (Leonide, 2010).

Ohmic losses are mainly due to the resistance of O^{2-} transport through the electrolyte but also have contributions from the electronic resistance of the

electrodes and contact resistances between cell components. Ohmic polarisation η_Ω is given by:

$$\eta_\Omega = iR_\Omega \quad [2.7]$$

where i is the current density: current per unit area (A/cm^2). The total ohmic resistance R_Ω is independent of i, hence the ohmic polarisation contribution is proportional to current density.

Diffusion polarisation originates from mass transport restrictions in gas diffusion through the porous electrodes and depends on the thickness of the electrodes, their microstructure and the diffusivity of the gases. It is seen particularly at the fuel electrode, at large currents, where water and carbon dioxide must diffuse towards the TPBs and hydrogen and carbon monoxide must diffuse away from them to the bulk gas.

Conversion polarisation also relates to gas transport restrictions, in this case due to consumption of fuel gases. Conversion increases with current and hence this polarisation increases with current. In contrast, *activation polarisation* dominates at low current. It results from the activation energy needed to overcome the energy barrier for the reactions to occur; as temperature increases, the activation polarisation decreases.

Current density-voltage (i-*V*) curves are used to show the voltage response of a cell as a function of current density. The initial gradient of the curve is equal to the total cell resistance, often quoted as an Area Specific Resistance (ASR) with the units Ωcm^2. The lower the ASR, the lower the energy requirements. Ebbesen et al. (2009, 2012) and Stoots et al. (2009) found the ASR of an SOC undergoing CO_2 electrolysis was higher than for H_2O electrolysis, seen in Figure 2.3 by the steeper gradient of the green line compared to the blue line. H_2O and CO_2 co-electrolysis gave an ASR close to that for just H_2O, as shown in Figure 2.3 by the nearly parallel blue and black lines. Therefore, co-electrolysis is advantageous as it has lower energy requirements than obtaining both products by individual electrolysis. This is thought to be due to a significant percentage of CO being produced *via* the RWGS reaction, rather than *via* electrolysis (Stoots et al., 2009).

While i-*V* curves show overall polarisation as a function of current, it is impossible to extract information on the individual polarisation contributions from such graphs. However, as different processes have different time scales associated with them, when an oscillating current is applied, they respond differently depending on the frequency of oscillation. At slow oscillation, processes with large time scales are rate-limiting, such as ion/gas diffusion, whereas at fast oscillation, processes with small time scales are rate-limiting, for example electronic conduction. This is the basis for Impedance Spectroscopy (IS), described in Section 2.2.

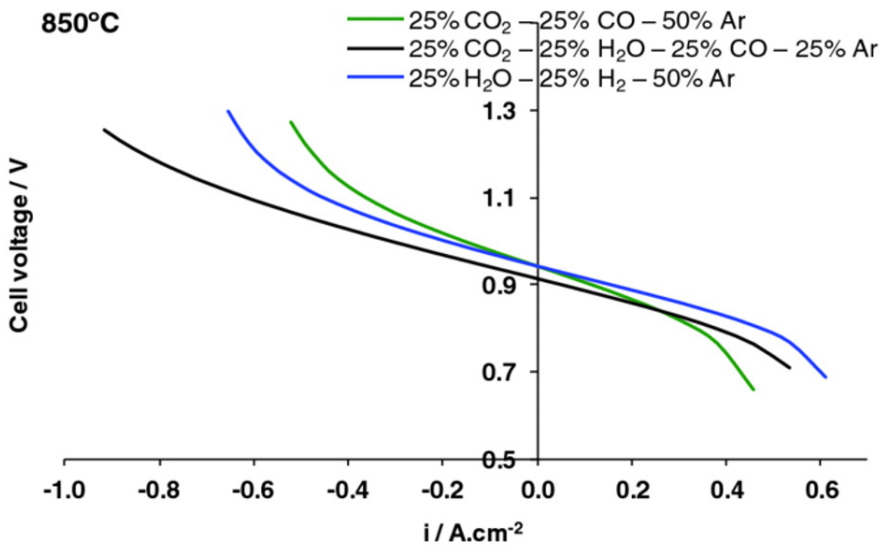

Figure 2.3: Current-voltage curves at 850 ^{o}C for: a CO_2/CO system, a CO_2/H_2O/CO system and for a H_2O/H_2 system (Ebbesen et al., 2012).

2.2 FUNDAMENTALS OF IMPEDANCE SPECTROSCOPY

In Impedance Spectroscopy (IS), a sinusoidal voltage or current is applied across a cell at a range of frequencies and the resulting current or voltage is measured. The voltage and current can be expressed as:

$$V = V_0 \sin(\omega t + \phi_V) \quad [2.8]$$

$$I = I_0 \sin(\omega t + \phi_I) \quad [2.9]$$

Here, V_0 and I_0 are the peak voltage and current values, ϕ_V and ϕ_I are the phases of the voltage and current signals, respectively, and ω is the angular frequency, equal to $2\pi f$, where f is the frequency in Hz.

Impedance Z* is equal to the ratio of the voltage to the current in the frequency domain. It is given by:

$$\mathrm{Z}^*(f) = |\mathrm{Z}^*| e^{\mathrm{j}\theta} \quad [2.10]$$

where j is the square root of -1. The modulus $|\mathrm{Z}^*|$ and phase θ are given by:

$$|\mathrm{Z}^*| = \frac{V_0}{I_0} \quad [2.11]$$

$$\theta = \phi_V - \phi_I = \frac{\Delta t}{T} \quad [2.12]$$

where Δt is the time difference between the peak voltage and current signals and *T* is the time period of the wave (see Figure 2.4), equal to the reciprocal of the frequency f. Impedance is a complex quantity, denoted by *, allowing for the possibility of the voltage and current signals being out of phase with each other. Z* can also be written in terms of real and imaginary components:

$$\mathrm{Z}^*(f) = \mathrm{Z}'(f) + \mathrm{jZ}''(f) \quad [2.13]$$

where Z' and Z'' are the real and imaginary components, respectively. Impedance represents the complex resistance to alternating current; the real part represents resistance and the imaginary part represents reactance.

Resulting data are typically plotted on a Z* Nyquist plot, showing the imaginary component versus the real component for different frequencies. Note that often –Z'' is plotted so that the resulting data appears in the upper right-hand quadrant of the

graph. Data can also be represented on a spectroscopic plot, showing either |Z*| and θ, or Z' and Z'' against the logarithm of frequency.*

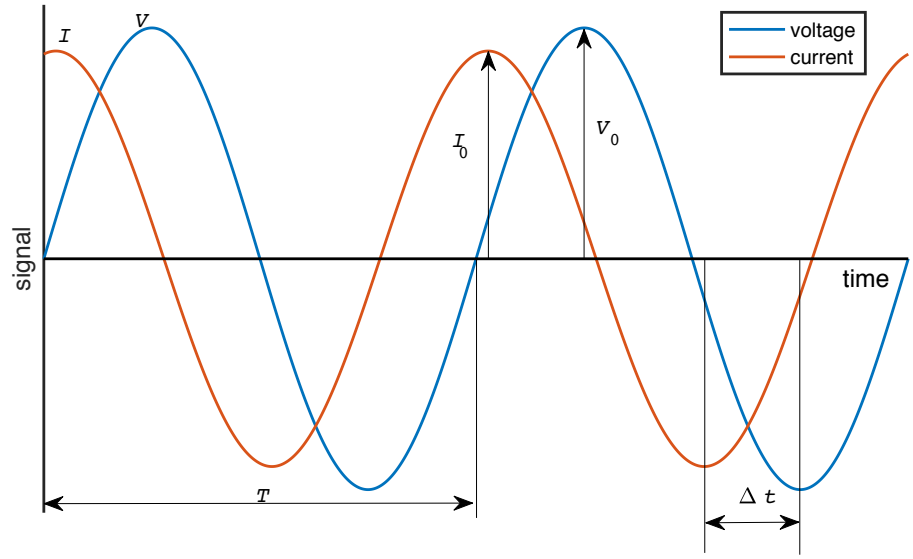

Figure 2.4: Schematic of voltage and current signals to illustrate the calculation of impedance

In addition to impedance Z*, data can also be expressed in other immittance formalisms: admittance Y*, electric modulus M* and permittivity ε* (Abram et al., 2003), which are related by the following equations.

$$\mathrm{Y}^* = \frac{1}{\mathrm{Z}^*} \quad [2.14]$$

$$\mathrm{M}^* = j\omega C_o \mathrm{Z}^* \quad [2.15]$$

$$\varepsilon^* = \frac{1}{\mathrm{M}^*} \quad [2.16]$$

where C_0 is the vacuum capacitance of the cell, given by:

$$C_o = \varepsilon_o \frac{A}{t} \quad [2.17]$$

Here, ε_o is the permittivity of free space, *A* is the electrode area perpendicular to the electric current and *t* is the thickness of the sample.

For fuel cells, Z* is often quoted in units of $\Omega.\mathrm{cm}^2$, dividing the impedance by a geometric factor, gf:

$$\mathrm{gf} = \frac{1}{A} \quad [2.18]$$

The thickness of the cell is left uncorrected due it containing multiple layers, which are made of different materials, making it impossible to standardise the impedance results.

* In this work, the following notation is used: **X* plot** refers to a Nyquist plot of X'' versus X', and **X'** (or **X''**) **spectroscopic plot** or **spectrum** refers to a plot of X' (or X'') against the logarithm (base 10) of frequency, where X is one of the immittance formalisms: Z, Y, M or ε.

2.3 EQUIVALENT CIRCUIT THEORY

Equivalent circuits can be fitted to impedance data. This enables the extraction of physical parameters that describe the system and hence processes occurring in a sample can be characterised.

2.3.1 FUNDAMENTAL COMPONENTS

An equivalent circuit is made up of electrical components. The three fundamental components are a resistor, a capacitor and an inductor, illustrated in Figure 2.5.

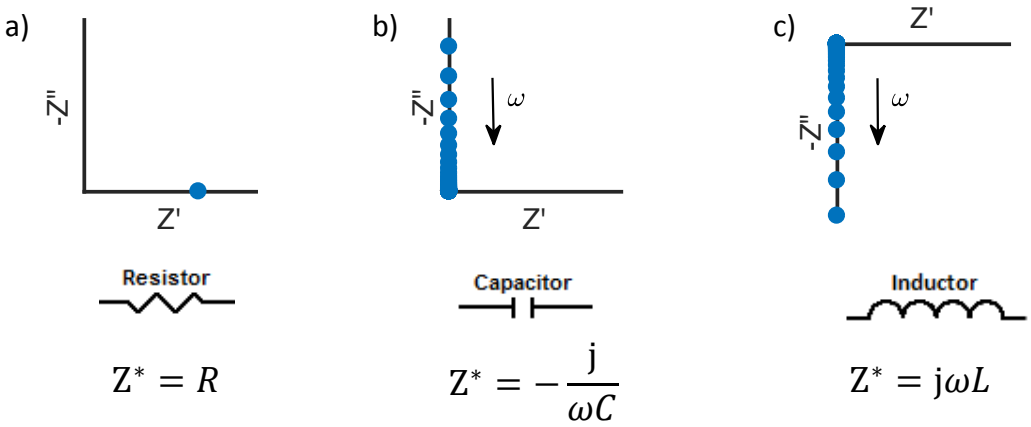

Figure 2.5: Z* Nyquist plot and electrical symbol for a resistor, capacitor and inductor. *R* stands for resistance, *C* for capacitance and *L* for inductance. ω is the angular frequency ($2\pi f$).

An ideal resistor has a constant impedance, equal to the resistance, *R*, measured in Ohms (Ω). There is no imaginary component, hence the voltage and current signals are always in phase. In contrast, a capacitor or an inductor has only an imaginary impedance component. The voltage and current signals are 90° out of phase, with current lagging voltage for an inductor, and current leading voltage for a capacitor. The impedances of both components are a function of frequency (see Figure 2.5), with the impedance of the capacitor decreasing in magnitude as frequency increases, while that of the inductor increases with frequency. A capacitor is characterised by its capacitance, *C*, measured in Farads (F) and an inductor by its inductance, *L*, measured in Henrys (H).

Components can be joined together to create additional features. When components are joined in series, impedance is additive (Gamry, 2015):

$$\mathrm{Z}^* = \mathrm{Z}_1^* + \mathrm{Z}_2^* \qquad [2.19]$$

For example, combining a resistor and capacitor in series gives a Z' contribution equal to the resistance and a Z'' contribution equal to that of the capacitor. Plotted on a Z* Nyquist diagram, this shifts the impedance from that of the capacitor to the right of the plot by the value of the resistance (see Figure 2.6a).

The impedance of components in parallel is obtained by summing the admittance of each component. This is equivalent to summing the reciprocals of the impedances:

$$\frac{1}{Z^*} = \frac{1}{Z_1^*} + \frac{1}{Z_2^*} \qquad [2.20]$$

Hence for a resistor and capacitor in parallel (termed an *RC* element):

$$Z^* = \frac{1}{\frac{1}{R} + j\omega C} = \frac{R}{1 + (\omega RC)^2} - j\frac{\omega R^2 C}{1 + (\omega RC)^2} \qquad [2.21]$$

This results in a semi-circle on the Z* Nyquist diagram (see Figure 2.6b) with a diameter equal to *R*. As frequency increases, the impedance moves anticlockwise around the arc. The angular frequency at the peak of the arc ω_0 is given by 1/*RC*. The inverse of ω_0 is termed the time constant, or relaxation time, τ:

$$\tau = \frac{1}{\omega_0} = RC \qquad [2.22]$$

The addition of a resistor R_s in series with an *RC* element shifts the semi-circle to the right by the amount R_s, as shown in Figure 2.6c; R_s is known as the series resistance; the polarisation resistance, R_{pol} is given by the difference between the total resistance (Z′ as ω tends to zero) and the series resistance. In this case R_{pol} is equal to the parallel resistor, *R*. Similarly, the polarisation impedance Z^*_{pol} is equal to the difference between the total impedance and any series components present.

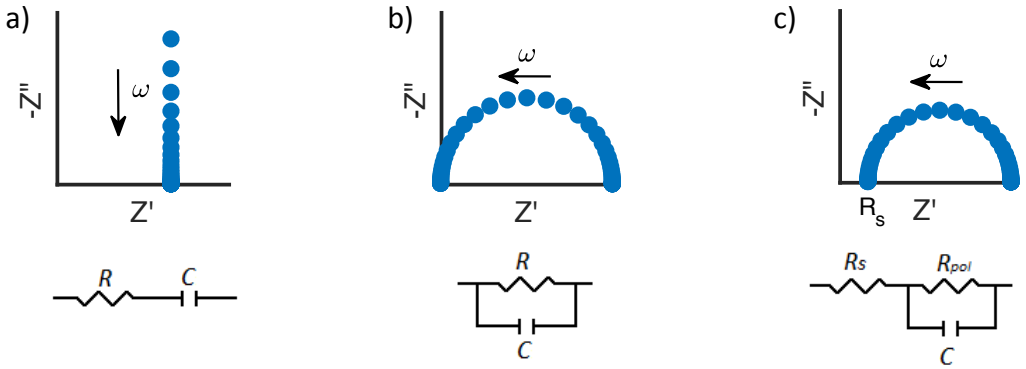

Figure 2.6: Z* Nyquist diagrams for a) resistor and capacitor in series, b) resistor and capacitor in parallel (RC element) and c) a resistor in series with an RC element.

The responses for a resistor and capacitor, both individually and combined in series and in parallel, for the remaining immittance formalisms (Y*, M* and ε*) are shown in Figure 2.7.

The electric modulus is additive for components in series and the reciprocals are additive in parallel, as for impedance. In contrast, Y* and ε* are additive for components in parallel and the reciprocals are additive in series.

A resistor gives a constant admittance equal to 1/*R* (Fig. 2.7a) and a capacitor gives only an imaginary component, the magnitude of which scales proportionally to ω (Fig. 2.7b). For a resistor and capacitor in series, the reciprocals of the admittance sum to give a semicircle with a diameter equal to 1/*R*, whereas for a parallel RC element the Y* values add to give the capacitance response shifted by 1/*R* (Figs

2.7c&d). This illustrates that the admittance magnitude is proportional to the inverse of the resistance, whereas impedance is proportional directly to the resistance.

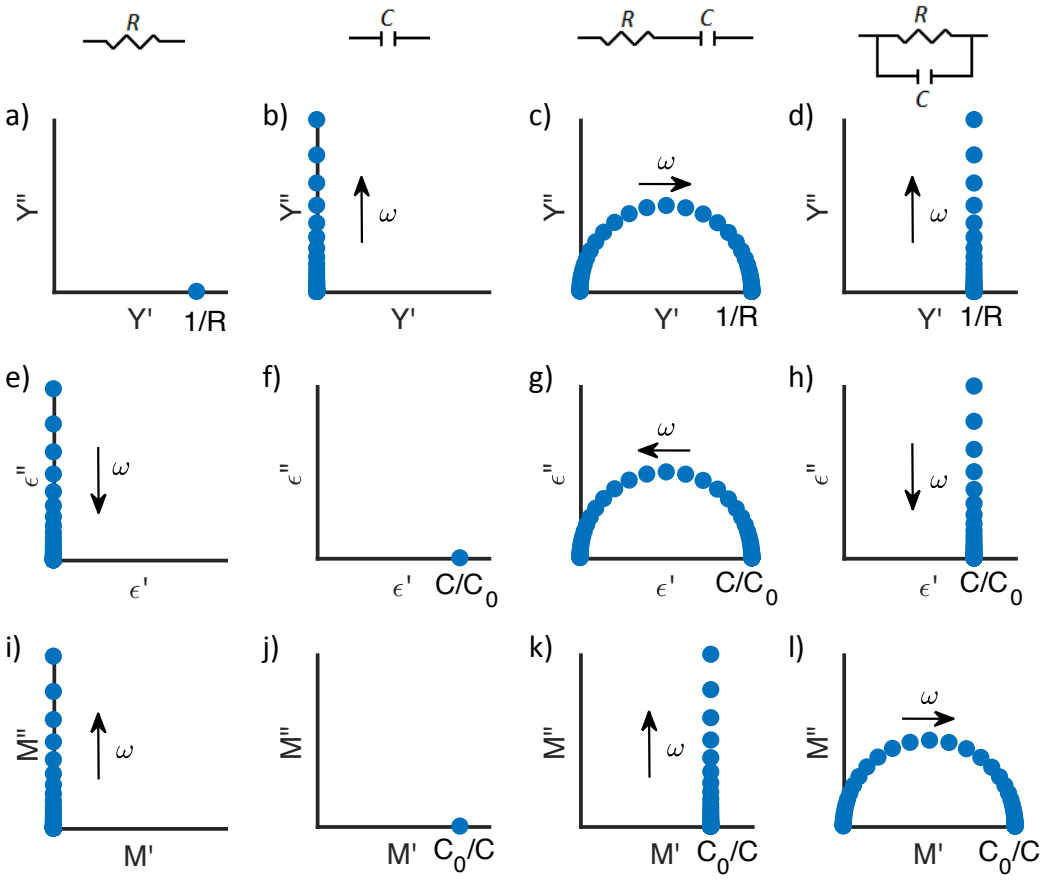

Figure 2.7: Nyquist diagrams showing the admittance (a-d), electric modulus (e-h) and permittivity (i-l) for a resistor (a, e, i), a capacitor (b ,f, j), a resistor and capacitor in series (c, g, k) and a resistor and capacitor in parallel (d, h, l).

In contrast, permittivity and electric modulus scale with the capacitance and the inverse of the capacitance, respectively. A capacitor is hence represented as a single point, constant with frequency (Figs 2.7f,j), while a resistor gives only an imaginary component ε^* or M* that changes with frequency (Figs 2.7e,i). When the components are added, they give a straight line offset by the capacitance scaling (Figs 2.7h,k), and when the reciprocals are added, a semicircle is obtained (Figs 2.7g,l).

Z* and Y* are used primarily to examine resistances, with Z* dominated by large resistances and *Y** by small resistances; conversely, ε^* and M* are used primarily to examine capacitances, and are dominated by large and small capacitances, respectively.

For electro-ceramic materials, for example YSZ, the Brickwork layer model (Verkerk et al., 1982), see Section 5.1.3, is often used to describe the bulk and grain boundary components; each are represented by a parallel RC-type element connected in series, see Section 4.3.1 (van Dijk and Burggraaf, 1981). Similarly for fuel cells, elements for

different processes tend to be connected to each other in series, illustrated later in Section 2.4.3.

When two *RC* elements are combined in series, the result depends on the magnitudes of the components. When the relaxation times of each arc are significantly different from each other, two distinct semicircles are seen with diameters R_1 and R_2 (Figure 2.8b, blue line); if the resistances are the same order of magnitude as each other, which is usually true for SOCs, then $C_1 \ll C_2$ for this case. As the time constants tend towards each other, the arcs merge together (Figure 2.8b, purple and green lines). The total resistance of the two arcs is still equal to the sum of R_1 and R_2 but the individual arcs are less well defined or not distinguishable. This becomes a problem when attempting to characterise each individual process occurring, as discussed further in Section 2.4.1.

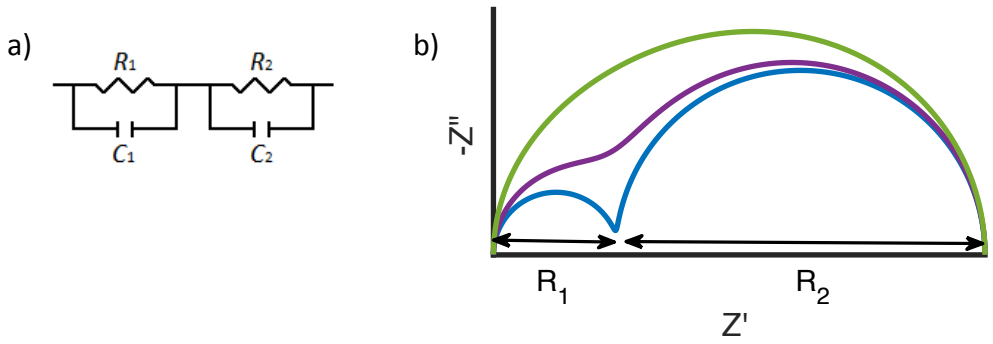

Figure 2.8: a) Equivalent circuit for two RC elements connected in series. b) Resulting Z* Nyquist diagram for: $R_1C_1 << R_2C_2$ (blue line), $R_1C_1 < R_2C_2$ (purple line) and $R_1C_1 \sim R_2C_2$ (green line).

2.3.2 Additional components

In addition to the fundamental components described above, there are three further components commonly used to describe diffusion effects: the constant phase element, Warburg element and Gerischer element.

A *constant phase element* (CPE), *Q*, is given by:

$$Y^* = Y_0(j\omega)^n = Y_0\omega^n\left[\cos\left(\frac{n\pi}{2}\right) + j\sin\left(\frac{n\pi}{2}\right)\right] \qquad [2.23]$$

and has two definable parameters that vary with fitting, Y_0 and n. Y_0 is a proportional factor and n is the exponential coefficient. On a Z* Nyquist plot, it is represented by a straight line with the phase angle $0.5n\pi$, relative to the real axis (see Figure 2.9a). When $n = 1$, it represents a capacitor with capacitance Y_0 and when $n = 0$ it behaves as a resistor with a resistance $1/Y_0$. For values close to 0 or 1, it behaves as an imperfect resistor or capacitor, respectively. A constant phase element in parallel with a resistor gives a depressed semi-circle, with the extent of depression depending on the value of n (see Figure 2.9b). Note that to illustrate the extent of depression of the arcs, it is important to plot Z* plots with equally scaled axes.

A *Warburg element* in its simplest form, the infinite Warburg, is merely a *Q* element with $n = 0.5$. This gives identical imaginary and real impedance components and a phase angle of 45° (see Figure 2.10a). It is used to model diffusion in electrodes; impedance increases with decreasing frequency, as concentration changes in the electrode become more significant because a longer period of time allows more reactant to be converted to product.

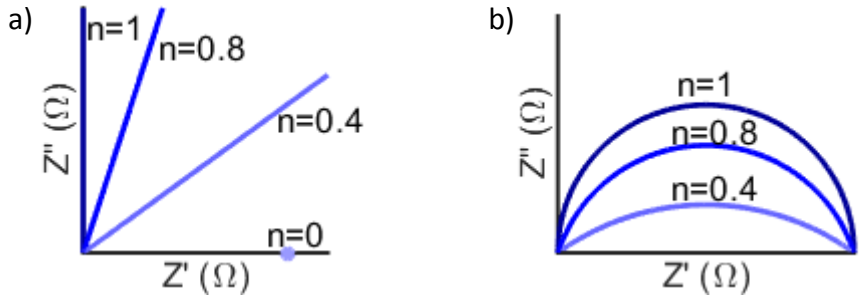

Figure 2.9: a) Z* Nyquist plot for a constant phase element (*Q* element) at varying values of n. b) The corresponding Z* Nyquist plot for a *Q* element in parallel with a resistor.

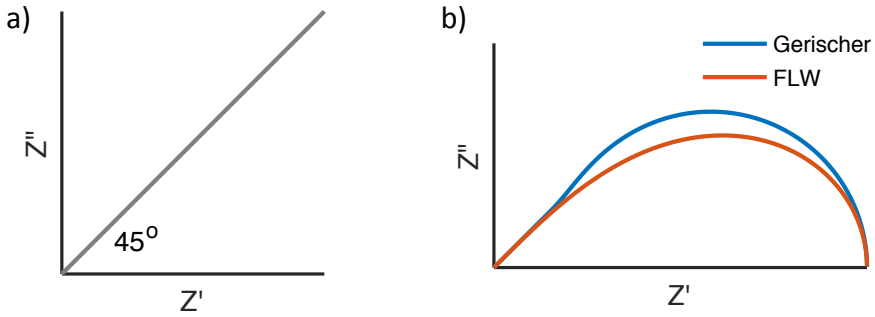

Figure 2.10: a) Nyquist diagram for an infinite Warburg element and b) for a Finite Length Warburg (FLW) element and a Gerischer element.

Due to the finite length of electrodes, however, when frequency tends to zero the impedance response deviates from this model. In SOCs the electrodes have a continual supply of fuel at the electrode boundary, which can be modelled as a Finite Length Warburg (FLW) element (Scribner Associates, 2000), given by:

$$\mathrm{Z}^{*}_{FLW} = W_R \frac{\tanh((j\omega W_T)^P)}{(j\omega W_T)^P} \qquad [2.24]$$

where W_R, W_T and P are model parameters. For a pure diffusion limitation, P = 0.5 and W_T is given by:

$$W_T = \frac{d^2}{\mathcal{D}_{\text{eff}}} \qquad [2.25]$$

where d is the depth of the electrode and $\mathcal{D}_{\text{eff}}$ is the effective diffusion coefficient. In this case, the high frequency response is identical to the infinite Warburg element. At low frequencies the impedance remains finite and tends towards the behaviour of a resistor as the frequency tends to zero, see Figure 2.10b (orange line). There is also a Finite Space Warburg (FSW) element (Jossen, 2006), which models a finite length

electrode with a finite amount of fuel, occurring in closed systems, for example: a battery. However, this is irrelevant for SOCs.

Another extension to the infinite Warburg element is the Gerischer element:

$$\mathrm{Z}^{*} = \frac{Z_0}{(k_a + j\omega)^{0.5}} \qquad [2.26]$$

where Z_0 and k_a are model parameters (Scribner Associates, 2000). It combines semi-infinite diffusion with a chemical side reaction (Boukamp and Bouwmeester, 2003) and is derived from Fick's second law by incorporating a sink term from the chemical reaction occurring, with reaction rate k_a (Boukamp, 2004). It is similar to the FLW element and again resembles a CPE at high frequency. It is shown in Figure 2.10b, blue line.

2.4 Literature Review

2.4.1 Impedance Spectroscopy

IS spectra of SOCs contain information about the different processes that contribute to cell polarisation, discussed in Section 2.1, as different processes become rate-limiting at different frequencies. IS can hence be used to characterise these processes as they occur.

An advantage of IS is that it is a non-destructive method so multiple measurements can be taken for the same cell (Huang et al., 2007). Also, measurements can be taken *in situ* (Nechache et al., 2014), enabling data to be compared for a range of operating conditions. However, it can be non-trivial to determine the physical origin of the features present in the spectra; fuel cells contain multiple components each of which may contribute to multiple processes. In addition, to resolve the processes clearly, the time constants associated with each process need to differ from each other by at least two orders of magnitude.

There are a variety of methods used to help separate the processes and identify the physical origin of each individual one. For example, processes occurring at a specific electrode can be assigned by studying the responses of fuel and oxygen electrodes separately, using either reference electrodes or symmetrical cells.

Reference electrode cells contain three electrodes: a working electrode, a counter electrode and a reference electrode (Finklea et al., 2013). A current is applied between the two conventional electrodes, the working and counter electrodes, and their electrode potentials are measured with respect to the reference electrode, thus producing signals for each electrode that are in theory separable from the total cell performance (Huang et al., 2007). The two signals should add to give the total cell resistance (Mogensen and Hendriksen, 2003).

To obtain accurate results, the geometry and position of the electrodes is of great importance (Nagata et al., 1994, Winkler et al., 1998); however, even a slight misalignment causes large errors in the separate electrode impedance measurements and is unavoidable due to uncertainties from fabrication methods (Adler, 2002). Even with perfect alignment, the electrode results often do not add up to the total cell response, for example because fabrication methods for three electrode cells differ to those for conventional cells (Adler, 2002, Mogensen and Hendriksen, 2003, Hsieh et al., 1997). The use of reference electrodes is hence limited and often wholly inappropriate (Finklea et al., 2013).

Another technique to separate the processes occurring at the fuel and oxygen electrodes is to use symmetrical cells. They contain the same electrode on each side

of the electrolyte and are fed with the same gas composition on both sides; hence Barfod et al. (2007) states that these cells are suitable only for measurement at open circuit voltage. However, degradation experiments have been undertaken by Hughes et al. (2012, 2013) under applied current. In current-switching operation, the current direction was switched every thirty minutes, so that the electrodes should evolve identically and maintain symmetry (Hughes et al., 2012). Impedance results from these cells were halved to give the polarisation resistance for a single electrode and the ohmic resistance for half the electrolyte thickness. Experiments were also carried out with fixed current direction (Hughes et al., 2013), where cells were presumed to become asymmetric and hence this complicated IS interpretation. A disadvantage of symmetrical cells, as with reference electrodes, is that the cell differs from the operational cell, and hence the processes occurring will not be identical (Jensen et al., 2009).

An example spectrum from a symmetrical cell with Ni-YSZ electrodes is shown in Figure 2.11 (Barfod et al., 2007). Two individual arcs stemming from the fuel electrode side are seen and are marked by a dotted line.

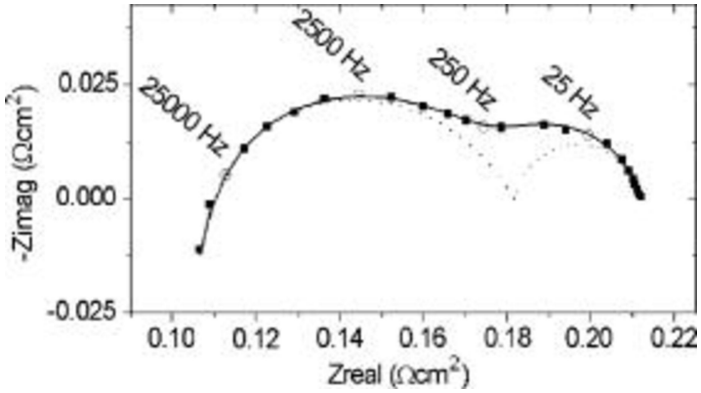

Figure 2.11: Z* plot of a symmetrical cell with Ni-YSZ electrodes, under a fuel composition of 95:5% H_2:H_2O and a temperature of 850 ^{o}C (Barfod et al. 2007).

An alternative to altering the cell setup is to compare spectra from a full cell taken under different operating conditions, to observe how spectra are affected by such changes; for example, fuel rate and composition, partial oxygen pressure at the oxygen electrode and the operating temperature (Barfod et al., 2007, Leonide et al., 2008). Further data analysis techniques can then be used to elucidate which processes are specifically affected. One such technique is the Analysis of Differences in Impedance Spectra (ADIS), discussed further in Section 2.4.2.

Distribution of Relaxation Times (DRT), first proposed for use in fuel cell applications by Schichlein et al. (2002), has also been used by several authors to investigate the dependence of parameters such as temperature and gas concentration on the individual processes, which allows them to be assigned to individual electrodes (Leonide et al., 2008, Graves et al., 2011a). DRT is the result of deconvolving the

impedance spectrum (see Section 2.4.6), giving enhanced resolution of processes occurring. Schichlein et al. (2002) found that up to three processes per decade can be resolved, in contrast to the one process per two decades that can be resolved clearly in conventional Z* plots. This is discussed further in Section 2.4.6.

2.4.2 Analysis of Differences in Impedance Spectra (ADIS)

The Analysis of Differences in Impedance Spectra (ADIS) is a method outlined by Jensen et al. (2007) & (2009) where spectra are subtracted from each other to highlight the differences seen with a change of operating conditions, such as gas composition and temperature (Barfod et al., 2007), and also with a change in time (Ebbesen and Mogensen, 2009, Jensen et al., 2013). Two possible subtraction methods are compared below to highlight how they are related and the differences there are between them.

The simplest subtraction method is to subtract the imaginary part of the impedance of one spectrum, *A* from another, *B*, at each frequency point, i:

$$\Delta \mathrm{Z''}_i = \mathrm{Z''}_{B,i} - \mathrm{Z''}_{A,i} \qquad [2.27]$$

Alternatively, the differential of the real part of the impedance with respect to the natural log of frequency $\dot{\mathrm{Z}}'$ can be found for each spectrum, and these can then be subtracted from each other:

$$\Delta \dot{\mathrm{Z}}'_k = \left.\frac{dZ'}{d\ln f}\right|_{B,i} - \left.\frac{dZ'}{d\ln f}\right|_{A,i} \qquad [2.28]$$

This has the effect of accentuating the peaks, when plotting against log frequency, illustrated in Figure 2.12. Firstly, the Z'' spectroscopic plot is shown for an equivalent circuit with two RC elements, with a slight change in parameters between *A* and *B*. Figure 2.12b shows $\dot{\mathrm{Z}}'$ for both *A* and *B* which has narrower peaks than Z''. Figure 2.12c shows ΔZ'' and $\Delta\dot{\mathrm{Z}}'$. The peaks from $\Delta\dot{\mathrm{Z}}'$ are sharper than for ΔZ''.

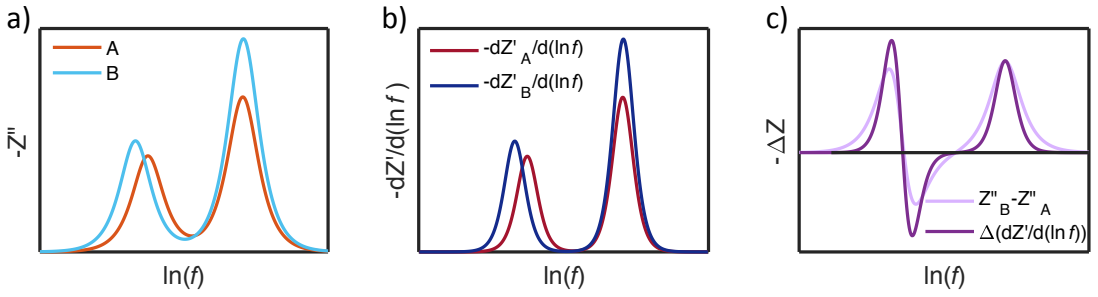

Figure 2.12: Response A and B, each for two RC elements in series, with a slight change in parameters between A and B. a) Z'' spectroscopic plot for A and B, b) the differential of Z' with respect to log frequency ($\dot{Z}'$), c) the subtraction of A from B for both *Z*'' and $\Delta\dot{Z}'$.

The reason for this is demonstrated using an *RC* element, where the impedance is given by:

$$\mathrm{Z}^* = \frac{R}{1+x} \qquad [2.29]$$

where $x = j\omega\tau$, with the angular frequency $\omega = 2\pi f$ and time constant $\tau = RC$. Differentiate with respect to the natural logarithm of frequency and use the chain rule to find the solution:

$$\dot{\mathrm{Z}}^* = \frac{\partial \mathrm{Z}^*(x)}{\partial \ln f} = \frac{\partial \mathrm{Z}^*}{\partial x}\frac{\partial x}{\partial f}\frac{\partial f}{\partial \ln f} = \frac{-R}{(1+x)^2}\, j2\pi\tau f = \frac{-Rx}{(1+x)^2} \qquad [2.30]$$

Multiply through by $(1-x)^2$ so that the denominator is in terms of x^2:

$$\dot{\mathrm{Z}}^* = \frac{-Rx(1-x)^2}{(1+x)^2(1-x)^2} = \frac{R[2x^2 - x - x^3]}{(1-x^2)^2} \qquad [2.31]$$

Substitute for x:

$$\dot{\mathrm{Z}}^* = \frac{-2R(\omega\tau)^2 + jR((\omega\tau)^3 - \omega\tau)}{[1+(\omega\tau)^2]^2} \qquad [2.32]$$

Hence an expression for the differential of the real part of the impedance is found:

$$\dot{\mathrm{Z}}' = -2R\left(\frac{\omega\tau}{1+(\omega\tau)^2}\right)^2 \qquad [2.33]$$

Compare to Z'':

$$\mathrm{Z}'' = -R\frac{\omega\tau}{1+(\omega\tau)^2} \qquad [2.34]$$

Therefore:

$$\dot{\mathrm{Z}}' = \frac{2}{R}(Z'')^2 \qquad [2.35]$$

This shows that for an *RC* element $\dot{\mathrm{Z}}'$ is proportional to the square of Z'', hence accentuating the peaks.

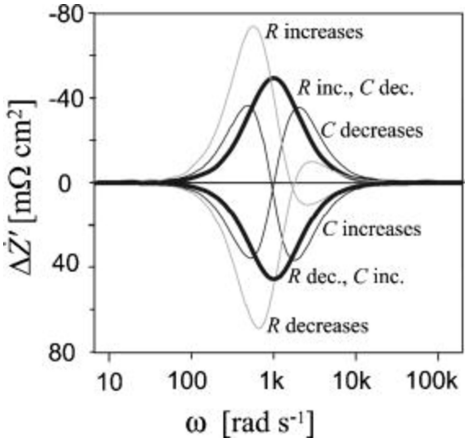

Figure 2.13: Theoretical $\Delta\dot{\mathrm{Z}}'$ spectra for various changes in an *RC* circuit, with initial values of *R* and *C* at 1 cm^2 and 1 mF/cm^2, respectively. All increases are by 10% and decreases by 9% (Jensen et al., 2007).

The nature of ΔZ'' and $\Delta\dot{\mathrm{Z}}'$ gives information about the change between the spectra. If τ is the same for both *A* and *B*, then ΔZ'' and $\Delta\dot{\mathrm{Z}}'$ are symmetrical about the characteristic frequency; values are either all positive if *B* is more resistive and less

capacitive than *A*, or all negative if *B* is less resistive and more capacitive than *A*, see Figure 2.13. If τ changes, then the curves are no longer symmetrical. $\Delta\dot{Z}'$ spectra for a change in only *R* or *C* are also shown in Figure 2.13 and contain both positive and negative values. In Figure 2.12c, the high frequency feature has the same constant for both spectra, whereas for the low frequency feature, both *R* and *C* increase.

2.4.3 Equivalent Circuits

Equivalent circuits (ECs) are fitted to IS data to describe the processes occurring, and are constructed from a number of components. Different circuits can give the same fit mathematically, hence the fitting of circuits can be somewhat arbitrary (Huang et al., 2007) and the physically correct equivalent circuit is often unknown (Jensen et al., 2013), particularly when there are processes with time constants of similar orders of magnitude. Plotting IS spectra and their corresponding equivalent circuits using a variety of immittance formalisms can help determine the accuracy of a fit, as fitting an equivalent circuit to data in the Z* formalism might overlook features seen in the other formalisms (Abram et al., 2003). To the author's knowledge, Z* is the only immittance formalism that has been used to describe SOCs. However, individual components, such as YSZ, have been analysed in other formalisms, such as Y* (Bauerle, 1969).

To optimise the fitting parameters, a complex non-linear least squares (CNLS) fit can be carried out, for example, using ZView (Scribner Associates, 2000) or EQIVCT (Boukamp, 1986). By repeating for spectra at a range of operating conditions, such as temperature and gas composition, trends of the electrical parameters can be obtained. These can then be related back to trends in physicochemical processes with the caveat that their physicality is limited by the physicality of the equivalent circuit applied (Nechache et al., 2014).

Internal factors such as cell materials and microstructure also affect impedance spectra; hence different cells can give significantly different impedance responses. An equivalent circuit should therefore only be used for the specific type of cell it is defined for (Barfod et al., 2007), highlighting the complexity of fitting equivalent circuits to spectra from SOCs.

A number of equivalent circuits for full cells have been reported in the literature. For example, Barfod et al. (2007) found five distinct processes occurring in their cells, which were anode (or fuel electrode[†]) supported cells with a Ni-YSZ fuel electrode, a YSZ electrolyte and an LSM-YSZ oxygen electrode (Hagen et al., 2006). Experiments were carried out with a fuel gas composition of 75:25% H_2:H_2O, with air at the

[†] In fuel-cell-mode, the fuel electrode is the anode and the oxygen electrode is the cathode. However, in electrolysis, the current direction is reversed so the fuel and oxygen electrodes are now the cathode and anode, respectively. Here, the fuel-cell-mode notation is used.

oxygen side and an operating temperature of 700 °C. The impedance spectrum, along with the proposed equivalent circuit, is shown in Figure 2.14. The circuit consists of a series inductance (discussed in Section 2.4.5) and resistance, and five *RQ* elements; 17 parameters in total. Some processes might be better described by Warburg or Gerischer elements but the analysis was not detailed enough to distinguish between them, hence *RQ* elements were used for convenience.

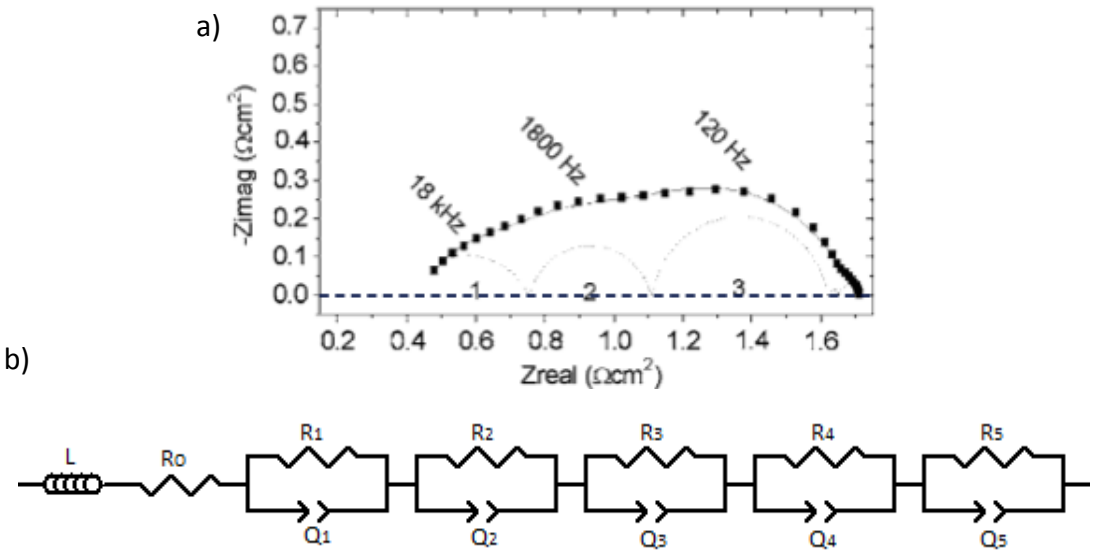

Figure 2.14: a) Z* Nyquist plot of an SOC at 700 °C with a fuel gas composition of 75:25% H_2:H_2O, and air at the oxygen side (Barfod et al., 2007). Measured data is shown as squares, the fitted spectrum is marked with a full line and the dotted lines show the individual elements within the model. b) The corresponding equivalent circuit.

The first, or highest frequency process, denoted in the figure by 1, is thought to describe the transport of oxide ions at the LSM-YSZ interface, through the YSZ of the electrode. Process 2 is a fuel-side process, involving dissociative adsorption of hydrogen onto the electrode and the transport of the resulting species to the TPBs. The third process is related to the dissociative adsorption of oxygen and the transfer of oxygen species to or from TPBs. The remaining processes 4 and 5 are small in magnitude, under the conditions at which this spectrum was acquired, and correspond to gas diffusion and gas conversion, respectively.

A cross-section micrograph of a different cell is shown in Figure 2.15 (Leonide, 2010, Leonide et al., 2008). This cell is also a fuel-electrode supported cell with a Ni-YSZ fuel electrode and a YSZ electrolyte but here the oxygen electrode is made from LSCF, with a thin layer of GDC. An impedance spectrum from this cell, along with its corresponding equivalent circuit with 15 parameters, is shown in Figure 2.16 (Leonide, 2010).

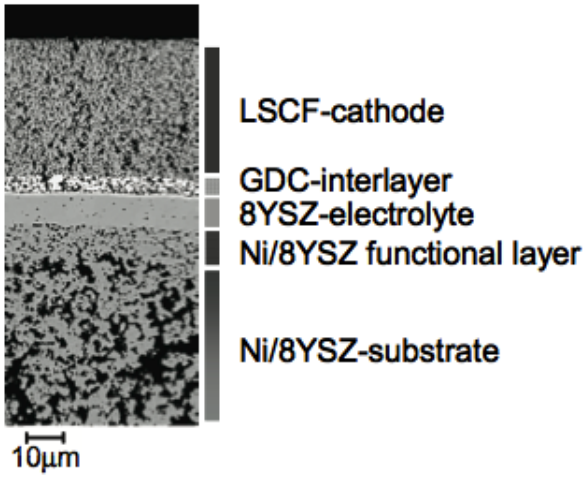

Figure 2.15: Micrograph of the cross section of a cell, showing the cell components present (Leonide, 2010).

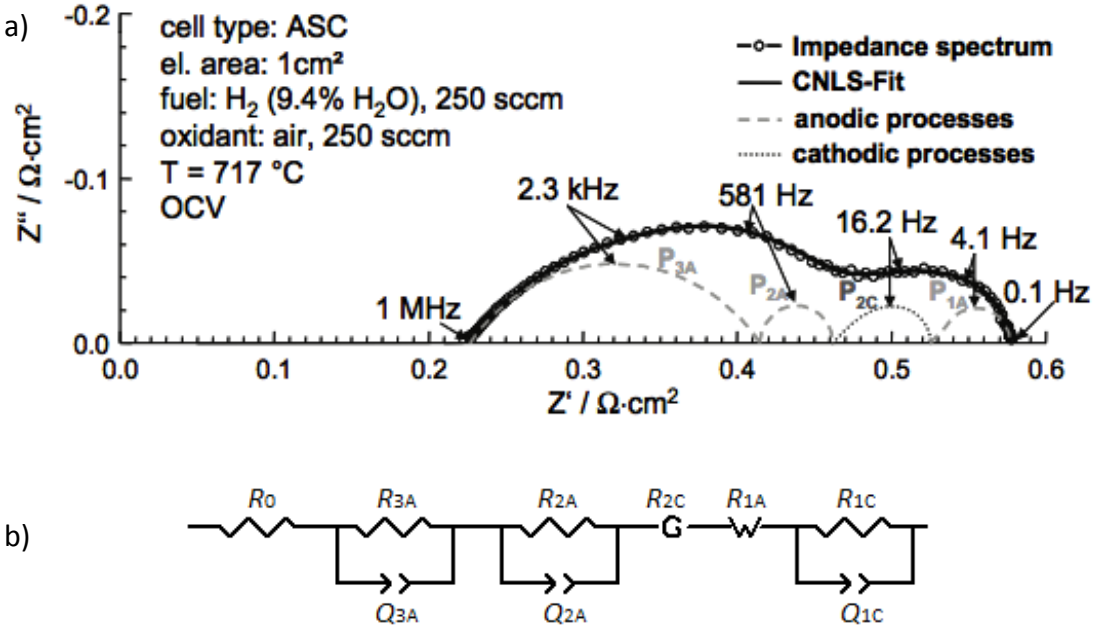

Figure 2.16: a) Z* plot of an SOC taken at 717 °C with a fuel concentration of 90.6: 9.4% H_2: H_2O, and air at the oxygen side, taken at OCV. The data points are shown by circles, the fit is a solid line and the individual processes are shown with dotted lines (Leonide, 2010). b) The corresponding equivalent circuit.

The equivalent circuit also contains five processes: two cathodic (oxygen electrode related), denoted by C, and three anodic (fuel electrode related), denoted by A. Here, the two highest frequency processes P_{3A} and P_{2A} are thought to be related to three coupled processes: oxygen ion transport in YSZ in the fuel electrode, charge transfer resistance at the TPBs and gas diffusion loss in the Ni-YSZ functional layer, the last of which is only present before initial cell activation. P_{2A} is sensitive to the fuel concentration, whereas P_{3A} is less dependent. Both have pronounced activation with temperature and are hence related to activation polarisation, as is Process P_{2C}, which

is represented by a Gerischer element and originates from oxygen surface exchange kinetics of LSCF and diffusivity of oxygen ions through the bulk LSCF. Processes P_{1A} and P_{1C} are gas diffusion in the Ni-YSZ substrate and the LSCF substrate, respectively. P_{1A} is represented by a FLW element, whereas P_{1C} is represented as an *RQ* element and is only seen at oxygen partial pressures significantly lower than that of air.

The processes seen in each cell are summarised in Table 2.1, in order of decreasing frequency. The frequencies are listed at 850 ^{o}C for the Barfod cell and at 860 ^{o}C for the Leonide cell, as there is a temperature dependence associated with these values. Both cells are assigned three anodic processes and two cathodic processes. Both show a process at around 50 kHz but they are assigned to different electrodes; the same is true of the lowest frequency process in each cell. Conversion polarisation is negligible for the gas pressures used so diffusion and activation polarisation are seen to dominate.

Table 2.1: Summary of equivalent circuit parameters for two SOCs from literature. (A and C represent anode and cathode, respectively. *G* and *W* represent Gerischer and Warburg elements, respectively.)

f^{o} (Hz) at 850^{o}C	Barfod (2007) Ni-YSZ|YSZ|LSZ-YSZ anode-supported		f^{o} (Hz) at 860^{o}C	Leonide (2010,2008) Ni-YSZ|YSZ|GDC|LSCF anode-supported	
50,000	C *RQ*	transport of O^{2-} ions at LSM-YSZ interface	50,000	A *RQ*	3 coupled processes: - Oxygen transport in YSZ in fuel electrode - Charge transfer resistance at TPBs - Gas diffusion loss in Ni-YSZ functional layer
8,000	A *RQ*	dissociative absorption of H_2 onto electrode and transport of resulting species to TPBs	3,000	A *RQ*	
1,100	C *RQ*	dissociative absorption of O_2 onto electrode, electrochemical reduction, & transport of oxygen species to TPB	200	C *G*	diffusivity of oxygen ions through bulk LSCF
20	A *RQ*	gas diffusion through the Ni-YSZ support	10	A *W*	gas diffusion in Ni-YSZ
3	A *RQ*	gas conversion at anode	0.3	C *RQ*	gas diffusion in LSCF

2.4.4 KRAMERS-KRONIG CONDITIONS

To describe impedance data using equivalent circuits, the system should be at steady state; equivalent circuits are inherently at steady state, whereas electrochemical processes tend to be dynamic (Agarwal et al., 1992), hence introducing systematic errors if the system is not sufficiently stable, for example due to changes in temperature, or sample aging (Boukamp, 1995).

Systematic errors can be detected using Kramers-Kronig (KK) transforms. They enable the transformation of the real part of the impedance to the imaginary part and vice versa, on condition of causality, linearity, stability and the data values being bounded for all frequencies from zero to infinity (Boukamp, 1995). Causality means the response must only be related to the excitation signal and not to any future events; linearity means only first order terms should be present in the input and response signals, and for stability the system must not change with time and the response should stop oscillating after the applied signal is removed. For practical applications, the stability criterion is the most important one, whereas the condition of finite data values is not critical (Boukamp, 1995).

The linearity condition requires impedance spectra to be independent of the excitation amplitude. This is achieved when the amplitude of the applied signal is sufficiently small, as shown in Figure 2.17 (Nechache et al., 2014). The non-linearity of the overall current-voltage response is due to the combination of chemical, electrochemical and mass transfer processes (Huang et al., 2007), which contribute to different polarisation processes, as discussed in Section 2.1.

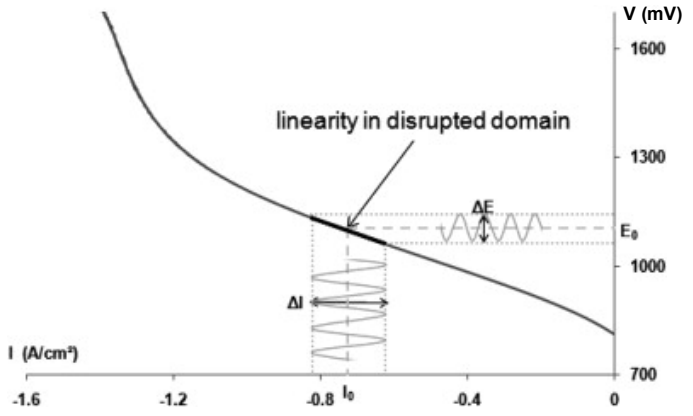

Figure 2.17: A current-voltage curve illustrating pseudo-linear behaviour when small excitation voltages are applied (Nechache et al., 2014).

The applicability of the KK conditions is determined by comparing the KK transformed data, defined below, to the measured data by calculating residuals Δ:

$$\Delta_{Re,i} = \frac{Z'_i - \hat{Z}'_i}{|Z_i^*|} \qquad [2.36]$$

$$\Delta_{Im,i} = \frac{\mathrm{Z}''_i - \hat{\mathrm{Z}}''_i}{\left|\mathrm{Z}_i^*\right|} \quad [2.37]$$

where $\left|\mathrm{Z}_i^*\right|$is the modulus of the impedance at the i^{th} frequency point and $\hat{\mathrm{Z}}$ represents the KK transformed data. A small scatter in the residuals indicate the KK conditions are satisfied and the data is KK compliant, whereas a systematic error highlights questionable data.

The KK transformed data $\hat{\mathrm{Z}}'$ and $\hat{\mathrm{Z}}''$ are given by the following integrals (Schoenleber et al., 2014), as a function of frequency:

$$\hat{\mathrm{Z}}'(\omega) = \frac{2}{\pi} \cdot \int_0^\infty \frac{x \cdot \mathrm{Z}''(x)}{\omega^2 - x^2}\, dx \quad [2.38]$$

$$\hat{\mathrm{Z}}''(\omega) = \frac{-2}{\pi} \cdot \int_0^\infty \frac{x \cdot \mathrm{Z}'(x)}{\omega^2 - x^2}\, dx \quad [2.39]$$

where x is a dummy integration variable. $\hat{\mathrm{Z}}'$ and $\hat{\mathrm{Z}}''$ are inter-dependent, as KK integrals transform the real part to the imaginary part, and vice versa. For discrete data, a discrete KK transform should be used to approximate these integrals. Converting the above integrals into summations is a possibility (Boukamp, 1993) but gives the need to extrapolate Z* to zero and infinite frequency, adding uncertainty. Instead, for discrete data Boukamp (1995) proposes using a “linear fit”, where data are fitted using a generic equivalent circuit; equivalent circuits are by nature KK compliant. When the KK conditions hold, an equivalent circuit can be fitted to the impedance data. For impedance data, a string of parallel *RC* elements or Voigt circuits is used, whereas for admittance data, a ladder of series *RC* elements or Maxwell circuits is used. Both circuits are illustrated in Figure 2.18. While it is most usual to investigate SOC data in Z*, performing KK transformations in the Y* formalism is useful if data are unbounded in Z* in the frequency range analysed (Boukamp, 1995). This is illustrated, for example, by a circuit containing only a resistor and capacitor in series. In terms of Z*, this is unbounded, see Figure 2.6a, whereas it gives a bounded arc in Y* (Figure 2.7c).

The number of *RC* elements used, *M* should be chosen with care. In principle, any value up to the number of measured data points, *N* can be used; however, if *M* is too small, the residuals contain oscillations, regardless of whether data is KK compliant or not, and if *M* is too high, noise is fitted in addition to the useful data. Schoenleber et al. (2014) devised a method to determine the optimum value of *M*, based on the observation that oscillations in the measured spectrum originate from noise. Over-fitting is hence avoided by ensuring that no oscillations occur in the fit data $\hat{\mathrm{Z}}'$ and $\hat{\mathrm{Z}}$. (Note, this is different to oscillations in the residuals Δ_{Re} and Δ_{Im}). This method is discussed in further detail in Section 3.4.1.

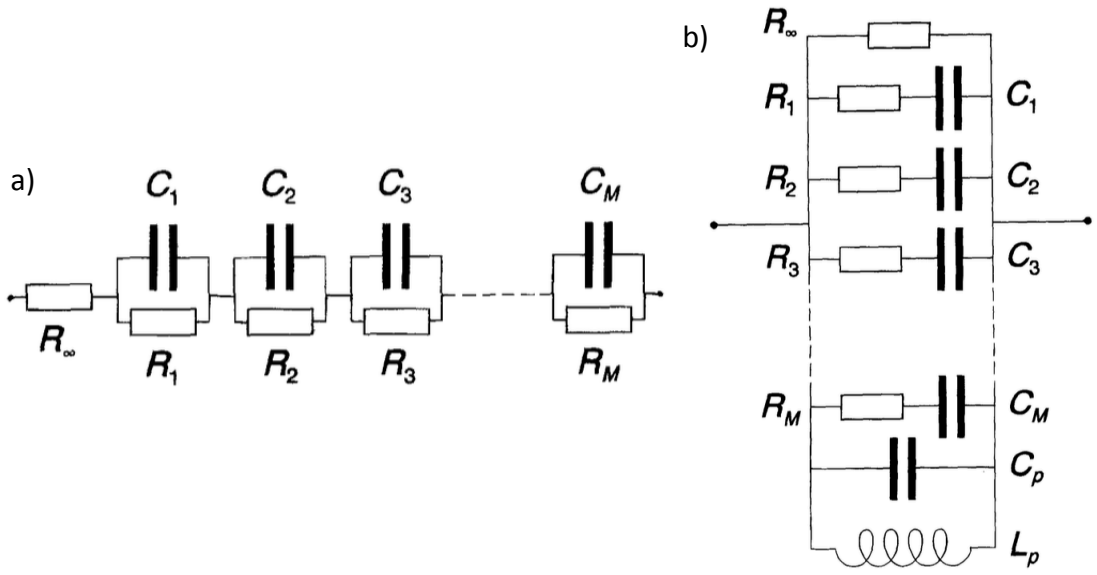

Figure 2.18: Possible equivalent circuits used to evaluate Kramers-Kronig relations in the linear fit method. a) Voigt circuit, b) Maxwell circuit (Boukamp, 1995).

When checking for KK compliance, although Z' and Z'' (or Y' and Y'') can be calculated separately, it is generally more appropriate to fit both the real and imaginary parts of the data simultaneously by minimising the following error sum (Boukamp 1995):

$$s = \sum_{i=1}^{N} w_i \left[\left(\mathrm{X}'_i - \widehat{\mathrm{X}}'_i \right)^2 + \left(\mathrm{X}''_i - \widehat{\mathrm{X}}''_i \right)^2 \right] \qquad [2.40]$$

where w_i is the weight factor:

$$w_i = \frac{1}{X'^2_i + X''^2_i} \qquad [2.41]$$

and X' and X'' represent the measured immittance data and $\widehat{\mathrm{X}}$' and $\widehat{\mathrm{X}}$'' represent the results of the curve fitting, both in terms of either impedance or admittance, where:

$$\widehat{\mathrm{Z}}'_i = R_s + \sum_{k=1}^{M} \frac{R_k}{1 - (\omega_i \tau_k)^2} \qquad [2.42]$$

$$\widehat{\mathrm{Z}}''_{i,} = -\frac{1}{C_p \omega_i} + L_s \omega_i - \sum_{k=1}^{M} \frac{R_k \omega_i \tau_k}{1 - (\omega_i \tau_k)^2} \qquad [2.43]$$

$$\widehat{\mathrm{Y}}'_i = \frac{1}{R_p} + \sum_{k=1}^{M} \frac{C_k \omega_i^2 \tau_k}{1 + (\omega_i \tau_k)^2} \qquad [2.44]$$

$$\widehat{\mathrm{Y}}''_i = C_p \omega_i - \frac{1}{L_p \omega_i} + \sum_{k=1}^{M} \frac{C_k \omega_i}{1 + (\omega_i \tau_k)^2} \qquad [2.45]$$

For the Z* fit R_s, C_s and L_s are the series resistance, capacitance and inductance, respectively, whereas R_p, C_p and L_p are the parallel resistance, capacitance and inductance, respectively, for the Y* fit. These parameters improve the mathematical

fit of the data and only strictly have meaning within the measured frequency range (Boukamp, 1995). Each *RQ* element is defined with a time constant τ_k and either a resistance R_k (Z* fit) or a capacitance C_k (Y* fit). The remaining variable can be inferred, noting that $\tau_k = R_k C_k$.

By fixing the τ distribution of the *RC* elements, the fit function becomes linear in R_k (or C_k) values, hence the name "linear fit". The values of τ are defined to give an even spacing in $\log \tau$, for example:

$$\tau_k = \tau_1 \exp\left[\frac{k-1}{M-1} \ln\left(\frac{\tau_M}{\tau_1}\right)\right] \qquad [2.46]$$

where τ ranges between τ_1 and τ_M, given by $1/\omega_1$ and $1/\omega_N$, respectively. The range can be extended beyond this, if practical for the data analysed.

2.4.5 EXPERIMENTAL JIG EFFECTS

Before analysing impedance spectra, it is important to account for any contributions that are not from the sample of interest, in particular, processes associated with the experimental jig. Edwards et al. (1997) state that possible jig contributions include a series resistance R_s and inductance L_s, and a parallel capacitance C_p and resistance R_p, illustrated in Figure 2.19. The parallel capacitance and resistance become a significant problem when the sample has a high resistance and a low capacitance, comparable to the value of C_p. In contrast, the series inductance, L_s and resistance, R_s become a significant problem when the sample has a small resistance and a large capacitance, which is typical of fuel cells, particularly when operating at high temperature (Savova-Stoynov and Stoynov, 1987). This effect can be reduced by using a sample with a smaller area-to-depth ratio but this decreases the performance of fuel cells and hence is not practicable. L_s (and C_p) can also be reduced to some extent by using shorter leads, but there is a limit to how short they can be, particularly when taking measurements at high temperatures (Edwards et al., 1997).

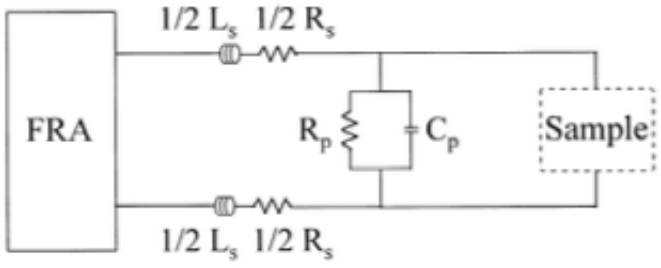

Figure 2.19: Equivalent circuit showing the series and parallel jig contributions to the measured impedance (Edwards et al., 1997).

To obtain the sample data, Edwards et al. (1997) advise calculating the series and parallel contributions of the jig and subtracting them from the raw data, before correcting for geometry. Parallel contributions can be estimated from open circuit

measurements, where the sample is removed and the sample holder contacts are kept at the same distance apart as the width of the sample. Series contributions can be estimated from short-circuit measurements, where the sample holder contacts are directly in contact with each other. Open and short-circuit measurements can vary with furnace temperature, so measurements should be taken at identical operating conditions to those of the sample measurement.

Edwards et al. (1997) found that high frequency series inductance corrections never completely matched the true response of a sample and suggested that some stray immittance is introduced in closed circuit measurements. Instead of merely a series inductance, Shin et al. (2013) proposed modelling high frequency inductive loops with a resistor and inductor in parallel, illustrated in Figure 2.20, to take into account resistive as well as inductive effects. As the value of the stray inductance increases, increasingly the fuel cell response is altered or obscured, as illustrated by the blue circles, red triangles and green diamonds, each with increasing inductance. At small values of stray resistance R_{STR}, the inductance tail curves towards higher values of Z' (purple squares in Figure 2.20) and when R_{STR} tends to infinity, the model tends to the conventional series inductance (Figure 2.5c).

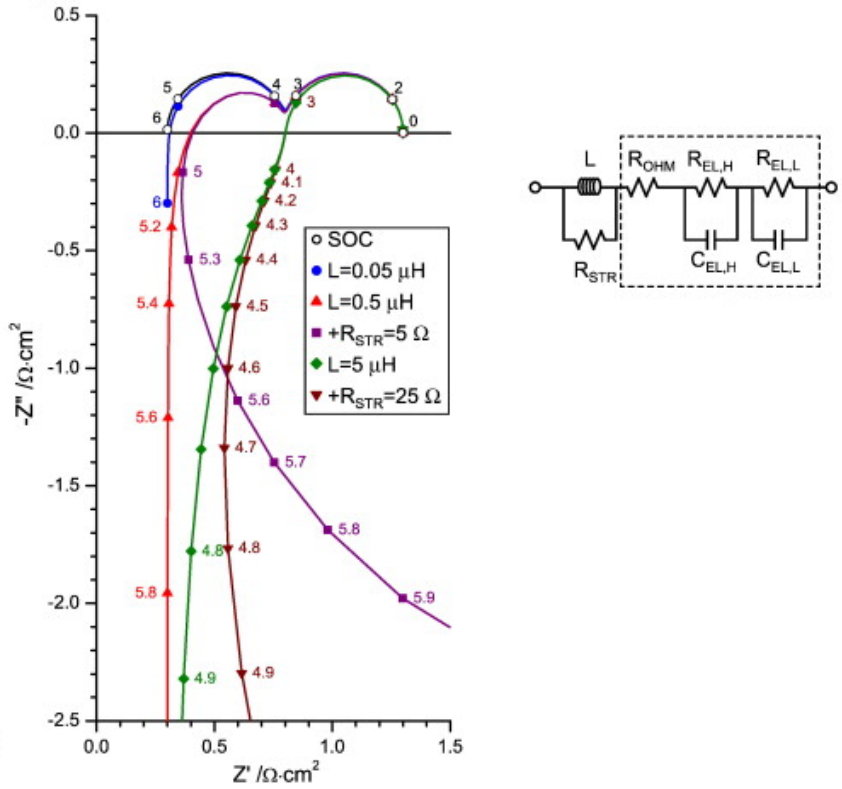

Figure 2.20: Effect of parasitic inductance and resistance in parallel with the inductance to a model impedance spectrum (Shin et al., 2013). The numbers on the spectra correspond to the logarithm of the frequencies the points refer to.

There are a number of cases in the literature where short-circuit measurements are used to correct for series inductance seen in SOC impedance measurements (Barbucci et al., 2006, Vladikova et al., 2006, Graves et al., 2011a); however, there

are many cases where inductance effects are present but either ignored or poorly considered. For example, Hauch et al. (2008) and Ebbesen et al. (2009) show data with clear inductance tails but make no mention of it. Zhang et al. (2015) cut off the top frequency decade of their measurements, where inductance is most dominant, to "eliminate the effects of external circuit". However, as inductance still contributes over the middle range frequencies (Savova-Stoynov and Stoynov, 1987), this approach is insufficient.

Despite the inductance contribution resulting mainly from external sources, it is not uncommon for equivalent circuits describing SOCs to contain a series inductance element, for example, as seen in Barfod et al. (2007). Shin et al. (2013) state this is often necessary, as the cell impedance and the artefact are not clearly distinguishable from each other. Complex non-linear least squares fits are then used to estimate the magnitude of the inductance. Similarly, Kramers-Kronig transforms (see Section 2.4.4) can be used to estimate the series inductance (Graves et al., 2015).

2.4.6 Distribution of Relaxation Times

DRT is a method that enables better resolution of impedance data by deconvolution of the spectrum. It gives the relative magnitudes of resistances associated with processes as a function of either τ or frequency. An example schematic is given in Figure 2.21 (left) for a system with two *RC* elements. When this input is convolved with the characteristic impedance of a unit *RC* element (Fig. 2.21 (middle)), the output (right) is the impedance response obtained from the cell. *RC* elements have a single time constant and so each element gives a single peak in the DRT, whereas non-ideal elements such as *RQ* elements have a spread of distribution times; however, resolution is still higher than the convolved impedance data.

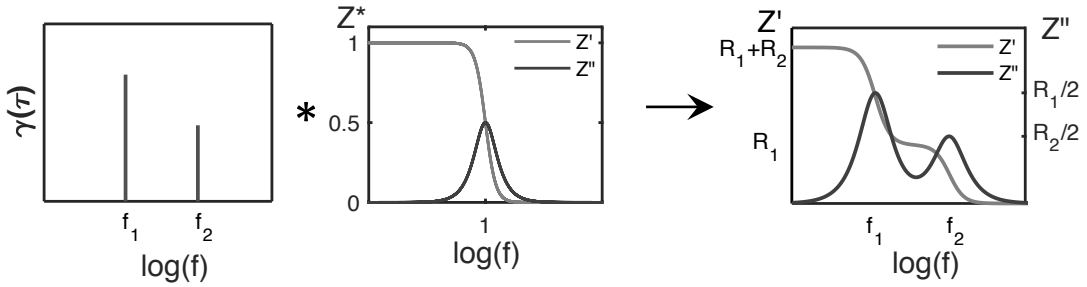

Figure 2.21: Schematic of the convolution of an example DRT (2 RC elements) with the real and imaginary components of impedance for a unit RC element, giving the impedance response.

There are several different methods to reconstruct the DRT from the impedance, such as Fourier transformation and filtering (Schichlein et al., 2002, Leonide et al., 2008) and Tikhonov regularisation (Buschel et al., 2012, Leonide, 2010). All methods contain a degree of uncertainty as the problem is ill-posed.

In the Fourier transform method, outlined by Schichlein et al. (2002), a sample is modelled as a series of *RC* elements with time constants distributed across the whole frequency range, with even spacing in log τ, as with the KK "linear fit" method (see Section 2.4.4). DRT should only be performed on the polarisation impedance Z^*_{pol} (see Section 2.3.1), so any series components, R_s, C_s, L_s (see equations [2.42 – 2.43]) should first be subtracted out. Provided Z^*_{pol} satisfies the Kramers-Kronig conditions, it is adequate to look only at the imaginary component Z''_{pol}. Initially, an infinite number of *RC* elements will be considered.

The impedance of a single RC element k is given in [2.21]; therefore, for an infinite number of RC elements, the imaginary component is given by:

$$Z''_{pol}(\omega) = -R_{pol} \int_0^\infty \frac{\omega\tau}{1+(\omega\tau)^2}\, \gamma(\tau)\, d\tau \qquad [2.47]$$

where γ is a scaling factor which satisfies:

$$\int_0^\infty \gamma(\tau) d\tau = 1 \qquad [2.48]$$

representing the normalised resistance as a function of τ across the infinite range of *RC* elements.

Data are logarithmically sampled with respect to frequency. To reflect this, a change of variables is applied, so that it is represented with equal spacing. Define x and y as:

$$x = \ln\left(\frac{\omega}{\omega_0}\right), \quad y = \ln(\omega\tau) \qquad [2.49, 2.50]$$

where ω_0 is a constant. Rearranging these equations gives:

$$\omega = \omega_0 e^x, \quad \omega\tau = e^y \qquad [2.51, 2.52]$$

Equations [2.51] and [2.52] can be combined to give:

$$\tau = \frac{e^{y-x}}{\omega_0} \qquad [2.53]$$

Z''_{pol} is therefore written:

$$Z''_{pol}(\omega) = -R_{pol} \int_{-\infty}^\infty \frac{e^y}{1+e^{2y}}\, \gamma\left(\frac{e^{y-x}}{\omega_0}\right).\left(\frac{e^{y-x}}{\omega_0}\right) dy \qquad [2.54]$$

Note that:

$$\frac{e^y}{1+e^{2y}} = \frac{\mathrm{sech}(y)}{2} \qquad [2.55]$$

Define a new scaling term, g, equal to the original scaling term multiplied by τ:

$$g(y-x) = \gamma\left(\frac{e^{y-x}}{\omega_0}\right).\left(\frac{e^{y-x}}{\omega_0}\right) = \gamma(\tau).\tau \qquad [2.56]$$

Hence equation [2.48] becomes:

$$\int_{-\infty}^\infty g(y-x)\, dy = 1 \qquad [2.57]$$

Combining [2.54], [2.55] and [2.56], gives the following expression for $Z"_{pol}$:

$$\mathrm{Z}"_{pol}(x) = -R_{pol} \int_{-\infty}^{\infty} \frac{\mathrm{sech}(y)}{2}\, g(y-x)\, dy \qquad [2.58]$$

This takes the form of a convolution product:

$$\mathrm{Z}"_{pol} = -\frac{R_{pol}}{2}\, \mathrm{sech}\,(x) * g(x) \qquad [2.59]$$

As convolution products multiply together in the Fourier domain, it can be solved using Fourier Transforms (FTs):

$$FT(g) = \frac{FT\left(Z"_{\mathrm{pol}}\right)}{FT\left(-\frac{R_{pol}}{2}\mathrm{sech}(x)\right)} \qquad [2.60]$$

Up to this point, a continuous input has been assumed; however, experimental spectra have discrete data points. Here, Discrete Fourier Transforms (DFTs) can be used. This adds a length scale to the Fourier transformed value, given by *NT*, where *T* is the sampling interval and *N* is the number of data samples. The transformed variables are given by:

$$DFT(Z"_{pol,\,k}) = NT\, \tilde{Z}"_n \qquad [2.61]$$

$$DFT\left(-\frac{R_p}{2}s_k\right) = -NT\,\frac{R_p}{2}\,\tilde{s}_n \qquad [2.62]$$

$$DFT(g_k) = NT\, \tilde{g}_n \qquad [2.63]$$

where ~ represents the Fourier transformed value. Here s represents $\mathrm{sech}(y)$ and $k, n = 0,1 \ldots, N\text{-}1$, where k and n are the counters in the original domain and the Fourier transformed domain respectively. Hence equation [2.60] becomes:

$$\tilde{g}_n = -\frac{1}{NT}\frac{2}{R_{pol}}\frac{\tilde{Z}"_n}{\tilde{s}_n} \qquad [2.64]$$

thus g can be obtained from the inverse Fourier transform of $\tilde{g}_n$.

To minimise errors from the finite frequency range used in experimental data, Z'' data is extrapolated before the FT is performed: Z'' $\rightarrow 0$ for $\omega \rightarrow 0$ and for $\omega \rightarrow \infty$, achieved by approximating a straight line in the $\log|\mathrm{Z}"|$ plot. This assumes there is only one polarisation process occurring at the edge of the spectrum (Leonide et al., 2008). In addition, a window is applied to $\tilde{g}_n$ before computing the inverse FT to obtain g_k, which reduces noise from artefacts that occur beyond the sampled region. The window used is the Hanning filter $\widetilde{w}_n$, see Figure 2.22, described by:

$$\begin{aligned} \widetilde{\mathrm{w}}_n &= \frac{1}{2}\left[1 - \cos\left(\frac{2\pi\left(n - (n_o - n_{\mathrm{filt}})\right)}{2n_{\mathrm{filt}}}\right)\right] && \text{for } |n - n_o| \le n_{filt} \\ &= 0 && \text{for } |n - n_o| > n_{filt} \end{aligned} \qquad [2.65]$$

where n_o is the central data point and n_{filt} is half the filter width. The filter shape prevents excess noise in the inverse FT (iFT); if all values were weighted equally within the window, the abrupt cut-off would cause the appearance of artefacts.

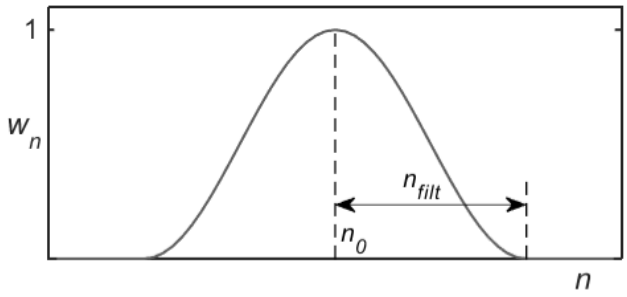

Figure 2.22: Hanning filter

The resulting DRT g_k is hence:

$$iFT(\tilde{g}_n.\tilde{w}_n) = g_k \quad [2.66]$$

The magnitude of g_k is affected by the frequency range, the extrapolation range, the number of data points and the size of the window used. These factors must be kept consistent, when comparing data sets.

2.5 SUMMARY & CONCLUSIONS

To summarise the observations from the literature, it is possible to utilise carbon dioxide by co-electrolysis of CO_2 and steam, using solid oxide cells (SOCs) at high temperature. If the rate-limiting processes occurring during electrolysis are known, the performance can be optimised. Possible rate-limiting processes include: the activation energy required for the electrochemical and chemical reactions, mass transport restrictions due to either consumption of fuel gases or the limitation of gas diffusion through the porous electrode, and Ohmic contributions such as oxide ion transport through the electrolyte and electronic resistances of the electrodes. These processes have different time scales and hence can be investigated using Impedance Spectroscopy (IS).

In IS, impedance is measured across a large range of frequency. Resulting data can be modelled using equivalent circuits, provided that the results are causal, linear, stable and finite across the entire frequency spectrum. In a physical model, each circuit element represents a process. Despite methods that increase the resolution of individual processes (such as determination of Distribution of Relaxation Times (DRT)) and aid determination of their physical origin (reference electrodes, symmetrical cells, Analysis of Differences in Impedance Spectra (ADIS)), fitting equivalent circuits remains more an art than a science, as does the assignment of model elements to physicochemical processes occurring. Fuel cells of different compositions and microstructures have different impedance spectra, so the fitting processes needs to be repeated for each individual sample.

In the literature, equivalent circuits for fuel cells tend to be fitted using only one formalism: impedance; therefore, although resistance fitting is optimised, capacitances are often neglected. The suitability of a proposed equivalent circuit can be more fully assessed by representing data with a variety of formalisms. A suitable model should give a good fit in all immittance formalisms.

Data validity should be considered and equivalent circuits should only be fitted if the Kramers-Kronig conditions are satisfied by the data. In addition, external jig effects should be accounted for, in particular inductive effects, either by subtraction before equivalent circuit fitting, or by adding suitable elements to the circuit. Inductive effects are frequently overlooked but they influence the spectra obtained significantly for SOCs so it is important to account for them.

CHAPTER 3: IMPEDANCE SPECTROSCOPY OF SOLID OXIDE CELLS: EXPERIMENTAL INVESTIGATION

3.1 INTRODUCTION

In this chapter, impedance spectroscopy is carried out on a commercial solid oxide cell (SOC) and the experimental results are analysed in light of the previous chapter. This includes computing Kramers-Kronig transformations and correcting for jig effects, to determine/enhance the reliability of the immittance data, as well as using Analysis of Differences in Impedance Spectra (ADIS) and Distribution of Relaxation Times (DRT) techniques to aid the interpretation of immittance data. Fitting using equivalent circuits (ECs) is considered inappropriate here, as there is large uncertainty associated with the full cell immittance data.

AIMS & OBJECTIVES

The aim of this chapter is to devise a methodology for determining the suitability of IS data for equivalent circuit fitting and to determine the number of processes occurring in an SOC, to aid with characterisation of the fuel cell.

To achieve this aim, the objectives of the chapter are to:

(i) record immittance spectra for an SOC *in situ*, at different concentrations;

(ii) use Kramers-Kronig to determine which data are suitable for equivalent circuit fitting;

(iii) use short circuit experiments to correct SOC spectra for jig inductance;

(iv) display results using all four immittance formalisms;

(v) use ADIS and DRT to determine both the number of processes that are distinguishable from the spectra and how they are affected by fuel concentration.

3.2 EXPERIMENTAL METHODS

Impedance measurements were taken for a solid oxide cell under different operating conditions. The SOCs used in this study, NextCells (see Figure 3.1), were sourced from FuelCellMaterials™ and contain an LSM /LSM-GDC oxygen-side electrode, a NiO-YSZ/NiO-GDC fuel-side electrode and a zirconia based Hionic™ electrolyte that contains scandia. They are electrolyte supported, with a total diameter of 20 mm and an active area of 1.227 cm^2.

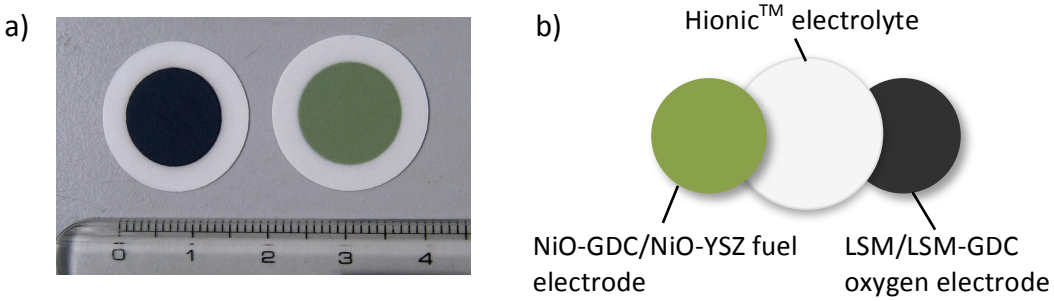

Figure 3.1: NextCell (Fuel Cell Materials, 2012): a) photo, b) schematic

The experiment setup was developed by Omojola (2014) and is shown in Figure 3.2. The experiment is set up using a Probostat™; the SOC sits on top of an alumina tube, sealed with a gold gasket, to prevent the atmospheres on either side of the cell from mixing. Platinum mesh current collectors are placed on the top and bottom of the cell and are used to connect the cell electrically. The whole arrangement is held in place using an alumina plate attached to spring loaded rods. A thermocouple is placed against the alumina tube, near the SOC, and is secured using nickel wire. The base of the Probostat has connections for the gas inlets and outlets, as well as electrical connections.

The top of the Probostat is placed in a furnace and heated to around 850 ^oC. A fuel mixture of equal parts H_2 and N_2 is applied for 10 hours, to reduce nickel oxide to nickel, so that the electrode becomes electrochemically active. During testing, the oxygen electrode is exposed to ambient air, while the fuel gas composition is altered. The fuel compositions used are listed in Table 3.1. The total fuel gas flow rate is kept at 20 ml/min, with 5 ml/min N_2, to ensure the nickel electrode remains reduced, and the remainder consisting of CO_2 and H_2 in varying ratios.

Table 3.1: Testing conditions under which IS spectra were collected (NextCell)

Data label	Composition of fuel (ml/min)		
	CO_2	H_2	N_2
A	3	12	5
B	5	10	5
C	10	5	5
D	12	3	5

a)

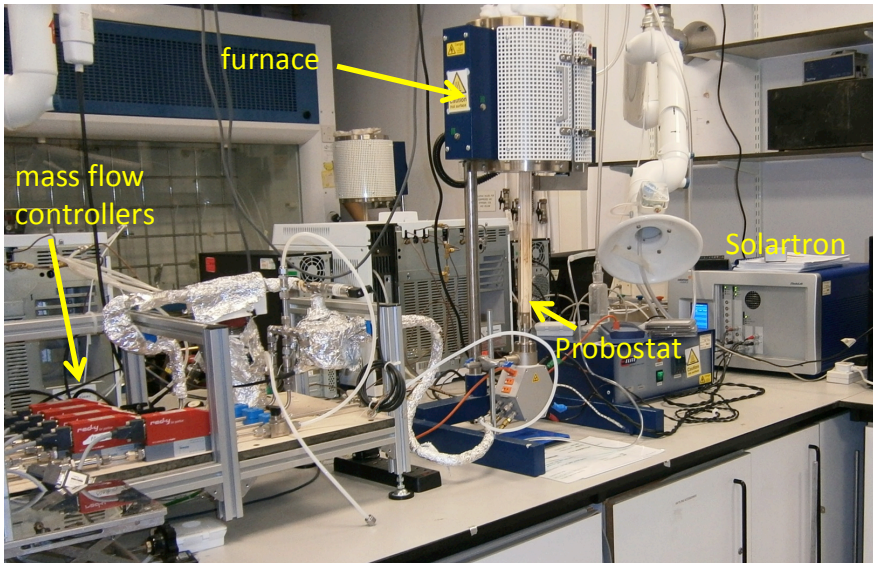

b)

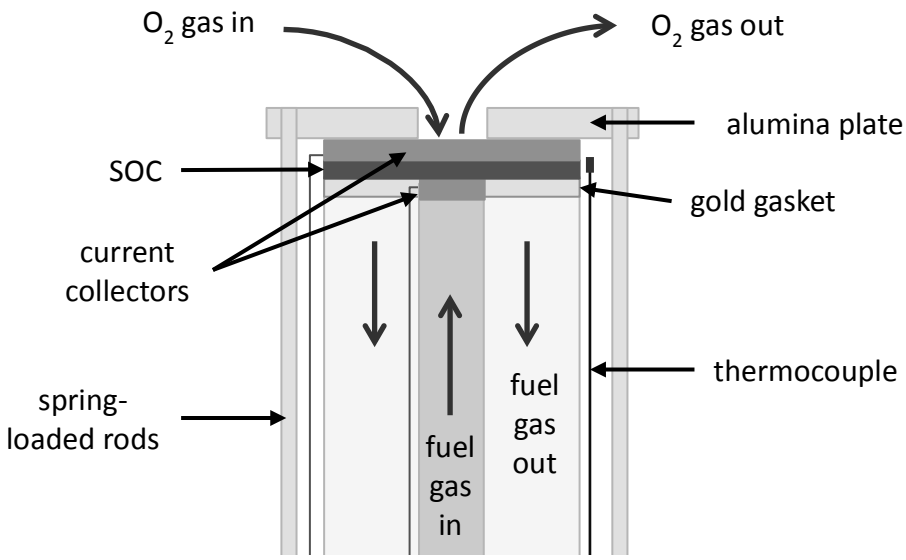

Figure 3.2: a) A photo of the experimental setup, and b) a schematic of the top of the Probostat™.

IS measurements were taken using a Solartron Modulab at open circuit voltage with a perturbation amplitude of 10 mV for a frequency range of 1 MHz to 0.01 Hz with 10 measurements per decade. 1 MHz was the upper limit of the equipment; Measurements below 0.01 Hz were possible but took significant time to record.

In addition, short-circuit tests were carried out. Here, the current collectors were placed directly in contact with each other. Impedance measurements were carried out in ambient air at 650 and 850 ^{o}C, at a voltage amplitude of 10 mV. Short-circuit test results did not vary significantly with temperature but were observed to vary after the jig was disassembled and then reassembled.

Open-circuit tests were not carried out due to difficulties relating to the jig; however, the parallel resistance and capacitance of the jig are not expected to influence SOC data significantly, see Section 2.4.5.

3.3 JIG INDUCTANCE

Raw Z* data are shown in Figure 3.3 for the SOC at a fuel concentration of 3, 12, 5 ml/min of CO_2, H_2 and N_2. A large inductive tail is seen at high frequency that originates from the test jig; the cables connecting the jig to the Modulab and the leads in the jig have an associated inductance. They also have an associated resistance, shifting the Z* plot to the right, and a capacitance; however, the capacitance is insignificant in comparison to that of the SOC. Test jig effects need to be accounted for before data analysis on the SOC is carried out.

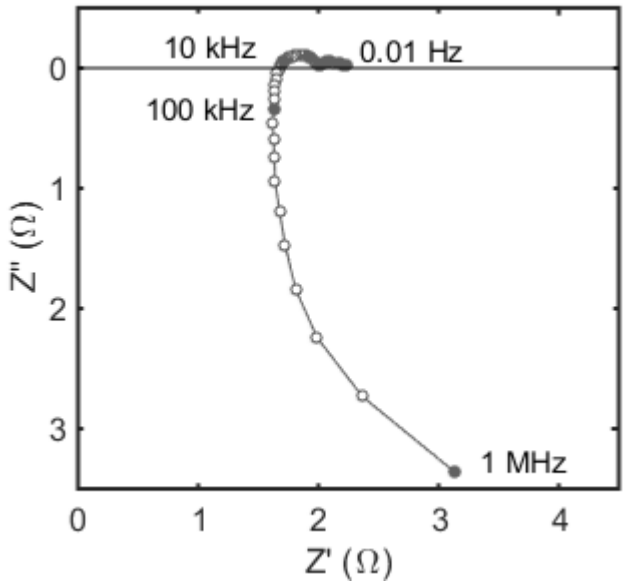

Figure 3.3: Z* plot for an SOC at a fuel concentration of 3, 12, 5 ml/min of CO_2, H_2 and N_2.

In this section, short-circuit measurements are used to estimate jig contributions, firstly by calculating the series inductance and resistance at each frequency and then by applying equivalent circuits. The results are compared and used to give suggestions on how to correct for jig effects.

3.3.1 EXPERIMENTAL ESTIMATES USING SHORT-CIRCUIT DATA

The inductance of the test jig can be estimated using the short-circuit data obtained. It is impossible to take such measurements immediately before or after sample measurements due to the nature of the setup: the sample is sealed so that the fuel and oxygen-side gases remain separate. The jig must be disassembled and reassembled, hence the short-circuit values obtained may not completely resemble the jig artefacts present in the sample data.

Data are shown in Figure 3.4 for two short-circuit trials, both at 850 ^{o}C and with a voltage amplitude of 10 mV, taken on different occasions. These are representative of multiple data sets measured. Both trials give an inductance tail in the Z* plot (Figure 3.4a) but the Z* values differ. The Z' spectra (Figure 3.4b) each have base

value, R_s with additional contributions at high frequency, $Z'_{\text{jig-hf}}$. R_s differs by an order of magnitude between the trials, at 4.9 mΩ and 58 mΩ. The additional resistance could originate from non-flat contact between the two mesh current collectors.

The inductance $L_{s,i}$ was calculated at each frequency point:

$$L_{s,i} = \frac{Z''_i}{2\pi f_i} \qquad [3.1]$$

and is shown in Figure 3.4c. Values converge at higher frequency, although they tail off in the last frequency decade measured for one of the trials. Taking an average of the values between 10^4 and 10^5 Hz gives a series inductance of 6.4 $\times 10^{-7}$ and 5.1 $\times 10^{-7}$ H for the two trials.

Both the inductance and resistance values illustrate that there is a significant degree of uncertainty from the test jig. The next subsections consider whether equivalent circuits can be used to give an accurate representation of the jig effects, and the sensitivity of the SOC Z* data to the inductance correction value.

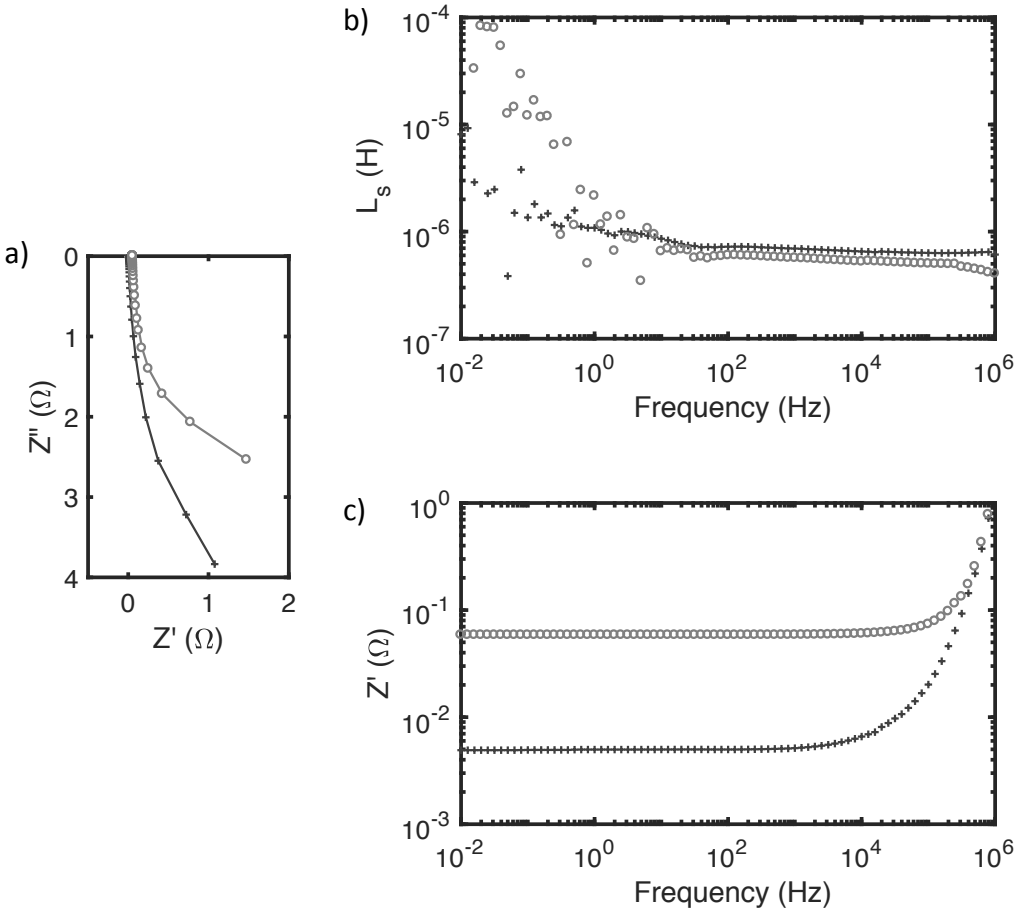

Figure 3.4: a) Z* plot showing short-circuit data for two trials, both at 850 °C and a voltage amplitude of 10mV, b) corresponding Z' spectroscopic plot, c) inductance values extracted from Z'' for each frequency point, for trials 1 and 2 (dark grey '+' and light grey 'o', respectively).

3.3.2 ESTIMATING JIG EFFECTS USING EQUIVALENT CIRCUITS

Estimates of the jig inductance and resistance were also obtained by fitting equivalent circuits to the short-circuit data. Two circuits were used: a) a resistor in series with an inductor, to compare the method with that in the previous sub-section, and b) a resistor in series with a parallel inductor-resistor element. The equivalent circuits are illustrated in Figure 3.5 and the results for two short-circuit trials are presented in Table 3.2.

Table 3.2: Equivalent circuit parameters for short-circuit data trials

Short circuit	Circuit (see Fig 3.5)	R_s (mΩ)	L_s $(\times 10^{-7}\ \mathrm{H})$	R_0 (Ω)
Trial 1	(a)	5.0	6.5	-
	(b)	5.0	6.5	16
Trial 2	(a)	59	4.9	-
	(b)	59	5.0	7.2

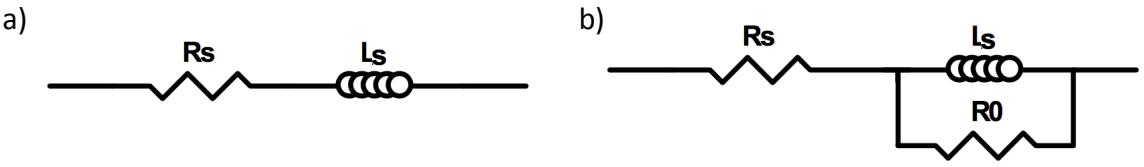

Figure 3.5: Equivalent circuits used to fit inductive effects from the jig: a) series resistance and inductance, and b) resistance in series with an inductor and resistor in parallel.

For both short-circuit trials, the series resistance and inductance both vary negligibly between circuits (a) and (b), despite the addition of the resistance R_0, indicating little sensitivity in L_s and R_s to the value of R_0. In contrast, there is a significant difference in all variables between the two trials, despite being nominally under the same experimental conditions.

3.3.3 COMPARISON OF ESTIMATES OF JIG EFFECTS

Short-circuit estimates of L_s and R_s, using both individual frequency points and equivalent circuit fitting, are listed in Table 3.3. The results for the two methods are comparable; therefore, the main concern is the variability of jig effects between trials, rather than extracting parameters from the data.

Table 3.3: Comparison of estimates of jig series resistance R_s and inductance L.

Method	R_s (mΩ)		L_s $(\times 10^{-7}\ \mathrm{H})$	
Trial:	**1**	**2**	**1**	**2**
Individual *f* points	4.9	58	6.4	5.1
EC fitting values	5.0	59	6.5	4.9-5.0

The jig series resistance R_s varies by an order of magnitude between the two short-circuit trials and is around 1% and 10% of the SOC polarisation resistance R_{pol} seen in Figure 3.3, where R_{pol} is the difference between the Z' values at low and high frequency Z'' intercepts (see Section 2.3.1). Correcting for R_s could therefore give a sizeable shift in Z' values but, with such a large uncertainty in the magnitude of R_s, it cannot be corrected for precisely. Instead it must be accepted that the SOC series resistance will contain an unknown contribution from the jig. However, some correction can be made to Z' for the additional high frequency parasitic resistance $\mathrm{Z}'_{\text{jig-hf}}$ by subtracting its contribution from the raw values Z'_{raw}:

$$\mathrm{Z}'_{\text{corrected}} = \mathrm{Z}'_{\text{raw}} - \mathrm{Z}'_{\text{jig-hf}} \quad [3.2]$$

for example, $\mathrm{Z}'_{\text{jig-hf}}$ can be approximated using the short-circuit Z' data, see Figure 3.4b, with the base series resistance value $R_{s,\,jig}$ subtracted:

$$\mathrm{Z}'_{\text{jig-hf}} = \left(\mathrm{Z}'_{\text{jig}} - R_{\text{s-jig}}\right) \quad [3.3]$$

Alternatively, $\mathrm{Z}'_{\text{jig-hf}}$ can be estimated by fitting a parallel resistor-inductor equivalent circuit R_oL_s to the short circuit data, which gives:

$$\mathrm{Z}'_{\text{jig-hf}} = \frac{R_0(\omega L_s)^2}{R_0^2 + (\omega L_s)^2} \quad [3.4]$$

The jig inductance varies between 4.9×10^{-7} H and 6.5×10^{-7} H for the two trials, giving an average of 5.7×10^{-7} H. Z'' is corrected by subtracting the jig contribution $\mathrm{Z}''_{\text{jig}}$ from the raw data:

$$\mathrm{Z}''_{\text{corrected}} = \mathrm{Z}''_{\text{raw}} - \mathrm{Z}''_{\text{jig}} \quad [3.5]$$

$\mathrm{Z}''_{\text{jig}}$ can either be represented as just the impedance of the inductor L_s:

$$\mathrm{Z}''_{\text{jig}} = \omega L_{\text{s}} \quad [3.6]$$

or as the impedance of the resistance R_0 in parallel with the inductor L_s:

$$\mathrm{Z}''_{\text{jig}} = \frac{\omega L_s R_0^2}{R_0^2 + (\omega L_s)^2} \quad [3.7]$$

which tends to ωL_{s}at small frequency, i.e. when $\omega \ll R_0/L_s$.

The sensitivity of example SOC data to both the magnitude of inductance correction and the high frequency resistance is investigated in the following sub-section.

3.3.4 Sensitivity of jig inductance on SOC results

To investigate the sensitivity of SOC data to inductance correction, two values of inductance, estimated from the two short-circuit trials using the method of individual frequency points (see Table 3.3), were used to correct raw SOC Z'' data, using equations [3.5] and [3.6]. The resulting Z* plots are shown in Figure 3.6. Data sets 1a and 2a are both corrected in Z', as well as Z'', using equations [3.2] and [3.3],

whereas sets 1b and 2b are corrected in Z'' only. Trial 1 over-corrects for the inductance, with - Z'' increasing at high frequency, whereas Trial 2 under-corrects, giving positive high frequency Z'' values. In this instance, the jig inductance for the SOC data appears to be somewhere between that of the two trials; therefore, it seems sensible to correct for L_s using an average of the two values.

It has been seen that correcting for $Z'_{jig\text{-}hf}$ gives a notable shift in Z' data above 10^4 Hz, altering the value of $R_{s\text{-}SOC}$ for Trial 2; therefore, it is important to consider $Z'_{jig\text{-}hf}$ effects during jig correction.

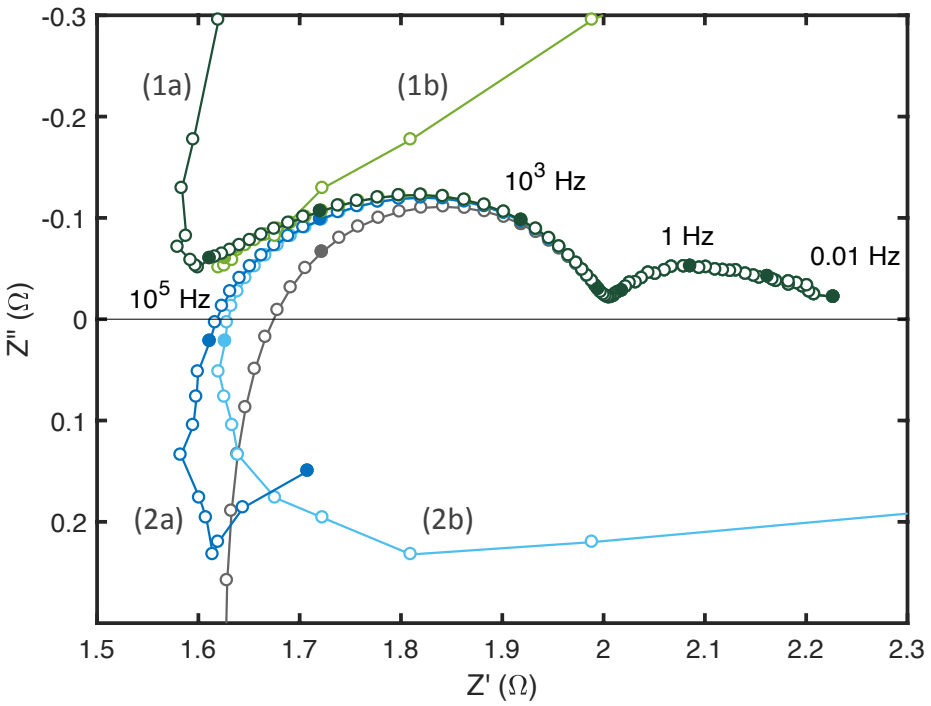

Figure 3.6: Z* plot for an SOC at a fuel concentration of 3, 12, 5 ml/min of CO_2, H_2 and N_2, corrected using inductance values of: 1) 6.4×10^{-7} H (Trial 1) and 2) 5.1×10^{-7} H (Trial 2), for a) *R* correction using the short-circuit Z' values minus the base $R_{s,jig}$ value for the respective trial, and b) no *R* correction. The original data are also shown (grey).

$Z'_{jig\text{-}hf}$ correction from the equivalent circuit method, equation [3.4] with R_0 equal to 11 Ω, is compared to that from equation [3.3] for each trial. The inductance is set to the average value, 5.7×10^{-7} H, and the results are displayed in Figure 3.7. The Z* Nyquist plots are very similar up to 10^5 Hz. Above this frequency, the accuracy of the results is very poor and hence will be discarded; these data are shown in muted colours. The similarity of the remaining data indicates that the results are not particularly sensitive to the method used in this frequency range. Results will hence be corrected using equation [3.4], with R_0 equal to 11 Ω and L_s equal to 5.7×10^{-7} H.

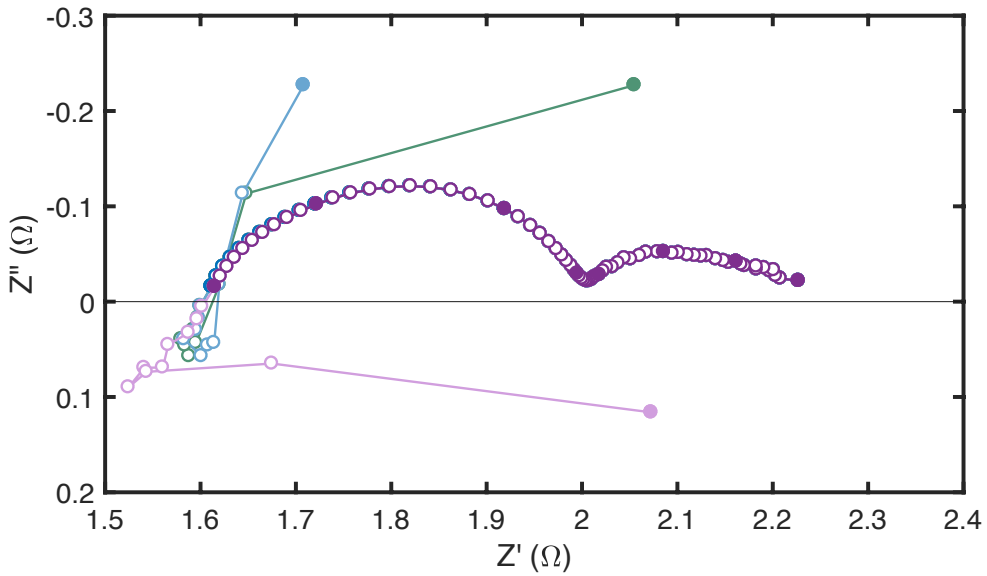

Figure 3.7: Z* plot of example SOC data, corrected using an inductance of 5.7×10^{-7} H. The high frequency jig parasitic resistance is corrected using, i) Trial 1 (green), ii) Trial 2(blue), and iii) resistance R_0 (11 Ω) in parallel with the inductance (purple).

3.3.5 Conclusions

To summarise, Z* data taken for a commercial SOC at high temperature contain large inductive contributions from the test jig. Short-circuit experiments gave a rough starting point for determining the jig inductance L_s but were not very precise, as the jig contributions vary during different runs. An average value of L_s from two short-circuit trials was used but it is recognised there is still some uncertainty in Z'', particularly at frequencies above 10^3 Hz.

The jig series resistance varies significantly between different short-circuit trials and hence a suitable correction could not be applied with any accuracy; however, the extra high frequency contributions could be estimated, either by subtracting the jig series resistance from the short-circuit Z' values, or by modelling a resistor R_0 in parallel with the inductor. The results below 10^5 Hz were not particularly sensitive to the method or the value of R_0 used. Results above this frequency were discarded as they were unreliable.

3.4 DATA VALIDATION – KRAMERS-KRONIG CONDITIONS

To investigate the reliability of the SOC admittance data obtained, in particular their stability, Kramers-Kronig residuals were calculated. Firstly, the 'linear fit" KK method is implemented and then the results are presented. Results with residuals larger than ±0.5% are considered unreliable.

3.4.1 METHOD

Matlab was used to create a program to perform the "linear fit" KK transforms, introduced in Section 2.4.4, and the code can be found in the Appendix (A.1). The advantage of using an in-house program rather than readily available software, such as LinKK (KIT, 2015) and KKtest (Boukamp, 1995), is the greater freedom possible. For example, the program allows KK transforms to be calculated for either Z* or Y* formalisms and the values of τ_1 and τ_N can be input manually, which is useful if the characteristic frequency f° is just outside the measured frequency range. The values of the additional series or parallel elements can also be seen, which provides useful evidence of the effect of jig inductance, and there is more flexibility with the style of data input.

In the in-house program, the working formalism is defined as X*. The fitted values $\widehat{\mathrm{X}}'$ and $\widehat{\mathrm{X}}''$ are defined using the following equations:

$$\widehat{\mathrm{X}}' = \mathbf{A}\mathrm{V} \qquad [3.8]$$

$$\widehat{\mathrm{X}}'' = \mathbf{B}\mathrm{V} \qquad [3.9]$$

which represent equations [2.42-2.45] in matrix form; **A** and **B** are matrices and V is a vector containing resistance values R_k for Z* and capacitance values C_k for Y*, with the additional series or parallel elements defined at the end of the vector:

$$\mathrm{V}_{\mathrm{Z}^*} = \begin{pmatrix} R_1 \\ \vdots \\ R_k \\ \vdots \\ R_M \\ R_s \\ L_s \\ 1/C_s \end{pmatrix}, \qquad \mathrm{V}_{\mathrm{Y}^*} = \begin{pmatrix} C_1 \\ \vdots \\ C_k \\ \vdots \\ C_M \\ 1/R_p \\ 1/L_p \\ C_p \end{pmatrix} \qquad [3.10, 3.11]$$

For Z*, the elements of **A** and **B** (with k = 1 to M) describe the RC elements, given by:

$$a_{i,k} = \frac{1}{1 + (\omega_i \tau_k)^2} \qquad [3.12]$$

$$b_{i,k} = -\frac{\omega_i \tau_k}{1 + (\omega_i \tau_k)^2} \qquad [3.13]$$

each with time constant τ_k; ω_i represents the angular frequency at the measured frequency i. The additional terms for k = $(M+1)$ to $(M+3)$ describe the series resistance, inductance and capacitance, respectively:

$$a_{i,M+1} = 1 \qquad b_{i,M+1} = 0 \qquad [3.14,3.15]$$

$$a_{i,M+2} = 0 \qquad b_{i,M+2} = \omega_i \qquad [3.16, 3.17]$$

$$a_{i,M+3} = 0 \qquad b_{i,M+3} = -1/\omega_i \qquad [3.18, 3.19]$$

For Y*, the elements for k = 1 to M are given by:

$$a_{i,k} = \frac{\omega_i^2 \tau_k}{1 + (\omega_i \tau_k)^2} \qquad [3.20]$$

$$b_{i,k} = \frac{\omega_i}{1 + (\omega_i \tau_k)^2} \qquad [3.21]$$

with the additional terms to describe the parallel resistance, inductance and capacitance respectively:

$$a_{i,M+1} = 1, \qquad b_{i,M+1} = 0 \qquad [3.22, 3.23]$$

$$a_{i,M+2} = 0\,, \qquad b_{i,M+2} = -1/\omega_i \qquad [3.24, 3.25]$$

$$a_{i,M+3} = 0\,, \qquad b_{i,M+3} = \omega_i \qquad [3.26, 3.27]$$

As ω_i and τ_k are defined (see equation [2.46] for τ_k), **A** and **B** are known; therefore, V can be optimised by fitting $\widehat{\mathrm{X}}'$ and $\widehat{\mathrm{X}}''$ to experimental data. The following equations are minimised simultaneously using a least squares method:

$$f_1 = \left(\hat{X}' - \mathbf{A}\mathrm{V}\right) \cdot \sqrt{\mathrm{W}} \qquad [3.28]$$

$$f_2 = \left(\hat{X}'' - \mathbf{B}\mathrm{V}\right) \cdot \sqrt{\mathrm{W}} \qquad [3.29]$$

where W is a vector of the weighting values at each frequency (see equation [2.41]). Note that equations [3.28] and [3.29] are a square-root form of equation [2.40]; f_1 and $f_2$are squared during the least squares procedure. After optimisation of ***V***, the KK fit values are calculated using equations [3.8 & 3.9] and the residuals are obtained using equations [2.36 & 2.37].

To determine the optimum number of RC elements, *M,* used for the fit, the method outlined by Schoenleber et al. (2014) was implemented. They define a parameter μ:

$$\mu = 1 - \frac{\sum_{V_k<0}|V_k|}{\sum_{V_k\geq 0}|V_k|} \qquad [3.30]$$

where the numerator is the sum of the negative V_k values and the denominator is the sum of the positive V_k values. When μ is approximately unity, the sum of the negative elements is small, preventing oscillations in Z* (or Y*), and there is no chance of over-fitting. As more RC elements are added, μ decreases; over-fitting is present when μ tends towards zero, indicating that there is significant oscillation in the fit data. An example of μ as a function of *M* is shown in Figure 3.8 for sample

SOC data, using the in-house program. The optimum value of RC elements is that which gives a value of μ just before the rapid decrease. μ is set to 0.5 in the in-house program, as this was found to give an appropriate number of elements. Initially the number of RC elements per decade is set to 2 and the KK transforms are calculated. *M* is then increased incrementally until μ decreases below 0.5.

Note that this method assumes all features can be described by positive resistances and capacitances, implying all Z'' data are negative; however, as seen in Section 3.3, this is not always the case, even after inductance correction. For fit results that include positive Z'' data after inductance correction, the optimum value of *M* is instead determined manually, ensuring that *M* is sufficiently high to avoid oscillations in the residuals, a sign of under-fitting.

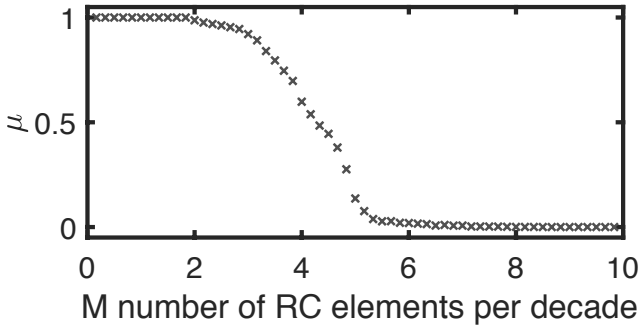

Figure 3.8: Plot of μ (see equation [3.30]) as a function of the number *M* of RC elements used in the "linear KK" model, displayed as *M* per frequency decade, calculated for SOC data at 12,3,5 ml of CO_2, H_2, N_2, using the in-house model.

3.4.2 KRAMERS-KRONIG RESULTS

KK transforms were performed on the SOC impedance data, firstly across the entire frequency range (0.01 to 10^6 Hz) for uncorrected data. As an equivalent circuit is used to correct the data for jig effects, if the data are KK compliant, both corrected and uncorrected data should be transformable and should give the same results. This way, the value of *L* obtained can be compared, for interest. Example data for case *D* (Table 3.1) is shown in Figure 3.9.

The Z* Nyquist plot illustrates the presence of considerable noise at low frequency (i.e. at the right-hand end), which is reflected in the residuals, see Figure 3.9c. At high frequency, the residuals show an error of a different nature; instead of scattered noise, it is systematic. This is present in the KK residuals, regardless of which value of *M* is used. Excluding the top decade and instead fitting for the frequency range of 0.01 to 10^5 Hz, gives a much better high frequency fit, eliminating the systematic error in the residuals, see Figure 3.10a. This implies the upper frequency decade is not KK compliant so it is therefore justifiable to discard these frequency points, as was found necessary during jig correction (see Section 3.3.4).

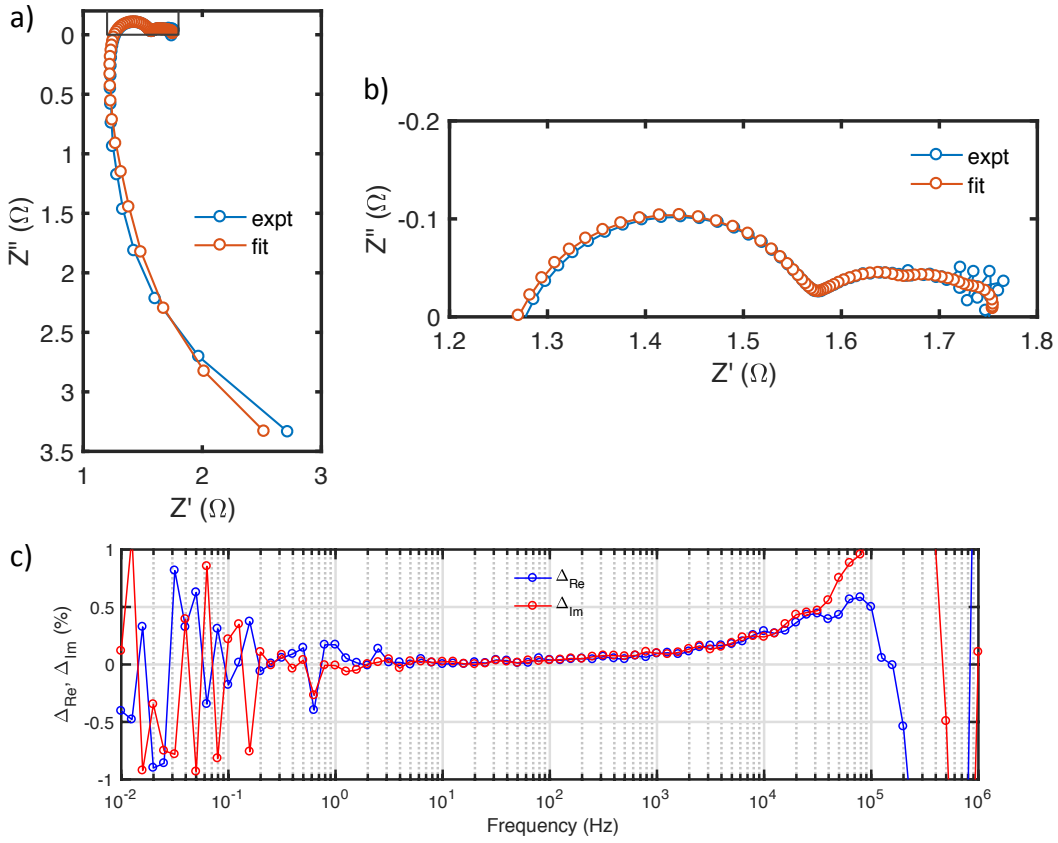

Figure 3.9: a) Z* plot of SOC experimental data (12,3,5 ml CO_2,H_2,N_2) and corresponding KK fit data (M=35) b) zoom of (a), and c) the resulting KK residuals analysed for the frequency range of 0.01 – 10^6 Hz.

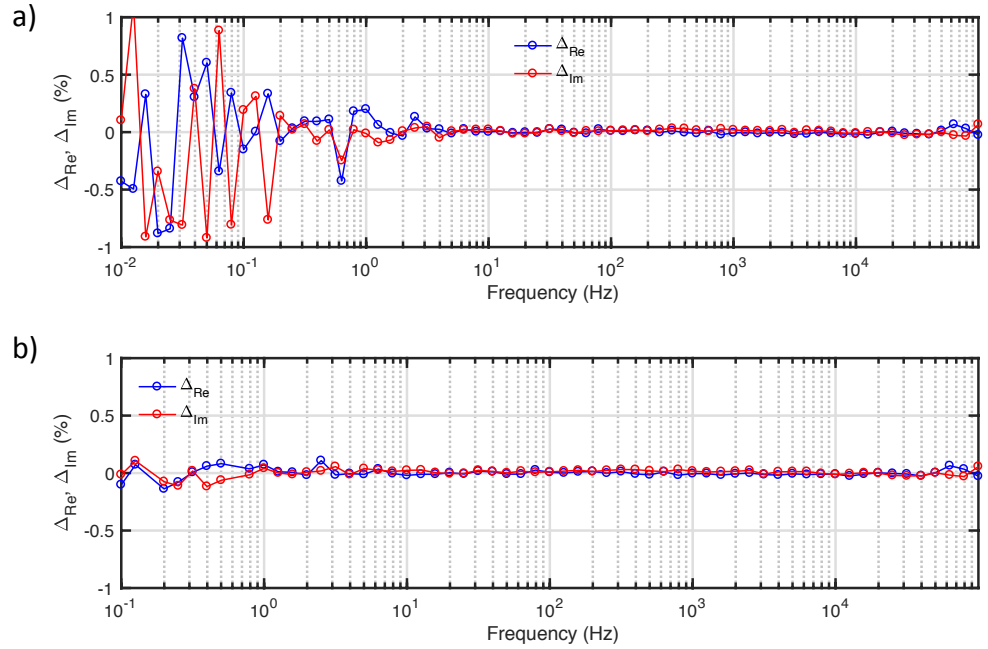

Figure 3.10: Spectroscopic plot of the residuals obtained from KK transformations on SOC data at 12,3,5 ml CO_2, H_2, N_2, for a) a frequency range of 0.01 – 10^5 Hz, and b) a frequency range of 0.1 – 10^5 Hz, with additional anomalous points removed before KK analysis.

Most data sets contain substantial errors below 0.1 Hz and hence these data points are also discarded, as well as any anomalous points at additional frequencies[‡]. The corresponding residuals are shown in Figure 3.10b for case *D* and are well within the recommended limits of ±0.5%, showing these data to be KK compliant and hence stable.

The values of L_s determined during KK fitting ranged between 5.6 and 5.8 $\times 10^{-7}$ Hz. Despite being a mathematical fit parameter rather than a physically representative variable, these sit between the values estimated from the two short-circuit trials across the frequency range measured here and agree with the average value of L_s chosen.

Based on the above example, the suggested protocol for SOC data correction is hence as follows:

- Carry out KK transforms and discard unreliable data, highlighted by the residuals, for example noisy low frequency data and high frequency data with systematic errors.
- Estimate the series inductance based on the values obtained from short-circuit experiments and those seen from KK, recognising the sizeable uncertainty associated with this estimate.
- Ignore the series resistance contribution from the jig, R_s, as it cannot be separated from the SOC series resistance with any confidence.
- Estimate the parallel resistance R_0 associated with the inductance by fitting a parallel RL circuit to short-circuit data. (Alternatively, subtract R_s from the short-circuit Z' values and use the result to correct for Z'_{SOC}).
- Correct for L_s and R_0 (see Section 3.3.3).
- Apply a geometric correction by multiplying Z* by the SOC surface area (see Section 2.2).

Note that the correction for the geometry should be applied last, otherwise the jig correction is inappropriate.

[‡] The term anomalous is used here to mean data points with substantially larger residual values than those at similar frequencies.

3.5 IMPEDANCE RESULTS

The measured results obtained for the commercial SOC were checked for KK compliance, corrected for jig effects and then a geometric factor was applied, as outlined in the previous section. Resulting data are shown as Z* Nyquist plots in Figure 3.11 and as spectroscopic plots in Figure 3.12 for all formalisms. Data were collected at four different fuel compositions, see Table 3.1, and the data sets collected on each day are described in Table 3.4. Two spectra were recorded back-to-back at the same composition to check for reproducibility (i and ii). For compositions *A* and *B*, the results are similar, whereas cases C_i and C_{ii} have marginally different series resistances (see Figure 3.11c); this could be due to changes in the SOC or further jig artefacts from the mesh contacts. Case D_{ii} was not KK compliant and is hence not plotted.

Table 3.4: Experimental data collected on the first day, and two days later. *A* represents a CO_2:H_2:N_2 fuel composition of 15:60:25%, *B* is 25:50:25%, *C* is 50:25:25% and *D* is 60:15:25%.

Day 1	A_i, A_{ii}, B_i, B_{ii}, C_i, C_{ii}, D_i, D_{ii}
Day 3	C_{iii}, D_{iii}

For compositions *C* and *D*, another data set was recorded two days after the first, with the cell held at 850 ^{o}C in the interim: cases C_{iii} and D_{iii}. These results are displayed with a cross (x) symbol and differ considerably from the initial results recorded. The low frequency arc is comparable but the high frequency arc is larger; however, the series resistance decreases. Curiously, for case D_{iii}, the low frequency arc occurs at around the same values of Z' as for case D_i, despite the difference in high frequency data. The differences seen with time could be due to degradation of the SOC; however, the reduction of R_s is unexpected and suggests there is a large, varying series resistance associated with the jig, giving large uncertainty to the SOC results and posing a significant problem.

For SOCs, the Z* and Y* spectroscopic plots are of most interest. The series resistance, and indeed Z' at all frequencies, decreases with an increase in CO_2/H_2 ratio, while Y′ follows the opposite trend. Z'' and Y'' both show two main peaks in the frequency range measured. The magnitude of the high frequency Z'' peak decreases as the CO_2/H_2 ratio increases, while that of Y'' decreases. The trends are less clear for the magnitude of the peak at low frequency but the value of the characteristic frequency f^{o} shifts to higher frequency as the CO_2/H_2 ratio increases. The magnitudes of the high frequency peak for the data taken at a later date, cases C_{iii} and D_{iii}, are larger for both Z'' and Y'', with a small shift in f^{o}.

On a log-log scale, there is little visible change in M* and ε* between the different fuel compositions; however, when M′ is plotted on a linear scale, Figure 3.12g, it can be seen that the peak at 50 kHz decreases in magnitude with increasing CO_2/H_2 fuel

ratio. Further data analysis methods could help determine the effect of fuel concentration on the performance of SOCs.

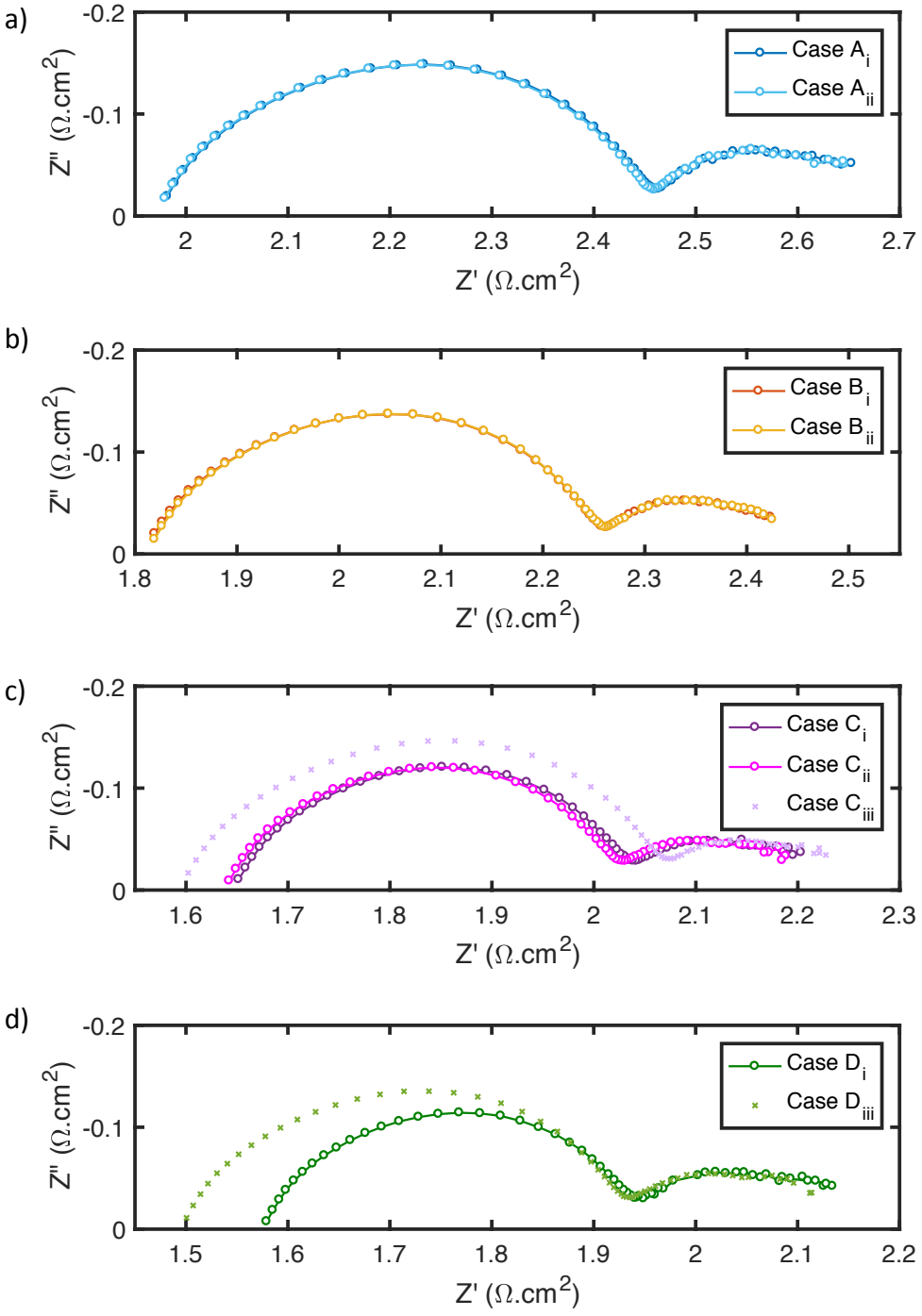

Figure 3.11: Z* plots of geometry- and inductance-corrected SOC data at 850 °C at four different fuel compositions of CO_2, H_2 and N_2: a) 3, 12, 5 ml, b) 5, 10, 5 ml, c) 10, 5, 5 ml, and d) 12, 3, 5 ml. Data marked with (x) were taken several days later for the same cell at setup.

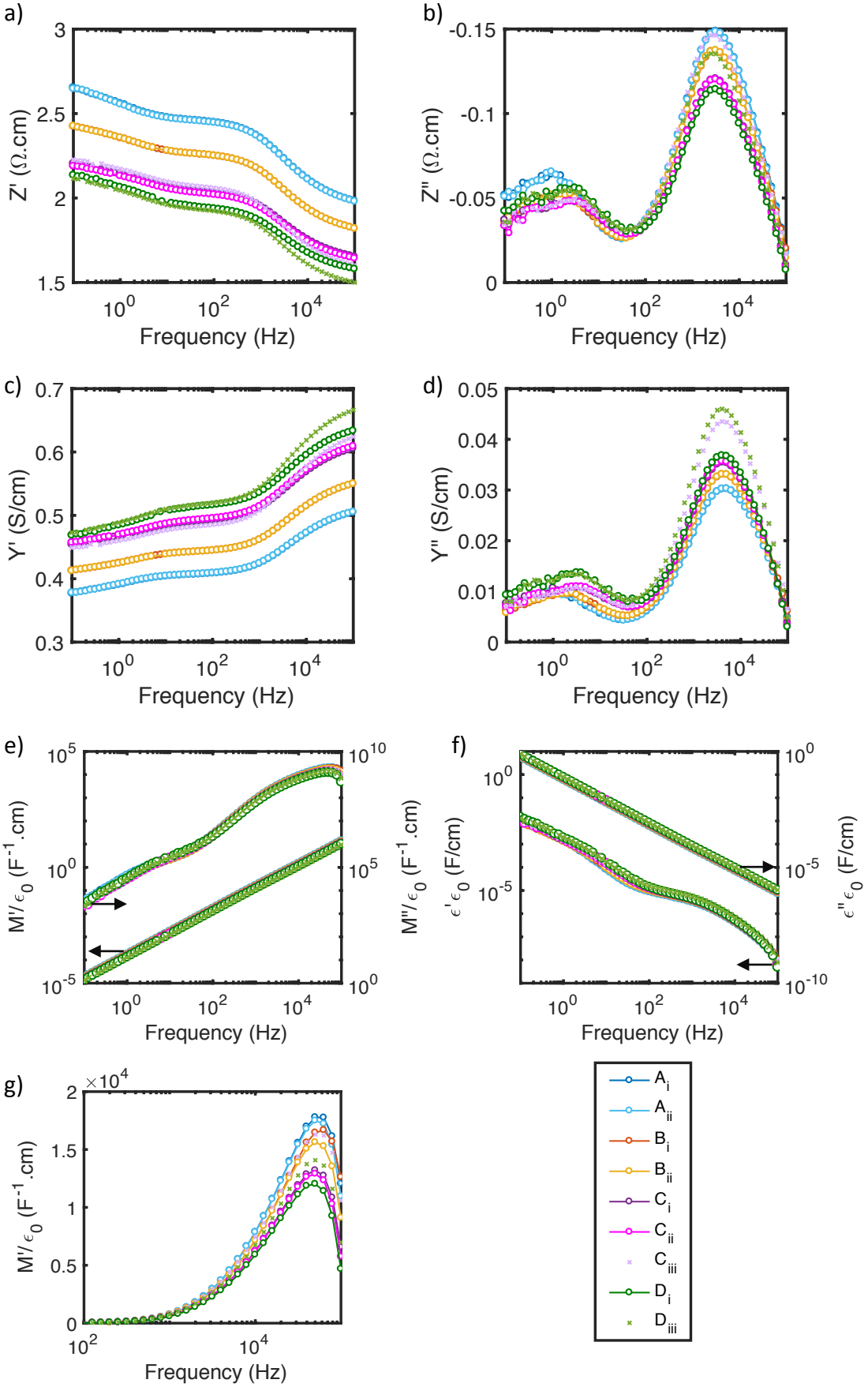

Figure 3.12: Spectroscopic plots of immittance data at 850 °C taken at different fuel concentrations. a) Z' b) Z'', c) Y', d) Y'', e) M' and M'' f) ε 'and ε'' and g) linear plot of M' (high frequency only). Plots (e) and (f) have two y-scales, indicated by arrows.

3.6 Analysis of Differences in Impedance Spectra (ADIS)

The differences between Z* spectra for the cases obtained are investigated using ADIS. Codes were written in Matlab (see Appendix A.2): firstly, any missing frequency points (due to anomalous points being discarded) were estimated using interpolation, to enable subtraction at every point. Then both $\Delta Z''$ and $\Delta \dot{Z}'$ (see Section 2.4.2) were calculated, for comparison.

The two subtractions each use only one component of Z*: either the real or the imaginary part. The same information can be obtained from either component, due to the Kramers-Kronig conditions being satisfied; however, noise can cause some differences in the spectra. To investigate the effect of noise, spectra taken back-to-back at the same conditions were subtracted from each other; the results are shown in Figure 3.13.

There is marked noise at low frequency, oscillating around zero, showing there is noticeable uncertainty in the Z* values measured. This noise is comparable between the two subtraction methods, although in general it has a greater magnitude for $\Delta \dot{Z}'$ spectra.

At high frequency, $\Delta \dot{Z}'$ (Fig. 3.13c) shows negligible change between consecutive measurements, whereas there is a systematic increase in $\Delta Z''$ (Fig. 3.13b). A change in Z'' but not Z' that increases with increasing frequency correspond to an inductive effect; jig inductance was corrected using a constant value for all spectra presented, yet even consecutive measurements appear to have varying inductance contributions from the jig.

ADIS results for an increasing CO_2/H_2 fuel ratio are presented in Figure 3.14. Both $\Delta Z''$ and $\Delta \dot{Z}'$ are shown; although the high frequency peak of $\Delta \dot{Z}'$ is slightly narrower, the noise is amplified and the results are less clear than those for $\Delta Z''$.

In $\Delta Z''$, the high frequency feature is entirely negative and largely symmetrical, indicating that τ is the same for the compared samples, see Figure 2.13). However, there is a slight shift in the frequency between 4 and 6 kHz where the maximum difference in the spectra occurs. Also, the assumed change in inductance affects values at high frequency, particularly noticeable for case B_{ii} (see Figure 3.14b). The curve is less symmetrical in terms of $\Delta \dot{Z}'$, and could possibly be a combination of two features at 3-4 kHz and 30-40 kHz. Both sets of spectra illustrate the decrease in – Z'' for an increase in CO_2/H_2 ratio.

The low frequency feature between 0.1 and 60 Hz in Figure 3.14 has a poor-signal to-noise ratio, particularly for $\Delta \dot{Z}'$, and there are no discernable trends with increasing CO_2/H_2 fuel ratio. The change in sign at around 2-4 Hz in Figures 3.14b and 3.14c indicates that τ varies. There is no rotational symmetry in the feature, which

indicates that the resistance varies too (see Figure 2.13), decreasing with increasing CO_2/H_2 fuel ratio. There is also likely to be a change in capacitance.

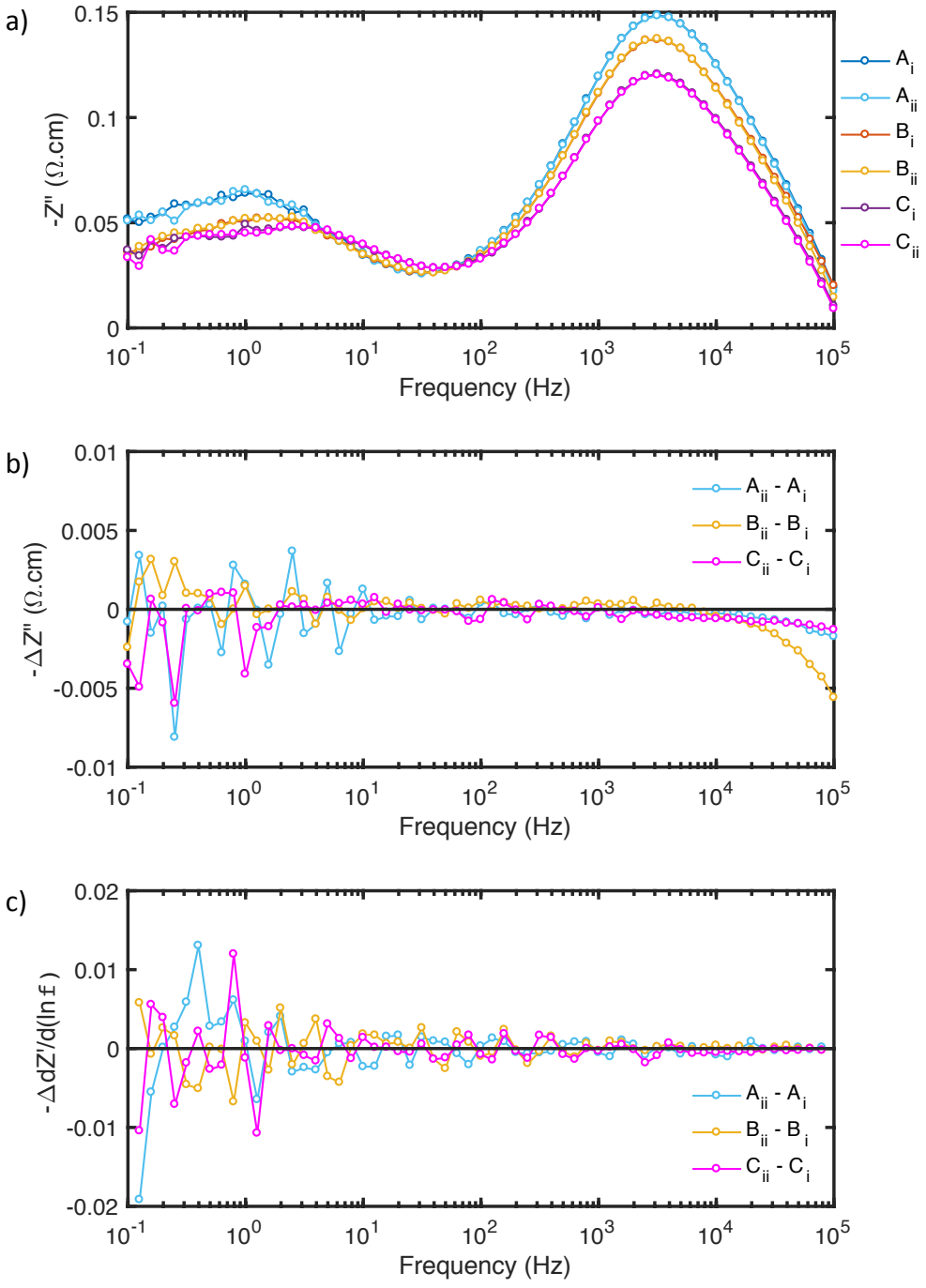

Figure 3.13: Comparison of IS data taken immediately after each other at a range of concentrations (see Table 2.2) a) Z" spectroscopic plot, b) ADIS Z'' subtraction with respect to the initial case (i) at each concentration, and c) ADIS Ż' subtraction with respect to case (i).

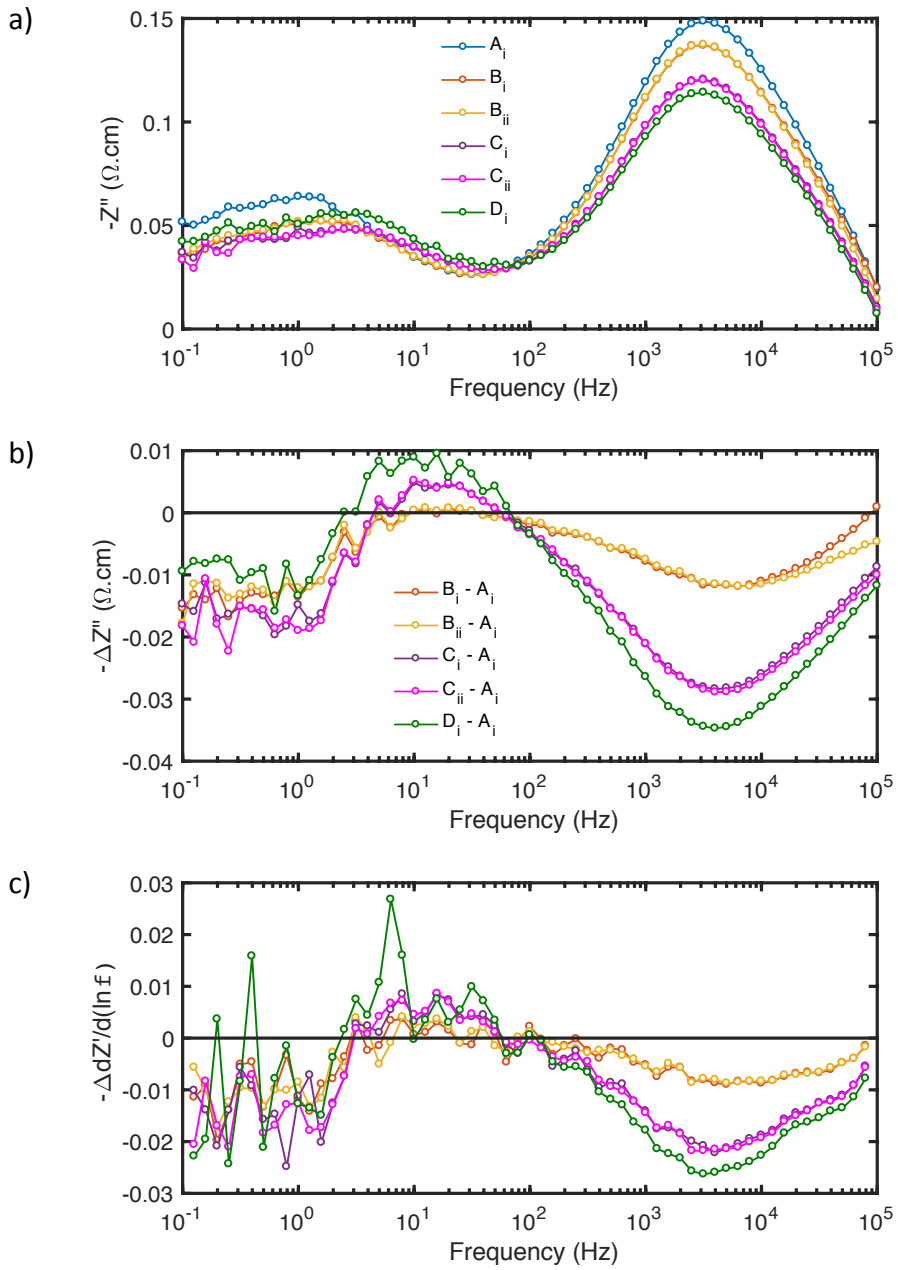

Figure 3.14: Comparison of IS data at different concentrations. a) Z'' spectroscopic plot, b) ADIS Z'' subtraction with respect to A_i, and c) ADIS $\dot{Z}'$ subtraction with respect to A_i.

ADIS results for spectra taken under the same conditions on different days are shown in Figure 3.15. At low frequency the results are noisy, but have negligible systematic change, with points scattered around zero. The high frequency points are all positive but not symmetrical, possibly due to there being two features present, seen particularly in $\Delta\dot{Z}'$. The original Z'' spectra show a marked increase in Z'' with aging; hence, as the peak frequency only varies slightly in Figures 3.15b and 3.15c, the capacitance is also likely to change.

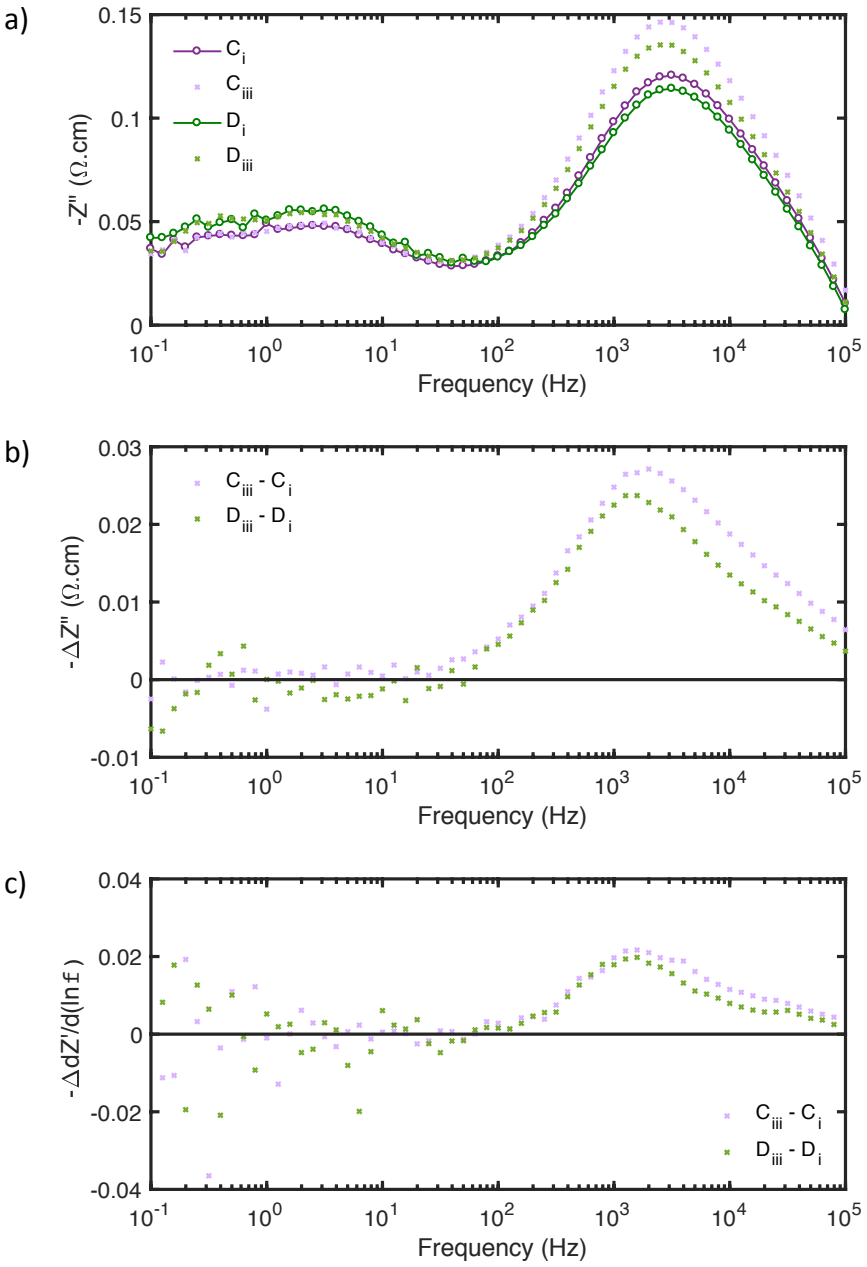

Figure 3.15: Comparison of IS data for the same cell taken a couple of days apart; a) Z'' spectroscopic plot, b) ADIS Z” subtraction with respect to cases C_i and D_i and c) ADIS Ż’ subtraction with respect to cases C_i and D_i.

3.7 Distribution of Relaxation Times (DRT)

3.7.1 Method

A program was written in Matlab, see Appendix A.3, to compute DRT as outlined in Section 2.4.6. The process is represented as a flow chart in Figure 3.16. The polarisation resistance R_{pol} is estimated from the Z* Nyquist plot; firstly, the Z'' intercepts are estimated and then the series resistance is subtracted from the total resistance. Z_0'' represents the experimental data only, whereas $\mathrm{Z}_{\mathrm{tot}}''$ represents the experimental data combined with the extrapolated low and high frequency data, which are calculated using $grad_1$ and $grad_2$. These represent the gradient of $\ln|\mathrm{Z}_0''|$ versus the logarithm of the frequency at low and high frequency, respectively. N_0 and N_{ext} represent the number of experimental and extrapolated data points, respectively, and the size n_{filt} of the Hanning window is determined manually, as illustrated in the following section.

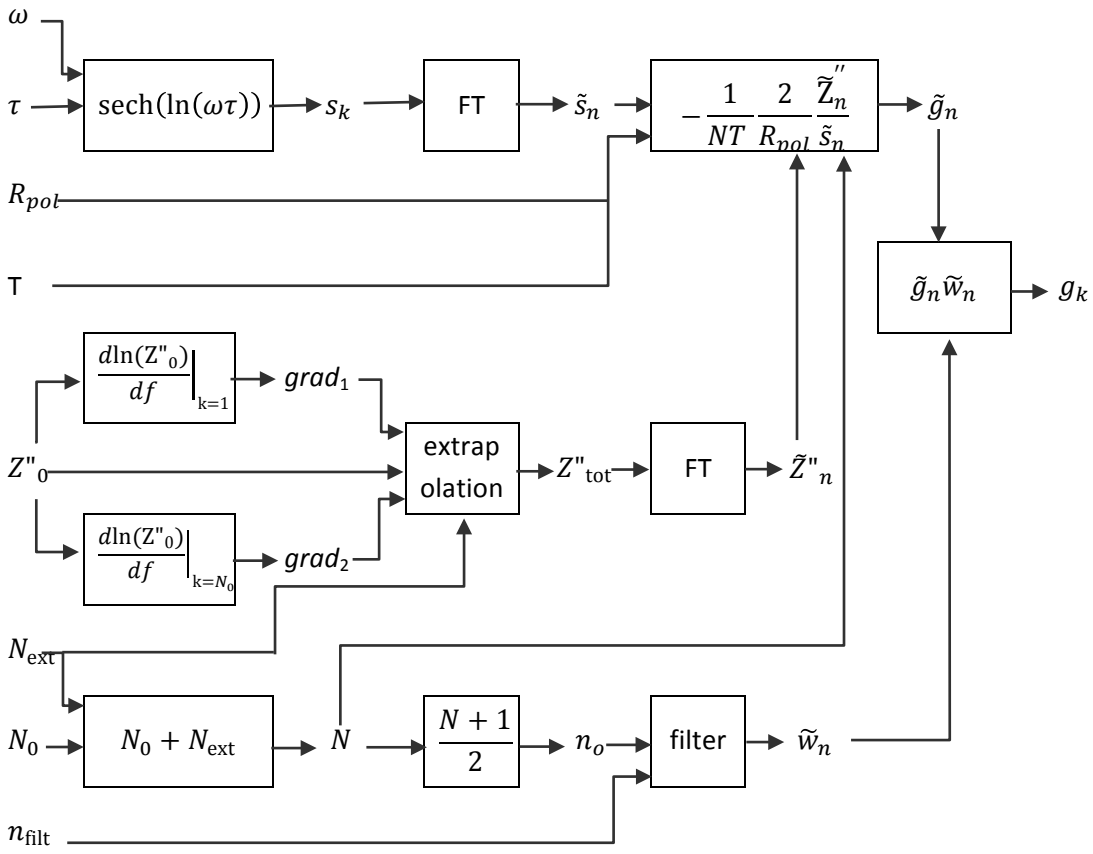

Figure 3.16: DRT flow chart.

3.7.2 Effect of parameters on DRT data

To obtain meaningful DRT graphs, a number of parameters need to be fine-tuned. The size n_{filt} of the Hanning window used has a large influence on the shape of the resulting DRT, as illustrated in Figure 3.17. When the filter size is too large, the spectrum contains excessive noise (green line), producing artefacts. However, if it is

too low (orange line), then the graph features merge together, hiding features that are occurring and offering no benefit over the spectroscopic plot.

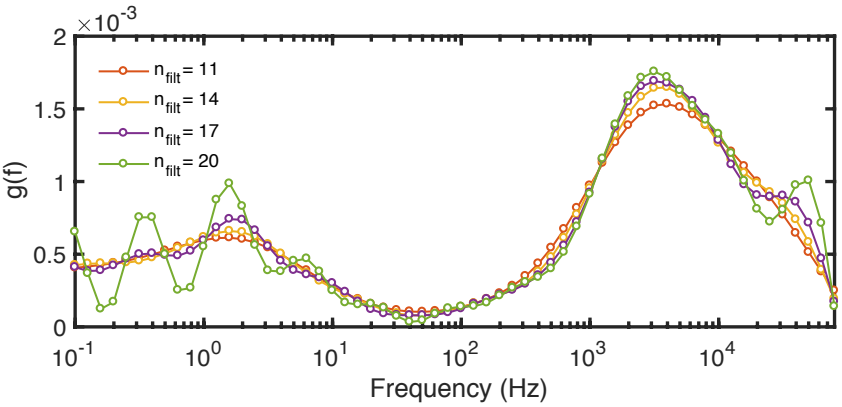

Figure 3.17: DRT for case A_i, using a variety of window sizes, n_{filt}, during the computation.

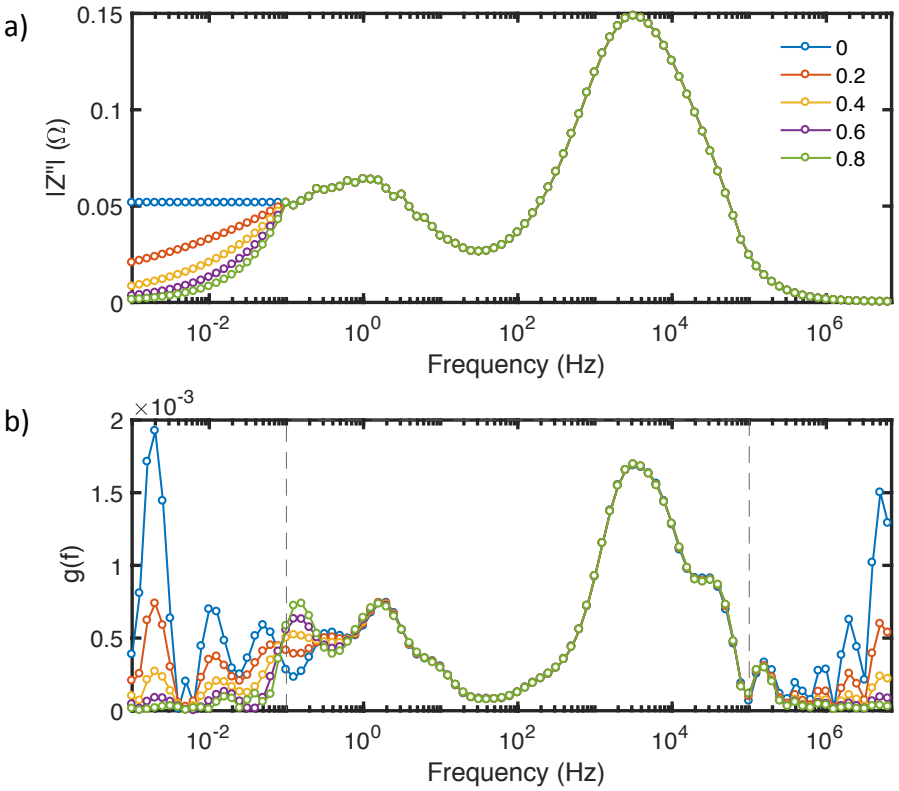

Figure 3.18: a) Bode plot of Z'' vs frequency for an SOC, using different gradients for the extrapolation of data at low frequency, and b) corresponding DRT.

The value of the gradient used during extrapolation also affects the DRT. In Figure 3.18, curves are plotted for a number of different gradient values used for extrapolation at low frequency. Points are extrapolated over two decades of frequency. The DRT results at both low and high frequency are affected, although mostly contained to the extrapolated frequency region, indicated by the dashed lines in Figure 3.18. However, DRT values in the frequency range of 0.1 – 1 Hz vary considerably with the gradient value; hence, unless the gradient can be estimated to

a high precision, there is significant uncertainty associated with the data within the lowest measured frequency decade.

Z'' spectra contain noise, particularly at low frequency, which can produce artefacts in DRT if the data are not of sufficient quality. The Z'' spectrum and the corresponding DRT are shown in Figure 3.19 for the low frequency data of two consecutive measurements: cases A_i and A_{ii}. The experimental Z'' spectra (blue and orange circles) are identical to within the experimental error; however, the DRTs appear to be different. Both show three peaks between 0.1 to 30 Hz but their relative magnitudes and peak frequency values differ. To investigate the effect of experimental noise, data points in case A_{ii}, with particularly large error, were removed and recalculated using interpolation (maroon circles). This caused a slight frequency shift in the DRT spectrum compared to the original spectrum (orange circles) but is still not comparable with case A_i. To reduce noise further, DRT was calculated using the KK-transformed values for both cases. The results (cross symbols) vary both from each other and from the corresponding experimental results, particularly for case A_{ii}. This illustrates how the low frequency Z'' data is insufficiently precise here to obtain reliable DRT results and that DRT is very sensitive to noise; therefore, only high frequency data are potentially usable.

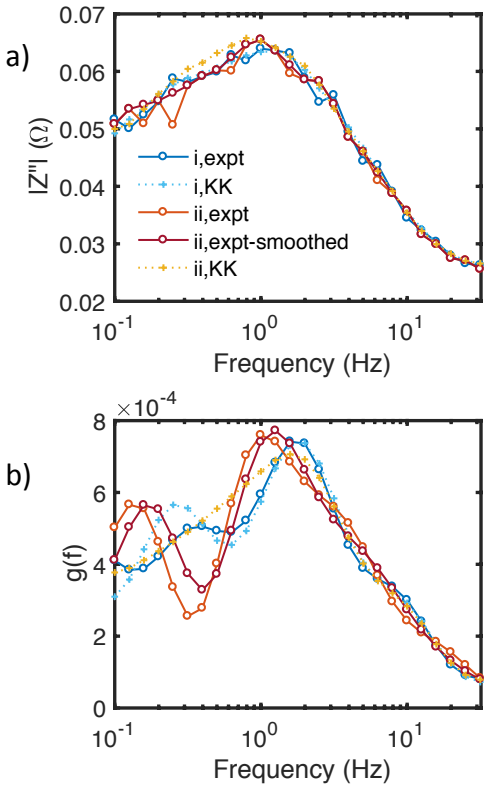

Figure 3.19: Z'' spectroscopic plot, and b) corresponding DRT for low frequency data for case A_i and A_{ii}, both for direct experimental data (o) and that from Kramers-Kronig transformation (+). The maroon line is case A_{ii} with noisy data removed.

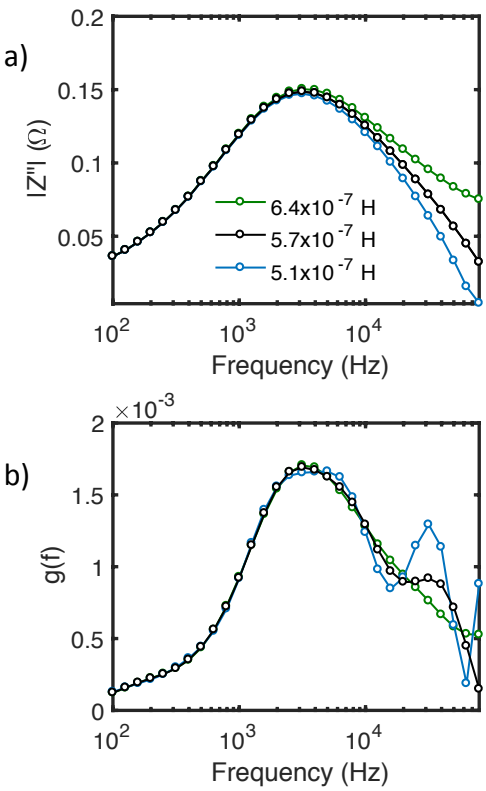

Figure 3.20: Z'' spectroscopic data, and b) corresponding DRT for high frequency A_i data with three different inductance correction values applied: both short-circuit experiment values and the average value used.

The uncertainty associated with the jig inductance can also affect the DRT results. In Figure 3.20, the high frequency results are shown for three inductance correction values: the two short circuit values and the average value used (see Section 3.3). If L_s is too low, the peak at around 30 kHz is overemphasised and looks noisy, with a large jump between consecutive DRT values. If L_s is too high, this peak is hidden within the more prominent peak at around 3 kHz. The average value used gives reasonable results. This emphasises the importance of accurate correction of immittance data for the jig inductance.

3.7.3 RESULTS

The DRT for the initial (non-aged) measurements (see Table 3.4, Day 1) for compositions *A* to *D* are shown in Figure 3.21 for high frequency data. The corresponding Z'' data are shown in Figure 3.14a. There are two resolvable processes between 100 and 10^5 Hz, with peaks around 3 and 30 kHz in all measurements, complementing the ADIS results in Figures 3.14a and 3.15a. The peak DRT values also all have similar magnitudes to each other. There is no clear trend in the heights of the peak with fuel composition and the difference could be due to the uncertainty of the value of R_{pol}, estimated from the Z* data; the DRT is scaled by the inverse of R_{pol}, see Equation [2.64].

The DRT for both non-aged (circles) and aged (crosses) samples are shown in Figure 3.22 for cases *C* and *D*. The corresponding Z'' spectra are displayed in Figure 3.15a. The peak at around 30 kHz appears virtually unchanged, whereas the peak at around 3 kHz shifts to 2.5 kHz and its relative magnitude increases by 7 to 11% for the aged samples.

In summary, DRT is of limited use as there are substantial uncertainties associated with the method: both from input parameters and from its high sensitivity to noise. Only high frequency data are useable and this gives very little extra information to that obtainable from other methods.

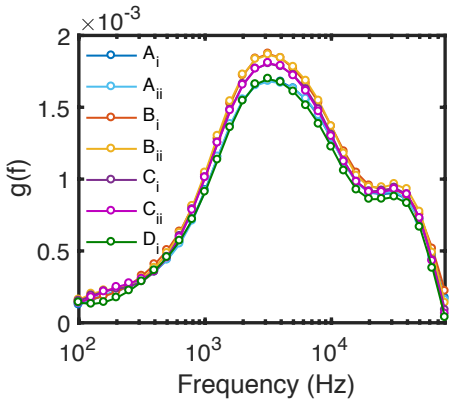

Figure 3.21: DRT for a range of concentrations

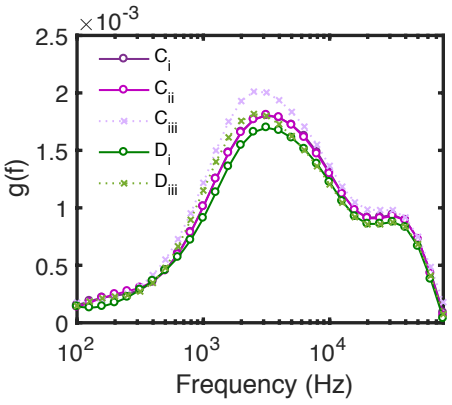

Figure 3.22: DRT for cases *C* and *D* taken a few days apart

3.8 COMPARISON WITH LITERATURE RESULTS

IS data for the NextCell investigated in this chapter contain two peaks in the frequency region 100 – 100,000 Hz, whereas three peaks were seen for both the Barfod and Leonide cells, see Table 2.1, (Barfod et al., 2007, Leonide et al., 2008, Leonide, 2010). They both have an extra lower frequency peak that they attribute to the cathode. Cathode processes were not investigated specifically for the NextCell but should still appear in admittance data for a full cell. However, it is not appropriate to compare the processes occurring below 200 Hz, as the data obtained here were not sufficiently accurate.

Both IS peaks for the NextCell (3 kHz, 30 kHz at 850^{o}C) vary with fuel concentration, as seen by ADIS, and are hence associated with the fuel electrode, which is denoted the anode in fuel cell mode. The characteristic frequencies are similar to those for the Leonide cell (3, 50 kHz) measured at 860 ^{o}C. The Barfod cell also has a peak at 50 kHz but it is attributed to the cathode; its anode peak is at 8 kHz, which is a little higher than seen here.

The NextCell is electrolyte-supported whereas the other two cells are anode-supported, and hence have an anode substrate layer as well as an active layer. There are therefore microstructural differences between samples. Further differences could also occur from different sintering conditions. These differences are likely to cause differences in the immittance response of the cells; however, as all three cells contain the same anode material Ni-YSZ, the two anode peaks seen for the NextCell could well be attributed to the same processes as the two anode peaks in the Leonide cell, namely: oxygen transport in YSZ, charge transfer resistance at triple phase boundaries, and, during start-up only, gas diffusional loss in the functional layer. More experiments are necessary to confirm such suggestions, such as immittance measurements at different temperatures so that activation energies can be obtained for the processes. Also, measurements in different oxygen atmospheres could aid in determining any cathodic peaks occurring.

Prior to data analysis, Leonide et al. (2008) checked for KK compliance of their immittance data; however, during EC fitting, there was an inductive artefact seen above 300 kHz, with no mention of inductance correction. In contrast, Barfod et al. (2007) included an inductor in the SOC equivalent circuit but made no mention of KK. Here, the NextCell IS data were both checked for KK compliance and corrected for jig inductance effects.

3.9 CONCLUSIONS

In this chapter, the use of Impedance Spectroscopy (IS) for the characterisation of Solid Oxide Cells (SOCs) was discussed, and IS data were measured for a commercial SOC sample under a range of fuel concentrations. Characterisation can be achieved by fitting Equivalent Circuits (ECs) to the resulting spectra. Reliable data are crucial if meaningful results are to be obtained; confidence is needed in both experimental results and in the data analysis. To that end, the methodology of data correction and subsequent analysis is discussed, before presenting the experimental results obtained.

METHODOLOGY:

- The impedance results obtained had a significant contribution from the test jig: an inductance associated with lead resistance is a particular problem for IS data on SOCs at operating temperatures.
- Short-circuit experiments only gave approximate values to use for jig inductance correction for SOC samples, as values obtained differed between short-circuit trials. The jig had to be dismantled and reassembled between sample measurements and short-circuit experiments, hence the method is not accurate.
- A constant value of jig inductance, L_s was used to correct the SOC sample data, equal to the average of the two short-circuit measurements obtained; however, L_s can vary even between consecutive measurements at identical conditions, highlighted by the difference in ADIS results for Z'' subtraction compared to those from Z'.
- It is not possible to correct for the series resistance associated with the jig, R_s with any confidence, as it varied by an order of magnitude between short-circuit trials; however, the additional high frequency behaviour can be corrected and is not particularly sensitive to the correction method used.
- Not all data collected were Kramers-Kronig (KK) compliant; in particular, data above 10^5 Hz contained a systematic error. Also, low frequency data (below 0.1 Hz) had a poor signal-to-noise ratio and were hence also discarded.
- ADIS using the natural log of the differential of Z' ($\Delta\dot{Z}'$) gave sharper peaks than from the subtraction of Z'' but contained a lower signal-to-noise ratio; therefore, both subtractions were carried out, to aid interpretation.
- DRT relies on the input of several parameters, such as the gradient used to extrapolate the input data and the size of the window used to filter the results. DRT is extremely sensitive to these values, as well as to sample noise and inductance correction values; therefore, results from this method should be verified using other methods.

RESULTS:

- In the SOC results, a high frequency feature is visible in both *Z*'' and *Y*'' spectroscopic plots, with a resistance that decreases with increasing CO_2/H_2 fuel concentration, and a roughly constant characteristic frequency f^o value.
- ADIS (using Z') and DRT results suggest the feature is made up of two resolvable processes: one at around 3 kHz and one at 30 kHz. Both peaks scale similarly with CO_2/H_2 fuel concentration, implying they are anodic processes. The frequencies are comparable with those of the two high frequency anodic peaks listed for the cell investigated by Leonide (2008), which are thought to represent a combination of oxygen transport in YSZ, charge transfer resistance at triple phase boundaries, and gas diffusional loss in the functional layer during start-up.
- The spectra taken after the sample had been left at high temperature for a couple of days have a larger resistance at the high frequency feature, but low frequency data appears unaffected.
- Data below 100 Hz appear as a broad arc in Z* Nyquist plots, with a value of f^o that shifts to higher frequency as the fuel ratio increases. The signal-to-noise ratio of this region is insufficient to produce meaningful results using ADIS. Similarly, DRT is too sensitive to enable reliable analysis in this low frequency region.

CHAPTER 4: YSZ SINGLE CRYSTAL[§]

In the first part of this chapter, theory is presented about the structural properties of yttria stabilised zirconia (YSZ) and its polarisation mechanisms and literature is reviewed relating to its electrical properties. The electrical responses of several possible equivalent circuits are also explored. The aims for the remainder of the chapter are then given. This is followed by a description of experimental methods, results and a discussion of the most appropriate equivalent circuit to describe the bulk electrical response from a YSZ single crystal.

4.1 INTRODUCTION

In the previous chapter, SOCs were investigated using impedance spectroscopy (IS). It was shown that many polarisation processes were occurring with comparable relaxation frequencies f^{o}, which makes the characterisation of such complex devices challenging. As an alternative to such post-experimental analysis, information about single components can be obtained by carrying out experiments on the materials separately. In this chapter, therefore, the focus shifts to IS on samples of a single material, namely 8 mol% YSZ.

YSZ, or yttria stabilised zirconia, is commonly used for the electrolyte as well as for the oxygen-ion-conducting phase in the electrodes of SOCs, for example a porous YSZ/Ni mix is used for the fuel-side electrode and a porous YSZ/LSM mix for the oxygen-side electrode, see Section 2.1. The investigation of both dense (electrolyte) and porous (electrode) YSZ can therefore help with the electrical characterisation of fuel cells. By looking at one material, the number of processes occurring is reduced significantly. In IS results collected at 850 ^{o}C (the typical operating temperature of conventional SOCs), the electrolyte component is represented as an Ohmic resistance, as the YSZ features occur at frequencies above the range measured. However, it is possible to shift these features into the measurable frequency range by measuring at lower temperatures. For IS on a single material, the features of interest are polarisation from microstructure and from intrinsic materials parameters, discussed later.

YSZ is an oxygen ion conductor, so IS reflects its ability to conduct oxygen ions. As YSZ is not electronically conductive, electrodes need to be applied to enable impedance measurements to be carried out. These typically consist of an unreactive and precious metal such as platinum or gold. The addition of the electrode affects

[§] Further work after the examination of this thesis revealed that the “single crystal” was actually a textured crystal (see Appendix A.5 for further discussion).

the impedance results, causing a further response at lower frequency; if the electrodes are partially oxygen-ion blocking, diffusion polarisation is seen.

Microstructurally, YSZ consists of a bulk lattice and, for a polycrystalline sample, there are grain boundaries between the grains. Additionally, porous samples contain pores within and/or between grains. Pores and grain boundaries are the subject of Chapter 5.

In general, there are four *intrinsic polarisation mechanisms*: atomic, ionic, dipolar and space charge polarisation, see for example Moulson and Herbert (2003). They all involve localised movement in the presence of an electric field. *Atomic* polarisation is present in all solids and originates from electron charge movement. *Ionic* polarisation is present in all ionic solids, including oxides, and is due to the localised movement of cation and anion sub-lattices. *Dipolar* polarisation occurs due to the formation of local dipoles, which align under the presence of an electric field. Finally, *space charge* is a large-scale polarisation, occurring due to long-range migration of charge carriers, such as electrons or ions, and dominates the polarisation of metals.

Not all materials exhibit all four polarisation mechanisms; for example, covalent solids do not undergo ionic polarisation, and not all materials form dipoles. YSZ exhibits atomic, ionic and space charge polarisation; the presence of dipoles is still debated (see Section 4.2.4).

The macroscopic property relating to polarisation is permittivity ε'. The imaginary component ε'' represents leakages, and losses are commonly quantified by the dimensionless parameter $\tan\delta$, equal to the ratio of ε''/ ε'.

The polarisation mechanisms are usually observed on different frequency scales; these vary with temperature for both dipolar and space charge polarisation. For d.c., all mechanisms that are possible in a given material are present, whereas for a.c., as frequency increases, space charge and then dipolar effects are relaxed out (i.e. their effects become negligible in ε') at around 0-10^3 Hz and ~10^{10} Hz, respectively. In contrast, ionic and atomic polarisation have resonance peaks at around 10^{13} and 10^{15} Hz, respectively (Moulson and Herbert, 2003). Each resonance or relaxation effect is represented by a peak in ε''. Schematics for these processes are shown in Figure 4.1 for both ε' and ε'' versus frequency.

Once IS results are obtained, equivalent circuits (ECs) can be used to fit the data and, provided the EC is a sufficient physical representation of the processes occurring, material parameters can be extracted, namely conductivity and permittivity, see Section 4.4.

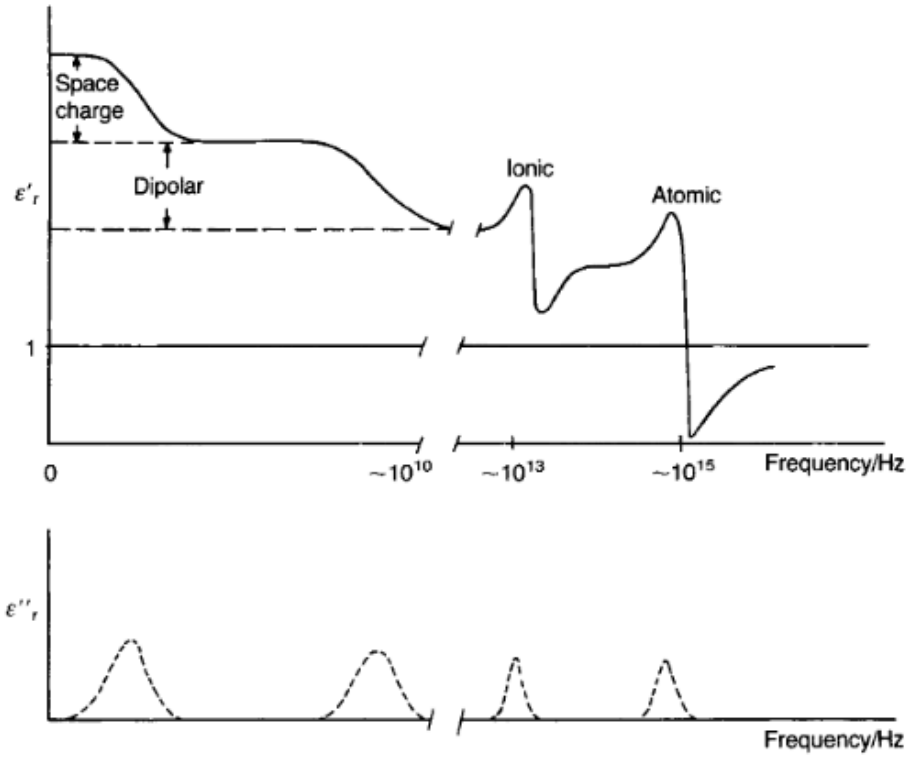

Figure 4.1: Schematic of the variation of ε' and ε'' with frequency for a material exhibiting space charge, dipolar, ionic and atomic polarisation (Moulson and Herbert, 2003).

4.2 YSZ PROPERTIES

4.2.1 LATTICE PROPERTIES

The structure of zirconia (ZrO_2) is monoclinic at room temperature, becoming tetragonal at around 1200 ^{o}C and cubic at 2400 ^{o}C (Scott, 1975). It is possible to stabilise the cubic structure at lower temperatures by doping with yttria (Y_2O_3). This is achievable at room temperature with an yttria concentration of around 7-8 mol% and above (Subbarao and Maiti, 1984). The minimum concentration varies with the exact conditions used to produce it (Kharton et al., 2004). Typically, 8 mol% is used for fuel cell applications as it gives the highest conductivity, although 3 mol% is sometimes favoured as it is stronger mechanically; however, 3 mol% is tetragonal, not cubic, and is termed partially stabilised (Ciacchi et al., 1994).

Cubic zirconia has a fluorite structure (space group Fm3m); cations (Zr^{4+}) form a close-packed structure, with the anions (O^{2-}) filling the tetrahedral sites and the octahedral sites left empty. This is illustrated in Figure 4.2 (top left).

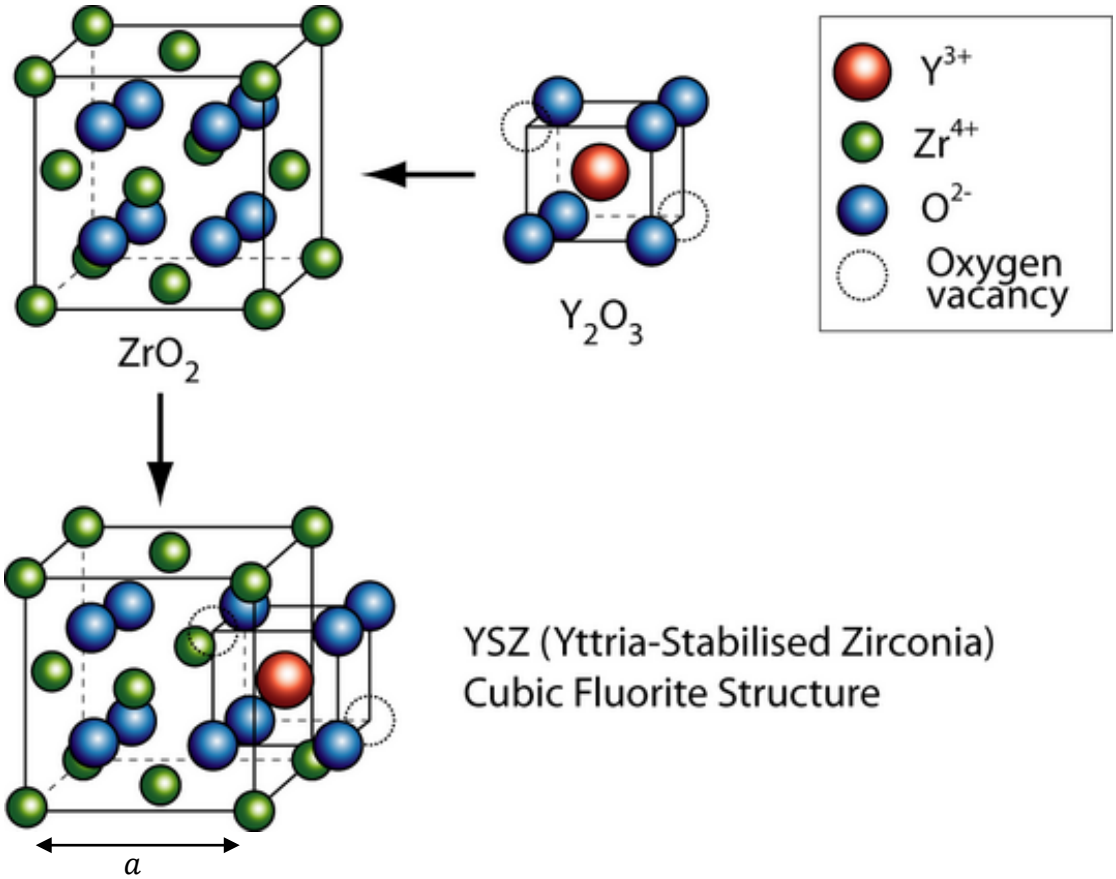

Figure 4.2: Fluorite structure of zirconia (top left) and the addition of yttria (top middle) to give yttria stabilised zirconia (bottom left). The lattice parameter a is illustrated. (DoITPoMS, 2018)

Using Kroger-Vink notation, the addition of yttria gives the following defect reaction:

$$2\mathrm{Zr}_{\mathrm{Zr}}^{\mathrm{x}} + 4\mathrm{O}_{\mathrm{O}}^{\mathrm{x}} \rightarrow 2\mathrm{Y}_{\mathrm{Zr}}^{\prime} + 3\mathrm{O}_{\mathrm{O}}^{\mathrm{x}} + \mathrm{V}_{\mathrm{O}}^{\cdot\cdot} \qquad [4.1]$$

Here, the main symbol represents the species involved: either the chemical element symbol, or V to represent a vacancy. The subscript represents the crystallographic position occupied by the species and the superscript represents the effective electric charge on the defect, where ^{x} is neutral, $'$ is negative and $^{\cdot}$ is positive. In cubic YSZ (Fig. 4.2 bottom left), some Zr sites are hence occupied by Y and, in order to balance the charge, anion vacancies are produced; therefore, the tetrahedral sites are no longer fully occupied. This allows for the movement of oxygen ions in the lattice, which is enhanced as oxygen ions can migrate between tetrahedral sites via the empty octahedral sites. This results in a high ionic conductivity, particularly at higher temperatures (Kilner, 2000). The lattice parameter a (see Figure 4.2) of 8 mol% YSZ is 5.14 Å (Itoh et al., 2015).

The chemical formula for 8 mol% YSZ is $(ZrO_2)_{0.92}(Y_2O_3)_{0.08}$; however, it is more usual to normalise this for the total number of cations, Zr and Y, which results in: $Zr_{0.852}Y_{0.148}O_{1.926}$, or 14.8 mol% $YO_{1.5}$ stabilised zirconia. The general formula is given by: $Zr_{1-4x}Y_{4x}O_{2-2x}$.

4.2.2 IONIC CONDUCTIVITY TRENDS

The movement of oxygen ions in the lattice gives the compound a sizable ionic conductivity, the magnitude of which varies with the level of doping. If all oxygen vacancies are mobile, then the conductivity σ is expected to be proportional to:

$$\sigma \propto c(1-c)\, e^{-\Delta H_m/kT} \qquad [4.2]$$

where c is the fraction of occupied oxygen sub-lattice sites, $1-c$ is the fraction of unoccupied sites, ΔH_m is the migration enthalpy of the oxygen sites (Kilner, 2000), k is the Boltzmann constant and *T* is temperature in Kelvin. Hence, at a constant temperature, the ionic conductivity is proportional to $c(1-c)$, see Figure 4.3, with a maximum conductivity when half the oxygen sites are vacant.

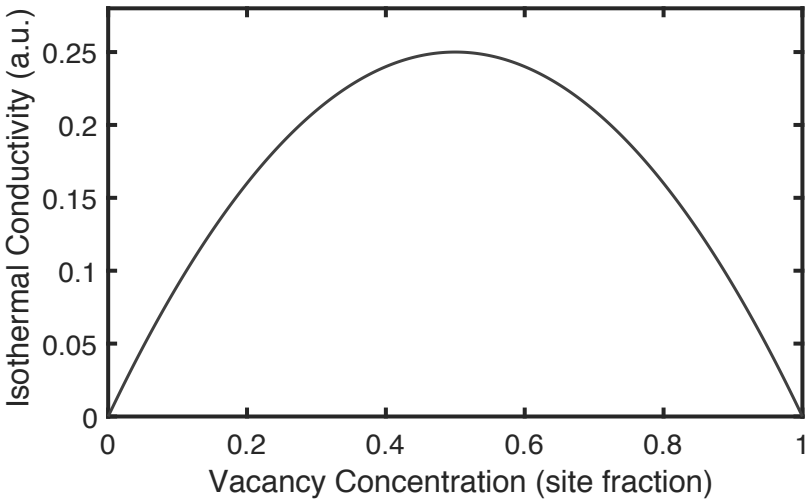

Figure 4.3: Isothermal conductivity as a function of the fraction of vacancies, assuming all vacancies are mobile. Adapted from Kilner (2000).

However, the conductivity of anion-deficient fluorite oxides does not follow this trend; the maximum ionic conductivity occurs at a vacancy concentration well below the predicted value (Kilner and Steele, 1981), implying that the number of mobile vacancies is smaller than the number of stoichiometric vacancies present (Kilner, 2000). For zirconium-based solid solutions, the maximum ionic conductivity occurs at an oxygen vacancy concentration of around 2.0 – 3.5 mol%, equivalent to 8-14 mol% $YO_{1.5}$, see Figure 4.4. The vacancy concentration varies with the chemical identity of the dopant but is independent of temperature (Kharton et al., 1999). The magnitude of the conductivity also varies with the dopant ion (Kilner and Steele, 1981).

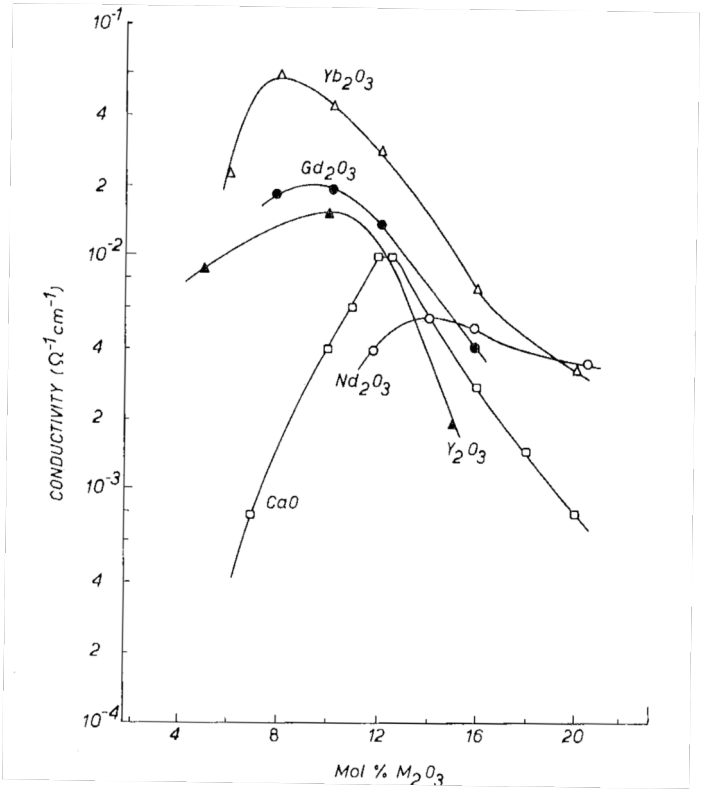

Figure 4.4: Variation of ionic conductivity with dopant concentration for various zirconia solid solutions (Kilner and Steele, 1981).

Conductivity is related to the temperature T by the simplified Arrhenius law, with an activation energy E_{act}:

$$\sigma = \sigma_0 \mathrm{e}^{-\frac{E_{act}}{kT}} \qquad [4.3]$$

where k is the Boltzmann Constant, σ_0 is the pre-exponential factor, and T is given in Kelvin. The variation in activation energy with oxygen vacancy concentration is displayed in Figure 4.5 for various fluorite oxides. Note that for the zirconium-based compounds there are no data at very low oxide ion vacancy concentrations as the cubic fluorite structure is not stabilised at room temperature. There is an initial decrease in activation energy, close to the limit of cubic stability, followed by an increase in activation energy, proportional to the increase in vacancy concentration.

In this region, the pre-exponential factor is also linearly dependent on the vacancy concentration but varies negligibly at low concentrations (Kilner and Steele, 1981).

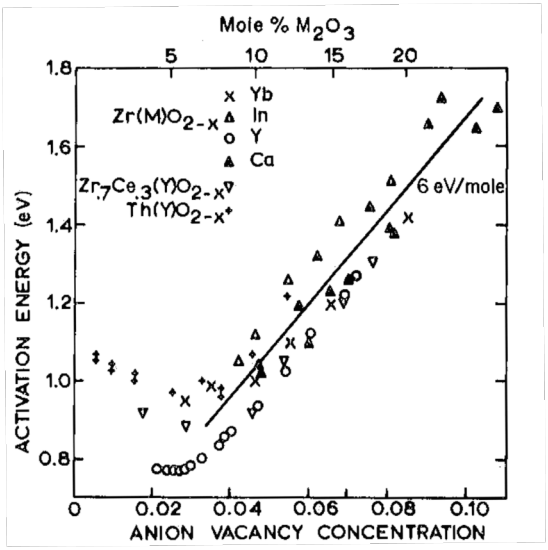

Figure 4.5: Variation of the activation energy with oxygen vacancy concentration for various (mainly zirconia) solid solutions (Kilner and Steele, 1981).

It is commonly thought that the decreased number of mobile vacancies present is due to oxygen vacancies binding with the dopant cations to form a defect associate. For YSZ, possible defect associates include $\left(Y'_{Zr}V^{\cdot\cdot}_{O}\right)^{\cdot}$, made of one oxygen vacancy and one yttrium site giving a net positive charge, or alternatively the neutral associate $\left(Y'_{Zr}V^{\cdot\cdot}_{O}Y'_{Zr}\right)^{x}$, with two yttrium sites per oxygen vacancy (Kilner and Steele, 1981). At low yttrium concentration the charged associate is favoured, as the yttrium sites are immobile and essentially randomised, making it unlikely for them to be nearest neighbours (Kilner and Steele, 1981). For $\left(Y'_{Zr}V^{\cdot\cdot}_{O}\right)^{\cdot}$, the activation energy and the pre-exponential factor, and therefore the conductivity, are predicted to be independent of the dopant concentration, for all trivalent ions. The theoretical activation energy is the migration enthalpy of oxygen vacancies ΔH_m plus an additional term, the enthalpy of association ΔH_A of the defect. As an aside, a slightly different trend is predicted for *di*valent dopant ions: the activation energy is independent of vacancy concentration x, but σ_0 is proportional to the square root of x, hence the conductivity also increases proportional to $x^{1/2}$. Experimentally, however, the activation energy and conductivity vary with dopant concentration, for both di- and tri-valent dopant ions, in contrast to this theory (Kilner and Steele, 1981, Kilner, 2000, Strickler and Carlson, 1964).

The origin for the minimum in activation energy, seen in Figure 4.5, is unclear but is thought to be related to defect association (Kilner, 2000). As x becomes large, there is a larger likelihood that complex associates form, involving multiple yttrium ions that further reduce the mobility of oxygen vacancies. The cause of the linear

dependence of E_{act} and σ_0 at higher dopant concentrations is also unclear. Hohnke (1979) attributes it to the presence of an extra Gibbs free energy-like term that varies with composition and is associated with the free energy for long-range ordering.

In addition to dopant concentration and valency, the conductivity of zirconium-based compounds with the fluorite structure also depends on the ionic radius of the dopant. The closer the ionic radius of the dopant ion to the radius of the host ion, the larger the magnitude of the ionic conductivity observed (Butler et al., 1983). This is attributed to minimisation of the lattice elastic strain energy by size matching. The trivalent dopant ion closest in size to Zr^{4+} is Sc^{3+}, which gives the highest conductivity, see Figure 4.6. However, as scandia stabilised zirconia (ScSZ) has only a small temperature and dopant concentration window in which it exhibits cubic fluorite behaviour, it is not often practical to use as an oxide conductor. Therefore, YSZ is more common, despite its lower conductivity (Norberg et al., 2011).

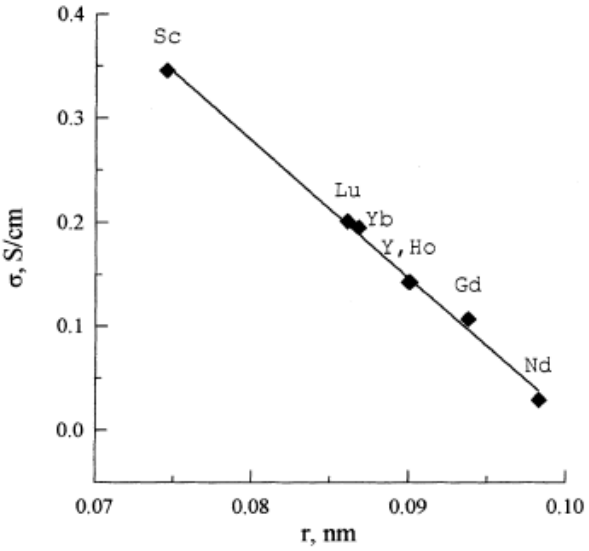

Figure 4.6: Variation of conductivity with ionic dopant radius, for ceramics at 1000 ^{o}C with the composition $Zr_{0.90}R_{0.10}O_{1.95}$, where R is a trivalent ion (Kharton et al., 1999).

4.2.3 LOCAL STRUCTURAL EFFECTS

The emergence of techniques such as partial radial distribution (PRD) has enabled examination of the local structure of materials, both experimentally from the diffuse scattering seen in neutron powder diffraction, and using molecular dynamics simulations (Norberg et al., 2011). For YSZ, comparison of the PRD functions for vacancy-Zr^{4+} ion interactions $g_{Zr-v}(r)$ and vacancy-Y^{3+} ion interactions $g_{Y-v}(r)$ showed that oxygen vacancies associate preferentially with the host Zr^{4+} ions, rather than the larger dopant Y^{3+} cations (Norberg et al., 2011), contradicting the earlier theories that vacancies are associated with the Y^{3+} ions. Preferential binding hinders the diffusion of oxygen ions and is seen in compounds with a size mismatch between dopant and host cation radii.

In contrast to YSZ, PRD studies of scandia stabilised zirconia (ScSZ) gave very similar results for $g_{Zr-v}(r)$ and $g_{Sc-v}(r)$, indicating that oxygen vacancies associated non-preferentially to Zr^{4+} and Sc^{3+} ions (Norberg et al., 2011). Sc^{3+} has roughly the same ionic radius as Zr^{4+} ions (Shannon, 1976); hence the lattice strain is negligible in ScSZ. However, the maximum ionic conductivity still occurs at a vacancy concentration well below the value of 0.5 predicted by assuming all vacancies are mobile. Marrocchelli et al. (2011) propose that this is due to the interaction between the vacancies, which minimises the lattice distortions caused by the charged vacancies. The possible vacancy pairs are shown in Figure 4.7. The PRD function for vacancy-vacancy interactions $g_{v-v}(r)$ shows that <111> ordering of vacancy pairs is favoured over <100> or <110>. As the dopant concentration (and hence the number of vacancies) increases, there is additional ordering: the <111> pairs pack together along the <112> direction, forming clusters. This reduces the mobility of the vacancies and hence lowers the ionic conductivity. This occurs on a local scale only, as the concentration of vacancies is insufficient to form a long-range structure.

These results were seen for both YSZ and ScSZ, as well as for a simulated compound i-YSZ_x, where all cations have an identical size and effective charge, designed to eliminate cation-vacancy interaction effects. Vacancy-vacancy interactions thus appear to be an effect intrinsic to the lattice. For i-YSZ_x, the maximum conductivity occurred at a dopant concentration of 23 mol%, which corresponds to a vacancy concentration of 5.8 mol%, and implies that vacancy-vacancy interactions play a significant role in the value of the concentration that corresponds to the maximum conductivity. Minor differences between compounds with different dopants are then attributed to the differences in vacancy-cation interactions, due to the lattice strain from the relative sizes of the dopant and host cations (Norberg et al., 2011, Marrocchelli et al., 2011).

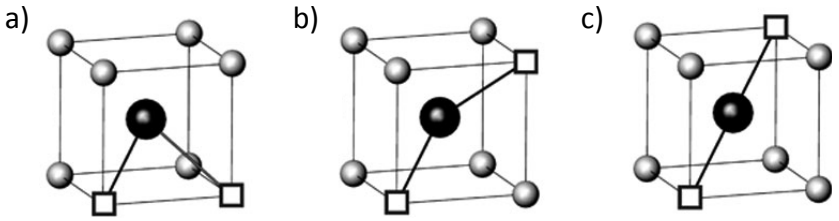

Figure 4.7: Schematic of a vacancy pair of orientation: a) <100>, b) <110> and c) <111> (Mohn et al., 2009).

4.2.4 DIPOLES

Dipolar polarisation is one of the four intrinsic material polarisation effects, see Section 4.1, and arises from the interaction of local, oppositely charged species. Dipoles align in the presence of an electric field, to give an enhanced ε'. The presence of dipoles in YSZ is debated, due to the uncertainty in the oxygen vacancy trapping mechanism(s) discussed above.

If vacancy trapping in YSZ is due to the presence of $(\mathrm{Y}'_{\mathrm{Zr}}\mathrm{V}_{\mathrm{O}}^{\cdot\cdot})^{\cdot}$ defect associates, then it is plausible that the oppositely charged $\mathrm{Y}'_{\mathrm{Zr}}$ and $\mathrm{V}_{\mathrm{O}}^{\cdot\cdot}$ sites form a dipole (Abelard and Baumard, 1982, Hernández and West, 2016, Perry et al., 2011, Yamamura et al., 2007). Perry et al. (2011) used the trend in relative permittivity ε_r with temperature to postulate the presence of dipoles and found dipolar relaxation to be thermally activated. At low temperatures, the oxygen vacancy was immobile in the frequency range measured. As temperature increased, the additional thermal energy enabled the oxygen vacancy to hop locally around the $\mathrm{Y}'_{\mathrm{Zr}}$ site, producing an enhanced ε_r under an applied electric field due to dipole reorientation. Their permittivity results are discussed in more detail in Section 4.4.4. Hernández and West (2016) used an alternative approach. As no direct evidence of a separate Z* arc had been found in impedance data to indicate the presence of dipoles, they proposed that the bulk arc contains a contribution from dipolar polarisation, and used a combined equivalent circuit to model this, see Section 4.3.1.

If, instead, vacancies are trapped by the formation of <111> vacancy-vacancy associates, ε' is unlikely to be enhanced via the application of an electric field, due to the fixed orientation of the associates, particularly if they group to form clusters in the <112> direction.

4.3 YSZ IMMITTANCE DATA IN THE LITERATURE

The immittance response of YSZ contains a high frequency bulk component, a low frequency electrode response and, for polycrystalline samples only, a grain boundary response at mid frequencies. On a Z* plot, see Figure 4.8, the bulk and grain boundary responses are represented as depressed arcs, which are generally non-symmetric (Hernández and West, 2016, Abelard and Baumard, 1995). The electrode response appears as a diffusion spike. A charge transfer effect can also occur, originating from electron transfer associated with the oxygen ions at the ceramic-electrode interface (Abram et al., 2001), which appears as an arc at intermediate frequencies, with a capacitance in the range of 10^{-7} to 10^{-5} F/cm (Irvine et al., 1990). It is visible in single crystal measurements (Abelard and Baumard, 1982) but has not been reported for YSZ ceramics, possibly because it is obscured by the grain boundary arc. The features visible in the data depend on the temperature and frequency range used in the measurements. At higher temperature, the bulk response shifts beyond the frequency range measured.

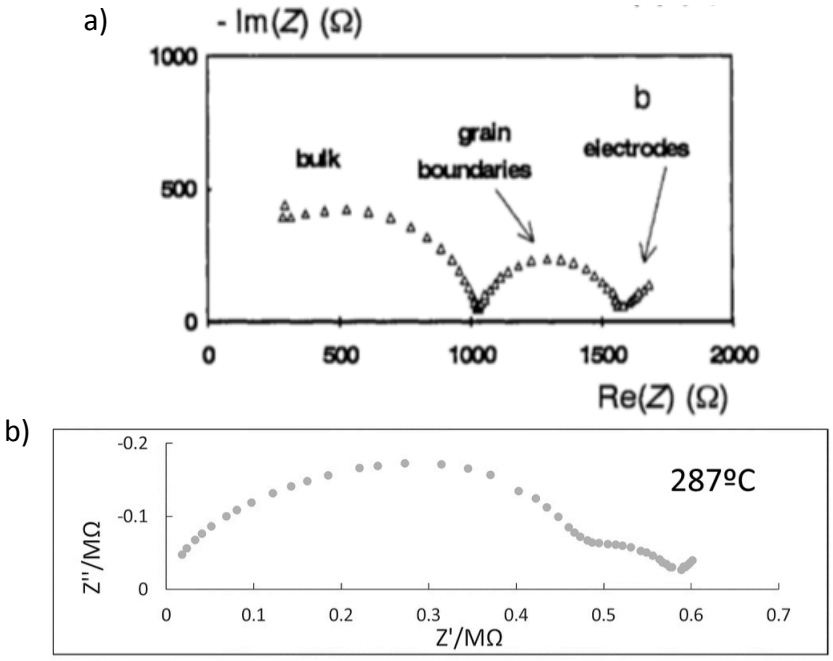

Figure 4.8: Z* complex plane plot for a 8 mol% YSZ ceramic at 400 ^{o}C (Abelard and Baumard, 1995) and for a different ceramic (also 8 mol% YSZ) at 297 ^{o}C (Hernández and West, 2016).

Data can also be represented spectroscopically using any of the four immittance formalisms: Z*, M*, Y* and ε*.

Spectroscopic plots of Z'' give peaks for both the bulk and grain boundary that deviate from the ideal Debye response; according to the Debye theory, one would expect a symmetric peak with a full-width-half-maximum (FWHM) of 1.14 decades on a log(f) scale, tending to a slope of ±1, on a log-log plot. The peaks are instead

non-symmetric, broader at low frequency, and have larger FWHM values (Bruce et al., 1982, Almond and West, 1983).

The M'' plot is dominated by the bulk response, as it is the feature with the lowest capacitance (Hodge et al., 1976). This peak also deviates from Debye behaviour but, in contrast to Z'', it is broader at higher frequency (Almond and West, 1983). The bulk characteristic frequency values for M'' and Z'', denoted f_M^o and f_Z^o, do not coincide; f_M^o is generally higher (Hodge et al., 1976). Instead of a single relaxation time, as assumed in the ideal case, there is a distribution of relaxation times present.

In Y', the main feature of interest is the high frequency dispersion, seen most clearly at lower temperatures, corresponding to the bulk. This is seen experimentally for all materials (Jonscher, 1977).

Example ε' spectra are shown in Figure 4.9. Features between 10^{-12} and 10^{-11} F/cm correspond to the bulk, features between 10^{-11} and 10^{-10} F/cm correspond to the grain boundary, if present, and features above this correspond to electrode effects (Irvine et al., 1990). The high frequency plateau, seen particularly at lower temperatures, is a bulk feature, and is the permittivity arising from both the atomic and ionic lattice polarisation, denoted ε'_∞, or relative permittivity ε_r. At lower frequencies in the bulk range, some curvature is seen.

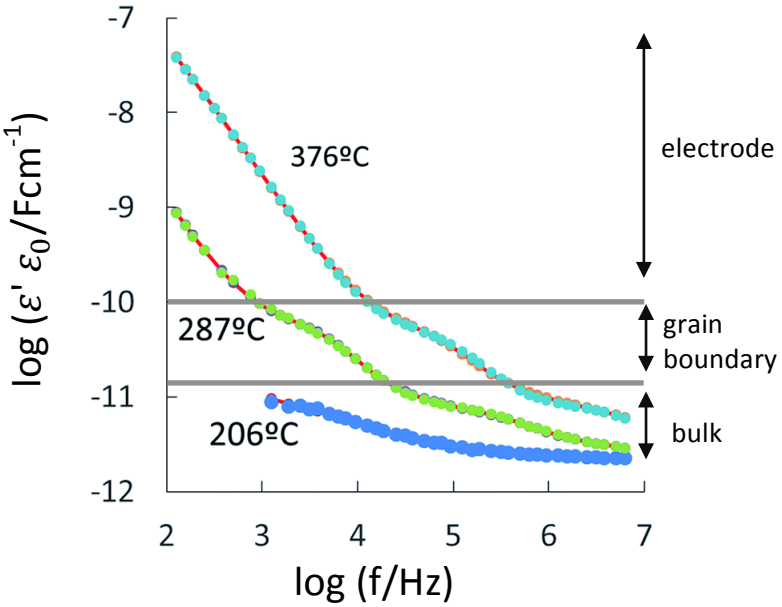

Figure 4.9: ε' spectroscopic plot of 8 mol% YSZ ceramic at three temperatures (Hernández and West, 2016), annotated to show the responses attributed to the bulk, grain boundary and electrode regions.

The ε' response is masked at low frequency by the grain boundary and/or electrode response, the latter of which shows the space charge associated with oxygen diffusion at the electrode. Using DRT, Kežionis et al. (2015) found it possible to separate out the bulk response; the bulk ε' tends to a low frequency value ε'_0, see Figure 4.10.

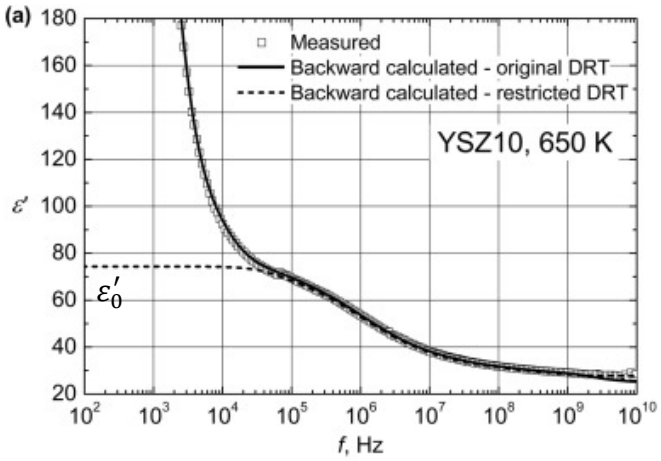

Figure 4.10: ε' spectroscopic plot of a single crystal of 10 mol% YSZ at 377 ^{o}C, showing experimental (measured) values as well as values calculated from DRT results, based on all data (original) and bulk data only (restricted). (Kežionis et al., 2015)

The type of electrodes used affects the immittance data obtained. The ability of oxygen to diffuse through the electrode material affects the electrode response (Schwandt and Weppner, 1997). An ideal electrode diffusion response gives a 45^{o} spike in the Z* plot, that becomes a semicircle at low frequency (see Section 2.3.2), if the oxygen ions are able to diffuse through the whole layer (Irvine et al., 1990, Abram et al., 2001). In contrast, an ideal blocking electrode is purely capacitive and results in a 90^{o} spike in the Z* plot (Bruce and West, 1983). Experimental electrodes often show non-ideal behaviour, with a spike at an angle between these limits.

The method used to apply the electrodes to the sample also affects the electrode response. Possible methods include using a sputter coater or painting on electrodes and then firing them (Abram et al., 2001). Regardless of the method used, even if the same protocol is followed every time, the electrode response is unlikely to be identical due to the effects of the exact electrode geometry.

4.3.1 EQUIVALENT CIRCUITS PROPOSED FOR YSZ IN LITERATURE

For electro-ceramic materials such as YSZ, equivalent circuits (EC) are most commonly fitted in the Z* formalism, using a brickwork-layer-style model, described below. Separate elements represent bulk, grain boundary and electrodes responses, and are combined with each other in series. Within the elements, components are joined in parallel; each element represents a feature in the Z* plot. Alternatively, elements can be combined in parallel and fitted using Y* data (Bauerle, 1969). This enables the representation of a blocking region within the grain boundary rather than the grain boundary itself, but this is of little interest here.

In the original Brickwork Layer Model (BLM) (van Dijk and Burggraaf, 1981), each feature is represented by a parallel *RC* element (Fig. 4.11a), described in Section 2.3.1. *R* is used to quantify long range migration of ions through the lattice and is the limiting low frequency resistance of the sample, and *C* is used to represent the

lattice polarisation. The values of *R* and *C* can be estimated using hand-fitting, *R* from the diameter of the Z* arc, and *C* by two possible methods. *C* can be inferred from *R* and f^{o}, the characteristic frequency of the arc, as:

$$f^{o} = \frac{1}{2\pi RC} \quad [4.4]$$

Alternatively, *C* can be estimated from the peak in M'':

$$C = \frac{1}{2M''_{\max}} \quad [4.5]$$

An ideal *RC* element gives a single relaxation time, τ, the reciprocal of the angular frequency ω_0, which is equal to $2\pi f^{o}$. The peaks in M'' and Z'' occur at the same frequency. However, this is not the case for experimental data; hence, the two hand-fitting methods will yield different values of *C*. The *RC* element cannot give an accurate fit in all formalisms, due to the non-ideal nature of the immittance data. To describe the distributed nature of the relaxation times, Jonscher (1978) introduced the constant phase element (CPE), *Q* (see Section 2.3.2). This is often used instead of a capacitor, creating a parallel *RQ* element (Fig. 4.11b), for example in the work of Perry et al. (2011). Alternatively, a CPE can be used in addition to a capacitor, to create a parallel *RQC* element (Masó and West, 2015, Hernández et al., 2016), see Figure 4.11c. Hernández and West (2016) proposed that their particularly skewed bulk arc (Figure 4.8b) represents two processes: both long range oxygen ion migration through the lattice, and local dipole interactions between yttrium cations and oxygen vacancies. The former is modelled with a parallel *RQC* element and the latter with a series *RC* element, most commonly used to fit polar dielectrics. The series *RC* element is incorporated into the bulk *RQC* element, see Figure 4.11d.

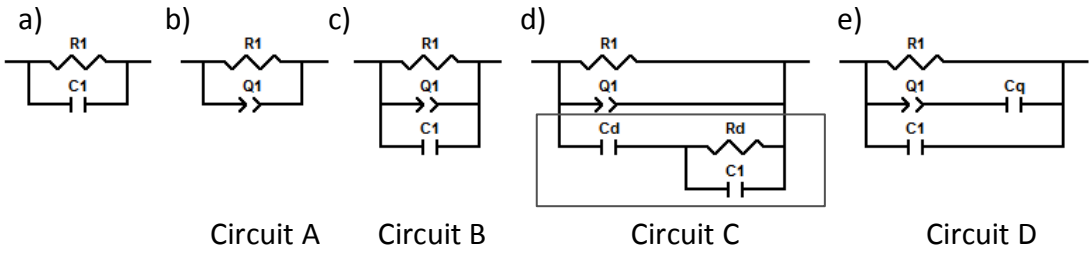

Figure 4.11: Schematics of possible equivalent circuits to describe the impedance response of bulk YSZ

Grain boundaries are also represented either by *RC* elements (Abelard and Baumard, 1995, Hernández and West, 2016) or *RQ* elements (Yang et al., 2010, Guo and Maier, 2001, Guo and Ding, 2004). Electrodes can be represented using a CPE if little or no curvature is seen in the Z* spike (Hernández and West, 2016), or else by an *RQ* element (Guo and Maier, 2001). Any additional charge transfer arc can be represented by an *RQ* element.

4.3.2 IMMITTANCE OF POSSIBLE EQUIVALENT CIRCUITS

The equivalent circuits seen in the literature for YSZ give similar Z* plot data; however, major differences are seen spectroscopically. In this sub-section, the ECs shown in Figure 4.11 are examined in terms of Y' and ε'. This analysis is introduced to illustrate how each EC parameter affects the fitting, and to highlight the differences between the ECs.

A single parallel *RC* circuit (Fig. 4.11a) gives an ideal semicircle in Z*, and Y' and ε' are both independent of frequency. ε' is determined by C_1, and Y' by the reciprocal of R_1. Experimental impedance data however give depressed arcs in Z*, and Y' and ε' vary with frequency, see Section 4.3. Hence, this circuit, with its two variables, does not provide a satisfactory fit.

The *RQ* circuit (Fig. 4.11b) has three parameters; the CPE component alone has two parameters Y_0 and n, described in more detail in Section 2.3.2. The circuit contains both a resistive and a capacitive component; the latter is given by (Hsu and Mansfeld, 2001):

$$C_{RQ} = {Y_0}^{1/n} R^{\frac{1-n}{n}} \qquad [4.6]$$

Schematics of the ε' and Y' spectroscopic responses are shown in Figure 4.12a&b, both for *R* and *Q* separately and for the resulting R_1Q_1 element. As the parallel resistor *R* has no effect on ε', the response of *Q* and *RQ* are identical. They give a constant negative gradient equal to n_1-1 on a log-log plot. ε' is now a function of frequency. *Q* also gives a straight line in Y', this time with a positive gradient of n_1. Combining with *R* in parallel gives a plateau at low frequency, equal to the response from *R*, and tends to the CPE dispersion response at higher frequency.

Responses from YSZ samples seen in the literature do not have a constant gradient of ε' with frequency but instead plateau to a finite value ε'_∞ at high frequency. Adding a parallel capacitor to the bulk element, Figure 4.11c, allows for this phenomenon; at high frequency, the capacitor response dominates, with increasing contribution from the CPE as frequency decreases, illustrated in Figure 4.12c. The capacitor *C* has no effect on Y', hence *RQ* gives the same response as *RQC*, see Figure 4.12d. The *RQC* element has four parameters: *R*, *C*, n and Y_0.

To incorporate local dipole effects, a capacitor in series with an *RC* circuit is added in parallel to an *RQ* element, giving an equivalent circuit with six parameters: R_1, n, Y_0, C_1, C_d and R_d. The ε' response is shown in Figure 4.12e for this arrangement, along with the separate *Q* and $C_dR_dC_1$ responses (the boxed area of Figure 4.11d). For the latter, C_d dominates at low frequency, as the R_d pathway is favoured over C_1. In contrast, at high frequency C_1 is favoured over R_d and ε' tends to that of C_1 and C_d in series, giving a limiting value of:

$$C_{lim} = \frac{C_d C_1}{C_1 + C_d} \quad [4.7]$$

In terms of Y', Figure 4.12f, the total $R_1Q(C_dR_dC_1)$ response is almost identical to the RQ response, only differing at intermediate frequency, where the magnitude of the $R_1(C_dR_dC_1)$ response is comparable to that of RQ. The $R_1(C_dR_dC_1)$ response tends to the inverse of R_1 at low frequency, whereas all components contribute to the high frequency limit.

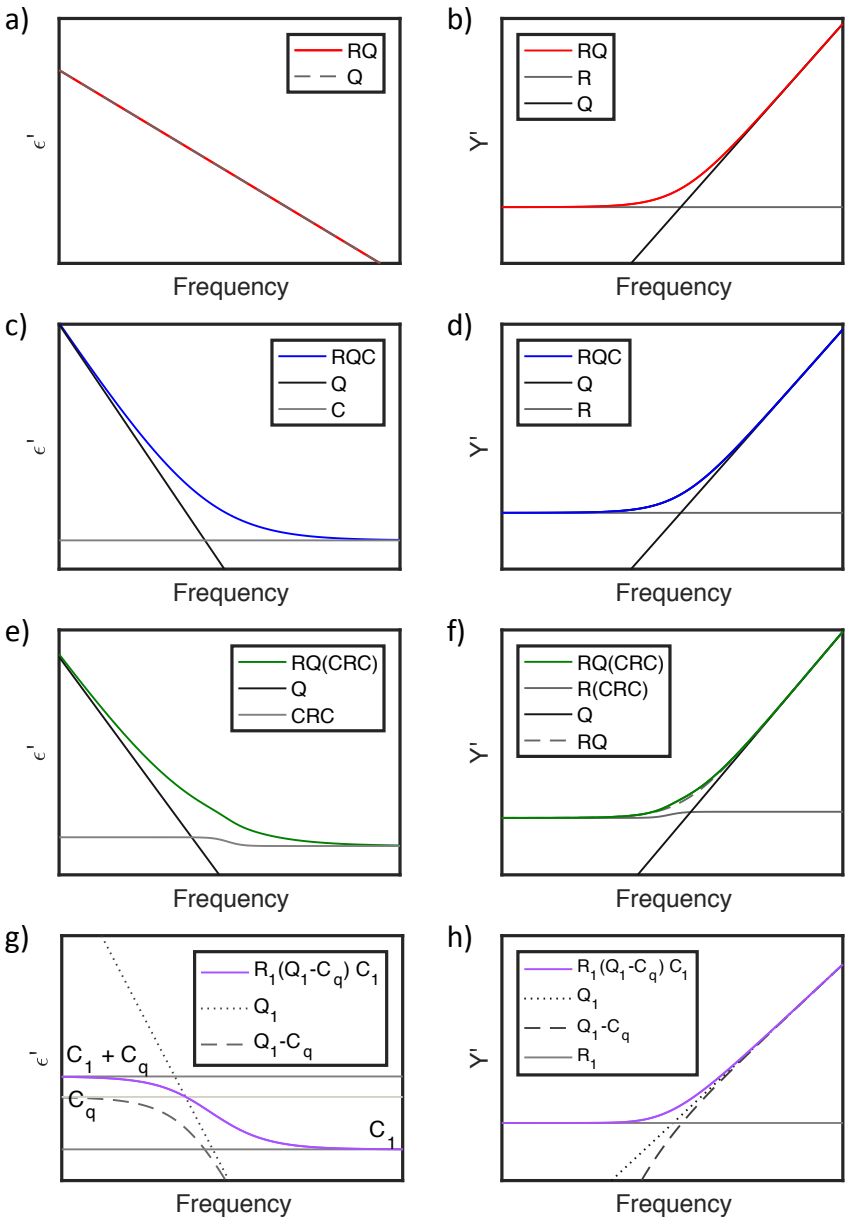

Figure 4.12: Schematics of ε' and Y' spectra showing equivalent circuit responses for the total bulk element and for smaller components: a&b) circuit A, c&d) circuit B, e&f) circuit C and g&h) circuit D, shown on log-log scales.

For each of the EC models listed so far, a plateau in ε' is only seen at high frequency, and not at low frequency, as suggested by Kežionis et al. (2015) for bulk YSZ.

Therefore, a new EC is needed for this feature to be included. In this thesis, the following modification to the *RQC* element is proposed: the addition of an extra capacitor C_q in series with *Q* (Fig. 4.11e), giving a circuit with five variables. C_q acts to limit the *Q* response at low frequency; hence, ε' is now limited at both high and low frequency, see Figure 4.12g. The high frequency limit is given by C_1 and the low frequency limit is the sum of C_1 and C_q. C_q here represents a distribution in characteristic frequencies associated with the bulk element, which we propose originates from local heterogeneity in the bulk due to micro-clusters of oxygen vacancies in the bulk lattice, see Section 4.2.3. The response for *Q* in series with C_q is shown on the same axis (Figure 4.12g); it tends to C_q at low frequency and to the *Q* response at high frequency. In terms of Y', Q-C_q tends to the *Q* response at high frequency and to zero at low frequency, the Y' response of a pure capacitor. This acts to pull down the $R_1(QC_q)C_1$ response compared to the response of R_1Q in the transition region between the low frequency plateau ($1/R_1$) and the *Q* response at high frequency.

When fitting equivalent circuits, there are two methods regarding n. The first is to let n go free; however, at high temperature, insufficient Y' dispersion is seen in the frequency range measured to be able to predict n accurately. Alternatively, the second method is to fix n at a value obtained at low temperature, and assume that n is independent of temperature (Abram et al., 2003). The temperature chosen should be high enough also to show the low frequency Y' plateau, so that R_1 can be extracted with sufficient accuracy.

So far, the bulk component has been treated in isolation to the electrode response. However, unless the characteristic frequency of each feature is separated by several orders of magnitude, the responses will overlap. The bulk material fitting parameters may therefore be affected if the electrode response is included in the frequency range analysed. By comparing bulk parameter results with and without fitting the charge transfer effect, the significance of the effect can be determined.

4.4 YSZ BULK ELECTRICAL MATERIAL PARAMETERS

4.4.1 CALCULATING CONDUCTIVITY, PERMITTIVITY & ACTIVATION ENERGY

The EC parameters, *R* and *C*, for the bulk response can be used to determine the bulk conductivity σ and relative permittivity ε_r of the sample:

$$\sigma = \frac{1}{R}\frac{t}{A} \ (\Omega.\,\mathrm{cm}) \qquad [4.8]$$

$$\varepsilon_r = \frac{C}{\varepsilon_0}\frac{t}{A}(\mathrm{a.\,u.}) \qquad [4.9]$$

Note that ε_r is different from the permittivity formalism ε^* (defined in Equations [2.15-2.17]), which varies with frequency and temperature. ε_0 is the electric permittivity of free space and *t*/*A* is the geometric factor, equal to the thickness, *t* divided by the area, *A* of the sample. This is different from the geometric factor used for fuel cells (Equation 2.18), where thickness is generally not taken into account, as there are multiple layers of different thicknesses.

IS data is typically normalised using the geometric factor to allow easy comparison between samples of different geometry:

$$Z^* = \frac{Z^*_{\mathrm{raw}}}{\mathrm{gf}} \ (\Omega.\,\mathrm{cm}) \qquad [4.10]$$

where

$$\mathrm{gf} = \frac{t}{A} \ (\mathrm{cm}^{-1}) \qquad [4.11]$$

If *R* and *C* are calculated from geometrically-corrected data, then the values already reflect the geometric factor and hence *t*/*A* can be treated as unity in Equations [4.8 & 4.9]. However, if *R* and *C* are calculated directly from raw data, this is not the case.

The Arrhenius law for conductivity is given in Equation [4.3]. Taking logs gives:

$$\log\sigma = \log\sigma_0 - \frac{1}{T}\frac{E_{act}}{k}\log e \qquad [4.12]$$

which represents a straight line for the plot of $\log\sigma$ versus inverse temperature, (typically shown as 1000/T). The activation energy can hence be determined from the gradient of this plot:

$$E_{act}(J) = \frac{1000\,k}{\log_{10} e} \times \mathrm{gradient} \qquad [4.13]$$

and can be converted into units of electron volts (eV) by dividing by the charge of an electron:

$$E_{act}(eV) = \frac{E_{act}(J)}{1.602\times10^{-19}\ (J/eV)} \qquad [4.14]$$

Alternatively, the stricter form of the Arrhenius equation can be used:

$$\sigma = \frac{\sigma_0}{T} \mathrm{e}^{-\frac{E_{act}}{kT}} \qquad [4.15]$$

where the activation energy is instead determined from the gradient of $\log \sigma T$ versus inverse temperature. The difference between the two equations is $\log T$, which by definition does not form a straight line versus inverse temperature. However, it can be approximated as unity in the temperature range of interest; hence both methods yield a straight line. The gradient of $\log \sigma$ is much steeper in this region than that of $\log T$; hence the two methods give very similar answers.

The simplified Arrhenius relationship, Equation [4.3], will be used here, as conductivity values can be read directly from the related figures.

4.4.2 CONDUCTIVITY & ACTIVATION ENERGY VALUES FOUND IN THE LITERATURE

Values of the bulk activation energy reported in the literature for polycrystalline 8 mol% YSZ, for temperatures below the critical value, T_c (around 600 ^{o}C), are shown in Table 4.1. Above T_c, the Arrhenius plot is no longer linear and activation energies become smaller (Abelard and Baumard, 1982, Guo and Maier, 2001, Ciacchi et al., 1994). Grain boundary activation energy values will be presented later in Table 5.1 and will be discussed in Section 5.1.2. Bulk values are generally agreed to range between ~ 1.00 and 1.11 eV for polycrystalline YSZ, and are insensitive to the starting powder used (Ciacchi et al., 1994) and to the sintering conditions (Steil et al., 1997). Hernández and West (2016) found the activation energy for R_d (see Figure 4.11d) to be between 1.00 and 1.17 eV for their samples, which is in the same region as both bulk and grain boundary values.

An estimate of the conductivity for each sample at 300 ^{o}C is also listed in Table 4.1, approximated from Arrhenius plots given in literature. Values range between 5×10^{-7} and 1×10^{-5} S/cm. A higher sintering temperature results in increased conductivity (Steil et al., 1997). Conductivity also varies with the starting powder used (Ciacchi et al., 1994), due to impurities and different surface areas and starting particle size.

The bulk material is expected to have the same properties as a single crystal of the same composition. Activation energies for YSZ single crystals are shown in Table 4.2 for a range of yttria concentrations, all with a cubic fluorite structure. As the yttria content increases, E_{act} also increases, in line with the discussion in Section 4.2.2. The values of E_{act} for 8 mol% bulk ceramics fit into this trend, within the degree of accuracy possible.

Table 4.1: Activation energy and conductivity at 300 °C for polycrystalline 8 mol% YSZ, from literature. (The conductvity was extracted from Arrhenius plots to give a common temperature for comparision).

Reference	$E_{act,\text{bulk}}$ **(eV)**	σ_{bulk} **(S/cm) at 300 °C**	**Sintering T, duration, heating/cooling rate**
Abelard and Baumard (1995)	1.03 ±0.05	4×10^{-6}	1500 °C, 4h
Ciacchi et al. (1994)	1.10 ±0.05	2×10^{-6} – 5×10^{-6}	1500 °C, 4h, 5 °C/min (five different starting powders)
Guo et al. (2002)	1.05	9×10^{-6}	1650 °C, 6h
Hernández and West (2016)	1.00 – 1.08	5×10^{-7} – 1×10^{-5}	1350 – 1600°C, 2h, 5 °C/min
Perry et al. (2011)	1.09 ±0.07	(not given)	1300 °C, 100h (av. grain size 1.0±0.6 μm, 97% density)
Steil et al. (1997)	1.03 1.03	1×10^{-6} 6×10^{-6}	1100 °C, 2h, 2 °C/min 1500 °C, 2h, 2 °C/min
Zhang et al. (2009)	1.11	4×10^{-6}	1400 °C, 5h

Table 4.2: Activation energy associated with bulk conductivity of YSZ single crystals with varying yttria content. (Error bounds given where known).

Reference	**yttria content (mol%)**	E_{act} **(eV)** ($T<T_c$)
Badwal (1984)	8.7	1.05±0.03
Abelard and Baumard (1982)	9	1.10
Kazlauskas et al. (2013)	10	1.23
Abelard and Baumard (1982)	12	1.33

4.4.3 Relative permittivity from the Clausius-Mossotti equation

The Clausius-Mossotti equation can be used to estimate the relative permittivity ε_r of materials (Shannon, 1993). This relates the dielectric polarisability α_D (a measure of the intrinsic atomic and ionic polarisation of a material) to the molar volume V_m (in Å^3) and to the relative permittivity ε_r, which is generally estimated by ε' measured in a frequency range of 10^3-10^7 Hz at room temperature:

$$\alpha_D = \frac{3}{4\pi}\left(\frac{V_m(\varepsilon_r - 1)}{\varepsilon_r + 2}\right) \qquad [4.16]$$

α_D contains both atomic and ionic components but does not reflect any dipole or space charge polarisability.

Shannon (1993) derived a set of ion dielectric polarisabilities which can be used to predict the total polarisability α_D^T of well-behaved oxides and fluorites, by assuming α_D^T is the combination of the ion polarisabilities, scaled by the number of moles of ion per mole of the compound. In the case of 8 mol% YSZ:

$$\alpha_{\mathrm{D}}^{\mathrm{T}}(\mathrm{Zr}_{0.852}\mathrm{Y}_{0.148}\mathrm{O}_{1.926}) = 0.852\alpha_{\mathrm{D}}(\mathrm{Zr}^{4+}) + 0.148\alpha_{\mathrm{D}}(\mathrm{Y}^{3+}) + 1.926\alpha_{\mathrm{D}}(\mathrm{O}^{2-}) \quad [4.17]$$

This gives a value of 7.20 Å^3 for $\alpha_{\mathrm{D}}^{\mathrm{T}}$, using the values in Table 4.3.

8 mol% YSZ is cubic, and hence its molar volume is given by:

$$V_m = \frac{a^3}{4} \quad [4.18]$$

where a is the lattice parameter, see Section 4.2.1, equal to 5.14 Å (Itoh et al., 2015).

By re-arranging the Clausius-Mossotti equation, it is possible to estimate ε_r:

$$\varepsilon_r = \frac{3V_m + 8\pi\alpha_D^T}{3V_m - 4\pi\alpha_D^T} \quad [4.19]$$

For materials with negligible dipole or space charge contributions, this gives a reasonable estimate. For 8 mol% YSZ, this results in a relative permittivity of 25. A lower value of 21 is obtained for monoclinic zirconia, due to the higher molar volume. Conversely, the molar volume of tetragonal YSZ is smaller than both cubic YSZ and monoclinic ZrO_2; hence, the predicted ε_r is largest for this polytype. ε_r is principally determined from the crystallographic form, rather than the dopant amount (Thompson et al., 1992).

Table 4.3: Ion polarisability values (taken from Shannon (1993) Table III, Column 2, recommended for most oxides).

	$\alpha_{\mathrm{D}}(\mathrm{Zr}^{4+})$	$\alpha_{\mathrm{D}}(\mathrm{Y}^{3+})$	$\alpha_{\mathrm{D}}(\mathrm{O}^{2-})$
Ion polarisability (Å^3)	3.25	3.81	2.01

4.4.4 Relative permittivity values found in the literature

Values of the bulk relative permittivity ε_r for 8 mol% YSZ samples have been compiled from literature, see Table 4.4 and Figure 4.13. There is agreement that room temperature (rt) values are around ~ 30-40 for dense samples, and are taken using a range of measuring techniques including radio frequencies, microwave measurements, and permittivity measured at high frequency, ε'_∞. The latter method is only appropriate if the high frequency ε' plateau is visible at the temperature and frequencies investigated; as temperature increases, the plateau shifts to higher frequencies. The methods used at higher temperatures are discussed below, along with their results.

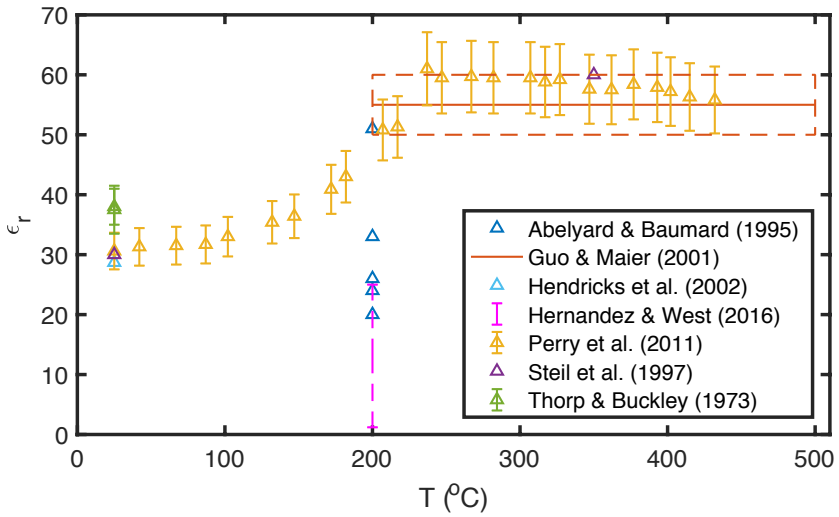

Figure 4.13: Values from the literature of the relative permittivity ε_r of 8 mol% YSZ as a function of temperature. *n.b*. The dashed orange box represents the error bars for Guo & Maier (2002).

Table 4.4: Values from the literature for the relative permittivity ε_r of 8mol % YSZ.

	Sample density (%)	**ε_r (a.u.)**	**T (°C)**	**Method**
Abelard and Baumard (1995)	(not quoted)	20, 24, 26 (33, 51, 306)	200°C	ε' at 16,000 Hz, Round-robin experiment (results considered inaccurate in brackets)
Guo and Maier (2001)	"highly dense"	55 ± 5	200 - 500 °C	hand-fitting from M"
Hendriks et al. (2002)	99	28.7	25°C	ε' at high frequency
Hernández and West (2016)	85-92%	1.2 - 25	200 °C	Circuit C (see Figure 4.11d)
Perry et al. (2011)	97*	30.6 30.6 – 60 (see Fig 4.13)	rt rt – 300 °C	RQ circuit (0.8 < n < 1)
Steil et al. (1997)	98	~30	rt	ε' at high frequency
		~60	350 °C	Bulk response – hand-fitting
Thorp and Buckley (1973)	100 (sc)	38.0 ± 3	rt	radio frequency measurements at 150 kHz and 40 MHz
	100 (sc)	37.5 ± 4	rt	microwave measurements

*NB. ε_r corrected for porosity

The high frequency ε'_∞ plateau method was used at 200 °C by Abelard and Baumard (1995) as part of their round-robin experiment. Six samples that originated from the same batch were measured in different laboratories. There was a large variation in values of ε_r measured for the different samples/laboratories. Aside from the value of 306, which was thought to be measured using inaccurate equipment, the

variation was attributed to stray capacitances in the setup. Some of the ε' spectra decrease steeply at high frequency beyond the range at which ε_r was determined, indicating the presence of parasitic jig effects. The values Abelard and Baumard regard as most accurate (those between 20-26) are lower than the room temperature values in Table 4.4. Permittivity is affected by sample porosity, and decreases with increasing porosity, see Section 5.3.3. Hence, the small magnitude of the Abelard and Baumard (1995) values could be due to a less dense sample.

In contrast to the Abelard and Baumard (1995) ε_r values, for temperatures between 200 and 500 ^{o}C, Guo and Maier (2001), Perry et al. (2011) and Steil et al. (1997) all quote values of around 55-60. Perry et al. (2011) also show a transition between the room temperature values (~30) and these high temperature values, which they suggest is due to the high temperature activation of dipoles (see Section 4.2.4). However, these high temperature readings are all based on either an *RC* equivalent circuit, such as the hand-fitting results of Steil et al. (1997) and Guo and Maier (2001), or an *RQ* element to describe the bulk material (Perry et al., 2011). As shown in Section 4.3.2, neither an *RC* or an *RQ* element is sufficient to fit experimental ε' spectra. Therefore, there is a large uncertainty associated with these high temperature results, which is likely to be far greater than the $\pm$10% estimated by Perry et al. (2011).

Calculating ε_r from the results of Hernández and West (2016), using the circuit shown in Figure 4.11e gave a bulk permittivity ranging between 1.2 and 25, measured around 200 ^{o}C. The variation stems from C_1 in particular; substantially different values of C_1 are quoted even for samples sintered at the same temperature with different electrodes. This calls into question the precision of the impedance measurements, the equivalent circuit fitting or the integrity of the sample preparation.

4.5 AIMS AND OBJECTIVES

In light of the literature reviewed, the aims of the remainder of this chapter are:

- to determine a means for relevant equivalent circuit (EC) fitting of immittance data from YSZ single crystals, to obtain the following bulk parameters and their temperature dependence:
    - ionic conductivity, σ
    - activation energy, E_{act}
    - relative permittivity, ε_r
- to determine whether or not the presence of dipoles in YSZ can be confirmed from immittance data and subsequent EC fitting.

To achieve these aims, four different equivalent circuits are compared to see which gives: i) the best fit in all formalisms, and ii) the most physical trends for the bulk parameters as a function of temperature. The ECs compared are:

- Circuit A - a parallel *RQ* element (Figure 4.11b), where *R* represents long range migration of ions through the lattice and *Q* is used as a non-ideal capacitance, representing lattice polarisation, to account for the depression in Z* plot arcs.
- Circuit B - a parallel *RQC* element (Figure 4.11c), where an additional capacitor is added to represent the high-frequency-limiting permittivity.
- Circuit C - the circuit used by Hernández and West (2016) that incorporates short range dipole interactions and long range conduction into a single circuit (Figure 4.11d). The additional series R_d-C_d element is used to represent local dipole interactions; R_d is the difficulty of reorientation in the field and *C* represents the dipolar contribution to the permittivity.
- Circuit D - a circuit that gives both high and low frequency limiting permittivity (Figure 4.11e). A capacitor C_q is added in series to the constant phase element of circuit B, and represents the additional permittivity present at low frequency.

Each circuit is fitted using n when it is free (f), and n when it is fixed (x). Additionally, the charge transfer arc is added as an RQ element in series with the bulk (*b+ct*), to determine the extent of the effect on the bulk parameter results. Finally, analysis of the temperature dependence of ε_r and the remaining capacitance parameters for each circuit enables a discussion on the likelihood of the presence of dipoles in YSZ.

4.6 EXPERIMENTAL METHODS

Experiments were carried out using a <100> oriented single crystal of 8 mol% YSZ (Pi-Kem), polished on both sides, as purchased. Electrodes were painted on both sides using gold paste and were fired at 850 ^{o}C for two hours. Platinum paste was also tested (fired at 900 ^{o}C for two hours) and the bulk resistance was found to be consistent for both electrodes. Impedance measurements were carried out in an in-house-built compression jig, comprising two alumina tubes with platinum wire connections, which the sample was sandwiched between, contained within an outer alumina tube, located in a tube furnace. Of the inner alumina tubes, one is fixed in place and the other is held by a spring clamp system (hence the name *compression jig*) to allow for samples with varying thickness. The experimental setup is illustrated in Figure 4.14. Measurements were taken in the temperature range 150 – 325 ^{o}C. IS data was obtained using a frequency response analyser (Modulab XM, Solartron), over a frequency range of 10^6 – 0.1 Hz, with an a.c. voltage amplitude of 100 mV. Results obtained using smaller voltage amplitudes gave the same immittance results; hence the linearity condition is satisfied (see Section 2.4.4).

Data obtained were corrected for sample geometry (see Equations [4.10, 4.11]). Data were also corrected for the parasitic jig series resistance and inductance, and parallel capacitance (see Section 4.7.3). The spectra were analysed and fitted in ZView software (Johnson, 2014).

ε' and $\tan\delta$ were measured as a function of temperature at a selection of frequencies using a compression jig, in a tube furnace, connected to an LCR meter (Hewlett Packard, 4284A). Measurements were recorded at the following frequencies: 10^3, 10^4, 10^5, 2.5×10^5, and 10^6 Hz. The furnace temperature was ramped at a rate of 1^{o}C/min from room temperature to 450 ^{o}C and back, which corresponds to a maximum sample temperature of around 400 ^{o}C, and the results were plotted as ε' against temperature for each frequency, where ε' was obtained from:

$$\varepsilon' = \frac{C't}{\varepsilon_0 A} \qquad [4.20]$$

C' is the real part of the capacitance, ε_0 is the vacuum permittivity (*i.e.* the permittivity of free space), t is the sample thickness and A is the sample area. In addition, $\tan\delta$ (the ratio of ε''/ ε') at the various frequencies was obtained as a function of temperature.

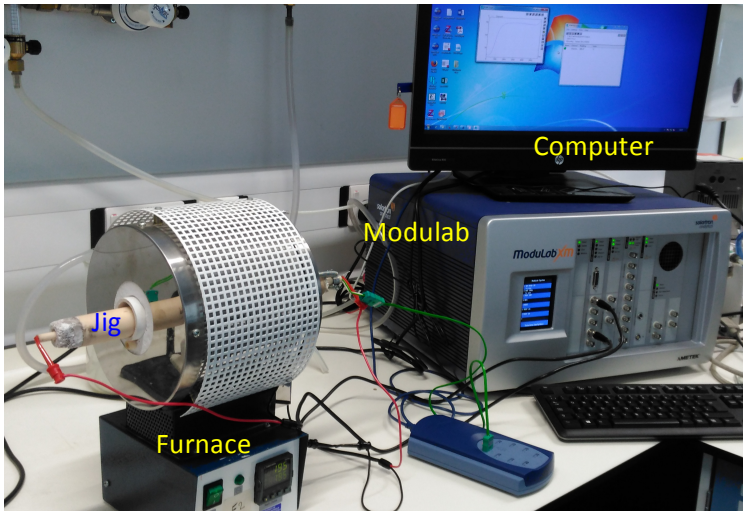

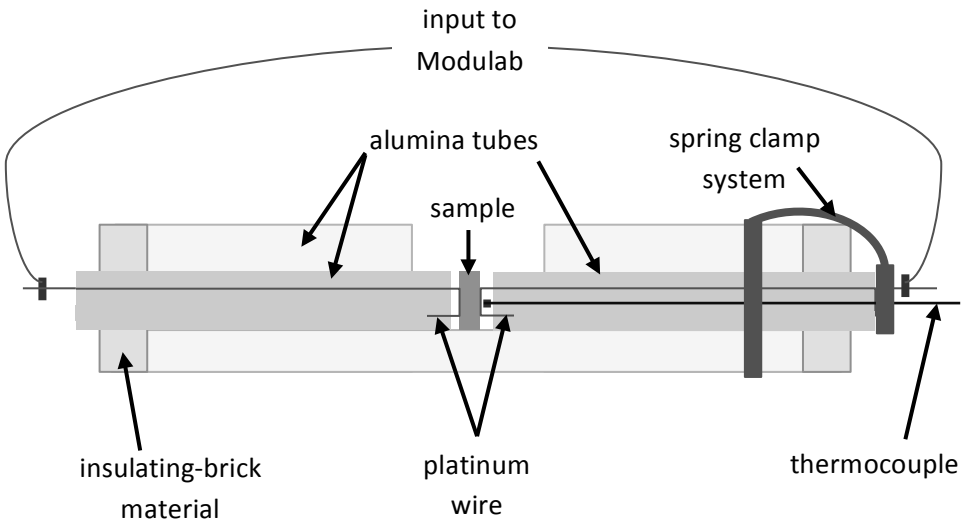

Figure 4.14: Photo and schematic of the experimental setup of the ceramic compression jig.

4.7 RESULTS

4.7.1 XRD

The surface and bulk of the single crystal sample were compared using X-ray diffraction (XRD)[**], to assess any changes to the composition or structure of the sample at the surface. The surface was characterised using glancing-angle XRD (GA-XRD), with the input radiation at angles of 0.5° and 1.5° to the sample, using reflection geometry. This gave two different surface penetration depths. The bulk material was assessed using conventional XRD (reflection geometry). The resulting diffractograms are shown in Figure 4.15, normalised with respect to the height of the most intense peak. The three data sets match well; all have the same number of peaks occurring at the same values of 2θ. The peaks are slightly broader for the GA-XRD data. The broad noise at low 2θ values is also larger, particularly for the 0.5° data, due to smaller absolute intensities detected, causing higher amplification of noise. The matching diffractograms indicate that the average structure is the same at the surface as it is in the bulk lattice, assuming there is no amorphous material present, which would not be readily detected by XRD.

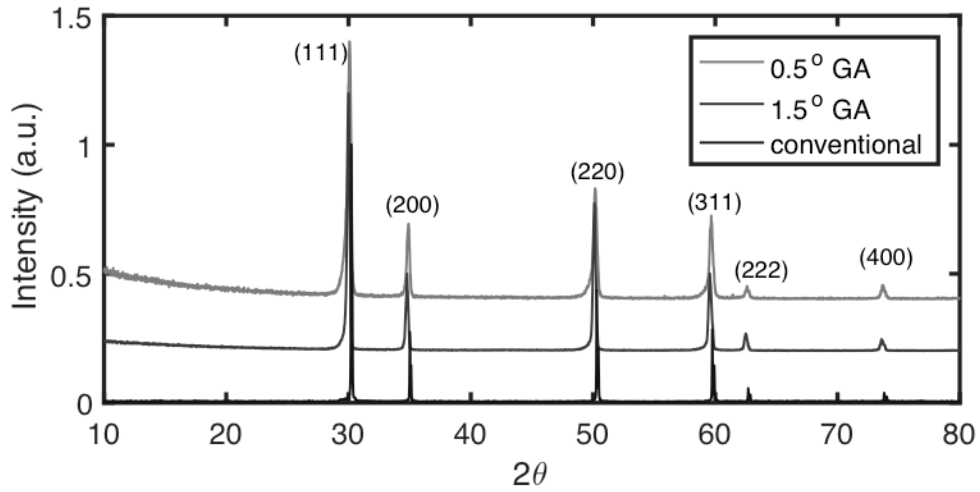

Figure 4.15: Diffractograms for glancing-angle and conventional XRD for a single crystal of 8 mol% YSZ.

The peaks were indexed, see Figure 4.15, and followed a simple Fluorite structure. All of the peaks matched those seen in the Inorganic Crystal Structure Database (ISCD) for 8 mol% YSZ (Itoh et al., 2015). The lattice parameter a, was calculated from the following equation:

$$a^2 = \frac{\lambda^2}{4} \frac{h^2 + k^2 + l^2}{(\sin\theta)^2} \qquad [4.21]$$

[**] XRD data courtesy of Richard Veazey

where λ is the wavelength of the X-rays (1.5406 Å), (*h*,*k*,*l*) are the Miller indices and 2θ is the scattering angle. The units of a and λ are angstrom, Å. The lattice parameter was found to be 5.14 ±0.01 Å, in agreement with the ICSD standard value for 8 mol% (Itoh et al., 2015).

4.7.2 ε' AND TAN δ AS A FUNCTION OF TEMPERATURE

Results from the LCR meter are shown in Figure 4.16 for both the single crystal with gold electrodes (solid line) and with platinum electrodes (dashed line). (a) and (b) show the permittivity and $\tan\delta$, respectively, for the whole temperature range measured and (c) is a close-up of the lower permittivity region on a linear scale. At and above a frequency of 10^5 Hz, both ε' and $\tan\delta$ appear identical for the two samples in the temperature range measured, whereas for 10^3 and 10^4 Hz, their responses differ above 270 and 340 °C, respectively, hence corresponding to an electrode effect.

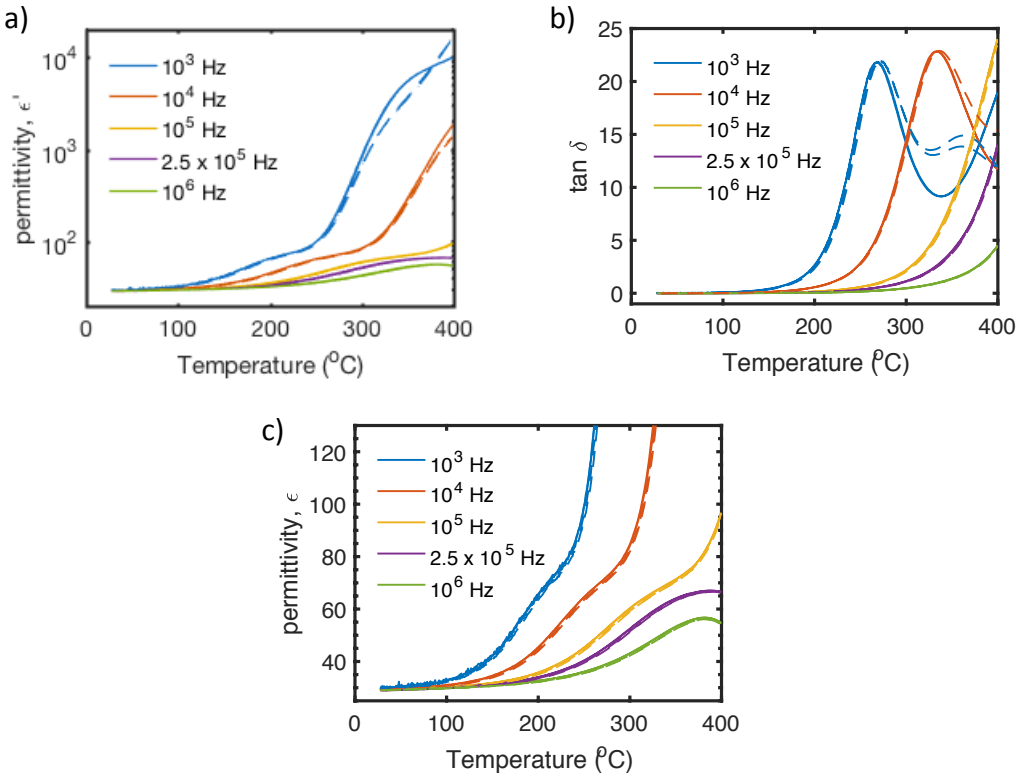

Figure 4.16: LCR results showing a) permittivity and b) $\tan\delta$ results as a function of temperature, at five frequencies, for an 8 mol% YSZ single crystal with gold electrodes (solid lines) and platinum electrodes (dashed lines). c) is a close-up of (a) on a linear scale.

In the results for ε', there is a flat region, at temperatures below ~100 °C, with values equal to around 30, which represents the high frequency-limiting permittivity ε'_∞. A curve is seen at intermediate temperatures, with a point of inflection that occurs at increasing temperature with an increase in frequency. The curve flattens out at high temperature, visible particularly in the higher frequency data, before increasing rapidly for 10^3 and 10^4 Hz, in the temperature range considered.

The values of $\tan\delta$ are very low at low temperature, rising as temperature increases. In the temperature range measured, the results at 10^3 and 10^4 Hz have a peak at 270 and 340 ^{o}C, respectively, seen for both samples. At temperatures above this peak, the two samples deviate; at 10^3 Hz, the platinum electrode sample gives a second smaller peak in the temperature range seen, whereas for the gold electrode sample this shifts to temperatures above 400 ^{o}C.

In the remainder of this chapter, only the results for the gold electrode sample are discussed, as the bulk responses for both sets of results look identical and the effects of the gold electrode have a slightly higher temperature onset than those of the platinum electrode.

4.7.3 JIG CORRECTION

The impedance response of bulk YSZ, measured at 150 – 325 ^{o}C, is more resistive and less capacitive than the SOC data of Chapter 2, measured at 850 ^{o}C. This is due to both the difference in the geometry of the sample – the single crystal is thicker than the fuel cell – and the difference in temperature. Fuel cells are operated at high temperature, to minimise the total resistance, whereas YSZ is characterised at lower temperature, where the bulk features are visible in the frequency range measured. Due to the increased resistance and decreased capacitance, jig effects for parallel resistance R_p and capacitance C_p should be accounted for, in addition to the series resistance and inductance, R_s and L_s, respectively. Although no inductance tail is seen in the results for the YSZ samples, there is still an inductive contribution from the jig present, affecting high frequency data in particular.

Short-circuit and open-circuit measurements were taken both before and after the IS measurement of each sample. Open-circuit measurements were obtained by unclamping the spring on the compression jig (see Figure 4.14). The easy access to the sample in this setup meant these measurements could be undertaken without complete disassembly of the jig, as was necessary for the Probostat (Section 3.3.1), which could account for the significant decrease in variability between spectra directly before and after sample measurements compared with the Probostat trials.

Example short-circuit data taken before and after the IS measurement of the YSZ single crystal with gold electrodes are given in Figure 4.17, representative of multiple data sets measured; (a) gives the Z* plot, and (b) and (c) are the Z' and L_s spectra, respectively, where L_s is calculated using equation [3.1]. The two measurements of inductance spectrum are consistent with each other, giving an average value of 1.62×10^{-6} H, in this instance, over a frequency range of 2×10^5 – 10^6 Hz. Z' varies marginally between trials at 0.49 and 0.53 Ω at low frequency (0.1 - 10^3 Hz), with an average value of 0.51 Ω. This is 0.02% of the YSZ bulk arc, at the highest temperature measured, and hence has a negligible effect on the sample results.

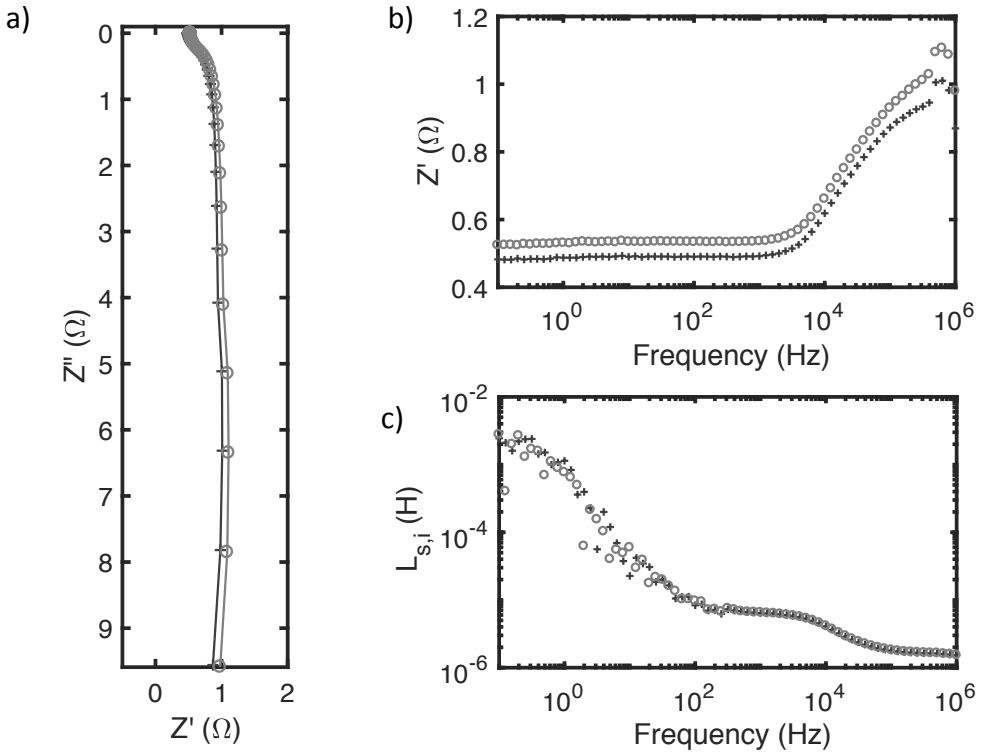

Figure 4.17: Short-circuit data obtained before (dark grey '+') and after (light grey 'o') measurements on the YSZ single crystal with gold electrodes. a) Z* plot, b) Z' spectrum, c) inductance spectrum.

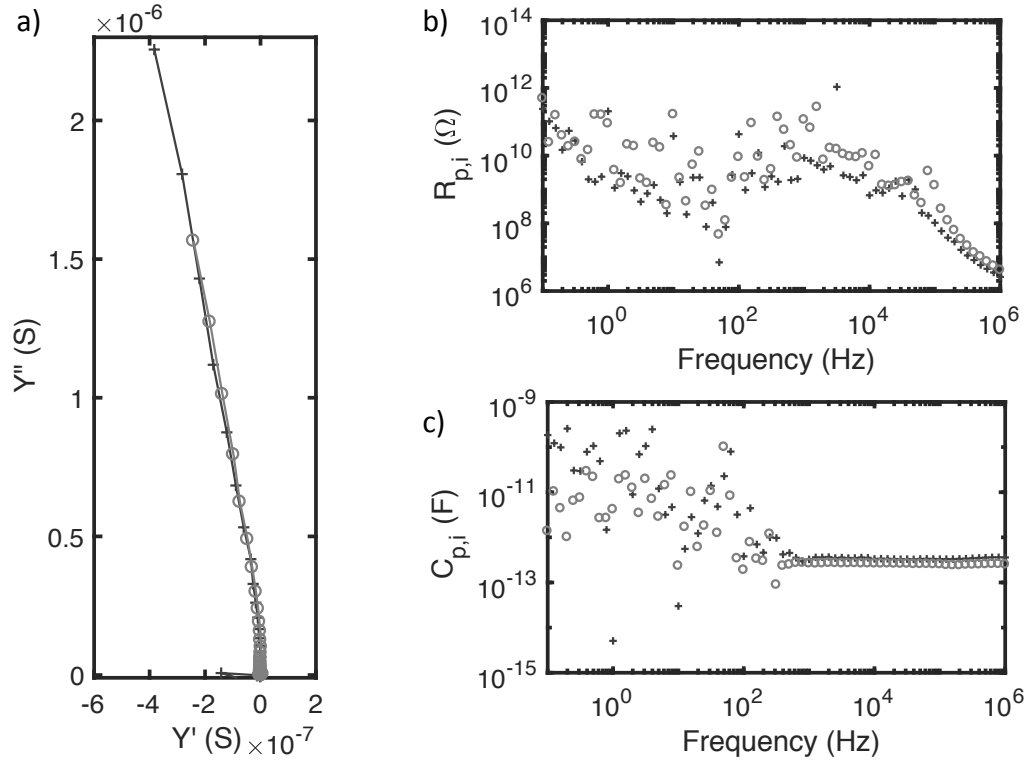

Figure 4.18: Open-circuit data obtained before (dark grey '+') and after (light grey 'o') measurements on the YSZ single crystal with gold electrodes. a) Y* plot, b) parallel resistance spectrum (see equation [4.22]), and c) parallel capacitance spectrum (see equation [4.23]).

The open-circuit Y* plot is shown in Figure 4.18, along with the resulting parallel resistance and capacitance spectra, $R_p(f)$ and $C_p(f)$, respectively, given by:

$$R_p(f) = 1/\mathrm{Y}'_{\mathrm{jig}}(f) \quad [4.22]$$

$$C_p(f) = \mathrm{Y}''_{\mathrm{jig}}(f)/2\pi f \quad [4.23]$$

The average capacitance value has been calculated across the frequency range 10^4 – 10^6 Hz, and gives a value of 3.0×10^{-13} F for the combination of the two trials. The precision of $R_p(f)$ is insufficient to define a correction value; however, the magnitude is sufficiently large for it to have a negligible effect on the sample. Sample results are therefore only corrected for R_s, L_s and C_p, using the average values in the frequency ranges quoted above.

4.7.4 KRAMERS-KRONIG TRANSFORMATIONS

Kramers-Kronig (KK) transformations have been used to check the quality of the IS data calculated. In order to meet the finite data criterion needed for KK, the effects of unbounded data were considered first; unbounded data results in large residuals that are erroneous if the data is bounded when presented in an alternative formalism. In Z*, the low frequency diffusion spike is unbounded. In Y*, these data are bounded but the high frequency bulk data are not. The low frequency spike is of least interest for the analysis of bulk YSZ; hence, KK transforms were computed using Z*, with the diffusion spike omitted.

The number of elements used in the KK fitting procedure was determined by setting μ to 0.95 (refer to Section 3.4.1). This is higher than the value of 0.5 used for SOCs, due to the higher quality of data obtained for YSZ; if 0.5 were used, *M* (the number of *RC* elements used) would equal or exceed the number of experimental data points, *N*. Any residuals that appeared sizeably different from those at adjacent frequencies were treated as anomalous points and the data point at the corresponding frequency was removed from the experimental spectrum. KK transforms were then recalculated for the modified data, to check that the anomaly had been removed.

Example KK residual spectra are shown in Figure 4.19 for the YSZ single crystal at 150, 175 and 200 ^{o}C. At 150 ^{o}C, the lowest temperature for which measurements were obtained, the residuals are noisy below 10^3 Hz. The values of Z' in this region are around 10^7 Ω (non-geometry corrected, not shown) and are at the limit of the accuracy of the set-up. (The equipment itself is accurate between 0.1-10^8 Ω (Solartron analytical, 2015) but the sample/electrode interface is a further source of noise). As the impedance of YSZ decreases with increasing temperature, the Z* data and corresponding residuals at 175 ^{o}C and above contain reduced noise. For 200 ^{o}C and above the residuals are all less than $\pm$0.5%, as desired.

In the remainder of this chapter, the impedance data at all temperatures measured are analysed, but the reduced accuracy of the lowest temperature data set is kept in mind.

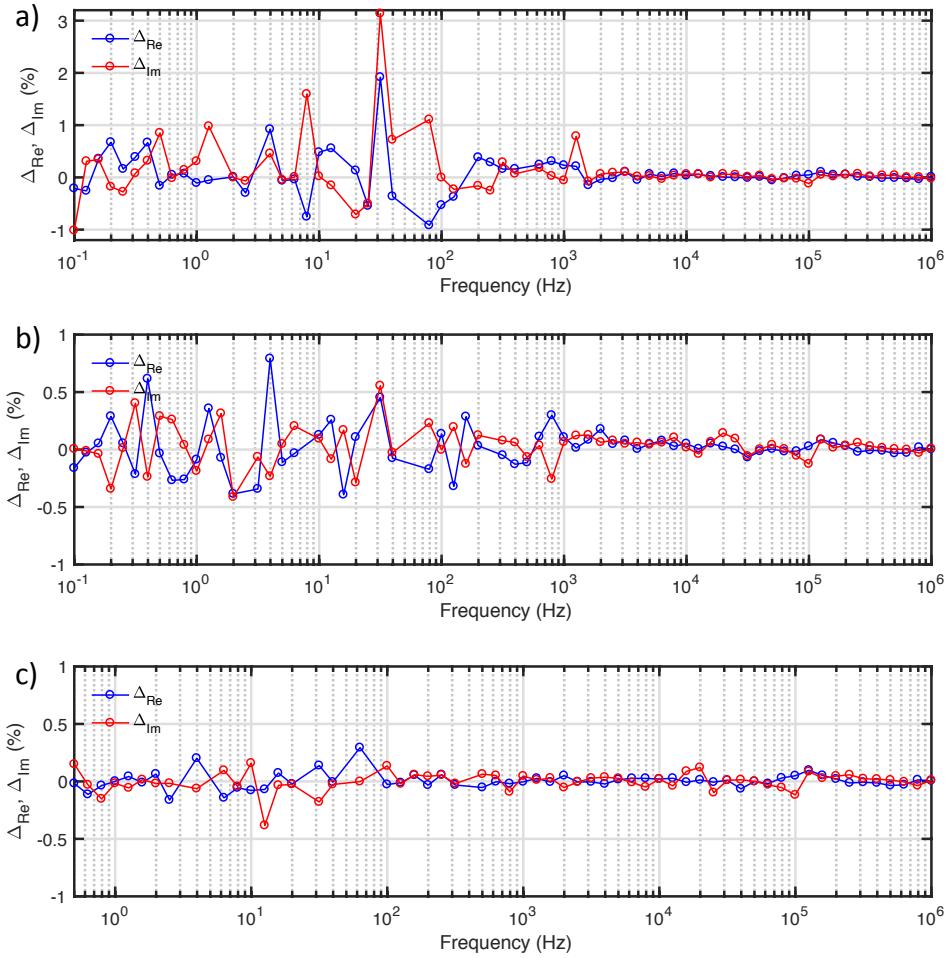

Figure 4.19: Spectroscopic plot of Kramers-Kronig residuals of Z* for YSZ single crystal (coated using gold paste) at: a) 150 ^{o}C, b) 175 ^{o}C and c) 200 ^{o}C.

4.7.5 IMMITTANCE DATA

Impedance complex plane plots (Z* plots) are shown in Figure 4.20a-c for 150, 225 and 325 ^{o}C; 150 and 325 ^{o}C are the lowest and highest temperatures where reliable impedance data associated with the bulk response can be obtained. At 150 ^{o}C, the bulk arc is clearly visible, with a resistance of 2.3×10^{8} Ω.cm. There is also a partial arc at lower frequency. At 225 ^{o}C, in addition to the bulk arc with a resistance of 3.3×10^{6} Ω.cm, there is a mid frequency arc, which can be attributed to charge transfer at the electrode, and a low frequency spike associated with diffusion at the electrode. At 325 ^{o}C, the bulk arc is only partly visible, with a resistance of 6.2×10^{4} Ω.cm. Data below 5 Hz are omitted on the plot for 325 ^{o}C, for the sake of visibility. The angle of the spike is 70^{o}, which indicates the partially blocking nature of the electrode. (For the platinum electrode, the spike has an angle of 60^{o}; hence, gold is more blocking than platinum. The bulk response, however, is independent of

the electrode material and both samples gave matching results). The Z'' spectra are shown in Figure 4.20d. For the three temperatures 150, 225 and 325 °C, the peak maximum f_Z^o occurs at 126, 10^4 and 5×10^5 Hz, respectively. There is also a peak at lower frequency, associated with the charge transfer effect, and the spike associated with low frequency diffusion.

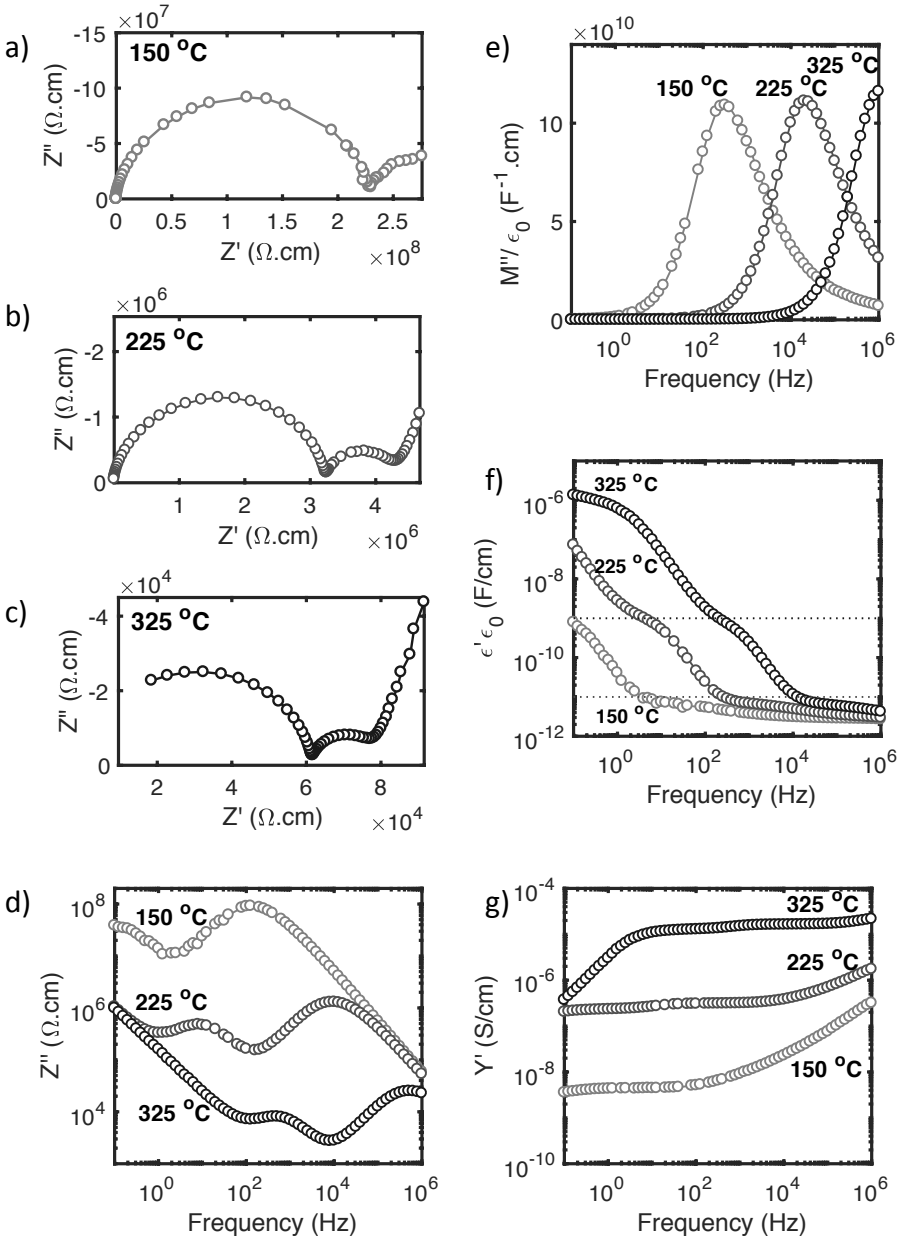

Figure 4.20: IS results for YSZ single crystal (Au electrodes). a-c) Z* plots for 150, 225 and 325 °C, respectively. d-f) Spectroscopic plots at 150, 225 and 325 °C for: d) Z'', e) M'', f) ε' and g) Y'.

The M'' response, see Figure 4.20e, is a non-symmetric Debye-type peak. The peak maximum, f_M^o occurs at 320 Hz.

In the permittivity response, Figure 4.20f, there are three main regions: data above 10^{-9} F/cm represent the electrode diffusion response, data between 10^{-9} – 10^{-11} F/cm represent the charge transfer response, and data of the order of 10^{-12} F/cm

correspond to the bulk response. The bulk response consists of two regions; there is a steeper gradient, visible at all temperatures recorded, and a plateau at high frequency, visible at low temperatures only, due to the frequency range employed.

In terms of Y', Figure 4.20g, there are two main regions at 150^{o}C: a low frequency plateau and high frequency dispersion, associated with non-ideality. There is less dispersion seen at 225 ^{o}C, and by 325 ^{o}C, the dispersion has shifted beyond the frequency range measured. At this temperature, the electrode diffusion response is visible at low frequency. The charge transfer response is less pronounced than in ε' and Z'', but is visible as a slight change in the magnitude of Y'.

Values of conductivity (resistance) and permittivity (capacitance) have been estimated by hand-fitting of Z* data. Both methods that are outlined in Section 4.3.1 were used to estimate *C*; namely, inferring from *R* and the frequency maximum of the arc in the Z* plot, and directly estimating from the peak in M'' spectroscopic plots. The resulting conductivity was found to follow Arrhenius behaviour, see Figure 4.21a. Figure 4.21b shows the capacitance[††] calculated from Z* (Equation [4.4]) and M'' (Equation [4.5]). There is a marginal decrease in the hand-fitted values of capacitance with increasing temperature. The two methods give different values, as the characteristic frequency for M'', f_M^o, is higher than that of Z'', f_Z^o, a feature of non-ideality. The more direct M'' method gives more precise values. Both sets of values are higher than the capacitance corresponding to the low-temperature high-frequency-limiting permittivity ε'_∞ from the LCR results, shown in Figure 4.21b as a solid line.

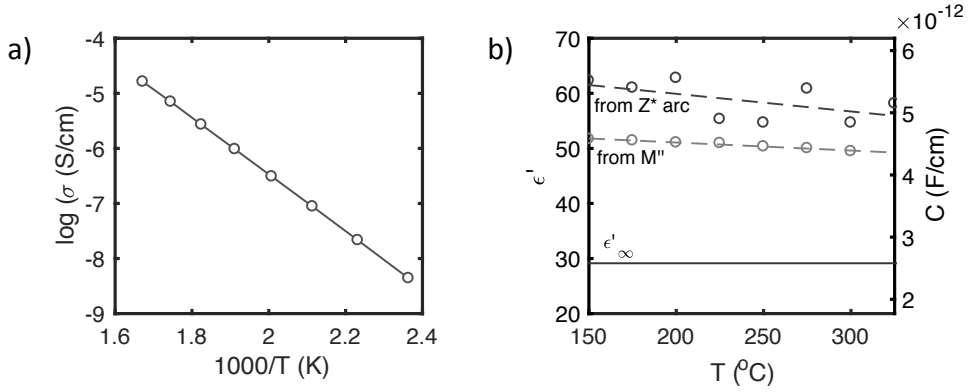

Figure 4.21: Hand-fitting results for YSZ single crystal (Au electrode). a) Conductivity Arrhenius plot. b) Capacitance values estimated from M'' (see Equation [4.4]), Z* (Equation [4.5]), and the high-frequency-limiting capacitance from LCR results.

[††] The figure is presented with dual C and ε' axes, for ease of comparison. The two are related according to equation [4.9]. In the following sections, capacitance values are quoted in terms of permittivity.

4.8 EQUIVALENT CIRCUIT FITTING

In this section, firstly, fittings for the bulk part of each circuit are presented for the case in which n is free: $A_{b,f}$, $B_{b,f}$, $C_{b,f}$ and $D_{b,f}$ (refer to Figure 4.11 and Section 4.5), and compared with experimental IS data. Results are shown at 200 and 275 ^{o}C, chosen to illustrate the fittings at low and high temperatures, respectively. Spectra recorded below 200 ^{o}C contain more noise and above 275 ^{o}C a significant part of the bulk arc is lost. Fittings are shown for the Z* plot and also for Y' and ε' spectroscopic plots, where the effect of n is more pronounced.

Secondly, n is fixed and the fittings $A_{b,x}$, $B_{b,x}$, $C_{b,x}$ and $D_{b,x}$ are examined, again using Y' and ε'. The trends in conductivity and permittivity for n both free and fixed are presented.

Finally, the charge transfer component is added, with the values of n fixed for both bulk and charge transfer, giving circuits $A_{b+ct,x}$, $B_{b+ct,x}$, $C_{b+ct,x}$ and $D_{b+ct,x}$. The fittings are examined in all formalisms, using spectroscopic plots, and the resulting permittivity values are obtained. Fittings including the electrode spike are not presented, as the presence of the extra element did not alter the values of the bulk parameters.

4.8.1 BULK-ONLY FITTINGS WITH FREE n

The Z* Nyquist plots for both the experimental results and the corresponding fittings for circuits $A_{b,f}$, $B_{b,f}$, $C_{b,f}$ and $D_{b,f}$ at 200 and 275^{o}C are shown in Figure 4.22a and 4.22b respectively. These results are for n is free, and fitting is carried out across only the bulk frequency region. At 275 ^{o}C, each fitting closely matches the experimental spectrum, whereas at 200 ^{o}C $A_{b,f}$ (red line) deviates slightly. Here, Z' is overestimated at high frequency and Z'' is underestimated at low frequency, as illustrated in Fig. 4.22c (dashed line). This illustrates the fitting obtained from ZView software: simultaneous optimisation of Z' and Z'' scaled with the Z* magnitude (Scribner Associates, 2000).

The same spectra are also shown in terms of Y' and ε' in Figure 4.23. The fittings are reasonable in Y' except for $A_{b,f}$ at 200 ^{o}C, which is inaccurate at high frequency. It gives a better fit at 275 ^{o}C, where less dispersion is visible. This is also reflected in ε'; the constant gradient of $A_{b,f}$ gives a reasonable fit at 275 ^{o}C but not at 200 ^{o}C, where there are two bulk regions visible in ε'. $B_{b,f}$ (blue line) also deviates slightly in ε' at low frequency.

The trend of n with temperature is shown in Figure 4.24. The index changes with temperature when all parameters are left free. For circuits $A_{b,f}$ and $D_{b,f}$, n decreases with increasing temperature, whereas for $B_{b,f}$ and $C_{b,f}$ n increases, apart from the noisy 150 ^{o}C spectrum and the highest temperature points where the bulk arc is disappearing out of the measured frequency range.

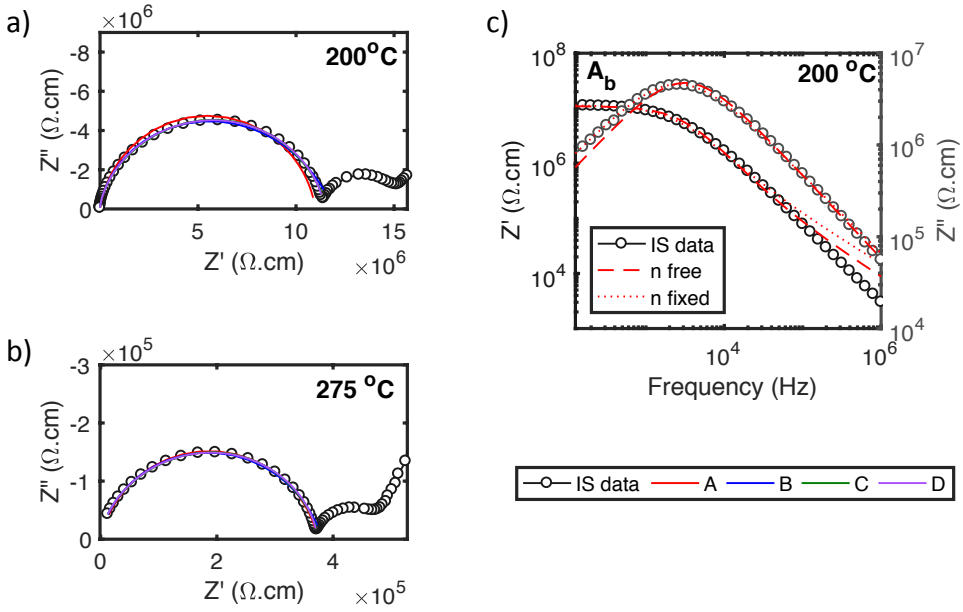

Figure 4.22: Z* plot measured at a) 275 °C (low frequency data omitted) and b) 200 °C, and the corresponding fittings for circuits $A_{b,f}$, $B_{b,f}$, $C_{b,f}$ and $D_{b,f}$ (bulk only, n is free). c) log-log spectroscopic Z' and Z'' plots measured at 200 °C and the fittings for circuits $A_{b,f}$ and $A_{b,x}$.

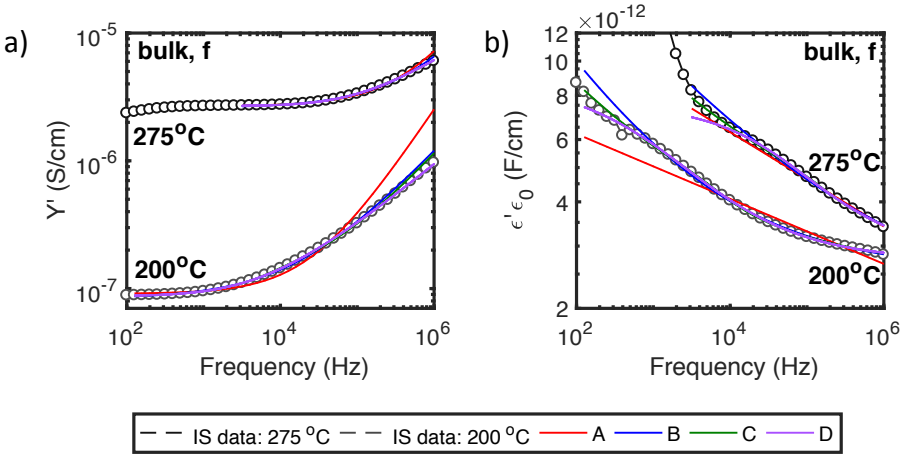

Figure 4.23: log-log spectroscopic plots of a) Y' and b) ε', measured at 275 °C (dark grey) and 200 °C (light grey), and the corresponding fittings for circuits $A_{b,f}$, $B_{b,f}$, $C_{b,f}$ and $D_{b,f}$ (bulk only, n is free).

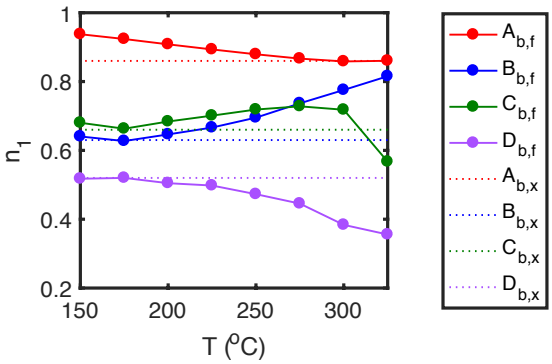

Figure 4.24: Variation of n with temperature for circuits $A_{b,f}$, $B_{b,f}$, $C_{b,f}$ and $D_{b,f}$ and the value that n is fixed at for circuits $A_{b,x}$, $B_{b,x}$, $C_{b,x}$ and $D_{b,x}$.

4.8.2 BULK-ONLY FITTINGS WITH FIXED n

Next, n was fixed for all four circuits, again fitting the bulk response only. For circuits $B_{b,x}$, $C_{b,x}$ and $D_{b,x}$, the low temperature value was taken at 175 °C, ignoring the noisy 150 °C spectrum, in accordance with the work of Abram et al. (2003). For $A_{b,x}$, however, this gave unreasonable fittings and hence, n was fixed at the high temperature value at 325 °C instead, as this gave the best fit in Z*. The fixed values are shown by the dotted lines in Figure 4.24.

All bulk fittings with fixed n give a respectable fit in Z* (not shown). However, for circuit $A_{b,x}$, although Z'' now gives a good fit at low frequency, there is more deviation in Z' at high frequency at 200 °C (Figure 4.22c, dotted line). The Y' and ε' spectroscopic plots are shown in Figure 4.25. Circuit $A_{b,x}$ is again inaccurate at high frequency in Y'. In ε' at 200 °C the gradient more closely matches the experimental response at lower frequency compared to $A_{b,f}$ (Fig. 4.23b), but has a larger deviation at higher frequency. The gradient of $A_{b,x}$ at both temperatures is the same in Figure 4.25b because it is controlled by n. $A_{b,x}$ gives a reasonable fit for ε' at 275 °C. Circuits $C_{b,x}$ and $D_{b,x}$ gave a good fit in Y' and ε' at all temperatures but circuit $B_{b,x}$ overestimated ε' at low frequency.

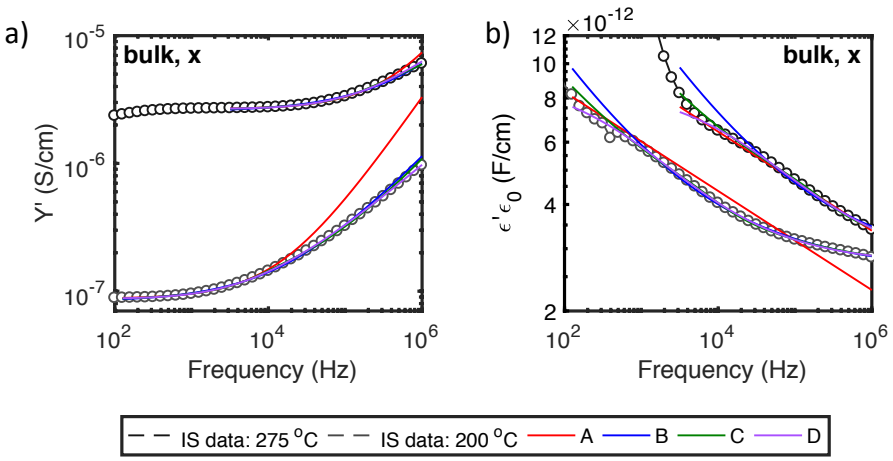

Figure 4.25: log-log spectroscopic plots of a) Y' and b) ε', measured at 275 °C and 200 °C (dark and light grey, respectively), and the corresponding fittings for circuits $A_{b,x}$, $B_{b,x}$, $C_{b,x}$ and $D_{b,x}$ (bulk only, n fixed).

4.8.3 PARAMETER TRENDS FOR BULK-ONLY FITTINGS

The material parameter trends obtained from the bulk-only fitting are now presented for both n is free and fixed, alongside results from hand-fitting. Firstly, the conductivity Arrhenius plot is shown in Figure 4.26. All fittings give essentially the same values for R_1, corresponding to an activation energy E_{act} of 1.03±0.01 eV and a conductivity of 6.9±0.04 x 10^{-6} S/cm at 300 °C. The conductivity derived from R_d (circuit C only) is also shown in Figure 4.26. When n is free, it gives a straight line, with an E_{act} of 0.89 eV, whereas when n is fixed, the R_d trend is no longer linear with inverse temperature.

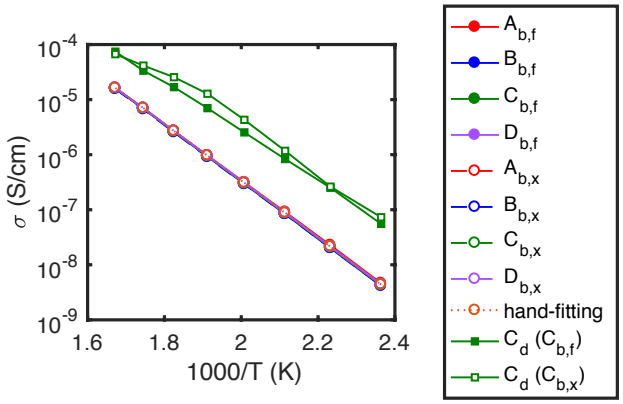

Figure 4.26: Bulk conductivity Arrhenius plot shown for n is free (filled circles, full line), n is fixed (open circles, dashed line) and hand-fitting (orange open circles, dotted line). The values of the inverse of R_d (Circuit C only) are also shown for n free (filled squares) and n fixed (open squares).

Additionally, the capacitance parameters, C_1, C_{RQ}, C_d and C_q, are shown as a function of temperature in Figure 4.27. The magnitude of C_1 for circuit C, see Figure 4.27a, is much higher than all other capacitance variables in all ECs studied here, ranging between 140 to 225[‡‡]. It has no clear trend at fixed n (open circles), whereas when n is free (filled circles), it decreases with increasing temperature, excluding the upper and lower points. A close-up of the values of C_1 from the remaining circuits is shown in Figure 4.27b, along with the combined parameter C_{lim} (Equation [4.7], green circles) for circuit C, and ε'_∞ (grey line) from LCR results. C_1 and C_{lim} give a value of around 30 at low temperature, closely matching ε'_∞, and represent the high-frequency-limiting capacitive response, ε_r[§§]. Deviation is seen at higher temperature, with a steep decrease for $B_{b,f}$ and a moderate increase for the remaining circuits with the exception of $D_{b,x}$, which is remarkably stable.

Circuit C has an extra parameter C_d, see Figure 4.27c, which is lower in magnitude than C_1 at around 35 and hence has a larger influence on C_{lim} (i.e. ε_r). C_d follows a similar trend to C_{lim}. Figure 4.27c also shows C_q from circuit D, which decreases with increasing temperature, ignoring the inaccurate data point at 150 °C. C_q decreases at a slower rate for $D_{b,x}$ than for $D_{b,f}$.

The values of C_{RQ} vary considerably between the different ECs, see Figure 4.27d. C_{RQ} is largest for circuit A, comparable to the hand-fitting capacitance values, and smallest for circuit C, ranging between 3 and 20. For circuit $A_{b,f}$, C_{RQ} increases with temperature, as seen in Perry et al. (2011), whereas for $A_{b,x}$ it decreases instead,

[‡‡] All capacitance values in Sections 4.8 onwards are quoted in terms of permittivity, unless otherwise stated. This is equal to the ratio of the geometrically-corrected capacitance to the permittivity of free space, giving a dimensionless number (see Equation [4.9]). Figures are presented with dual C and ε' axes, for ease of comparison.

[§§]For clarity, ε_r is used here to mean the high-frequency-limiting response from the EC, whereas ε'_∞ is reserved for the high-frequency response from the LCR data (see Section 4.7.2).

meeting at the temperature at which n was fixed. Data for the remaining circuits are stable at low temperature, at which n was fixed, but deviate at high temperature, increasing for $B_{b,f}$ and decreasing for the other circuits.

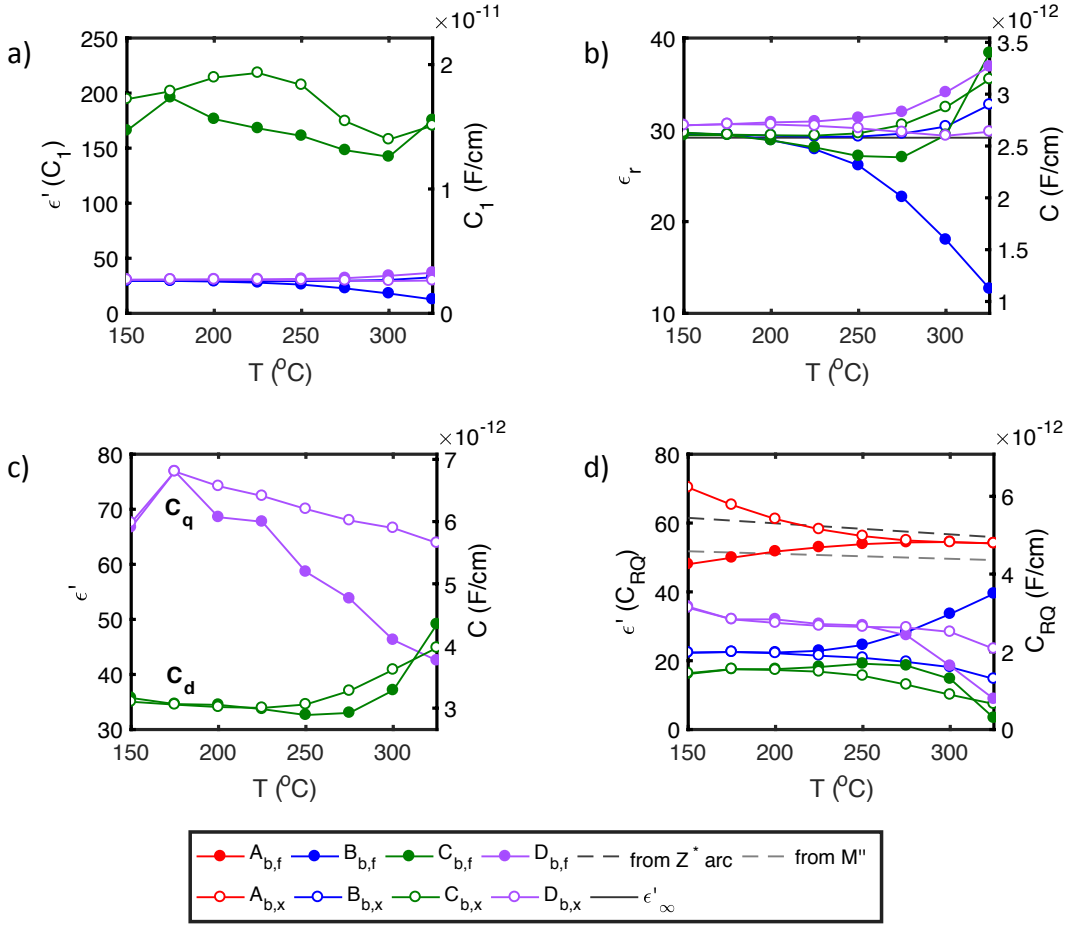

Figure 4.27: Capacitance parameters from fitting of the bulk element only, for both n is free (filled symbols) and n is fixed (closed circles). The figures are shown with dual axes: capacitance (F/cm) and permittivity. a) C_1, b) close-up of (a), with the addition of C_{lim} from circuit C, c) C_d (circuit C) and C_q (Circuit D), and d) C_{RQ}. The hand-fitting values are also shown (dashed grey lines).

4.8.4 FITTINGS INCORPORTATING BOTH BULK AND CHARGE TRANSFER RESPONSES

The charge transfer response was incorporated into the three fittings by adding a parallel *RQ* element in series with the bulk element, fixing both n values, giving $A_{b+ct,x}$, $B_{b+ct,x}$, $C_{b+ct,x}$ and $D_{b+ct,x}$. The bulk index was fixed as for the bulk-only fitting, see Figure 4.24. The charge transfer value was fixed at unity for $B_{b+ct,x}$ and $C_{b+ct,x}$, 0.9 for $A_{b+ct,x}$ and 0.86 for $D_{b+ct,x}$, roughly corresponding to the free value.

The fittings for 200 °C are shown in Figure 4.28 for all immittance formalisms, along with the experimental spectra. $A_{b+ct,x}$ deviates significantly at high frequency, as for $A_{b,x}$, most notably in Z'', M'', Y' and ε''. In contrast, $B_{b+ct,x}$ and $C_{b+ct,x}$ both give a good fit in all formalisms across all six frequency decades, albeit with a slight frequency shift in Z'', Y'', M' and ε' (Fig. 4.28e-h) at intermediate frequency, the region between the two Z* arcs. $D_{b+ct,x}$ gives an excellent fit across all frequencies in all formalisms.

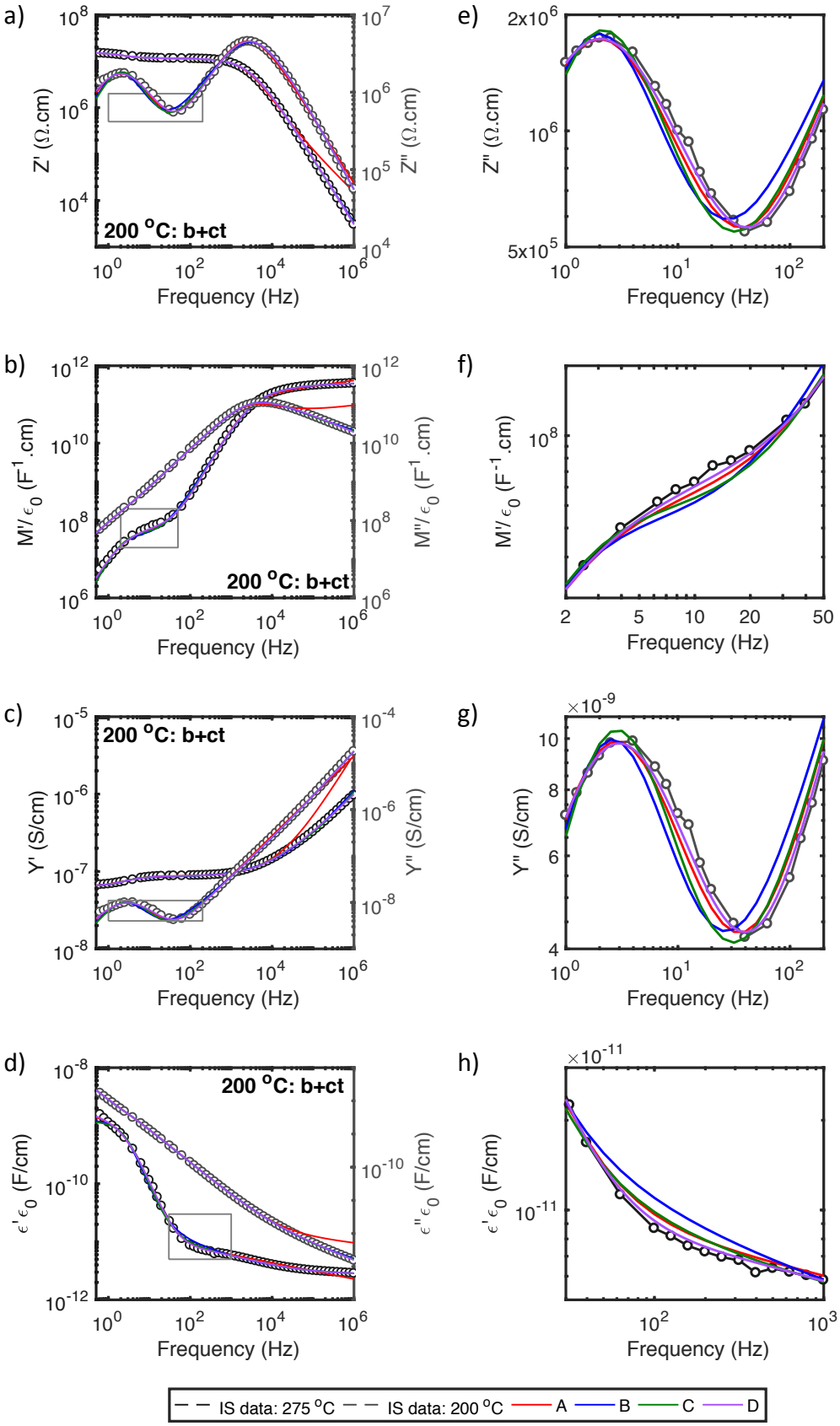

Figure 4.28: log-log spectroscopic plots of a) Z*, b) M*, c) Y* and d) ε*, measured at 200 °C, and the corresponding fittings for circuits $A_{b+ct,x}$, $B_{b+ct,x}$, $C_{b+ct,x}$ and $D_{b+ct,x}$ (bulk and charge transfer, fixed n). e,f,g,h) close-up of frequencies of interest from figures (a-d).

The results for fittings at other temperatures (not shown) are consistent with the findings at 200 °C, except for $A_{b+ct,x}$, which improves as temperature increases, in the same manner as $A_{b,x}$.

To give an indication of the quality of the fitting, the sum of the least squares error for $A_{b+ct,x}$, $B_{b+ct,x}$, $C_{b+ct,x}$ and $D_{b+ct,x}$ is shown in Figure 4.29 as a function of temperature. It was calculated using equation [2.40] in the Z* formalism and shows the summation of the real and imaginary components. Results from the remaining formalisms are almost identical to that of Z* but there is variation in the contribution of the errors associated with the real and imaginary components. Circuit $D_{b+ct,x}$ gives the best fit across all temperatures measured, except 325 °C, where circuit $C_{b+ct,x}$ gives a marginally better fit. The error values for both circuits $B_{b+ct,x}$ and $D_{b+ct,x}$ have minimal temperature dependence. In contrast, for circuit $C_{b+ct,x}$ the error decreases with increasing temperature above 250 °C, and for circuit $A_{b+ct,x}$, there is a sizable decrease with increasing temperature across the whole range measured.

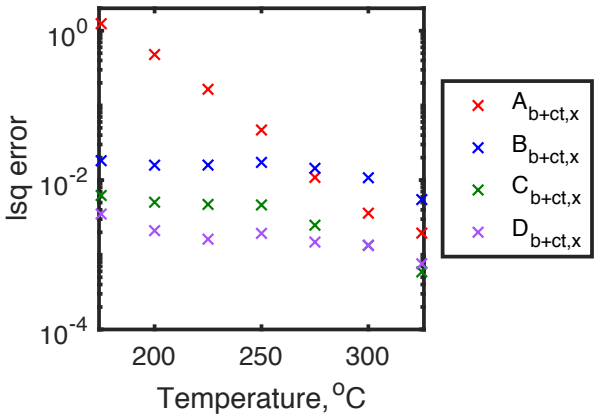

Figure 4.29: The least squares error for circuits $A_{b+ct,x}$, $B_{b+ct,x}$, $C_{b+ct,x}$ and $D_{b+ct,x}$, calculated using equation [2.40] in the Z* formalism.

The resulting bulk conductivity values are again essentially identical, regardless of the circuit used, matching those in Figure 4.26. The R_d trend with inverse temperature matches the trend seen in circuit $C_{b,x}$, again deviating from the straight line expected from a conductivity Arrhenius plot.

The bulk capacitance values, C_1, C_{RQ}, C_d and C_q, are shown in Figure 4.30 and are comparable to the values obtained from the bulk-only fittings when n was fixed. C_1 from circuit C is again significantly larger than the other capacitance parameters, see Figure 4.30a, and C_{RQ} varies notably between different equivalent circuits, see Figure 4.30d. For circuit $D_{b+ct,x}$, C_{RQ} is stable with temperature, whereas it decreased at higher temperatures for the bulk-only fittings (Figure 4.30d). The series combination of C_{RQ} and C_q is comparable to C_{RQ} from circuit $B_{b+ct,x}$ at lower temperatures. C_q for circuit $D_{b+ct,x}$ decreases with increasing temperature at a rate comparable to the rate of $D_{b,x}$ but with a reduction in magnitude of about 6.

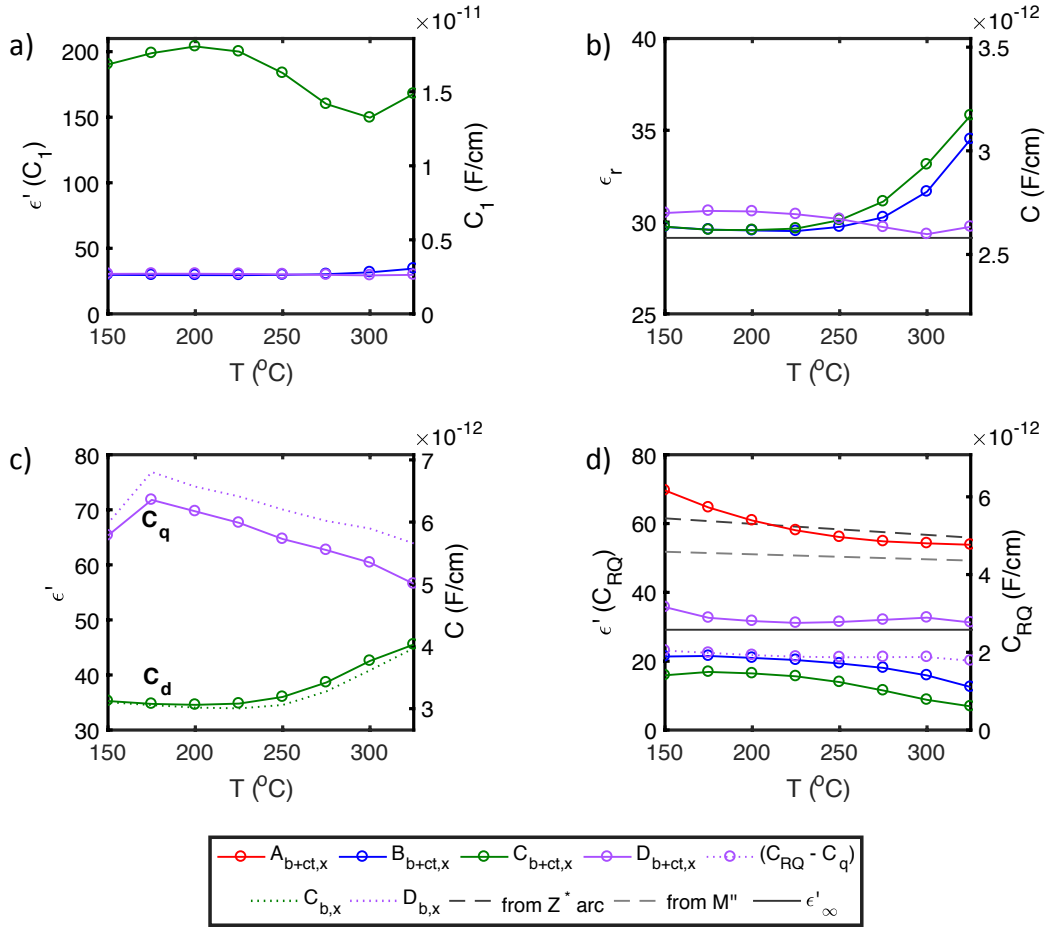

Figure 4.30: Bulk capacitance parameters taken from *b+ct* fittings. a) C_1, b) zoom of (a) with the addition of C_{lim} (circuit C), c) C_d (circuit C) and C_q (circuit D) (dotted line is from $D_{b,x}$, for comparison), and d) C_{RQ} plus the hand-fitting capacitance values (dashed lines) and the combination of C_q and C_{RQ} in series for circuit $D_{b+ct,x}$ (dotted line).

4.9 Accuracy of Fittings

All fittings gave reasonable spectra for the Z* Nyquist plot. This is to be expected as the fitting procedure in ZView specifically optimises the fit to Z' and Z'' data. Instead, the critical issue is how to fit well simultaneously in all four formalisms. Regardless of whether n is fixed or free and whether or not the charge transfer response is also fitted, circuit D fits very well and circuits B and C fit reasonably well; however, circuit A is unable to give a good fit simultaneously in all formalisms. The bulk ε' spectroscopic response is particularly problematic, as the circuit A response is limited to a line of constant gradient on a log-log plot. For a fixed value of n, the gradient is fixed across all temperatures. A constant gradient gives a reasonable fit at high temperature, as there is only one main bulk region in ε'. However, at low temperatures there are two regions within the bulk response each with distinct gradients. When n is free, the gradient lies between that of each region, giving a poor fit for ε' at all frequencies, see Figure 4.23b (circuit $A_{b,f}$). When n is fixed, it more closely resembles the lower frequency region, see Figure 4.25b (circuit $A_{b,x}$) but

presents significant error at high frequency not only in ε' but also in Z', M'', Y' and ε'', as visible in Figure 4.28 for circuit $A_{b+ct,x}$. The gradient of the Y' dispersion is determined by the value of n. For circuit A, the fit is poor for free n and worse for fixed n (Figure 4.23a and 4.25a), particularly at low temperature where more dispersion is visible in the measured frequency range. For circuits B, C and D, the effect of fixing n is more subtle.

The magnitude of n is visible at different frequencies in different formalisms, despite the formalisms all representing the same data in different ways. In Y', it is reflected in the high frequency dispersion, whereas in ε', it is reflected at lower frequency, see Figure 4.12. It affects frequencies above the bulk peak frequency in M'' and below the peak frequency in Z'', see Section 4.3. Fitting using different formalisms, for example, optimising for Y* rather than Z*, could hence have a significant effect on the fitting data obtained.

The addition of the high-frequency-limiting capacitor C_1 (as shown by Abram et al. (2003)) in circuit B enables both regions in the bulk ε' spectroscopic response to be described; hence, circuit B gives a much better fit than circuit A. Circuits $B_{b,f}$ and $B_{b,x}$ fit the experimental data well at high frequency, but deviate at lower frequency, nearing the charge-transfer response (especially when n is fixed). This is also present in $B_{b+ct,x}$, see Figure 4.28h, but is dwarfed by the charge-transfer response, which covers several orders of magnitude. This problem is therefore not solved by the addition of a charge transfer element in the EC and is more likely to stem from an extra feature in the bulk response; the bulk ε' spectroscopic response is not merely two different sections of constant gradient. This is similarly reflected in Z'' and Y'' spectra in the transition between bulk and charge transfer regions (~30 Hz at 200 ^{o}C, see Figure 4.28e,g), where there is a frequency shift in EC values compared to experimental data. This frequency shift is also present for fittings from circuit $C_{b+ct,x}$, based on work by Hernández and West (2016), although to a lesser extent than in circuit $B_{b+ct,x}$, despite the additional circuit parameters: R_d and C_d. At all other frequencies, it gives a good fit. Circuit $D_{b+ct,x}$, a new contribution in this work, describes the experimental data excellently across the whole frequency spectrum fitted, including the transition region.

For all circuits investigated, the effect of the charge transfer response on the bulk response is insignificant for these spectra, with characteristic frequencies separated by three decades and capacitances being four orders of magnitude apart.

For the bulk and charge transfer response, circuit $D_{b+ct,x}$ gives the best fit with four bulk variables, followed by circuit $C_{b+ct,x}$ with five bulk variables, then $B_{b+ct,x}$ with three bulk variables and lastly circuit $A_{b+ct,x}$ with two bulk variables. (Each circuit also has two charge-transfer variables). This implies that circuit C is more complicated than necessary to describe the features of bulk YSZ.

4.10 PARAMETER TRENDS & PHYSICAL RELEVANCE OF DATA

When aiming to use IS to characterise materials, the parameters in the EC should be physically relevant. In this section, the relevance of the bulk parameters in each model is discussed, along with a discussion of the parameter trends.

4.10.1 CONDUCTIVITY

The bulk conductivity, derived from R_1 for each circuit, decreases with inverse temperature, see Figure 4.26, as described by the Arrhenius equation (Equation [4.3]). The activation energy 1.03 ± 0.01 eV matches values reported in the literature for bulk YSZ, see Table 4.1, and the conductivity magnitude of 6.9×10^{-6} S/cm at 300 ^{o}C is also in agreement with the literature. Each circuit gives virtually identical results, showing R_1 is insensitive to the equivalent circuit fitted (for these four circuits, when fitting in Z*, using the protocol described above) and even the hand-fitting data is sufficient to determine the conductivity trend accurately. This confirms that IS data for YSZ can be used to extract bulk conductivity values reliably without the need for a detailed equivalent circuit.

Conversely, values of R_d (circuit C) are different depending on the treatment of n. A straight line in the Arrhenius plot is only obtained when n is free; therefore, fixing n does not result in physically realistic trends in R_d. The activation energy of 0.89 eV is lower than that of the bulk, contradicting the results of Hernández and West (2016), where the two are comparable, which led them to believe R_1 and R_d represent similar oxide ion hopping processes. Instead, R_d is unlikely to represent such a process, or indeed any physical process at all, given the permittivity results discussed below.

4.10.2 PERMITTIVITY OVERVIEW

In contrast to the bulk conductivity, permittivity values differ for each equivalent circuit. In fact, even for the same circuit, the value of n has a significant effect on the magnitude of the permittivity obtained, illustrated by the difference between the fittings when n is fixed and free in Figure 4.27. For a given value of n, however, the inclusion of the charge transfer has a negligible effect on the bulk permittivity values, seen by comparing Figures 4.27 and 4.30. The effect of n is explored further below. In the following sub-sections, the various permittivity trends are discussed, namely ε_r, C_{tot}, C_{RQ}, C_d and C_q, and their origins are considered.

4.10.3 INTERPLAY BETWEEN n AND ε_r IN CIRCUIT A

In circuit A, there is only one capacitive element for the bulk, which can hence contain contributions both from ε'_∞ and from any other bulk component, depending on the features present in the measured frequency range. The relative

permittivity*** for circuit $A_{b,f}$ is shown in Figure 4.31 as a function of temperature, along with the hand-fitting data and the value of ε'_∞ from the LCR data (Fig. 4.16). Data from Perry et al. (2011) for an 8 mol% YSZ poly-crystal, corrected for density, likewise fitted using an RQ element with n is free, is also displayed and includes lower temperature values that were not possible to measure accurately with the equipment used in the present study. The results are not identical, possibly due to the different sample microstructures used, see Chapter 5, but give the same trend of ε_r increasing with temperature. Values are comparable with those from hand-fitting at high temperature; a marginal downward trend is visible in the high temperature results of Perry et al. (2011), in particular. The low temperature values tend towards ε'_∞, and at intermediate temperatures, the values transition between the two.

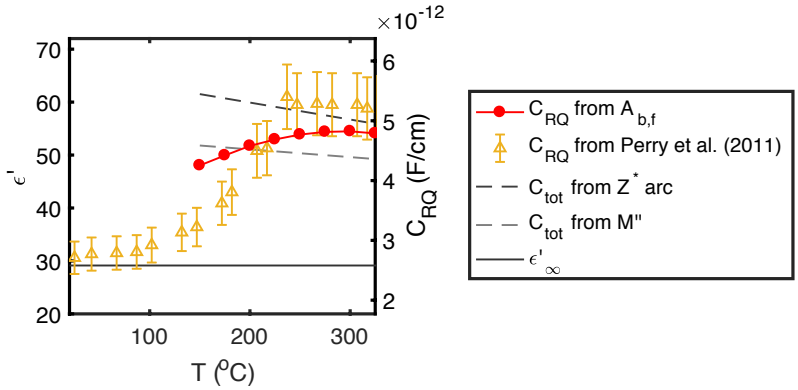

Figure 4.31: Variation with temperature of ε_r for circuit $A_{b,f}$ (circles) compared to data calculated by Perry et al. (2011) (triangles). The room temperature high frequency (solid line) ε' and the capacitance hand-fitting values (dashed lines) are also shown. The light and dark grey dashes are determined from M'' and Z* respectively (see equations [4.4]&[4.5]).

The reason for this trend is apparent from the ε' spectroscopic data, illustrated in Figure 4.32. At room temperature, in the frequency range measured, only the high frequency plateau is observed. Fitting using a straight line gives a gradient approaching zero, and hence n tends to unity, as the gradient is equal to n-1; the capacitance extracted is equal to ε'_∞. At high temperature, the dispersive part of ε' is the only portion seen in the frequency range measured, see Figure 4.32. The index n tends to about 0.86 (1 + gradient) and the value of ε_r extracted corresponds to the overall capacitance value seen: the sum of the dispersion and ε'_∞, matching values from hand-fitting. At intermediate temperature, both bulk regions of ε' are seen, see Figure 4.32. Fitting a straight line therefore gives a compromise; n is between 0.86 and 1, and ε_r similarly gives a value between the two limits.

*** For circuit A, relative permittivity ε_r is used in this sub-section to represent the capacitive response of the bulk element, as used by Perry et al. (2011). However, this does not necessarily correspond to the low frequency plateau: ε'_∞.

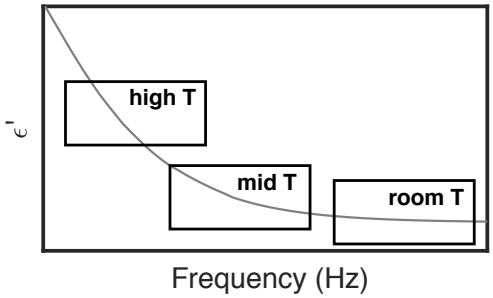

Figure 4.32: Schematic of the permittivity spectrum with three example temperature windows (high, mid and low temperatures).

Note that Perry's values of ε_r transition away from ε'_∞ at a higher temperature than data from this work, which could be due to measuring to a higher frequency limit of 13 MHz, compared to the limit of 1 MHz used here. A higher frequency range has the same effect as decreasing the temperature on how much of the limiting high frequency data is seen: the plateau pulls up the value of n and hence gives a smaller value of ε_r.

Furthermore, the parameter results are influenced by the weighting method used during complex non-linear least squares (CNLS) fitting. In ZView, the default weighting (used here) for CNLS fitting normalises data by the Z* magnitude of the fit. The magnitude of the experimental data can also be used but this is more likely to contain random noise (Scribner Associates, 2000). Alternatively, each real and imaginary data point can be normalised separately or a weighting of unity can be applied (although this is not advised as large magnitude points are overemphasised). Instead of using ZView, Perry et al. (2011) carry out fitting using a program by Boukamp (1986). If different weightings or methods are used to optimise the fitting parameters, then this is a further cause for variation between results.

In light of the analysis in this sub-section, the rise in the relative permittivity with temperature for circuit $A_{b,f}$ is merely an artefact of the fitting and does not indicate a temperature-induced presence of dipoles, such as Perry et al. (2011) suggest. Consequently, using this equivalent circuit to estimate ε_r is inappropriate. Circuits $A_{b,x}$ and $A_{b+ct,x}$ are also unsuitable; fixing n resulted in inaccurate fittings and caused ε_r to be overestimated at low temperature (Figures 4.27d and 4.30d). This is again due to a line of constant gradient (0.86) being inadequate to describe both regions of the bulk response simultaneously. These circuits do not contain sufficient bulk variables to ensure a decent fit across all formalisms, and hence fixing n for circuit A is not a good strategy.

4.10.4 Overall bulk capacitance, C_{tot} and relative permittivity, ε_r

The overall bulk capacitance C_{tot} for each circuit (*b+ct* fittings only) was calculated and is shown in Figure 4.33, along with the hand-fitting values from both methods (see Section 4.3.1). With the exception of circuit A, see the discussion above, there is

a moderate decrease in C_{tot} with increasing temperature. There is some uncertainty as to the exact magnitude; each hand-fitting method and each EC give different results. Circuits B and D give similar values to hand-fitting from M'', at around 47-53, whereas circuit C is notably lower, between 42 and 46. C_{tot} is a combination of ε_r and the extra bulk feature(s) seen at lower frequency. These features are separated out in the individual components.

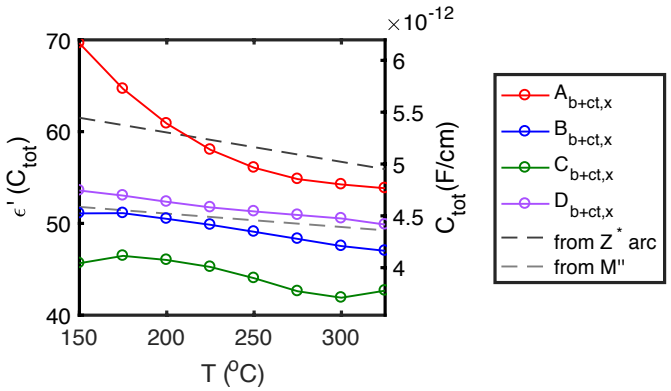

Figure 4.33: Variation with temperature of the total combined capacitance for each equivalent circuit (b+ct fittings only) and for each hand-fitting method.

ε_r is represented by C_1 in circuits B and D, and by the series combination of C_1 and C_d in circuit C, termed C_{lim}, see equation [4.7]. For circuits $D_{b,x}$ and $D_{b+ct,x}$, this parameter is independent of temperature (see Fig 4.27b & Fig 4.30b), as expected for ε_r, whereas the remaining circuits deviate at high temperature, with the shift of the bulk response towards frequencies beyond those measured. Circuit D hence appears to give the most physical trend for ε_r with temperature.

4.10.5 Constant phase element parameters: n and C_{RQ}

The constant phase element (CPE) has two parameters associated with it: the index n and the pre-exponential factor Y_0, expressed here in terms of the resulting capacitance C_{RQ}, see Equation [4.6]. In each equivalent circuit, the constant phase element (CPE) is used for different purposes; this is reflected in the difference between the trends for both n and C_{RQ} trends for each equivalent circuit. At low temperature, the magnitude of n varies from 0.52 in Circuit D, to 0.94 in Circuit A; hence n is clearly no longer a simple measure of the non-ideality of the sample, nor is it necessarily equal to the gradient of Y'. (The quality of the low temperature experimental data in the form of Y' is insufficient to calculate the gradient precisely, but it is approximately 0.65 and 0.59 at 150 and 175 °C, respectively). This is comparable to how C_{tot} from hand-fitting varies depending on the formalism used to estimate it.

Additionally, as temperature increases, n decreases for circuits A and D and increases for circuits B and C. The loss of immittance data at sufficiently high frequency causes the shift in values of n as temperature increases, which can be

simulated by reducing the frequency maximum used during fitting. This indicates that n cannot be calculated accurately for spectra measured at higher temperature. It is therefore best practice to fix n at a low temperature value for circuits B, C and D. For circuit C, this is at the expense of a linear R_d Arrhenius plot, see Section 4.10.1.

Furthermore, the value of C_{RQ} depends on which other EC components are present in the circuit. For circuit A, it was already seen that C_{RQ} attempts to describe the total capacitive response visible in the frequency range measured. In circuits B, C and D, the CPE instead enables a distribution of characteristic frequencies or relaxation times, associated with a non-ideal material, to be represented. In circuit D, the CPE specifically describes the mid-frequency ε' range, due to the presence of C_q influencing lower frequency data. A combination of C_{RQ} and C_q in series (dotted line in Fig. 4.30d) gives a capacitance comparable to the C_{RQ} response for circuits B and C, where the CPE is used to fit all capacitances that are present in addition to ε_r. The physical reasoning for the non-ideal electrical behaviour is still unclear, although a suggestion is given in Section 4.10.8.

The trends of n and C_{RQ} (Figures 4.24 and 4.27d) are interrelated. For circuits B, C and D, a higher magnitude of n at low temperature gives a higher value of C_{RQ}, whereas the trend with temperature for each circuit is comparable to that of n when it is free. Conversely, circuit A gives opposite trends of n and C_{RQ} with temperature, and both have larger magnitudes than for the other circuits. Additionally, when n is fixed, there is still some variation in C_{RQ} with temperature. Values are approximately stable at low temperature for circuits B, C and D, dropping off at higher temperature, with the exception of $D_{b+ct,x}$, which is remarkably stable across the whole temperature range.

4.10.6 Capacitances C_1 and C_d in circuit C

In circuit C, the capacitance C_1 does not give a clear trend and has a magnitude significantly higher than expected for processes associated with the bulk response (Irvine et al., 1990). The magnitude of C_d is more reasonable for a bulk response; however, if it represents a dipole effect, as claimed by Hernández and West (2016), it is unlikely to follow the same trend as ε_r. Instead of fixing n, they fix C_1 and C_d at a low temperature value to counteract the loss of high frequency ε'_∞ data. Comparing samples with varying electrodes, sintered at the same temperature, the values they obtained for C_1 and C_d are not consistent with each other. At a sintering temperature of 1450 ^{o}C, the permittivity from C_1 ranged between 1.2 and 91 and between 32 and 39 for C_d; n ranged between 0.58 and 0.69. Conversely, in this work, there was no notable difference between equivalent circuit parameters obtained for the YSZ sample with platinum or gold electrodes. The parameters C_1 and C_d do not appear to have separate physical meaning, which calls into question the relevance of the extra parameters.

4.10.7 LOW FREQUENCY LIMITING CAPACITANCE, C_q

The parameter C_q in circuit D shows a clear downwards linear trend with increasing temperature, see Figure 4.30c, with a physically realistic magnitude, in contrast to the unphysical capacitance parameters in circuit C. It represents the additional capacitance due to the distribution of characteristic frequencies or relaxation times of bulk processes, on top of the baseline ε_r. This is illustrated in Figure 4.12g, where the low-frequency-limiting permittivity value is the sum of the C_1 and C_q contributions. The decrease in C_q implies that the distribution narrows with increasing temperature. To investigate this hypothesis, the Full Width Half Maximum (FWHM) values for Z'' were determined for both the experimental IS data and for circuits B to D, see Figure 4.34a. For the EC data, the average value is displayed for each circuit; the error bars represent the standard error. The resolution of the experimental data was insufficient to discern any variation within the measurable temperature range (150 – 275 ^{o}C) and gave a constant value of 1.5±0.1. The EC values decreased approximately with increasing temperature; however, there was significant variation between the equivalent circuits. The values for circuits C and D were within the error bounds for the experimental values but those for circuit B at high temperature were not. As circuit D gives the most accurate fit, see Figure 4.29 and Section 4.9, the FWHM values are thought to be most accurate for this circuit and it seems likely that the distribution does indeed decrease modestly with temperature. A similar effect is expected for the FWHM values of M'', but much of the data is beyond the frequency range measured and so it is not investigated here.

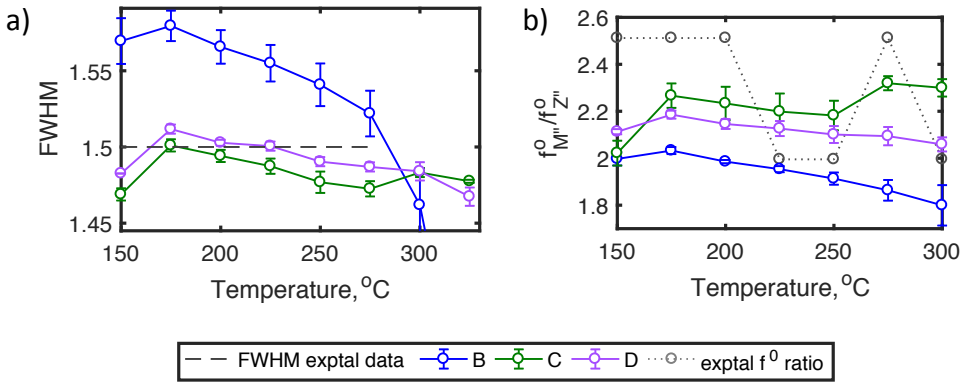

Figure 4.34: a) Full Width Half Maximum (FWHM) values for Z'' as a function of temperature, calculated from experimental results (dark grey dashed line) and from circuits B (blue), C (green) and D (purple). b) The ratio of the frequency peak of M'' to that of Z'' as a function of temperature: experimental results (grey dotted line), and circuits B (blue), C (green) and D (purple). Note, for each circuit, the value plotted is the average of $X_{b,f}$, $X_{b,x}$ and $X_{b+ct,x}$ (where X is the circuit) and the error bars represent the standard error between those fittings. Equivalent circuit measurements were calculated using a spacing of 0.0001 $\log_{10}$ frequency.

As spectra become more ideal, i.e. as the FWHM values for Z'' or M'' tend to 1.14 on a logarithmic frequency scale, the ratio of the frequency maximum in M'' to that in Z'', f_M^o/f_Z^o, decreases towards unity. Values are shown in Figure 4.34b for

experimental data (grey open circles) and for circuits B to D. Again, there is a large variation between each data set. Experimental values step between 2.0 and 2.5, with an error of approximately ±0.5. Again, circuits C and D lie within this range, whereas circuit B does not, and all circuits give a modest decrease in f_M^o/f_Z^o with temperature, except for circuit C at high temperature. Thus, as observed experimentally, peaks in Z'' and M'' occur at frequencies closer to each other at higher temperature. Curiously, this effect is independent of whether n is fixed or not; hence n is not the only parameter defining the extent of deviation from Debye behaviour.

4.10.8 POSSIBLE PHYISCAL ORIGINS OF THE EXTRA CAPACITANCE, C_q

The additional capacitance, C_q, introduced in circuit D, indicates the presence of an extra polarisation to that of the lattice of YSZ. It is visible in ε' at low frequency but does not appear to affect the d.c. bulk conductivity, R_1^{-1}, despite this being a low frequency effect. The d.c. conductivity is a result of the long-range conduction of oxide-ions through the lattice. Therefore, this extra phenomenon/a could be the result of a.c. local effects associated with variations in the local structure that influence either the polarisation and/or conduction processes in the material.

It is unlikely that this polarisation stems from a conventional defect dipole (local oxygen vacancy $V_O^{\cdot\cdot}$ rearrangement around the acceptor Y-dopant, Y'_{Zr}) as proposed by Perry et al. (2011). Instead, recent local structural data (Norberg et al., 2011) have shown that $V_O^{\cdot\cdot}$ associates preferentially with the neutral Zr_{Zr}^x sites rather than with the charged Y'_{Zr} sites, see Section 4.2.3. In addition, these tend to form clusters of defects as opposed to the conventional acceptor-oxygen vacancy point defect dipoles. Furthermore, C_q decreases with increasing temperature, which is in contrast to temperature-induced activation of dipoles suggested by Perry et al. (2011).

On the basis that $V_O^{\cdot\cdot}$ sites form clusters in localised regions (see Section 4.2.4), the material is homogeneous on a macroscopic scale but is heterogeneous on a local scale. Although these clusters have a small influence on the *average* conductivity and permittivity of the crystal, they can have a significant influence on the *local* polarisation and conduction pathways. The clusters could have a higher permittivity associated with them, compared with the regular lattice, due to the high effective charge of $V_O^{\cdot\cdot}$ and distortions (strain) in the lattice. This additional polarisation would influence the conduction mechanism in these regions as compared with the regular lattice and may give rise to an a.c. as opposed to a d.c. conduction mechanism. The clustered regions are randomly distributed (the doping level is insufficiently high to give rise to a long-range sub-lattice) and will be increasingly broken up with increasing temperature due to the influence of entropy. This results in a loss of heterogeneity and therefore the local structure will increasingly resemble the average structure. The non-ideal Z'' and M'' spectroscopic behaviour at lower temperatures is consistent with the presence of random clusters and therefore the

concept of a distribution of relaxation times. The break-up of these clusters at higher temperatures is consistent with the reduction in the distribution of relaxation times, the convergence towards more ideal Z'' and M'' spectroscopic responses and the decrease in C_q with increasing temperature.

4.11 CONCLUSIONS

To determine whether an equivalent circuit fitting is reasonable, it is necessary to examine the results in multiple immittance formalisms. A good fit in the Z* Nyquist plot does not guarantee a good fit overall, particularly if the fitting optimisation is carried out using data in the impedance formalism. Especially useful for YSZ and similar materials is the high frequency plateau in ε', to assist with intrinsic lattice polarisation ε_r.

To some extent, the more parameters are used to describe the bulk, the better the fit is. Circuit C is better than B, which is better than A, with 5, 3 and 2 variables, respectively, for the bulk element with fixed n. The best fit, however, is given by circuit D with only 4 variables, suggesting that circuit C is over-fitted. Circuit B is inaccurate at low frequencies associated with the bulk; however, it is expected to be sufficient when an additional response, such as that of a grain boundary, is present that obscures the low frequency limiting bulk behaviour of ε'. In contrast, the inclusion of the charge transfer response, fitted using a parallel RQ element in series with the bulk element, has a negligible effect on the bulk fit. However, the values of the EC parameters vary slightly between bulk-only and *b+ct* fittings; this is particularly notable for C_q (Fig. 4.30c) as it describes the bulk at frequencies close to the transition to the charge transfer region.

As temperature increases, EC results suggest the Z'' and M'' peaks become narrower and the corresponding frequency maxima get closer together, even if n is constant; hence, the deviation from Debye behaviour is not solely reflected in n.

For a given EC, the extracted values and their temperature dependence are influenced by a number of factors such as the formalism and the weighting method used for fitting. Different EC fitting programs are unlikely to be identical in their fitting procedures and so could be a further cause of variation.

Calculation of the bulk conductivity is very robust. Any of the circuits investigated here are sufficient to extract it, regardless of the quality of the fit; even hand-fitting in Z* is adequate. However, with *insufficient* bulk parameters, the resulting capacitance trend(s) with temperature are not physically meaningful. For example, for circuit A, the trend of its only capacitance parameter, C_{RQ}, is merely an artefact of fitting and not an indication of temperature-induced dipole behaviour, as suggested by Perry et al. (2011). If there are *too many* bulk parameters, their physicality is also questionable; for example, in circuit C, C_1 and C_d only appear to be physically meaningful when combined to give the high-frequency-limiting capacitance C_{lim}, thus calling into question the supposed presence of dipoles suggested by Hernández and West (2016).

The variable C_{lim} is comparable to the results obtained for C_1 for circuits B and D and matches ε'_∞ from LCR results. It hence represents the intrinsic atomic and ionic polarisation of the lattice, ε_r. The trend for ε_r is most stable with temperature for circuit D. The extra capacitance parameter C_q decreases with increasing temperature and represents the additional contribution from the non-ideal behaviour of the material. A possible physical explanation is the presence of localised clusters of oxygen vacancies that give rise to local regions with higher permittivity than the average lattice, giving rise to a distribution of relaxation times. At higher temperatures, the influence of entropy will cause the clusters to break up, resulting in a narrowing of the distribution times. Further experiments are necessary to investigate this hypothesis.

In summary, the newly-proposed circuit D gives both the best fit and the most physical representation of bulk parameters for a single crystal of YSZ, characterising both the lattice polarisation ε_r and the additional non-ideality, contributing to the low-frequency-limiting permittivity.

CHAPTER 5: EFFECT OF SINTERING TEMPERATURE ON THE ELECTRICAL PROPERTIES OF YSZ CERAMICS

5.1 INTRODUCTION

In the previous chapter, the bulk electrical properties of yttria stabilised zirconia (YSZ) were investigated using a single crystal. In many applications, however, YSZ is *poly*crystalline, termed *ceramic*. The presence of multiple grains gives the sample a complex microstructure, due to the addition of grain boundaries and pores, the nature of which vary with the sintering conditions and the initial powder used. The microstructure influences the electrical properties and hence affects impedance spectroscopy (IS) results; electrical properties of ceramics can be varied by controlling the sintering conditions. This is of significance in SOCs, where YSZ is present in many cells both as the dense electrolyte and also as the oxide-ion-conducting component in the porous electrodes.

In this chapter, the theory of sintering is presented and literature is reviewed related to the effects of grain boundaries and pores on IS data. Methods to model these electrically are explored. The aims and objectives are then listed and measured impedance results are given for YSZ ceramics sintered at a range of temperatures. Equivalent circuits are used both to fit the data and to extract material parameters, to determine the effect that sintering temperature has on the extent of porosity and on the grain boundary response. Finally, the results for polycrystalline ceramics are compared to those for the single crystal, looking particularly at the influence of the grain boundary contribution on the bulk response.

5.1.1 SINTERING THEORY

Sintering is the process of joining particles together into a solid body by heating at a temperature below the melting temperature of the material (Carter and Norton, 2007). Prior to firing, a powder compact (or “green body”) is made that consists of solid particles in contact with each other. The green body typically has a porosity between 25% and 60% (Kingery et al., 1976), which varies with the size distribution of particles and the nature of the packing. The relative density of a sample is the ratio of its density to that of a fully dense sample and is equal to the subtraction of the fraction of porosity from unity.

During firing, there is a transfer of material between different parts of the sample, due to a thermodynamic driving force to decrease surface area and lower the surface free energy. Matter is transferred for example, between the surface, bulk

and the grain boundary, either by diffusion or by evaporation and condensation (Kingery et al., 1976). Initially, necking occurs between particles, which causes the formation of pores, as illustrated in Figure 5.1 for the coalition of four spheres. Pores limit the growth of grains; hence, in the early stages of sintering, the main change that occurs is *densification*. Below a relative density of around 65%, the particles are still distinguishable (Julien and Pino, 2014). Above this, necks thicken considerably and *grain boundaries* form between particles. The pores are still connected, termed "open" porosity, but shrink as the relative density increases. By a relative density of around 92% (Julien and Pino, 2014), the pores have become isolated, or "closed" and only the solid is continuous, made of grains and grain boundaries. Pores can be present either between grains, termed inter-granular, or inside grains, termed intra-granular.

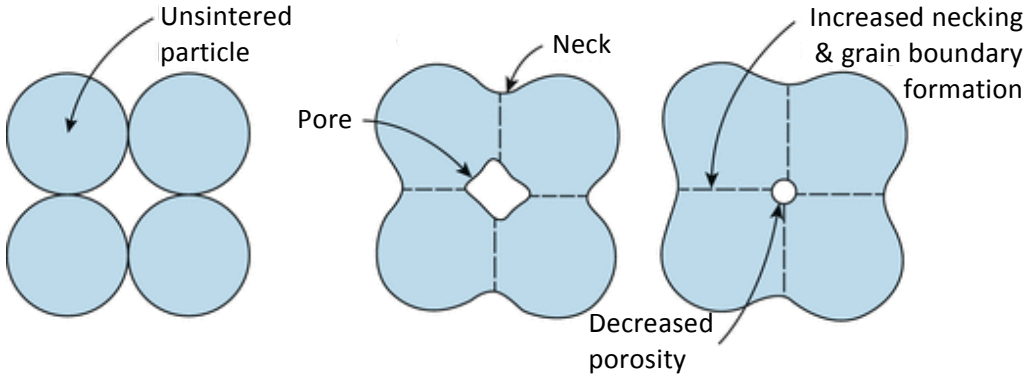

Figure 5.1: Initial stages of sintering: a) unsintered particles, b) the formation of necks and pores, and c) densification due to decreased porosity (Gibson et al., 2015).

Once densification is achieved, *grain growth* becomes the dominant mechanism. The driving force is the difference in free energy, ΔG, on each side of a grain boundary (Carter and Norton, 2007). This causes grains with a large number of connecting grains to grow and grains with a small number of connecting grains to shrink. Each grain is effectively a single crystal, separated from other crystals by the grain boundaries, which are associated with mechanical imperfections such as dislocations and with impurities. They are generally electrically blocking regions and exhibit low conductivity.

Control of sintering conditions, such as the temperature and the duration of firing, enables ceramics with different microstructures to be obtained (Kingery et al., 1976). For YSZ ceramics, the relative density was found to increase until a sintering temperature of around 1300-1350 ^{o}C (Steil et al., 1997, Chen et al., 2002) and, beyond this, a further increase in temperature caused a marked increase in grain size. Increased sintering duration also gave increased relative density and grain size, although with decreasing returns; a change in temperature had more of an effect (Chen et al., 2002). In addition, the microstructure of YSZ is influenced by the particle size and chemical composition of the starting powder. The rate of sintering is roughly

inversely proportional to the initial particle size (Kingery et al., 1976). Also, powders with high impurity content commonly form ceramics with a large concentration of impurities at the grain boundaries (Ciacchi et al., 1994).

5.1.2 ELECTRICAL PROPERTIES OF YSZ CERAMICS

The electrical properties of YSZ ceramics are influenced by sample microstructure and can hence can be varied using different sintering conditions. Immittance data from YSZ ceramics contain responses from the bulk and grain boundary components, each represented as an arc in a Z* plot (see Section 4.3), from which the permittivity, conductivity and its corresponding activation energy E_{act} can be estimated. There is also an additional component in Z* due to the electrode. Values found in literature for the bulk properties of 8 mol% YSZ ($E_{act,b}$, conductivity and permittivity) were quoted in Tables 4.1 and 4.4 and were discussed in Sections 4.4.2 and 4.4.4. In summary, the bulk conductivity increases with increasing temperature (in the densification region only (Chen et al., 2002)) but $E_{act,b}$ is not affected. The accuracy of the bulk permittivity data was insufficient to determine any trends at elevated measuring temperatures, as inappropriate equivalent circuits were used to extract ε_r, see Chapter 4. However, at room temperature, Steil et al. (1997) found ε_r to increase from a value of 12 for a sample with a relative density of 54% to a value of 31 at 97%.

Values reported in literature for the grain boundary conductivity activation energy, $E_{act,gb}$ are listed in Table 5.1, and range between 0.99 – 1.22 eV. This is a similar magnitude to the bulk activation energy (1.00-1.11 eV, see Table 4.1) but with a larger spread. It is dependent on the starting powder used (Ciacchi et al., 1994) and on the firing conditions (Steil et al., 1997, Hernández and West, 2016). The grain boundary conductivity values σ_{gb} are also listed in Table 5.1 for 300 ^{o}C and vary with both ceramic density and average grain size, peaking at the maximum density achieved (Chen et al., 2002). In addition, σ_{gb} increases with a decrease in impurity concentration (Ciacchi et al., 1994). Note that it is common practice to present conductivity as *apparent* values relative to the sample thickness *t*, rather than to the thickness of the bulk or grain boundary, d_b and d_{gb}, respectively. When the thickness of the grain boundaries is negligible compared to the bulk, the apparent and absolute bulk conductivities are equivalent. However, this is not the case for the grain boundary, where the difference in geometry gives an absolute conductivity several orders of magnitude larger than the relative value.

The influence of porosity on IS data is shown by comparing samples sintered at different temperatures. In the work of Steil et al. (1997), all samples showed two arcs on a Z* plot, see Figure 5.2. However, porous samples behaved differently from dense samples. Note that data for a 1300 ^{o}C sample is shown on both plots for comparison. For the porous samples, the high frequency bulk arc decreases in

magnitude as the sintering temperature increases. It becomes more distinct from the low frequency arc, the latter arc being attributed to geometrical differences due to necking/pores, as discussed in Section 5.1.4 below. In contrast, for the dense samples in the lower figure, the low frequency arc represents fully formed grain boundaries and is notably distinct from the bulk arc, which is invariable with sintering temperature in this regime.

In the following sub-sections, a few methods are discussed, which model the influence of geometry and microstructure on the electrical response of ceramics. This includes the Brickwork Layer Model (BLM), the modelling of necking and the effective medium theory.

Table 5.1: Grain boundary conductivity activation energy and the relative grain boundary conductivity of 8 mol% YSZ ceramic, from literature.

Reference	$\mathbf{E_{act,gb}}$ **(eV)**	$\boldsymbol{\sigma_{gb}}$ **(S/cm)**	**Sintering T, duration, heating/cooling rate**
Abelard and Baumard (1995)	1.16 ±0.04	5×10^{-6}	1500 °C, 4h
Ciacchi et al. (1994)	1.10 – 1.21 ±0.1	4×10^{-6} – 3×10^{-5}	1500 °C, 4h, 5 °C/min (five different starting powders)
Hernández and West (2016)	1.09 – 1.15	1×10^{-6} – 3×10^{-5}	1350 – 1600 °C, 2h, 5 °C/min
Steil et al. (1997)	1.01 0.99	1×10^{-6} 6×10^{-7}	1100 °C, 2h, 2 °C/min 1500 °C, 2h, 2 °C/min
Zhang et al. (2009)	1.22	2×10^{-5}	1400 °C, 5h

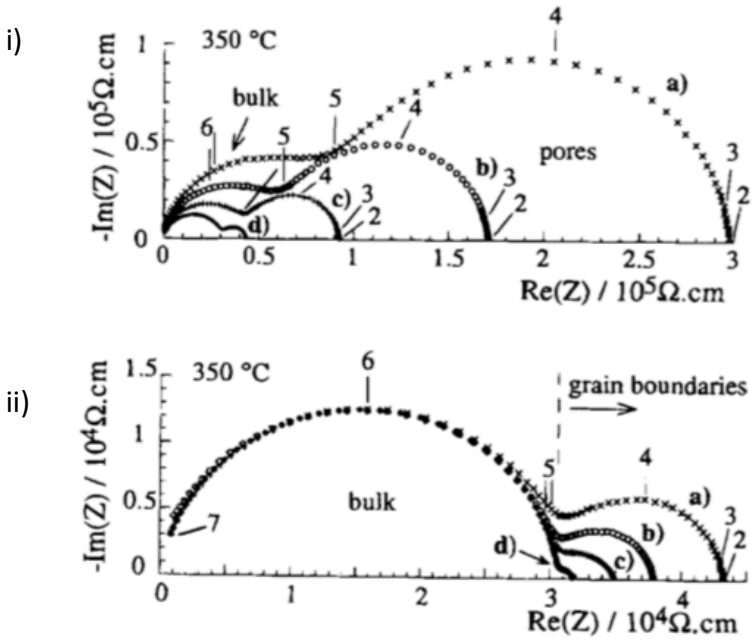

Figure 5.2: Z* plots of 8YSZ ceramics. i) Porous samples at the following sintering temperatures and corresponding porosities in brackets: a) 1150 (33%), b) 1185 (23%), c) 1220 (10%) and d) 1300 °C (3%). ii) dense samples at the following sintering temperatures: a) 1300, b) 1350, c) 1400 and d) 1650 °C.

5.1.3 BRICKWORK LAYER MODEL

In the Brickwork Layer Model (BLM) (Verkerk et al., 1982), grains are represented as regular, cubic bricks, joined together by mortar, signifying grain boundaries (see Fig. 5.3a). d_b and d_{gb} are used to represent the length of the grain and the grain boundary thickness, respectively. The grains and grain boundaries are both assumed to be homogeneous. The resulting equivalent circuit is two *RC* elements in series (or three if the electrodes are included), which represent separate bulk and grain boundary elements, denoted by subscripts *b* and *gb*, respectively. The grain length d_b (see Fig. 5.3a) can be estimated as the average grain size from SEM, and the grain boundary thickness d_{gb} is determined as follows (Irvine et al., 1990, Guo and Maier, 2001).

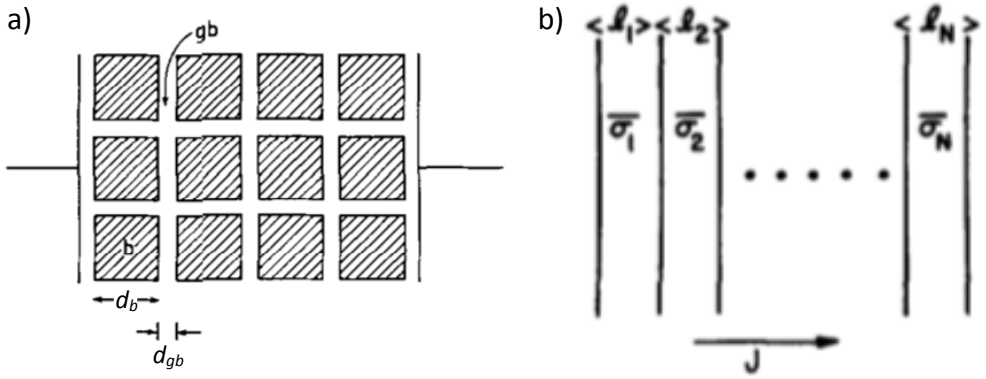

Figure 5.3: Schematics of systems used to describe the electrical behaviour of ceramics: a) Brickwork layer model (Irvine et al., 1990), b) 1D layer model (Brailsford and Hohnke, 1983).

The absolute bulk and grain boundary capacitances, C_b and C_{gb} are given by:

$$C_b = \varepsilon_0 \varepsilon_{r,b} \frac{A}{n d_b} \quad [5.1]$$

$$C_{gb} = \varepsilon_0 \varepsilon_{r,gb} \frac{A}{n d_{gb}} \quad [5.2]$$

where *A* is the surface area of the sample normal to the direction of the current measurement, n is the number of grains/grain boundaries crossed in the direction of the current measurement, ε_0 is the electric permittivity of free space and ε_r is the relative permittivity.

Assuming ε_r for both the bulk and the grain boundary is equal, which is considered viable as ε_r normally varies negligibly with concentration (Guo and Maier, 2001), then rearranging equation [5.1] in terms of $\varepsilon_0 \varepsilon_r$ gives:

$$\varepsilon_0 \varepsilon_r = C_b \frac{n d_b}{A} \quad [5.3]$$

Equation [5.2] can be written in terms of the grain boundary thickness:

$$d_{gb} = \varepsilon_0 \varepsilon_r \frac{A}{nC_{gb}} \quad [5.4]$$

Substituting for $\varepsilon_0 \varepsilon_r$ using equation [5.3] gives:

$$d_{gb} = d_b \frac{C_b}{C_{gb}} \quad [5.5]$$

Hence, the ratio of the thicknesses is related to the ratio of the capacitances.

In practice, YSZ ceramics do not have a uniform, cubic microstructure. To investigate the sensitivity of the impedance response to microstructure, Fleig and Maier (1998) used a Finite Element Method (FEM). They found that alternative grain shapes could either enhance or reduce the grain boundary conductivity. This is due to the presence of current detours, avoiding certain unfavourable boundary orientations, and due to differences in the true and perceived grain boundary lengths. These effects tend to cancel each other out and the deviations from the BLM are generally small. They found C_{gb}, and hence d_{gb}, to be accurate within a factor of 2, and concluded that the BLM gives a reasonable approximation for samples with isotropic conductivity and distribution of grain orientations, a relatively narrow, spatially uniform distribution of grain sizes, and uniform grain boundary properties, for dense samples. The BLM does not take porosity into account.

Electrically, the BLM is equivalent to a 1D simple layer system (Figure 5.3b), where each phase is represented as a slab in series (Bauerle, 1969). The length (or volume) fraction of each slab determines the overall impedance. This is appropriate for a bulk/grain boundary system but breaks down if localised porosity is represented in this way. A layer of air, which has a near-zero conductivity, would act to block conductivity through the sample and give a negligible total value, which is unrealistic (Brailsford and Hohnke, 1983). While the pores are blocking in nature, they are localised so there are current pathways *around* them.

5.1.4 Representation of necking

Porosity is a significant feature in poorly sintered samples that exhibit “necking”. These samples can be characterised electrically by two parallel *RC* elements connected in series (Bruce and West, 1983). One, R_1C_1, represents the intrinsic bulk effect, while the other, R_2C_2, represents the extrinsic effect of constriction and is dependent on the geometry of the neck (Fleig and Maier, 1997). A schematic is shown in Figure 5.4, where R_1 and R_2 are the resistances of the grain and constriction region, respectively, and C_1, C_c and C_a are the capacitances of the grain, the constriction region and the air gap, respectively. The equivalent circuit parameter, C_2, is the sum of C_c and C_a. The additional capacitance results in a lower characteristic frequency for the constriction than the grain, hence the presence of two elements in

the equivalent circuit. The conductivity of the grain and the neck are identical so the activation energy for both sections is the same.

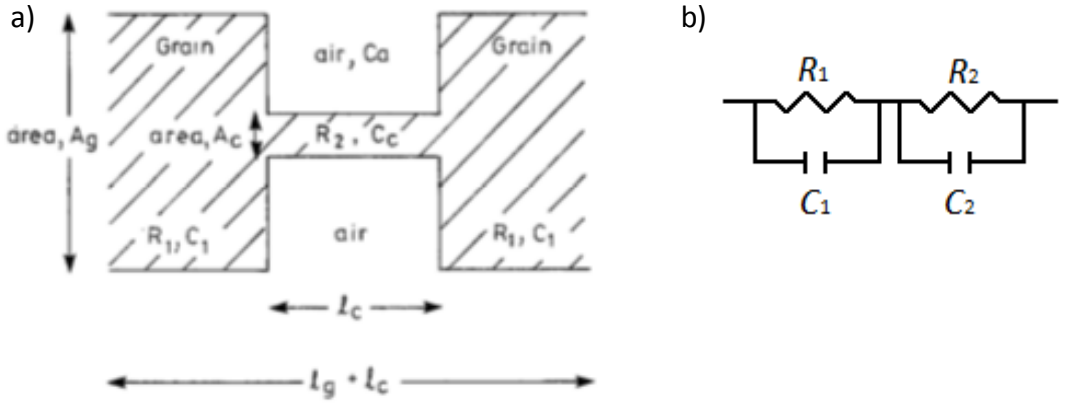

Figure 5.4: a) Schematic showing constriction, or "necking" occurring in a porous sample. b) The corresponding equivalent circuit. R_1 and R_2 represent the resistance of the grain and constriction region, respectively. C_1, C_c and C_a represent the capacitance of the grain, the constriction and the air gap, respectively. C_2 is the summation of C_a and C_c (Bruce and West, 1983).

5.1.5 EFFECTIVE MEDIUM THEORY

Another approach to model the impedance of a ceramic makes use of an effective medium originally devised by Maxwell. This is a random arrangement of spheres of one conductivity, coated in a shell of another conductivity, in a continuous medium, see Figure 5.5a (Brailsford and Hohnke, 1983). The properties of the medium are defined as the properties of the two layers combined. It is possible to include porosity in this model by altering the properties of some of the sphere cores. For inter-granular porosity, they can be replaced with pore properties and for intra-granular porosity, the properties can be set as composite values of the bulk and pores combined (Brailsford and Hohnke, 1983). This method does not result in an equivalent circuit element for porosity but it instead implies that equivalent circuit parameters obtained will be composite values that are a combination of the dense material and the insulating pore properties.

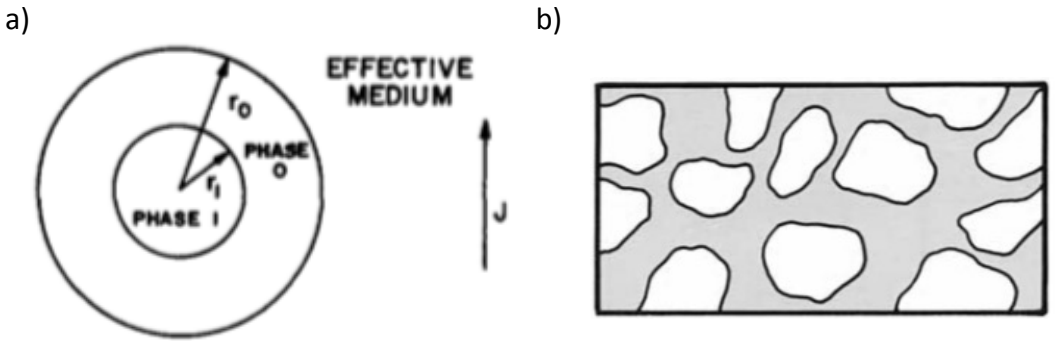

Figure 5.5: a) Maxwell's effective medium model (Brailsford and Hohnke, 1983), and b) an insulating phase (white) completely coated by a conducting phase (grey), for which Bruggeman's asymmetric medium equation is considered valid (McLachlan et al., 1990).

From Maxwell's theory, the conductivity of the effective medium, σ_m is:

$$\sigma_m(p) = \sigma_{dense}\left(1 - \frac{3}{2}p\right) \quad [5.6]$$

where p is the volume fraction of the pores and σ_{dense} is the conductivity of the material at a relative density of 100%. This equation is valid for porosity under about 10% (McLachlan et al., 1990). Alternatively, an insulating phase completely coated by a conducting phase (see Figure 5.5b) can be modelled by Bruggeman's asymmetric medium equation (McLachlan et al., 1990):

$$\sigma_m(p) = \sigma_{dense}(1-p)^{3/2} \quad [5.7]$$

This is used by Perry et al. (2011) to correct conductivities for materials with porosities between 10% and 14%. Above 14%, open porosity dominates and can no longer be modelled in this way. Note that Equation [5.6] is a first order binomial approximation of Equation [5.7]; hence the latter equation is also valid below 10 %.

Once σ_{dense} is obtained, the permittivity of the dense material ε_{dense} can be calculated from the characteristic frequency as the corresponding time constant τ remains the same (Perry et al., 2011):

$$\tau = R_{dense}C_{dense} = R_mC_m \quad [5.8]$$

where R_m and C_m are the resistance and capacitance of the effective medium, respectively, and R_{dense} and C_{dense} are the resistance and capacitance of the dense material. Hence,

$$\frac{C_{dense}}{C_m} = \frac{R_m}{R_{dense}} \quad [5.9]$$

As permittivity is proportional to capacitance *C* and conductivity is inversely proportional to the resistance *R*, this equation is equivalent to:

$$\frac{\varepsilon_{dense}}{\varepsilon_m} = \frac{\sigma_{dense}}{\sigma_m} \quad [5.10]$$

Therefore, the permittivity of the dense material is higher than that of the composite medium ε_m, with the same proportionality as the corresponding conductivity values.

5.1.6 Aim and Objectives

The aim of this chapter is to determine the effect of porosity on the microstructure and electrical properties of polycrystalline YSZ and to separate the grain boundary response from the bulk response. To achieve this, the following objectives are defined:

- Obtain samples sintered at a range of temperatures, to give a range of sample porosities
- Determine sample porosity and grain sizes
- Undertake impedance spectroscopy at a range of temperatures for each sample and use the results to fit equivalent circuits with separate bulk and grain boundary elements
- Analyse results to determine the effect of porosity on equivalent circuit components.

5.2 EXPERIMENTAL METHODS

5.2.1 PELLET PREPARATION

YSZ powder (TZ-8YS, Tosoh) was pellet-pressed and sintered for two hours at a range of temperatures between 1275 and 1500 ^{o}C to achieve varying porosity and microstructure. Four pellets (with a thickness of approximately 2 mm and a diameter of 8 mm) were produced per sintering temperature; one was used for Impedance Spectroscopy (IS) and one for Scanning Electron Microscopy (SEM). The mass of each pellet was determined using a mass balance (Precisa 923M-202A, with 0.1 mg resolution) and the thickness and diameter were determined using callipers (Mitutoyo Absolute AOS Digimatic with 0.01 mm resolution). The density of each pellet was calculated from the mass and geometry of the pellet and the theoretical density of YSZ (5.9 g/cm^3) was used to find the relative density.

Platinum electrodes were painted onto the surface of the IS pellets and fired at 900 ^{o}C for two hours, to provide electrical contacts. The electrical effects of the electrode were visible at frequencies sufficiently low to justify the use of platinum. The SEM pellets were thermally etched, to make the grain boundaries visible during microscopy. For thermal etching, samples were first polished using progressively finer sandpaper (400, 800, 1200), followed by 6 μm and 3 μm diamond pastes. They were then placed in a furnace 100 ^{o}C lower than the original sintering temperature. The furnace temperature was ramped at a rate of 5^{o}C/minute and held at temperature for one hour. After thermal etching, the SEM samples were sputter-coated (Agar B7340) with gold, using a current of 40 A under an argon atmosphere at 0.04 mbar for 30 s, which corresponded to an approximate deposition of 40 nm.

5.2.2 SCANNING ELECTRON MICROSCOPY

YSZ raw powder was dispersed in acetone and sonicated to break up the naturally-forming agglomerates. The mixture was then pipetted onto a glass slide, glued to a metal stub. Around 40 nm of gold was deposited on the surface, using a sputter coater (Agar B7340) and silver paste was used to create a conduction path from the gold surface to the stub.

The ceramic samples were mounted on stubs, using carbon tape, and a conduction path from the stub to the gold surface of the sample was created using silver paste. All samples were imaged using SEM (JEOL Ltd– JSM 6010LA).

To estimate the size of the grains for each sample, lines were drawn across each micrograph. The average grain size was taken to be the number of grains along the lines divided by the length of the line. Multiple lines were used for each image for increased precision.

5.2.3 IMPEDANCE SPECTROSCOPY

Impedance spectra were recorded for each sample using a frequency response analyser (Modulab XM, Solartron) for a frequency range of 1 MHz to 0.1 Hz with 10 points per decade and an ac voltage amplitude of 100 mV. The sample was positioned in an in-house-built ceramic compression jig (as described in Section 4.6), placed in an Elite furnace and connected to the frequency response analyser (Modulab XM, Solartron). Measurements were taken in the temperature range 175 to 325 ^{o}C. In this range two arcs were visible in the Z* plots. Below 175 ^{o}C, spectra were too noisy to interpret, whereas above 325 ^{o}C the high frequency arc shifts to frequencies beyond those measured.

Short circuit and open circuit measurements of the jig were recorded before and after each sample was tested. An average of the resulting jig inductance L_s and capacitance C_p, along with the measured series resistance, were used to subtract stray electrical contributions (see Section 4.7.3). Spectra were also corrected for the sample geometry (see equations [4.10 & 4.11]) and then analysed and fitted using ZView software (Johnson, 2014). Kramers-Kronig relations were used to determine the suitability of spectra for fitting and to aid in the determination (and subsequent elimination) of anomalous data points. The number of elements were determined using a cut-off value of μ equal to 0.95 (as in Section 4.7.4).

5.2.4 LCR DATA

LCR data were also taken for the 1450 ^{o}C sample using the setup described in Section 4.6, measuring from around 30 to 400 ^{o}C, at frequencies of 10^3, 10^4, 10^5, 2.5×10^5, and 10^6 Hz.

5.3 EXPERIMENTAL RESULTS

5.3.1 X-RAY-DIFFRACTION

The x-ray diffraction (XRD) pattern for the powder used to make the pellets is shown in Figure 5.6 (transmission geometry, 1.5406 Å wavelength), alongside the results from Chapter 4.[†††] The data match well. All peaks could be indexed on a face-centred cubic cell, (in this case a Fluorite structure) based on space group *Fm3m*. The peaks matched those reported in the Inorganic Crystal Structure Database (ISCD) for 8mol% YSZ (Itoh et al., 2015), indicating the powder to be phase-pure. The lattice parameter a, was calculated using equation [4.21], and matched the ICSD standard value of 5.14 Å for 8 mol% YSZ (Itoh et al., 2015).

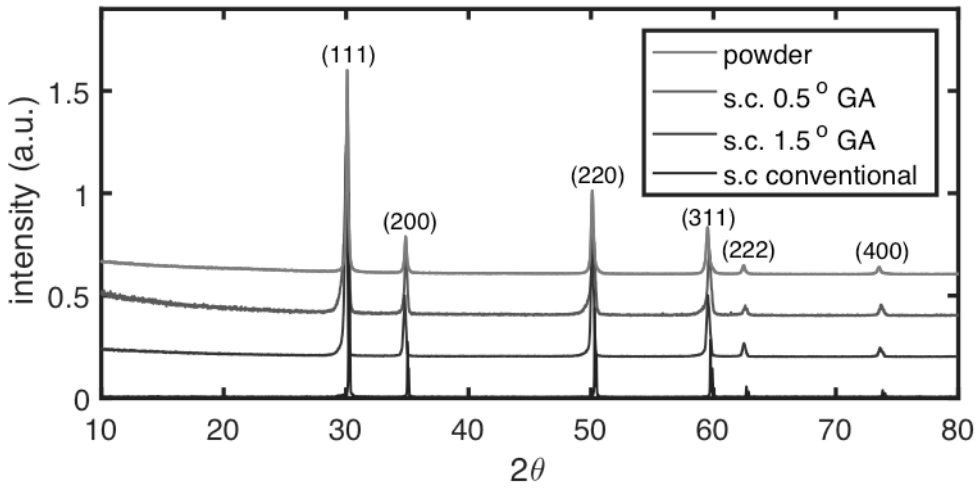

Figure 5.6: XRD powder diffraction pattern for 8mol% YSZ powder (TZ-8YS, Tosoh), in addition to those for both glancing-angle and conventional XRD for a single crystal of 8mol% YSZ.

5.3.2 SCANNING ELECTRON MICROSCOPY

SEM micrographs are shown in Figure 5.7 both for the starting powder (Fig. 5.7 a) and for samples produced at each sintering temperature (Figs 5.7b-h). The corresponding grain size and percentage density are displayed in Figure 5.8. The sample porosity is related to the percentage density:

$$\text{porosity (\%)} = 100 - \text{density (\%)} \qquad [5.11]$$

As the sintering temperature increases, grain size increases and porosity decreases.

The relative density, calculated geometrically, gives a maximum of 96% for samples sintered at 1450 °C and decreases slightly to 94% for samples sintered at 1500 °C, which indicates these latter samples have been over-sintered. The samples sintered

[†††] Powder and single crystal XRD data courtesy of Fan Yang and Richard Veazey, respectively

at 1500 °C are therefore not investigated using impedance spectroscopy as the focus of this chapter is the effect of porosity.

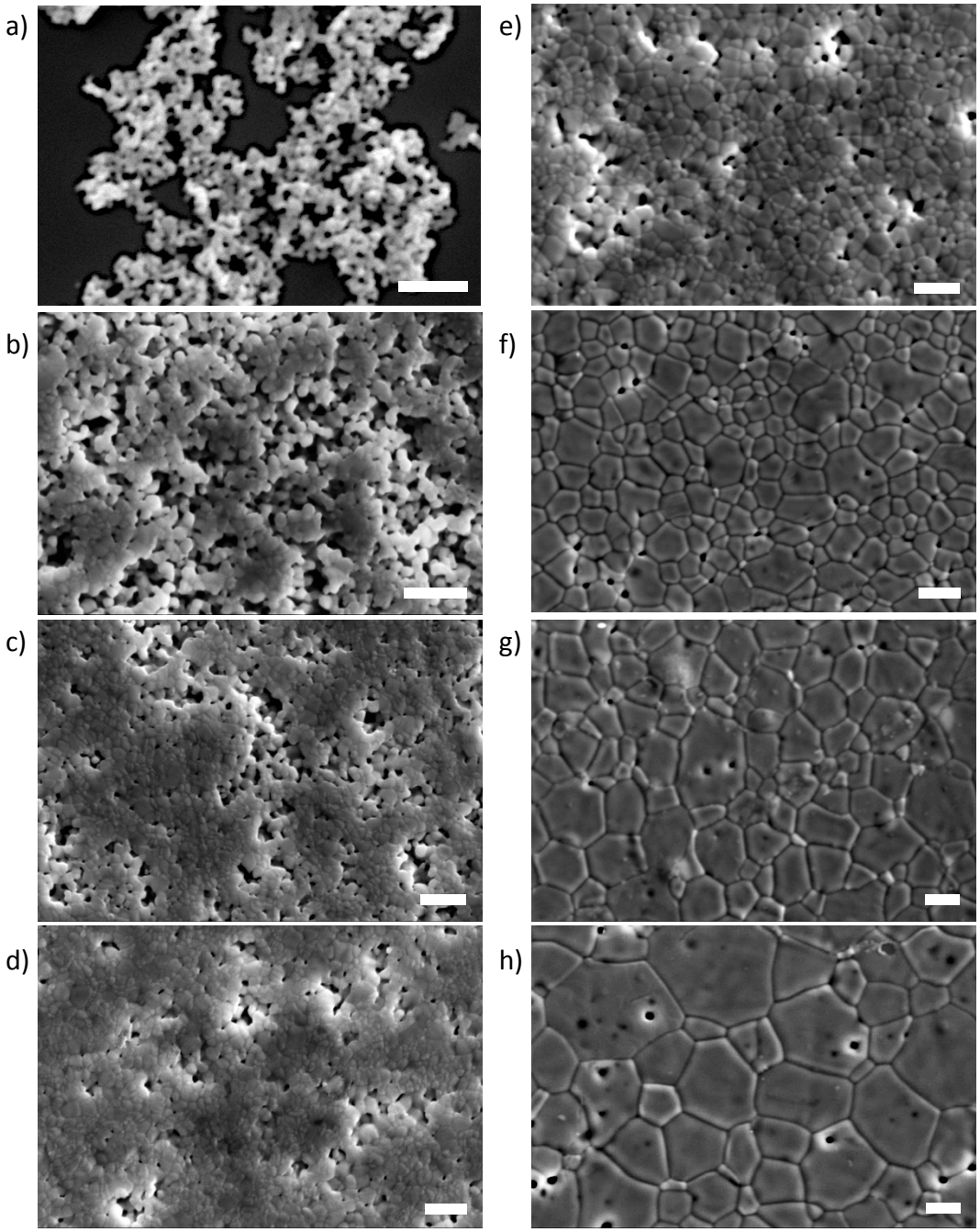

Figure 5.7: SEM micrographs for: a) YSZ starting powder, and for YSZ pellets at the following sintering temperatures: b) 1275 °C, c) 1300 °C, d) 1325 °C, e) 1350 °C, f) 1400 °C, g) 1450 °C and h) 1500 °C. (Scale bar represents 2 μm).

Samples sintered at 1275 °C (Fig. 5.7b) have a foam-like structure with open porosity, reflecting incomplete sintering; the diameters of the grains, at 0.33 μm (see Fig. 5.8), are larger than the primary particle diameter of the powder at 0.09 μm (TOSOH, 2014). Samples sintered at 1300 °C and above exhibit a more traditional grain/grain boundary structure. Between 1300 and 1350 °C, there are clusters of grains and

pores. Above this temperature pores are localised, appearing mainly at the grain boundaries for 1400 °C and in the grain for 1450 and 1500 °C.

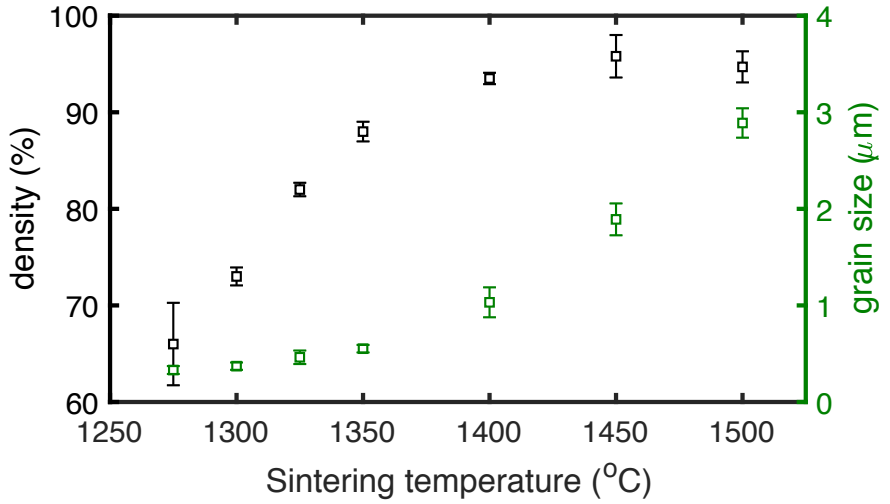

Figure 5.8: Percentage density and grain size of YSZ pellets for each sintering temperature. Error bars represent ± one standard deviation.

5.3.3 LCR DATA

LCR permittivity results for a 1450 °C ceramic are displayed in Figure 5.9 (solid lines) alongside the response of the single crystal from Chapter 4 (dotted lines), both with platinum electrodes. Any differences between the samples are hence due to the presence of grain boundaries; the effect of porosity is least likely to affect the most dense pellet. There is more hysteresis in the data for the ceramic, particularly at 10^3 and 10^4 Hz. At low temperature, the permittivity results (Figs. 5.9a,b) for the two samples are similar, with a bulk high-frequency-limiting permittivity ε'_∞ at around 30. The initial increase in ε' with temperature is also comparable; however, the subsequent flattening and point of inflection observed in the single crystal response is not present in the pellet. Instead, the rapid increase in ε' occurs at a lower temperature, implying that the high-temperature part of the bulk response is masked by the presence of the grain boundary. The temperature difference is most notable at high frequency.

The $\tan\delta$ responses for a 1450 °C ceramic and the single crystal are again comparable at low temperature and deviate with increasing temperature, at a similar point to the divergence of ε'. There is a point of inflection in $\tan\delta$ for the pellet at 270 and 340 °C for 10^3 and 10^4 Hz, respectively, whereas the single crystal response had a clear peak at these temperature and frequency points. The pellet response for 10^3 Hz is dominated by a peak at 370 °C, which shifts beyond the temperature range measured in remaining frequency responses. This response is attributed to the grain boundaries.

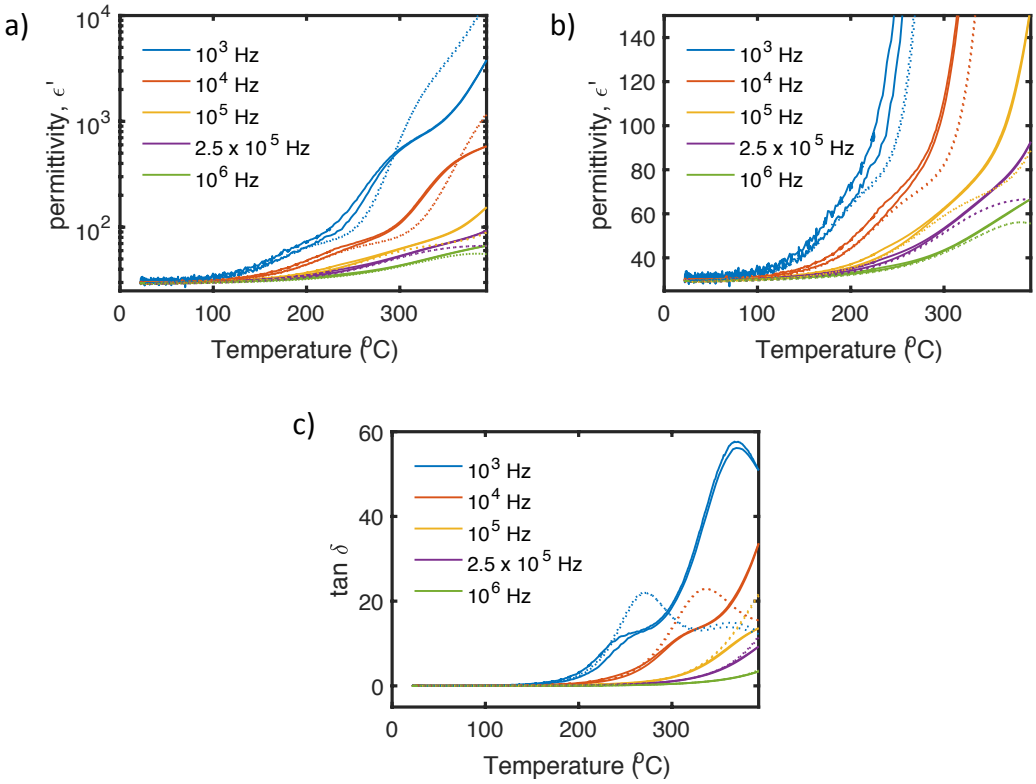

Figure 5.9: LCR results for a,b) ε' and c) $\tan\delta$ as a function of temperature, at five frequencies ranging between 10^3 and 10^6 Hz. Data are shown for a YSZ pellet sintered at 1450 °C (solid lines) and a YSZ single crystal (dotted lines), both with platinum electrodes.

5.3.4 KRAMERS-KRONIG TRANSFORMATIONS

Kramers-Kronig (KK) relations were used to determine the suitability of each data set obtained by impedance spectroscopy. Computations were carried out using the Z* formalism and the electrode spike was ignored, as discussed in Section 4.7.4. Residuals were free from systematic noise but contained varying levels of random noise. Anomalous points were deleted from the spectra. To summarise the results, chi-squared, χ^2 was calculated for both the real and imaginary residuals:

$$\chi^2_{Re} = \frac{1}{N}\sum_{i=1}^{N} \Delta_{Re,i}, \qquad \chi^2_{Im} = \frac{1}{N}\sum_{i=1}^{N} \Delta_{Im,i} \qquad [5.12, 5.13]$$

where the residuals $\Delta_{Re,i}$ and $\Delta_{Im,i}$ are defined in [2.36, 2.37]. The resulting values were then summed to obtain χ^2_{tot}:

$$\chi^2_{tot} = \chi^2_{Re} + \chi^2_{Im} \qquad [5.14]$$

χ^2_{tot} values for each pellet are plotted as a function of measuring temperature, see Figure 5.10. Salient residual plots are shown in Figure 5.11 for illustrative purposes. Figures 5.11a and 5.11b have χ^2_{tot} values of 5×10^{-5} and 2×10^{-6}, respectively, which correspond to average residual values of ±0.5% and ±0.1%, respectively. Smaller values of χ^2_{tot} correspond to smoother data with less random noise. The quality of

data improves as measuring temperature increases, see Figure 5.10, as values of Z* decrease and are more within the range of accurate measurement for the instrument.

In the remainder of the chapter, all spectra are analysed but it is recognised that the spectra at lower measuring temperatures have reduced accuracy compared with those at higher temperature.

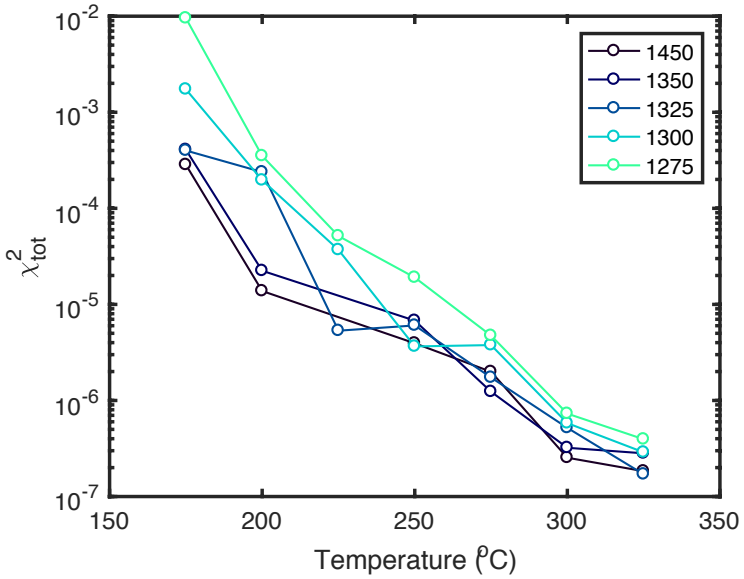

Figure 5.10: χ^2_{tot} values obtained at each measuring temperature by comparing Kramers-Kronig-transformed impedance values to the experimentally measured values. Values are plotted for each pellet, described by its sintering temperature.

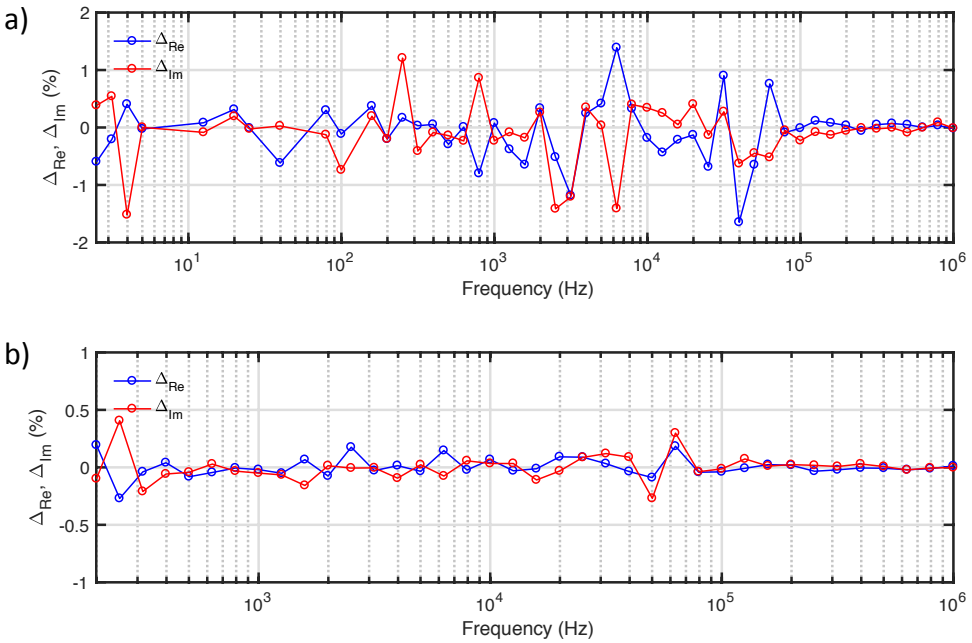

Figure 5.11: Example spectroscopic plots of Kramers-Kronig residuals for χ^2_{tot} values of: a) 5×10^{-5} and b) $\chi^2 = 2\times10^{-6}$, taken at 225 °C for a 1275 °C pellet, and at 275 °C for a 1450 °C pellet, respectively.

5.3.5 IMMITTANCE DATA

The thickness, *t*, and surface area, *A*, along with the resulting geometric factor (see Equation [4.11]) are shown in Table 5.2, and were used to correct immittance data for sample geometry. Example immittance data are shown in Figure 5.12. Figure 5.12a shows the spectrum of Z'' at 300 ^{o}C and the corresponding Z* plots are shown in Figure 5.12b, omitting the low frequency electrode tail visible around 100 Hz and below, for the sake of clarity. Z'' spectra are also shown at 200 ^{o}C, along with the spectra of M'', ε' and Y', see Figure 5.12c-g. The sample sintered at 1400 ^{o}C is omitted; it was not possible to resolve the bulk and grain boundary responses due to an additional feature with considerable Z* magnitude, the origin of which is unknown. It could, stem from either contamination during firing, or microstructural defects such as cracks.

More of the bulk response is visible in the Z'' spectrum at 200 ^{o}C than at 300 ^{o}C, but there is less random noise at 300 ^{o}C, as discussed in Section 5.3.4. In the M'' spectra at 200 ^{o}C (Fig. 5.12d), there is a high frequency peak visible at around 7×10^{3} Hz, corresponding to the bulk response. This peak is also seen in the corresponding Z'' spectrum (Fig. 5.12c), but at a marginally lower frequency of 3×10^{3} Hz, which is usual in experimental results (Hodge et al., 1976). There is also a peak in Z'' at 20 Hz, which represents the grain boundary response. Dispersion is seen in Y' (Fig. 5.12f) at high frequency. In the bulk region, the gradient of ε' (Fig. 5.12g) increases, as frequency decreases; no point of inflection is seen.

Immittance data for the ceramics are affected by the sintering temperature. In Z* data, both arcs get less resistive as the sintering temperature increases, and the low frequency (grain boundary) arc contributes less to the overall spectra. This is highlighted in Z'' spectra, where the grain boundary peak (*i.e*. 20 Hz at 200 ^{o}C) is less prominent at higher sintering temperature. The magnitude of Y' is smaller at lower sintering temperatures as samples are more resistive. However, the gradient at high frequency is comparable for all sintering temperatures and hence the index n of the constant phase element should be similar for all samples. In M'' spectra, the peak decreases with increasing sintering temperature, hence the 1450 ^{o}C sample has the highest capacitance in the bulk region. This is mirrored in the high frequency ε' results (Fig. 5.12g), where ε', and hence the capacitance, tends to higher values with increased sintering temperature.

Table 5.2: Geometric properties of the samples prepared for IS.

T_{sinter} (^{o}C)	1275	1300	1325	1350	1400	1450
% Density	66	73	82	88	93	96
Diameter, (mm)	8.72	8.37	8.12	7.87	7.87	7.65
Thickness, (mm)	2.81	1.61	2.06	1.56	1.92	2.18
Geometric factor, (cm^{-1})	0.471	0.293	0.398	0.321	0.418	0.474

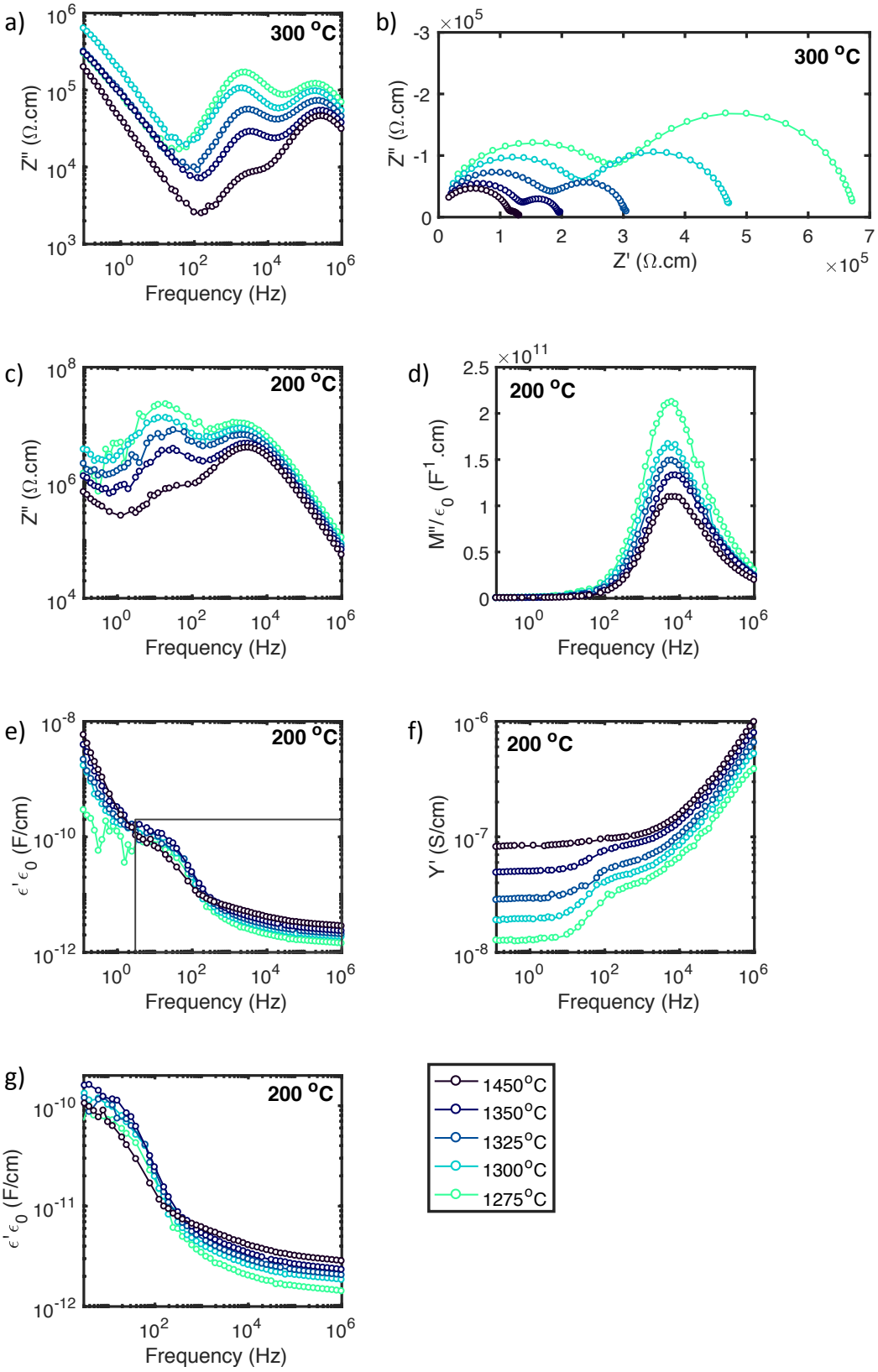

Figure 5.12: Immittance plots for samples sintered at a range of temperatures. a) Z'' spectroscopic plot at 300 °C; b) Z* plot at 300 °C, omitting low frequency data; c-f) spectroscopic plots at 200 °C for: Z'', M'', ε', and Y' respectively. g) is a close-up of (e).

5.4 EQUIVALENT CIRCUIT FITTING

In this section, data from Impedance Spectroscopy (IS) are analysed by fitting Equivalent Circuits (ECs). An *RQC* element (see Fig 4.11c) is used for the bulk response as it is able to fit both the high-frequency dispersion in Y' and the high-frequency-limiting capacitance in ε', see Section 4.3.2. There is no evidence of a low-frequency-limiting bulk capacitance in either the impedance or LCR results (Fig. 5.12 and Fig. 5.9, respectively) due to the high capacitance of the grain boundary response; therefore, an *RQCC* element (see Fig 4.11e) is inappropriate. An *RQ* element is used for the grain boundary and a constant phase element, *Q* for the electrode response.

The following notation is used (see Fig 5.13): circuit I is used to fit the bulk only, II to fit the bulk and grain boundary, and III to fit the bulk, grain boundary and electrode responses. Subscripts *f* and *x* stand for n being either free or fixed, respectively. Note that the parameter n_e associated with the electrode is always free; the notation only refers to n_b and n_{gb}.

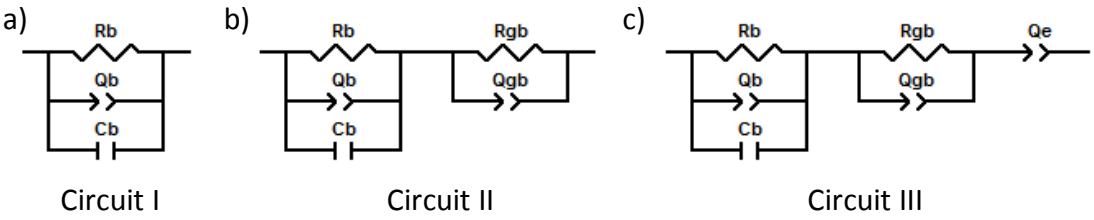

Figure 5.13: Equivalent circuit diagrams used to fit impedance data from YSZ ceramics in this chapter. a) Circuit I: bulk only, b) Circuit II: bulk and grain boundary, and c) bulk, grain boundary and electrode.

5.4.1 CHARACTERISTIC FREQUENCIES

Before fitting ECs, the characteristic frequencies f^{o} were estimated using hand-fitting, to check the consistency of the different samples. For each impedance spectrum, the frequency corresponding to the maximum Z'' value for each arc was plotted against the inverse of the temperature, see Figure 5.14. A linear dependence in log *f* is observed for all samples.

Characteristic frequencies of the *bulk* response are in agreement for all samples shown, which indicates the material in each of the samples is the same. There is also significant overlap for the *grain boundary* response for the ceramics, again implying that the material is the same and that the arc obtained comes from the same phenomenon. The grain and grain boundary values are two orders of magnitude apart and are therefore more likely to influence each other during EC fitting compared to how the charge transfer response affected the bulk response for the single crystal, which were 3 orders of magnitude apart, see Chapter 4.

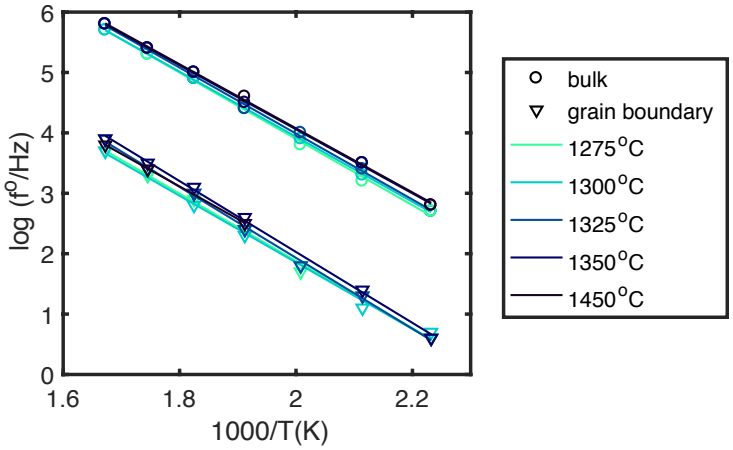

Figure 5.14: Characteristic frequencies obtained from hand-fitting of YSZ IS data, corresponding to the bulk and grain boundary components for the various ceramics. Lines of best fit are also shown.

5.4.2 Determination of n

To determine what value to use for the CPE index parameter n, initial fitting was carried out where all parameters were allowed to vary. The resulting values of n are shown in Figure 5.15 for circuits $\mathrm{I_f}$, $\mathrm{II_f}$ and $\mathrm{III_f}$. It was not possible to apply all fittings to the data at 175 °C as the electrode tail was often beyond the frequency range measured. Also, the data associated with the grain boundary arc were too noisy to fit for some samples at this temperature.

In general, the bulk parameter n_b is relatively stable at low temperature but deviates at high temperature. For the bulk-only fit, $\mathrm{I_f}$, as the operating temperature increases, n_b diverges; it increases with temperature for the highest density pellet but decreases for the remaining pellets. In the two other fittings, $\mathrm{II_f}$ and $\mathrm{III_f}$, the trend for each sample is more similar, with a general increase in n_b for an increase in measuring temperature, seen for all samples. The value of n_b at low temperature is around 0.6, for these fittings, whereas the values have a wider spread for $\mathrm{I_f}$, with values between 0.5 and 0.6.

The difference between $\mathrm{I_f}$ and $\mathrm{II_f}$ results indicates that the grain boundary response influences not only intermediate frequency but also high frequency data. IS data for samples prepared from lower sintering temperatures are increasingly affected by the grain boundary response, due to it being more pronounced, for example as illustrated in Z*, see Figure 5.12b. It is therefore important to include the grain boundary arc in the EC for polycrystalline YSZ.

In contrast, the electrode response has little effect on the bulk n_b parameter, seen by the similarity of the values of $\mathrm{II_f}$ and $\mathrm{III_f}$. There is also minimal effect on the grain boundary parameter n_gb values, see Figure 5.16. Points lie mainly between 0.9 and 1, with increased ideality at higher sintering temperatures.

The average of the values of n_b and n_{gb} at 175 and 200 °C was calculated for each sample, where applicable, and is displayed in Figure 5.17. These values were used for the fixed fittings: I_x, II_x and III_x.

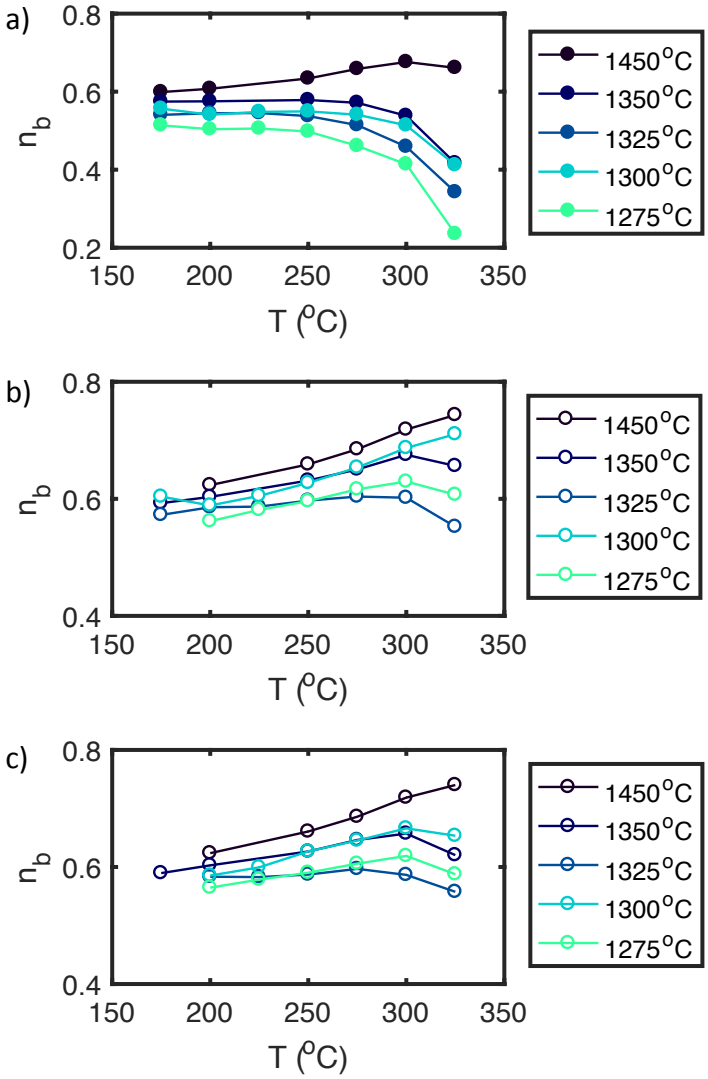

Figure 5.15: The bulk CPE parameter n_b as a function of temperature for each sample, for the following circuits: a) I_f, b) II_f and c) III_f.

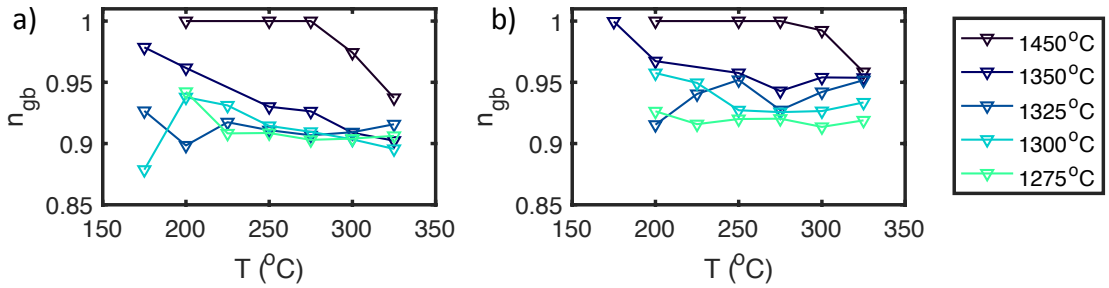

Figure 5.16: The grain boundary CPE parameter n_{gb} as a function of temperature for each sample, for the following circuits: a) II_f and b) III_f.

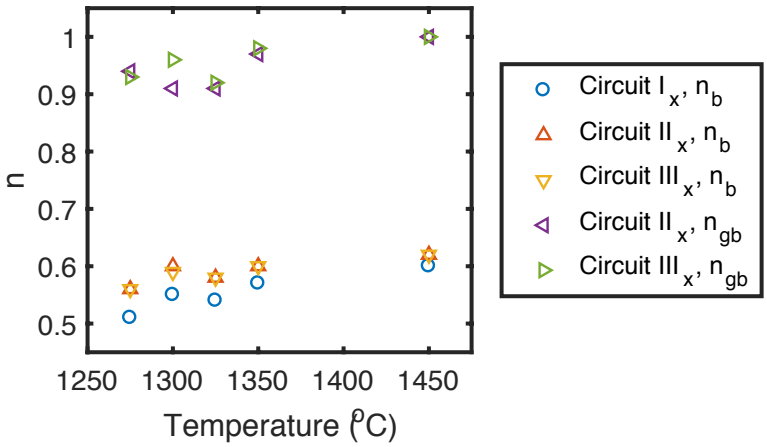

Figure 5.17: The value that n is fixed at for I_x, II_x and III_x, taken from the low temperature (175 to 200 °C) average value of n for each sample for fittings I_f, II_f and III_f. n_b and n_{gb} represent the bulk and grain boundary parameters, respectively.

5.4.3 Comparison of Experimental and Fitting Data

Experimental results for the 1325 °C sample measured at 250 °C are shown in Figure 5.18, as both spectroscopic plots, containing both real and imaginary parts, and as a Z* plot, alongside the fittings from circuits I_x, II_x and III_x. As well as the overall fittings, the individual bulk and grain boundary elements are shown separately in Z* (Fig. 5.18e), and, for I_x, the bulk response is extended to lower frequency. These are all marked with a dashed line (Figure 5.18e).

A good fit is observed in all formalisms for all three circuits. This is true of all samples analysed; therefore, an *RQC* element is sufficient to fit the bulk response. No extra components, such as C_q introduced in Section 4.3.2, are needed. There are slight deviations from the experimental data between 1 and 30 Hz in Z'' and Y'' for the III_x fitting, and for II_x at the low frequency limit of the fitting. The fit for I_x matches the experimental data well, despite grain boundary contributions not being accounted for.

In Figure 5.18e, the individual elements look very different from the combined results, indicating that the frequencies of the bulk and grain boundary responses are sufficiently close to have an influence on each other. There is a tiny difference in the grain boundary arc diameter between II_x and III_x fittings; the *RQC* element is comparable for these fittings, but has a larger resistance for I_x. It is therefore necessary to include the grain boundary arc in the fitting model to get precise resistance (and hence conductivity) values, especially at lower sintering temperatures where this arc is particularly prominent.

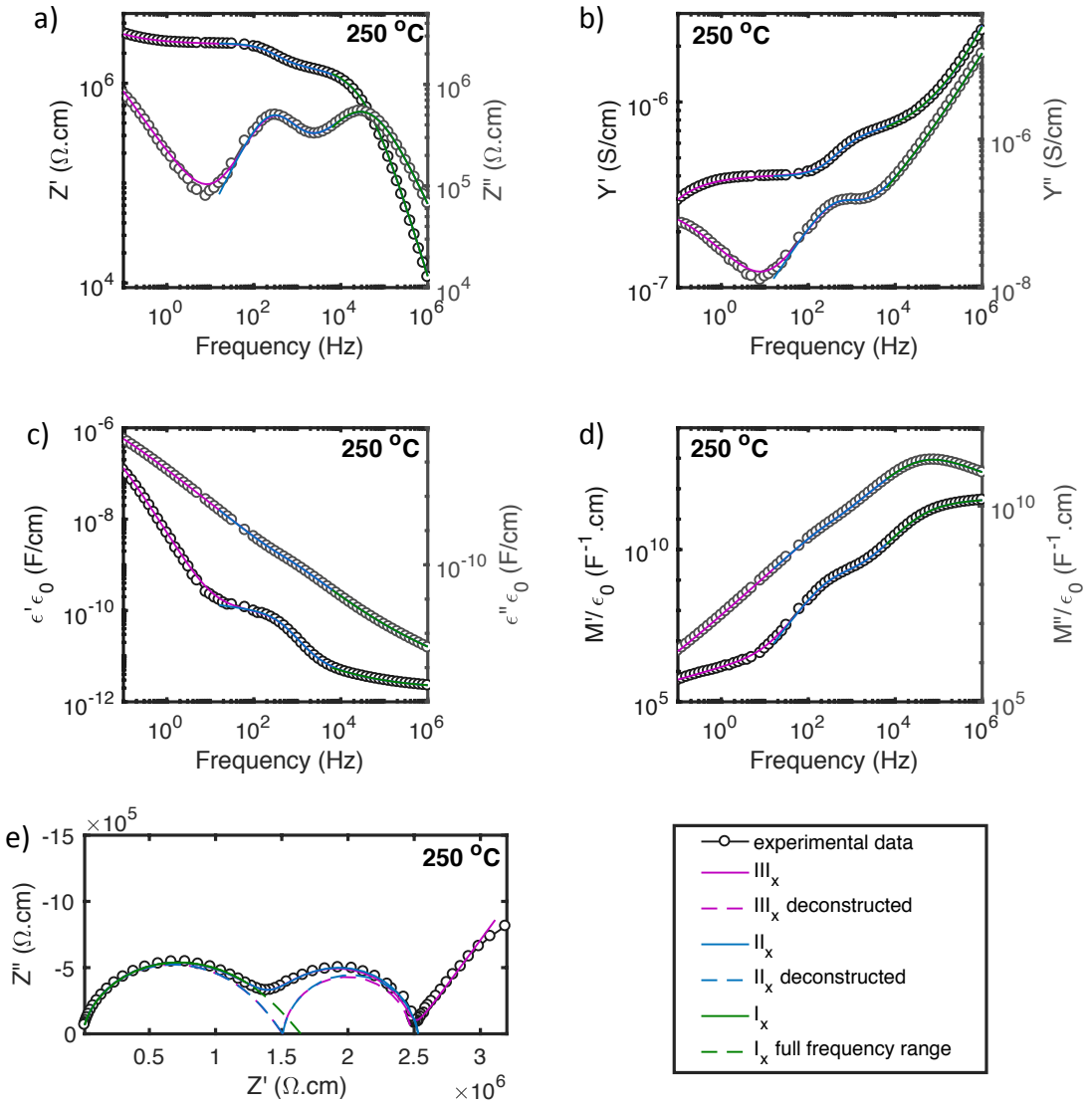

Figure 5.18: Spectroscopic graphs of a) Z*, b) Y*, c) E* and d) M* formalisms, showing EC fitting data overlaid on experimental IS data for the 1325 °C sample, measured at 250 °C; and e) the corresponding Z* plot, showing the deconstructed bulk and grain boundary contributions to the overall fit.

5.4.4 BULK FITTING-PARAMETER TRENDS

From the fitting parameters obtained, the conductivity and permittivity were calculated for each set of conditions (see equations [4.8 & 4.9]), for circuits II_x and III_x, and displayed in Figure 5.19. II_x and III_x results are represented using a solid line and a dashed line, respectively. Permittivity results, in Figure 5.19(b-d), are shown both in terms of dimensionless ε' and the geometry-corrected capacitance, with units of F/cm. The capacitance resulting from the *RQ* portion of the bulk element (see equation [4.6]) and the total bulk capacitance, given by C_{RQ} and C_1 combined in parallel, are displayed in Figure 5.19d.

For conductivity (Figure 5.19a), there is a negligible difference between the results from II_x and III_x; the results are insensitive to the EC applied. The magnitude of the conductivity at a given measuring temperature increases with increasing sintering temperature. The activation energy, calculated from the conductivity (see equations [4.13 & 4.14]) is between 1.05 and 1.06 eV for all samples.

The dependence on measuring temperature for all three extracted bulk capacitances (Figures 5.19b-d) show very similar values for circuit II_x and III_x results. The biggest difference observed was in the 1300 °C sample, particularly in $C_{RQ,b}$ (Fig. 5.19c), which is the only sample that has different bulk values of n assigned for fittings II_x and III_x (see Figure 5.17). This illustrates that n_b affects the resulting capacitance and hence there is an uncertainty that stems from the value at which n_b is fixed. For the 1300 °C sample, a change in n_b of 0.1 gave a change of around 4% in $C_{RQ,b}$. The magnitude of all three bulk capacitances increases with increasing sintering temperature. Trends with measuring temperature match those observed for the single crystal, for the same EC fitting (see Figures 4.30 and 4.33, blue lines), namely: a flat C_b with a slight rise as the bulk arc in the Z* data shifts out of the measurable frequency range, a downward turn in $C_{RQ,b}$ and a marginal decrease in C_{tot} with increased measuring temperature.

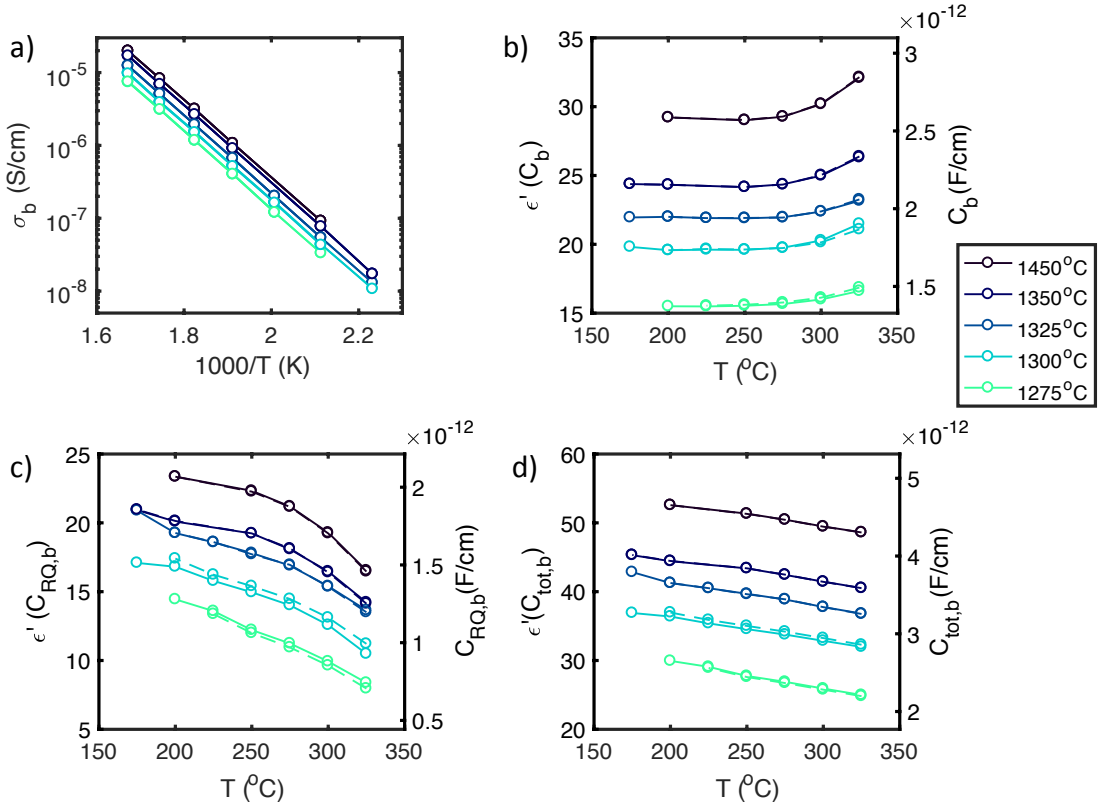

Figure 5.19: Bulk parameters, as a function of measuring temperature, extracted from equivalent circuit II_x (solid line) and III_x (dashed line) fittings, for samples sintered at different temperatures: a) conductivity (against inverse temperature, scaled by 1000), b) capacitance and relative permittivity of circuit component C_b (see Figure 5.13), c) resulting capacitance from RQ_b, and d) combined capacitance of RQ_b and C_b.

5.4.5 GRAIN BOUNDARY FITTING-PARAMETER TRENDS

The grain boundary conductivity and capacitance results for II_x and III_x are shown in Figure 5.20. They are presented as *apparent* values, based on the whole sample geometry; hence, permittivity values for the grain boundary appear significantly larger than the bulk values. In contrast, the *absolute* values of permittivity for the bulk and grain boundary are thought to be equal (Guo and Maier, 2001), see Section 5.1.3. There is a negligible difference between the fittings for II_x and III_x. As with the bulk results, for a given temperature, conductivity and permittivity values are higher for higher sintering temperature; however, the difference is more marked for the grain boundary results, with a variation approaching two orders of magnitude.

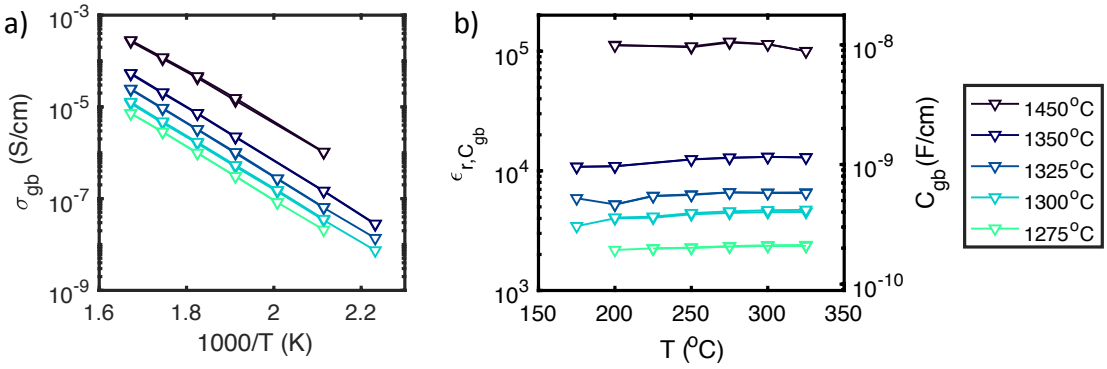

Figure 5.20: Grain boundary parameters, extracted from equivalent circuit II_x (solid line) and III_x (dashed line) fittings, for samples sintered at different temperatures: a) conductivity against inverse temperature, and b) capacitance as a function of temperature.

Activation energies, $E_{act,gb}$, were extracted from the grain boundary conductivity results and are displayed in Table 5.3. The values are marginally higher than the bulk activation energy of 1.05-1.06 eV. The difference between $E_{act,gb}$ and $E_{act,b}$ suggests that the mid-frequency feature is not merely due to constriction, see Section 5.1.4, but is a combination of both this and the more fully-formed, conventional grain boundary. The 1450 °C sample gives a value slightly lower than the remaining samples, which could be influenced by the significantly larger grain size of this dense ceramic.

Table 5.3: Grain boundary activation energies for each sample, listed by their sintering temperature, and the standard error associated with each pellet (taken for II_f, III_f, II_x and III_x) .

Sintering temperature (°C)	**1275**	**1300**	**1325**	**1350**	**1450**
$E_{act,gb}$ (eV)	1.15	1.14	1.16	1.16	1.09
Error (± eV)	0.002	0.002	0.003	0.006	0.009

5.4.6 ESTIMATE OF GRAIN BOUNDARY THICKNESS

The bulk and grain boundary capacitances extracted were used to calculate the grain boundary thickness d_{gb} for each pellet, based on the Brickwork Layer Model (BLM), see equation [5.5]. The grain size, d_b was estimated from the SEM images (see

Section 5.3.2) and the capacitances were the average values across all measured temperatures, from II_x fittings. The standard deviation was used to estimate errors for d_b and the capacitances, and the errors were combined to estimate the uncertainty in d_{gb}. Further errors could stem from the influence of porosity, which is not considered in the BLM.

Results for d_{gb} are listed in Table 5.4 and shown in Figure 5.21, plotted alongside d_b. Note that the scale of d_{gb} is about three orders of magnitude smaller than d_b. The grain boundary thickness decreases with increasing sintering temperature, in contrast to d_b which instead increases. There are insufficient data points at higher sintering temperature to determine the trend of d_{gb} in the grain-growth region. However, it is expected that the rate of decrease, which is approximately linear in the densification region (see line of best fit), reduces and flattens out. The decrease in d_{gb} matches the IS results, where the grain boundary contribution is reduced at higher sintering temperature, seen for example in the mid-frequency arc in Z*.

Table 5.4: Estimated grain boundary thickness d_{gb} for each pellet.

Pellet sintering temperature (°C)	**1275**	**1300**	**1325**	**1350**	**1450**
Grain boundary thickness (nm)	2.3	1.8	1.7	1.1	0.28
Error (±)	0.3	0.3	0.4	0.2	0.07

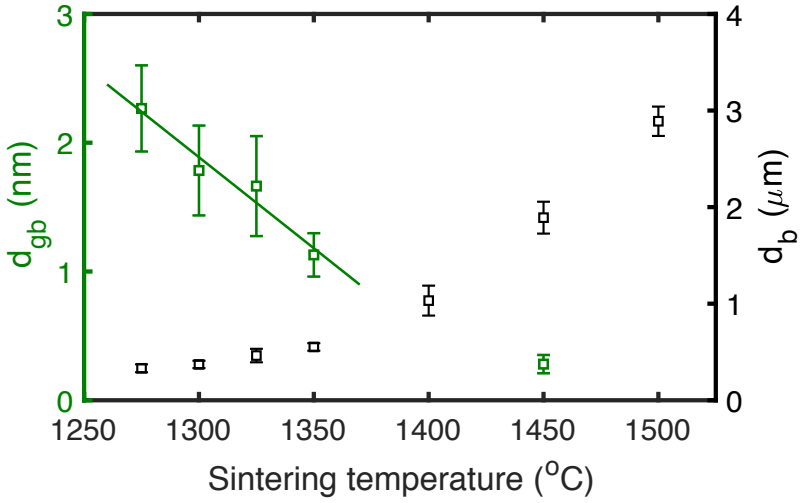

Figure 5.21: Grain and grain boundary thickness of each sample, plotted as a function of sintering temperature. The linear line of best fit is shown for d_{gb} in the densification region. Error bars are calculated from the standard deviation.

5.5 Discussion

The IS data for the ceramics differ from the results from the single crystal in a number of ways, due to the presence of pores and grain boundaries. The effect these have on the immittance data and equivalent circuit parameters are explored in turn below. Additionally, results for the bulk response for the most dense ceramic are compared with those of the single crystal.

5.5.1 Pores

There is no separate feature in the immittance data of the ceramics attributed to porosity. Instead, it is reflected in the magnitude of the data and hence also in the magnitude of the EC parameters extracted. They represent the effective values for a composite material containing both bulk YSZ and pores (air). A larger volume fraction of pores acts to lower the effective values of both the conductivity and the permittivity.

The ratio of the effective conductivity to the dense bulk conductivity for the samples investigated is shown in Figure 5.22 as a function of relative density. The dense bulk conductivity is estimated from the 1450 °C sample (96% dense), corrected using the Maxwell equation, see equation [5.6]. The Bruggeman correction (equation [5.7]) gives a very similar response. The ratios of C_b and $C_{RQ,b}$ to their corresponding theoretical fully-dense values were calculated in the same manner (see equations [5.8-5.10]). Results are an average of the ratio calculated at each temperature recorded. As the corresponding standard error bars are a similar size to the graph markers, they are not displayed, for the sake of clarity. In addition, the Maxwell and Bruggeman relationships (equations [5.6] and [5.7]) for effective media are represented as dark and light grey lines, respectively, and are considered accurate above 90% and 86% relative density, respectively.

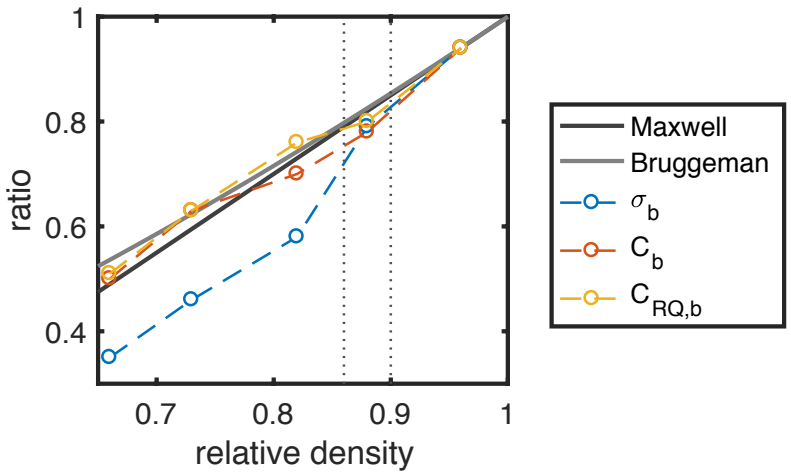

Figure 5.22: The ratio of the bulk conductivity σ_b, and capacitances C_b and $C_{RQ,b}$ to the corresponding dense value (taken as the Maxwell-corrected value for the 1450 °C pellet). The Maxwell and Bruggeman relationships (equations [5.6] and [5.7]) are also shown.

The ratios of C_b and $C_{RQ,b}$ to their dense values are comparable to the values obtained using the Maxwell and Bruggeman models across all densities investigated, despite these models only being reliable at higher densities. Note that the ratio for $C_{tot,b}$ (not shown) gives an average of the values of C_b and $C_{RQ,b}$. In contrast, the ratio of bulk conductivity σ_b deviates from the models below the density range considered accurate. The difference between the ratios of the conductivity and the capacitances implies that the time constant τ, and hence characteristic frequency f^o, is not strictly identical for all samples, as was assumed in equations [5.8] and [5.9], and is instead influenced by porosity. The jump in the ratio values between 82% and 88% relative density could be due to the resolution of the immittance data, at 10 points per frequency decade. A closer inspection of f^o (Figure 5.14) shows there is a slight decrease in magnitude with decreased sintering temperature. The extra decrease in the conductivity ratio is likely to stem from current detours through the sample due to the presence of open porosity (Fleig and Maier, 1998).

The grain boundary ratios for both the conductivity and the capacitance $C_{RQ,gb}$ relative to the "dense" case are shown in Figure 5.23. The values decrease dramatically at increased porosity. They are similar to each other at each density, indicating that the grain boundary characteristic frequency is not affected by the extent of porosity in the sample; equations [5.8] and [5.9] are hence applicable.

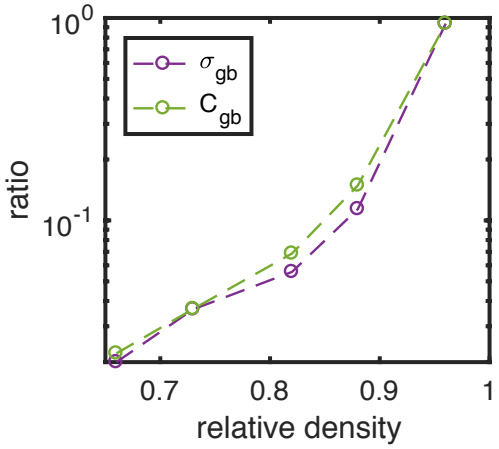

Figure 5.23: The ratio of the grain boundary conductivity, and capacitance to the corresponding dense value (taken as the Maxwell-corrected value for the 1450 °C pellet), displayed on a log scale.

5.5.2 Grain Boundary

An extra feature of the ceramics is the grain boundary response, which dominates the immittance data at mid-frequencies. If the charge transfer feature seen in the single crystal immittance data (see Section 4.7.5) is present, it is hidden by this more resistive feature.

In Z*, both the grain boundary arc and the bulk arc reduce in size as sintering of the ceramics becomes more complete (see Fig. 5.12b); however, the reduction in the grain boundary arc is more pronounced. Similarly, the increase in C_{gb} (Fig. 5.20b) with increasing sintering temperature is greater than the increase in C_b (Fig. 5.19b). This is reflected in the thickness of grain boundary (Figure 5.21), calculated from equation [5.5]. The combination of the decreasing grain boundary thickness and the increasing grain size (and hence a decreasing number of grains and grain boundaries), with increasing sintering temperature, implies that a larger proportion of the sample is bulk material.

5.5.3 Comparison of Bulk results between the single crystal and most dense ceramic sample

The bulk frequency region of the ε' spectrum is shown in Figure 5.24 for a dense ceramic (1450 ^{o}C, grey line) and a single crystal (Pt electrodes, red line), at three different temperatures. Results are comparable at high frequency; however, deviation occurs at lower frequency. The plateau partially visible in the single crystal data at low frequency is not observed in the ceramic, which is due to the onset of the grain boundary response in the frequency range of interest. In contrast, the onset of the mid-frequency charge transfer response of the singe crystal, seen as a rapid increase in ε', occurs at a lower frequency. Moreover, of all the ceramics investigated, the grain boundary response is least pronounced in the 1450 ^{o}C sample; the low frequency plateau is not visible in any of the ceramics investigated (Figure 5.12g). Consequently, it is not possible to fit the bulk data to Circuit D (Figure 4.11e) unless the parameter representing the additional low frequency capacitance C_q, is fixed at a value obtained from the single crystal fitting. Therefore, to investigate this phenomenon, it is necessary to use a single crystal, not a ceramic.

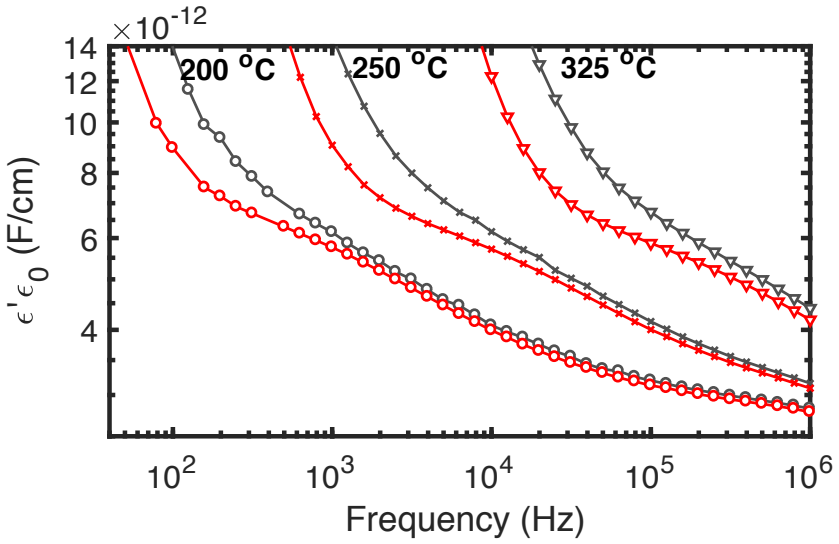

Figure 5.24: Permittivity vs frequency for both a single crystal (red) and a ceramic (sintered at 1450 ^{o}C) (grey) measured at 200, 250 and 325 ^{o}C (o, x and v symbols, respectively).

5.6 SUMMARY & CONCLUSIONS

YSZ ceramics are poly-crystals, containing grains, grain boundaries and pores. Their microstructure depends on the sintering conditions used, in particular the sintering temperature. During sintering, samples undergo densification and grain growth. There is some overlap in the two but extensive grain growth is not achieved until the sample is significantly densified. In addition to a change in porosity, the grain boundary response is also dependent on the sintering temperature, decreasing in thickness as the sintering temperature increased.

YSZ ceramics were fired at a range of temperatures, to produce samples with a range of densities, and then impedance spectra were recorded at different measuring temperatures. The grain boundary effect in IS data is most notable for ceramics sintered at lower temperatures and decreases with a decrease in sample porosity. This is reflected in the immittance results, for example in the relative magnitude of the grain boundary arc to the bulk arc in Z*, see Figure 5.12b. The grain boundary thickness d_{gb} (see Figure 5.21), calculated using the Brickwork Layer Model (see Section 5.1.3), also decreases with increasing sintering temperature, in contrast to the increasing grain size, d_b.

The low frequency bulk plateau in ε', observed for YSZ single crystals (Chapter 4), was not observed for the YSZ ceramics; hence it was not possible to fit the bulk data using circuit D (Figure 4.11e), as for the single crystal. The frequency range of interest was instead dominated by the grain boundary response, even for the most dense ceramic (sintered at 1450 ^{o}C), see Figure 5.24. The equivalent circuit chosen to fit the bulk data was circuit B (Figure 4.11c): a resistor, capacitor and constant phase element in parallel. The grain boundary was represented as an *RQ* element in series with the bulk element, and it was necessary to include this as the characteristic frequencies were close enough for the two responses to affect each other, at two orders of magnitude apart. The electrode response, however, had a negligible effect on the bulk and grain boundary fittings, and hence it is unnecessary to include this during fitting in this instance.

The effect of porosity is evident in the magnitude of both the immittance data and the corresponding equivalent circuit parameters obtained. Conductivities of both the bulk and grain boundary increased with increasing sintering temperature, as did all the capacitances measured: C_b, $C_{RQ,b}$, $C_{tot,b}$, and $C_{RQ,gb}$. The ratio of the bulk capacitances to their equivalent fully dense value approximately followed the Maxwell and Bruggeman equations for an effective medium. In contrast, the ratio of the bulk conductivity to that for a fully dense sample was significantly smaller at relative densities below 88%. This is thought to stem from current detours present due to open porosity in such samples. The characteristic frequency f^{o} therefore has a slight dependency on porosity that was previously undetected by hand-fitting.

CHAPTER 6: CONCLUSIONS AND FUTURE WORK

6.1 CONCLUSIONS

Impedance spectroscopy is a non-destructive technique that can be used to determine the magnitude of a variety of electrical polarisation mechanisms occurring in samples. These include both *intrinsic* polarisation due to the material of the sample, and *extrinsic* polarisation, for example, due to microstructure. Further polarisation mechanisms can be present, which originate from electrochemical reactions. If there are multiple mechanisms occurring in a sample, additional characterisation may be required to determine the *origin* of features seen in the resulting spectra, particularly if these processes can exhibit similar characteristic frequencies. Care must therefore be taken when interpreting impedance spectra.

Any effects from the jig should be reduced as far as practicable from the setup and any stray capacitance, resistance or inductance from the jig should be subtracted from the raw immittance data, to prevent the presence of artefacts. If left uncorrected, inaccurate values of resistance are obtained. SOC data, measured at a range of fuel concentrations, at 850 ^{o}C, were significantly affected by jig inductance, the value of which varied considerably between trials. Correction *via* the subtraction of a series inductor to the impedance response was insufficient to eliminate its effect. A resistor in parallel with this element (see Figure 6.1a) improved the correction but data above 10^5 Hz still contained artefacts and was considered unusable.

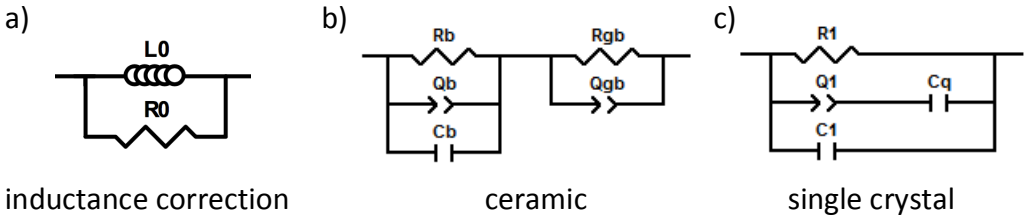

Figure 6.1: a) Equivalent circuit for inductance correction of SOC data. b&c) Equivalent circuits chosen to describe the electrical response of YSZ, for b) ceramic samples where 'b' represents the bulk and 'gb' represents the grain boundary, and c) single crystal. The electrode response is omitted.

Equivalent circuits (ECs) are a means to describe immittance data using a number of parameters, which can represent properties of the material or sample analysed. However, these are limited by the accuracy of the input circuit. If the only parameter of interest is the sample *resistance*, then the choice of equivalent circuit is less critical, and even hand-fitting is sufficient. Here, it is adequate to fit in the Z* formalism only. However, if the *capacitance* of the sample is of interest, it is imperative to view the fitting in all formalisms, as an EC that matches the response in Z* does not necessarily give a good fit in the other immittance formalisms. In addition, it is important to check the physicality of the magnitude of the high-

frequency-limiting capacitance parameter ε_r and its trend with temperature. In this work, equivalent circuits for both YSZ single crystals and ceramics were established in this way.

For solid oxide cells, equivalent circuits were not derived in this work but some examples were given from literature (see Section 2.4.3), which were presented in terms of Z* only. In light of the analysis undertaken in this thesis, it appears unlikely that these ECs would give appropriate fittings in the other immittance formalisms, as the elements used are basic and there is a large number of polarisation processes occurring. Therefore, resistances are the only parameters that should be analysed from these results.

It is necessary to use single crystals to characterise the bulk response of YSZ, as the grain boundary response present in ceramics obscures the low frequency bulk plateau in ε'. Moreover, equivalent circuits derived for YSZ ceramics are insufficient to describe the immittance response for single crystals. For the ceramics, a parallel *RQC* element was used to fit the bulk response, and a parallel *RQ* element was used to describe the grain boundary, these two elements being placed in series (see Figure 6.1b). In contrast, to fit the single crystal data, an extra capacitance C_q was added in series with the constant phase element Q_1, creating an extra arm to the ideal *RC* element (see Figure 6.1c). This could describe the local heterogeneity in the bulk response. The magnitude of C_q decreases with increasing temperature, which corresponds to a decreased distribution of relaxation times and implies the material becomes electrically more homogenous. At a sufficiently high temperature, C_q could become negligible, the effect of which is illustrated in Figure 6.2 for Y' and ε' spectra. In Y', the high frequency dispersion decreases with decreasing C_q and the response tends to that of an ideal *RC* element. Similarly, in ε', the magnitude of the low frequency plateau decreases with decreasing C_q and also tends to the response of an *RC* element.

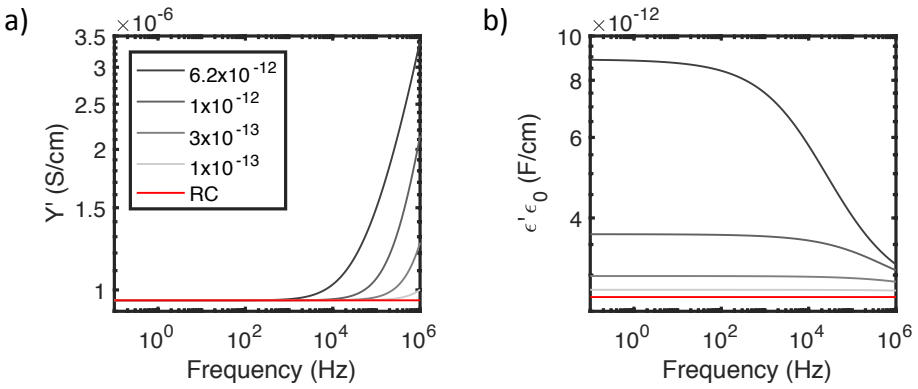

Figure 6.2: Spectra of a) Y' and b) ε' at 250 ^{o}C, showing fitting results for the bulk element using Circuit D (Figure 4.11e), changing the value of the parameter C_q from original value of 6.2×10^{-12} F/cm through a range of values to 1×10^{-13} F/cm. Spectra are also shown for the *RC* element which obtained when the Q_1-C_q arm is omitted.

6.2 RECOMMENDATIONS FOR FUTURE WORK

To investigate the nature of the bulk low-frequency plateau in ε' spectra, further experiments could include carrying out impedance spectroscopy on YSZ single crystals with a range of doping levels of yttria. The work of Hull et al. (Norberg et al., 2011, Marrocchelli et al., 2011), see Section 4.2.3, suggests that increased vacancy clustering occurs at increased dopant concentrations. According to the hypothesis proposed in this work, this would correspond to an increase in the distribution of relaxation times and would result in a larger value of C_q.

In addition, zirconia doped with different chemical species would be likely to give different magnitudes of C_q, as the size and charge of the dopant cation relative to Zr^{4+} influences the d.c. conductivity, and could also affect the a.c. conductivity. Alternatively, experiments using single crystals of different oxygen-ion conducting cubic-fluorite materials, such as gadolinia doped ceria (GDC), could be used to test hypothesis of localised vacancy clusters. The advantage of GDC is that ceria is stable in a cubic form at low temperature, whereas zirconia is not; hence it is possible to investigate lower dopant concentrations of GDC than of YSZ.

Quenching samples from high temperature can also be used to investigate the possibility of the presence of local heterogeneity within the bulk. Rapid quenching of a sample can preserve the high-entropy state at high temperature; if the vacancies were mobile, this could prevent local vacancy clusters from forming as a sample is cooled. In contrast, slow cooling allows the material to achieve a thermodynamically favourable state rather than being dominated by kinetics. A lower value of C_q for a quenched sample compared to a slow-cooled sample would strengthen the hypothesis for the presence of local vacancy clusters in YSZ being the origin of the low frequency permittivity effect observed in the IS response of single crystals.

The immittance response for different microstructures can be simulated using a Finite Element Method (FEM) based on Maxwell's equations (Dean et al., 2014). Each part of the sample is defined by a permittivity and a conductivity. The method results in current and electric potential distribution within the microstructure, for each frequency investigated, from which the IS response is calculated. FEM could be used to investigate further the effect of porosity in ceramics, looking at how the size and distribution of closed or open pores affect the current pathways in a sample. Considerable current detours are expected for samples with large amounts of open porosity. Grain boundaries could also be included in models, to investigate further the effect of thickness and the reliability of the brickwork layer model. Finally, FEM could be used to investigate the hypothesis of localised vacancy clusters by assigning local regions of the sample with a higher permittivity than that of the bulk.

REFERENCES

ABELARD, P. & BAUMARD, J. F. 1982. Study of the dc and ac electrical properties of an yttria-stabilized zirconia single crystal [$(ZrO_2)_{0.88}$-$(Y_2O_3)_{0.12}$]. *Physical Review B,* 26**,** 1005-1017.

ABELARD, P. & BAUMARD, J. F. 1995. The electrical conductivity of cubic stabilized zirconia: The results of an IUPAC collaborative study (Technical Report). *Pure and Applied Chemistry,* 67**,** 1891-1904.

ABRAM, E. J., SINCLAIR, D. C. & WEST, A. R. 2001. Electrode-Contact Spreading Resistance Phenomena in Doped-Lanthanum Gallate Ceramics. *Journal of Electroceramics,* 7**,** 179-188.

ABRAM, E. J., SINCLAIR, D. C. & WEST, A. R. 2003. A strategy for analysis and modelling of impedance spectroscopy data of electroceramics: Doped lanthanum gallate. *Journal of Electroceramics,* 10**,** 165-177.

ADLER, S. B. 2002. Reference electrode placement in thin solid electrolytes. *Journal of the Electrochemical Society,* 149**,** E166-E172.

AGARWAL, P., ORAZEM, M. E. & GARCIARUBIO, L. H. 1992. Measurement Models for Electrochemical Impedance Spectroscopy. 1. Demonstration of Applicability. *Journal of the Electrochemical Society,* 139**,** 1917-1927.

ALMOND, D. P. & WEST, A. R. 1983. Impedance and modulus spectroscopy of "real" dispersive conductors. *Solid State Ionics,* 11**,** 57-64.

ANEKE, M. & WANG, M. 2016. Energy storage technologies and real life applications – A state of the art review. *Applied Energy,* 179**,** 350-377.

BADWAL, S. P. S. 1984. Electrical conductivity of single crystal and polycrystalline yttria-stabilized zirconia. *Journal of Materials Science,* 19**,** 1767-1776.

BARBUCCI, A., VIVIANI, M., CARPANESE, P., VLADIKOVA, D. & STOYNOV, Z. 2006. Impedance analysis of oxygen reduction in SOFC composite electrodes. *Electrochimica Acta,* 51**,** 1641-1650.

BARFOD, R., MOGENSEN, M., KLEMENSO, T., HAGEN, A., LIU, Y.-L. & HENDRIKSEN, P. V. 2007. Detailed characterization of anode-supported SOFCs by impedance spectroscopy. *Journal of the Electrochemical Society,* 154**,** B371-B378.

BAUERLE, J. E. 1969. Study of solid electrolyte polarization by a complex admittance method. *Journal of Physics and Chemistry of Solids,* 30**,** 2657-2670.

BECKER, S., FREW, B. A., ANDRESEN, G. B., ZEYER, T., SCHRAMM, S., GREINER, M. & JACOBSON, M. Z. 2014. Features of a fully renewable US electricity system: Optimized mixes of wind and solar PV and transmission grid extensions. *Energy,* 72**,** 443-458.

BEIS 2017. *Clean growth strategy: executive summary*, Department for Business, Energy & Industrial Strategy. Available from: www.gov.uk/government/publications/clean-growth-strategy/clean-growth-strategy-executive-summary [Accessed Jan 2019].

BEIS 2018. *UK energy in brief 2018*, Department for Business, Energy & Industrial Strategy. Available from: https://www.gov.uk/government/statistics/uk-energy-in-brief-2018 [Accessed Jan 2019].

BLOOM ENERGY. 2019. *Better Electrons* [Online]. Available: www.bloomenergy.com [Accessed Jan 2019].

BLUM, L., MEULENBERG, W. A., NABIELEK, H. & STEINBERGER-WILCKENS, R. 2005. Worldwide SOFC Technology Overview and Benchmark. *International Journal of Applied Ceramic Technology,* 2**,** 482-492.

BODEN, T. A., MARLAND, G. & ANDRES, R. J. 2017. Global, Regional, and National Fossil-Fuel CO_2 Emissions. Carbon Dioxide Information Analysis Center, Oak Ridge National Laboratory, U.S. Department of Energy, Oak Ridge, Tenn., U.S.A. doi: 10.3334/CDIAC/00001_V2017.

BOOT-HANDFORD, M. E., ABANADES, J. C., ANTHONY, E. J., BLUNT, M. J., BRANDANI, S., MAC DOWELL, N., FERNÁNDEZ, J. R., FERRARI, M.-C., GROSS, R., HALLETT, J. P., HASZELDINE, R. S., HEPTONSTALL, P., LYNGFELT, A., MAKUCH, Z., MANGANO, E., PORTER, R. T. J., POURKASHANIAN, M., ROCHELLE, G. T., SHAH, N., YAO, J. G. & FENNELL, P. S. 2014. Carbon capture and storage update. *Energy & Environmental Science,* 7**,** 130-189.

BOUKAMP, B. A. 1986. A package for impedance admittance data-analysis. *Solid State Ionics,* 18-9**,** 136-140.

BOUKAMP, B. A. 1993. Practical Application of the Kramers-Kronig Transformation on Impedance Measurements in Solid-State Electrochemistry. *Solid State Ionics,* 62**,** 131-141.

BOUKAMP, B. A. 1995. A Linear Kronig-Kramers Transform Test for Immittance Data Validation. *Journal of the Electrochemical Society,* 142**,** 1885-1894.

BOUKAMP, B. A. 2004. Electrochemical impedance spectroscopy in solid state ionics: recent advances. *Solid State Ionics,* 169**,** 65-73.

BOUKAMP, B. A. & BOUWMEESTER, H. J. M. 2003. Interpretation of the Gerischer impedance in solid state ionics. *Solid State Ionics,* 157**,** 29-33.

BRAILSFORD, A. & HOHNKE, D. K. 1983. The electrical characterization of ceramic oxides. *Solid State Ionics,* 11**,** 133-142.

BRUCE, P., WEST, A. & ALMOND, D. 1982. A new analysis of ac conductivity data in single crystal β-alumina. *Solid State Ionics,* 7**,** 57-60.

BRUCE, P. G. & WEST, A. R. 1983. The A-C Conductivity of Polycrystalline LISICON, $Li_{2+2x}Zn_{1-x}GeO_4$, and a Model for Intergranular Constriction Resistances. *Journal of The Electrochemical Society,* 130**,** 662-669.

BUSCHEL, P., TROLTZSCH, U. & KANOUN, O. 2012. Calculation of the distribution of relaxation times for characterization of the dynamic battery behavior. 2012 9th International Multi-Conference on Systems, Signals and Devices (SSD), 20-23 March 2012. 1-3.

BUTLER, V., CATLOW, C., FENDER, B. & HARDING, J. 1983. Dopant ion radius and ionic conductivity in cerium dioxide. *Solid State Ionics,* 8**,** 109-113.

CARTER, C. B. & NORTON, M. G. 2007. Chapter 24: Sintering and Grain Growth. *Ceramic Materials.* New York: Springer-Verlag.

CERES POWER. 2016. Home power systems being trialled in UK. Available from: www.cerespower.com/news/latest-news/home-power-systems-being-trialled-in-uk [Accessed Jan 2019].

CHEN, X. J., KHOR, K. A., CHAN, S. H. & YU, L. G. 2002. Influence of microstructure on the ionic conductivity of yttria-stabilized zirconia electrolyte. *Materials Science and Engineering: A,* 335**,** 246-252.

CIACCHI, F., CRANE, K. & BADWAL, S. 1994. Evaluation of commercial zirconia powders forsolid oxide fuel cells. *Solid State Ionics,* 73**,** 49-61.

CLIMATE CHANGE ACT. 2008. *c.27* [Online]. London: HMSO. Available: www.legislation.gov.uk/ukpga/2008/27/introduction [Accessed Jan 2019].
CO2CHEM. 2014. *About CDU* [Online]. Available: http://co2chem.co.uk/background/about-cdu [Accessed Nov 2014].
DEAN, J. S., HARDING, J. H. & SINCLAIR, D. C. 2014. Simulation of Impedance Spectra for a Full Three- Dimensional Ceramic Microstructure Using a Finite Element Model. *Journal of the American Ceramic Society,* 97**,** 885-891.
DECC. 2014. *Climate change explained* [Online]. London: Department of Energy & Climate Change. Available: https://www.gov.uk/guidance/climate-change-explained [Accessed Jan 2019].
DOITPOMS. 2018. *Electrolyte* [Online]. University of Cambridge. Available: http://www.doitpoms.ac.uk/tlplib/fuel-cells/sofc_electrolyte.php [Accessed Jan 2019].
DUNN, B., KAMATH, H. & TARASCON, J. M. 2011. Electrical energy storage for the grid: a battery of choices. *Science,* 334**,** 928-35.
EBBESEN, S. D., GRAVES, C. & MOGENSEN, M. 2009. Production of synthetic fuels by co-electrolysis of steam and carbon dioxide. *International Journal of Green Energy,* 6**,** 646-660.
EBBESEN, S. D., JENSEN, S. H., HAUCH, A. & MOGENSEN, M. 2014. High temperature electrolysis in alkaline cells, solid proton conducting cells, and solid oxide cells. *Chemical Reviews,* 114**,** 10697-10734.
EBBESEN, S. D., KNIBBE, R. & MOGENSEN, M. 2012. Co-Electrolysis of Steam and Carbon Dioxide in Solid Oxide Cells. *Journal of the Electrochemical Society,* 159**,** F482-F489.
EBBESEN, S. D. & MOGENSEN, M. 2009. Electrolysis of carbon dioxide in Solid Oxide Electrolysis Cells. *Journal of Power Sources,* 193**,** 349-358.
EDWARDS, D. D., HWANG, J. H., FORD, S. J. & MASON, T. O. 1997. Experimental limitations in impedance spectroscopy: Part V. Apparatus contributions and corrections. *Solid State Ionics,* 99**,** 85-93.
ELDER, R., CUMMING, D. & MOGENSEN, M. B. 2014. Chapter 11: High Temperature Electrolysis. *In:* STYRING, P. (ed.) *Carbon dioxide utilisation: closing the carbon cycle.* Elsevier. 183-210.
EPA. 2017. *Global greenhouse gas emissions data* [Online]. United States Environmental Protection Agency. Available: http://www.epa.gov/ghgemissions/global-greenhouse-gas-emissions-data [Accessed Jan 2019].
FERGUS, J. W. 2006. Electrolytes for solid oxide fuel cells. *Journal of Power Sources,* 162**,** 30-40.
FINKLEA, H., CHEN, X., GERDES, K., PAKALAPATI, S. & CELIK, I. 2013. Analysis of SOFCs Using Reference Electrodes. *Journal of the Electrochemical Society,* 160**,** F1055-F1066.
FLEIG, J. & MAIER, J. 1997. The Influence of Laterally Inhomogeneous Contacts on the Impedance of Solid Materials: A Three-Dimensional Finite-Element Study. *Journal of Electroceramics,* 1**,** 73-89.
FLEIG, J. & MAIER, J. 1998. A Finite Element Study on the Grain Boundary Impedance of Different Microstructures. *Journal of The Electrochemical Society,* 145**,** 2081-2089.

FUEL CELL MATERIALS. 2012. *NextCell-2.0* [Online]. Available: http://www.fuelcellmaterials.com/site/sofc-components/cells-a-substrates [Accessed November 2014].
FUEL CELL MATERIALS. 2017. *NextCell versus NextCell-HP: comparing performance data* [Online]. Available: https://fuelcellmaterials.com/nextcell-versus-nextcell-hp-comparing-performance-data/ [Accessed Jan 2019].
GAMRY. 2015. *Basics of Electrochemical Impedance Spectroscopy* [Online]. Gamry Instruments. Available: http://www.gamry.com/application-notes/EIS/basics-of-electrochemical-impedance-spectroscopy/ [Accessed Oct 2014].
GIBSON, I., ROSEN, D. & STUCKER, B. 2015. Chapter 5: Powder Bed Fusion Processes. *Additive Manufacturing Technologies.* Springer, New York, NY. 107-145.
GRAVES, C., CHATZICHRISTODOULOU, C. & MOGENSEN, M. B. 2015. Kinetics of CO/CO_2 and H_2/H_2O reactions at Ni-based and ceria-based solid-oxide-cell electrodes. *Faraday Discussions*,182**,** 75-95.
GRAVES, C., EBBESEN, S. D. & MOGENSEN, M. 2011a. Co-electrolysis of CO_2 and H_2O in solid oxide cells: Performance and durability. *Solid State Ionics,* 192**,** 398-403.
GRAVES, C., EBBESEN, S. D., MOGENSEN, M. & LACKNER, K. S. 2011b. Sustainable hydrocarbon fuels by recycling CO_2 and H_2O with renewable or nuclear energy. *Renewable and Sustainable Energy Reviews,* 15**,** 1-23.
GUO, X. & DING, Y. 2004. Grain Boundary Space Charge Effect in Zirconia. *Journal of The Electrochemical Society,* 151**,** J1-J7.
GUO, X. & MAIER, J. 2001. Grain Boundary Blocking Effect in Zirconia: A Schottky Barrier Analysis. *Journal of The Electrochemical Society,* 148**,** E121-E126.
GUO, X., SIGLE, W., FLEIG, J. & MAIER, J. 2002. Role of space charge in the grain boundary blocking effect in doped zirconia. *Solid State Ionics,* 154-155**,** 555-561.
HAGEN, A., MENON, M., BARFOD, R., HENDRIKSEN, P. V., RAMOUSSE, S. & LARSEN, P. H. 2006. Properties and performance of SOFCs produced on a pre-pilot plant scale. *Fuel Cells,* 6**,** 146-150.
HALDOR TOPSOE. 2017. *Produce your own carbon monoxide* [Online]. Available: http://www.topsoe.com/processes/carbon-monoxide/site-carbon-monoxide [Accessed Jan 2019].
HARTFIELD, G., BLUNDEN, J. & ARNDT, D. S. 2018. A look at 2017: Takeaway points from the State of the Climate supplement. *Bulletin of the American Meterological Society,* 99**,** 1527-1539.
HAUCH, A. 2007. *Solid Oxide Electrolysis Cells - Performance and Durability.* PhD, Technical University of Denmark.
HAUCH, A., EBBESEN, S. D., JENSEN, S. H. & MOGENSEN, M. 2008. Solid oxide electrolysis cells: Microstructure and degradation of the Ni/yttria-stabilized zirconia electrode. *Journal of the Electrochemical Society,* 155**,** B1184-B1193.
HENDRIKS, M. G. H. M., TEN ELSHOF, J. E., BOUWMEESTER, H. J. M. & VERWEIJ, H. 2002. The electrochemical double-layer capacitance of yttria-stabilised zirconia. *Solid State Ionics,* 146**,** 211-217.
HERNÁNDEZ, M. A., MASÓ, N. & WEST, A. R. 2016. On the correct choice of equivalent circuit for fitting bulk impedance data of ionic/electronic conductors. *Applied Physics Letters,* 108**,** 152901.

HERNÁNDEZ, M. A. & WEST, A. R. 2016. Dipolar relaxation and impedance of an yttria-stabilised zirconia ceramic electrolyte. *Journal of Materials Chemistry A,* 4**,** 1298-1305.
HM GOVERNMENT. 2017. *CCUS Council* [Online]. Available: https://www.gov.uk/government/groups/ccus-council [Accessed Jan 2019].
HODGE, I. M., INGRAM, M. D. & WEST, A. R. 1976. Impedance and modulus spectroscopy of polycrystalline solid electrolytes. *Journal of Electroanalytical Chemistry and Interfacial Electrochemistry,* 74**,** 125-143.
HOHNKE, D. K. 1979. Ionic conduction in doped zirconia. *Fast ion transport in solids: electrodes and electrolytes.* North Holland: Elsevier. 669-672.
HSIEH, G., MASON, T. O., GARBOCZI, E. J. & PEDERSON, L. R. 1997. Experimental limitations in impedance spectroscopy: Part III. Effect of reference electrode geometry/position. *Solid State Ionics,* 96**,** 153-172.
HSU, C. H. & MANSFELD, F. 2001. Concerning the Conversion of the Constant Phase Element Parameter Y_0 into a Capacitance. *Corrosion,* 57**,** 747-748.
HUANG, Q.-A., HUI, R., WANG, B. & ZHANG, H. 2007. A review of AC impedance modeling and validation in SOFC diagnosis. *Electrochimica Acta,* 52**,** 8144-8164.
HUGHES, G. A., YAKAL-KREMSKI, K. & BARNETT, S. A. 2013. Life testing of LSM-YSZ composite electrodes under reversing-current operation. *Physical Chemistry Chemical Physics,* 15**,** 17257-62.
HUGHES, G. A., YAKAL-KREMSKI, K., CALL, A. V. & BARNETT, S. A. 2012. Durability Testing of Solid Oxide Cell Electrodes with Current Switching. *Journal of the Electrochemical Society,* 159**,** F858-F863.
HYDROGEN EUROPE. 2018. *Project ComSos* [Online]. Available: https://hydrogeneurope.eu/index.php/project/comsos [Accessed Jan 2019].
ICHEME ENERGY CENTRE. 2018. A chemical engineering perspective on the challenges and opportunities of delivering carbon capture and storage at commercial scale. Available: https://www.icheme.org/media/1401/ccs-report-2018.pdf [Accessed Jan 2019].
IPCC 2018. Summary for Policymakers. *In:* MASSON-DELMOTTE, V., P. ZHAI, H.-O. PÖRTNER, D. ROBERTS, J. SKEA, P.R. SHUKLA, A. PIRANI, MOUFOUMA-OKIA, C. PÉAN, R. PIDCOCK, S. CONNORS, J.B.R. MATTHEWS, Y. CHEN, X. ZHOU, M.I. GOMIS, E. LONNOY, MAYCOCK, M. TIGNOR, AND T. WATERFIELD (ed.) *Global Warming of 1.5°C. An IPCC Special Report on the impacts of global warming of 1.5°C above pre-industrial levels and related global greenhouse gas emission pathways, in the context of strengthening the global response to the threat of climate change, sustainable development, and efforts to eradicate poverty.* World Meteorological Organization, Geneva, Switzerland.
IRVINE, J. T. S., SINCLAIR, D. C. & WEST, A. R. 1990. Electroceramics: Characterization by Impedance Spectroscopy. *Advanced Materials,* 2**,** 132-138.
ITOH, T., MORI, M., INUKAI, M., NITANI, H., YAMAMOTO, T., MIYANAGA, T., IGAWA, N., KITAMURA, N., ISHIDA, N. & IDEMOTO, Y. 2015. Effect of Annealing on Crystal and Local Structures of Doped Zirconia Using Experimental and Computational Methods. *The Journal of Physical Chemistry C,* 119**,** 8447-8458.
JENSEN, S. H., GRAVES, C., MOGENSEN, M., WENDEL, C., BRAUN, R., HUGHES, G., GAO, Z. & BARNETT, S. A. 2015. Large-scale electricity storage utilizing

reversible solid oxide cells combined with underground storage of CO_2 and CH_4. *Energy & Environmental Science,* 8**,** 2471-2479.
JENSEN, S. H., HAUCH, A., HENDRIKSEN, P. V., MOGENSEN, M., BONANOS, N. & JACOBSEN, T. 2007. A method to separate process contributions in impedance spectra by variation of test conditions. *Journal of the Electrochemical Society,* 154**,** B1325-B1330.
JENSEN, S. H., HAUCH, A., KNIBBE, R., JACOBSEN, T. & MOGENSEN, M. 2013. Modeling Degradation in SOEC Impedance Spectra. *Journal of the Electrochemical Society,* 160**,** F244-F250.
JENSEN, S. H., HJELM, J., HAGEN, A. & MOGENSEN, M. 2009. Chapter 53: Electrochemical impedance spectropscopy as diagnostic tool. *Advances in Electrocatalysis, Materials, Diagnostics and Durability.* John Wiley & Sons. 7921-7933.
JOHNSON, D. 2014. ZView 2. 3.3f ed.: Scribner Asscoiates, Inc.
JONSCHER, A. K. 1977. The 'universal' dielectric response. *Nature,* 267**,** 673-679.
JONSCHER, A. K. 1978. Analysis of the alternating current properties of ionic conductors. *Journal of Materials Science,* 13**,** 553-562.
JOSSEN, A. 2006. Fundamentals of battery dynamics. *Journal of Power Sources,* 154**,** 530-538.
JULIEN, B. & PINO, D. 2014. Chapter 5: Finite Element Approach to the Sintering Process at the Grain Scale. *In:* BERGHEAU, J. M. (ed.) *Thermomechanical Industrial Processes.* John Wiley & Sons, Inc. 247-304.
KAZLAUSKAS, S., KEŽIONIS, A., ŠALKUS, T. & ORLIUKAS, A. F. 2013. Electrical properties of YSZ and CaSZ single crystals. *Solid State Ionics,* 231**,** 37-42.
KEŽIONIS, A., KAZLAUSKAS, S., PETRULIONIS, D. & ORLIUKAS, A. F. 2015. Relationship between charge carrier relaxation and peculiarities of electric response in some solid oxygen ion conductors. *Solid State Ionics,* 279**,** 25-31.
KHARTON, V., MARQUES, F. & ATKINSON, A. 2004. Transport properties of solid oxide electrolyte ceramics: a brief review. *Solid State Ionics,* 174**,** 135-149.
KHARTON, V. V., NAUMOVICH, E. N. & VECHER, A. A. 1999. Research on the electrochemistry of oxygen ion conductors in the former Soviet Union. I. ZrO_2-based ceramic materials. *Journal of Solid State Electrochemistry,* 3**,** 61-81.
KILNER, J. 2000. Fast oxygen transport in acceptor doped oxides. *Solid State Ionics,* 129**,** 13-23.
KILNER, J. A. & STEELE, B. C. H. 1981. Chapter 5: Mass Transport in Anion-Deficient Fluorite Oxides. *In:* SORENSEN, O. T. (ed.) *Nonstoichiometric Oxides.* Academic Press Inc. 233-269.
KINGERY, W. D., BOWEN, H. K. & UHLMANN, D. R. 1976. Chapter 10: Grain Growth, Sintering and Vitrification. *Introduction to Ceramics.* Second Edition ed. New York: John Wiley & Sons. 449-515.
KIT. 2015. Available: https://www.iam.kit.edu/wet/english/Lin-KK.php [Accessed Sept 2015].
LEONIDE, A. 2010. *SOFC Modelling and Parameter Identification by means of Impedance Spectroscopy.* PhD, Karlsruher Institut für Technologie.

LEONIDE, A., SONN, V., WEBER, A. & IVERS-TIFFEE, E. 2008. Evaluation and modeling of the cell resistance in anode-supported solid oxide fuel cells. *Journal of the Electrochemical Society,* 155**,** B36-B41.

LESSING, P. A. 2007. A review of sealing technologies applicable to solid oxide electrolysis cells. *Journal of Materials Science,* 42**,** 3465-3476.

MACDONALD-SMITH, A. 2017. Gorgon LNG project to show business case for carbon waste storage. June 21, 2017. *Financial Review*. Australia.

MAHATO, N., BANERJEE, A., GUPTA, A., OMAR, S. & BALANI, K. 2015. Progress in material selection for solid oxide fuel cell technology: A review. *Progress in Materials Science,* 72**,** 141-337.

MARKEWITZ, P., KUCKSHINRICHS, W., LEITNER, W., LINSSEN, J., ZAPP, P., BONGARTZ, R., SCHREIBER, A. & MÜLLER, T. E. 2012. Worldwide innovations in the development of carbon capture technologies and the utilization of CO_2. *Energy & Environmental Science,* 5**,** 7281-7305.

MARROCCHELLI, D., MADDEN, P. A., NORBERG, S. T. & HULL, S. 2011. Structural Disorder in Doped Zirconias, Part II: Vacancy Ordering Effects and the Conductivity Maximum. *Chemistry of Materials,* 23**,** 1365-1373.

MASÓ, N. & WEST, A. R. 2015. Electronic Conductivity in Yttria-Stabilized Zirconia under a Small dc Bias. *Chemistry of Materials,* 27**,** 1552-1558.

MCLACHLAN, D. S., BLASZKIEWICZ, M. & NEWNHAM, R. E. 1990. Electrical Resistivity of Composites. *Journal of the American Ceramic Society,* 73**,** 2187-2203.

MET OFFICE. 2016. *The science behind climate change* [Online]. Available: http://www.metoffice.gov.uk/climate-guide/science/science-behind-climate-change [Accessed Jan 2019].

MET OFFICE. 2018a. *What is climate change?* [Online]. Available: http://www.metoffice.gov.uk/climate-guide/climate-change [Accessed Jan 2019].

MET OFFICE. 2018b. *Why is our climate changing?* [Online]. Available: http://www.metoffice.gov.uk/climate-guide/climate-change/why [Accessed Jan 2019].

MOGENSEN, M. & HENDRIKSEN, P. 2003. Chapter 10: Testing of Electrodes, Cells and Short Stacks. *In:* SINGHAL, S. C. & KENDAL, K. (eds.) *High Temperature and Solid Oxide Fuel Cells: Fundamentals, Design and Applications.* Elsevier. 261-289.

MOHN, C. E., STOLEN, S., NORBERG, S. T. & HULL, S. 2009. Oxide-ion disorder within the high temperature delta phase of Bi_2O_3. *Physical Review Letters,* 102**,** 155502.

MOULSON, A. J. & HERBERT, J. M. 2003. Chapter 2: Elementary Solid State Science. *Electroceramics: Materials, Properties, Applications.* 2nd Edition ed. Chichester: Wiley. 5-93.

NAGATA, M., ITOH, Y. & IWAHARA, H. 1994. Dependence of observed overvoltages on the positioning of the reference electrode on the solid electrolyte. *Solid State Ionics,* 67**,** 215-224.

NATIONAL GRID. 2019. *Frequency response services* [Online]. Available: https://www.nationalgrideso.com/balancing-services/frequency-response-services [Accessed Jan 2019].

NECHACHE, A., CASSIR, M. & RINGUEDE, A. 2014. Solid oxide electrolysis cell analysis by means of electrochemical impedance spectroscopy: A review. *Journal of Power Sources,* 258**,** 164-181.

NORBERG, S. T., HULL, S., AHMED, I., ERIKSSON, S. G., MARROCCHELLI, D., MADDEN, P. A., LI, P. & IRVINE, J. T. S. 2011. Structural Disorder in Doped Zirconias, Part I: The $Zr_{0.8}Sc_{0.2-x}Y_xO_{1.9}$ (0.0 ≤x≤ 0.2) System. *Chemistry of Materials,* 23**,** 1356-1364.

NORTH, M. 2014. Chapter 1: What is CO_2? Thermodyamics, basic reactions and phyiscal chemistry. *Carbon dioxide utilisation: Closing the carbon cycle.* Elsevier. 183-210.

OMOJOLA, K. 2014. *High temperature co-electrolysis of carbon dioxide and steam in a solid oxide cell for synthesis gas production.* PhD, University of Sheffield.

PARIS AGREEMENT. 2015. *COP21* [Online]. Available: https://unfccc.int/documents/184656 [Accessed Jan 2019].

PERRY, N. H., YEH, T. C. & MASON, T. O. 2011. Temperature Dependence of Effective Grain Core/Single Crystal Dielectric Constants for Acceptor-Doped Oxygen Ion Conductors. *Journal of the American Ceramic Society,* 94**,** 508-515.

PILATOWSKY, I., ROMERO, R. J., ISAZA, C. A., GAMBOA, S. A., SEBASTIAN, P. J. & RIVERA, W. 2011. Chapter 2: Thermodynamics of Fuel Cells. *Cogeneration Fuel Cell-Sorption Air Conditioning Systems.* 1 ed.: Springer-Verlag London. 25-36.

RAVAL, A. & RAMANATHAN, V. 1989. Observational determination of the greenhouse effect. *Nature,* 342**,** 758-761.

RIEBEEK, H. & SIMMON, R. 2011. *The carbon cycle* [Online]. NASA earth observatory. Available: earthobservatory.nasa.gov/features/CarbonCycle/page1.php [Accessed Jan 2019].

SAVOVA-STOYNOV, B. & STOYNOV, Z. B. 1987. Analysis of the inductance influence on the measured electrochemical impedance. *Journal of Applied Electrochemistry,* 17**,** 1150-1158.

SCHICHLEIN, H., MULLER, A. C., VOIGTS, M., KRUGEL, A. & IVERS-TIFFEE, E. 2002. Deconvolution of electrochemical impedance spectra for the identification of electrode reaction mechanisms in solid oxide fuel cells. *Journal of Applied Electrochemistry,* 32**,** 875-882.

SCHOENLEBER, M., KLOTZ, D. & IVERS-TIFFEE, E. 2014. A Method for Improving the Robustness of linear Kramers-Kronig Validity Tests. *Electrochimica Acta,* 131**,** 20-27.

SCHULER, J. A., GEHRIG, C., WUILLEMIN, Z., SCHULER, A. J., WOCHELE, J., LUDWIG, C., HESSLER-WYSER, A. & VAN HERLE, J. 2011. Air side contamination in Solid Oxide Fuel Cell stack testing. *Journal of Power Sources,* 196**,** 7225-7231.

SCHWANDT, C. & WEPPNER, W. 1997. Kinetics of Oxygen, Platinum/Stabilized Zirconia and Oxygen, Gold/Stabilized Zirconia Electrodes under Equilibrium Conditions. *Journal of The Electrochemical Society,* 144**,** 3728-3738.

SCOTT, H. G. 1975. Phase relationships in the zirconia-yttria system. *Journal of Materials Science,* 10**,** 1527-1535.

SCRIBNER ASSOCIATES 2000. Equivalent Circuits - Circuit Elements. *ZView2 Help.*

SHANNON, R. D. 1976. Revised effective ionic radii and systematic studies of interatomic distances in halides and chalcogenides. *Acta Crystallographica Section A,* 32**,** 751-767.
SHANNON, R. D. 1993. Dielectric polarizabilities of ions in oxides and fluorides. *Journal of Applied Physics,* 73**,** 348-366.
SHIN, E. C., AHN, P. A., SEO, H. H., JO, J. M., KIM, S. D., WOO, S. K., YU, J. H., MIZUSAKI, J. & LEE, J. S. 2013. Polarization mechanism of high temperature electrolysis in a Ni-YSZ/YSZ/LSM solid oxide cell by parametric impedance analysis. *Solid State Ionics,* 232**,** 80-96.
SHRI PRAKASH, B., PAVITRA, R., SENTHIL KUMAR, S. & ARUNA, S. T. 2018. Electrolyte bi-layering strategy to improve the performance of an intermediate temperature solid oxide fuel cell: A review. *Journal of Power Sources,* 381**,** 136-155.
SOLARTRON ANALYTICAL 2015. Modulab XM: Materials Test System Brochure. Ametek.
STEELE, B. C. H. & HEINZEL, A. 2001. Materials for fuel-cell technologies. *Nature,* 414**,** 345-352.
STEIL, M. C., THEVENOT, F. & KLEITZ, M. 1997. Densification of Yttria-Stabilized Zirconia. *Journal of The Electrochemical Society,* 144**,** 390-398.
STOOTS, C. M., O'BRIEN, J. E., HERRING, J. S. & HARTVIGSEN, J. J. 2009. Syngas Production via High-Temperature Coelectrolysis of Steam and Carbon Dioxide. *Journal of Fuel Cell Science and Technology,* 6(1)**,** 011014.
STRICKLER, D. W. & CARLSON, W. G. 1964. Ionic Conductivity of Cubic Solid Solutions in the System CaO-Y_2O_3-ZrO_2. *Journal of the American Ceramic Society,* 47**,** 122-127.
STYRING, P., QUADRELLI, E. A. & ARMSTRONG, K. 2014. *Carbon dioxide utilisation: Closing the carbon cycle*, Elsevier.
SUBBARAO, E. & MAITI, H. 1984. Solid electrolytes with oxygen ion conduction. *Solid State Ionics,* 11**,** 317-338.
THE GEOLOGICAL SOCIETY. 2010. Climate change: evidence from the geological record. *A statment from the Geological Society of London, November 2010* [Online]. Available: http://www.geolsoc.org.uk/climaterecord [Accessed Jan 2019].
THOMPSON, D. P., DICKINS, A. M. & THORP, J. S. 1992. The dielectric properties of zirconia. *Journal of Materials Science,* 27**,** 2267-2271.
THORP, J. S. & BUCKLEY, H. P. 1973. The dielectric constants of current-blackened single crystral yttria-stabilized zirconia. *Journal of Materials Science,* 8**,** 1401-1408.
TIETZ, F., SEBOLD, D., BRISSE, A. & SCHEFOLD, J. 2013. Degradation phenomena in a solid oxide electrolysis cell after 9000 h of operation. *Journal of Power Sources,* 223**,** 129-135.
TOSOH 2014. Zirconia. *3901GX- 002C.* Japan. [Online]. Available: http://www.eskens.com/wp-content/uploads/2014/05/ZIRCONIA-BROCHURE.pdf [Accessed Jul 2018].
TROGLER, W. C. 1995. The Environmental Chemistry of Trace Atmospheric Gases. *Journal of Chemical Education,* 72**,** 973-976.

VAN DIJK, T. & BURGGRAAF, A. J. 1981. Grain boundary effects on ionic conductivity in ceramic $Gd_xZr_{1-x}O_{2-(x/2)}$ solid solutions. *Physica Status Solidi (a),* 63**,** 229-240.

VERKERK, M. J., MIDDELHUIS, B. J. & BURGGRAAF, A. J. 1982. Effect of grain boundaries on the conductivity of high-purity ZrO_2-Y_2O_3 ceramics. *Solid State Ionics,* 6**,** 150-170.

VLADIKOVA, D., KILNER, J. A., SKINNER, S. J., RAIKOVA, G. & STOYNOV, Z. 2006. Differential impedance analysis of single crystal and polycrystalline yttria stabilized zirconia. *Electrochimica Acta,* 51**,** 1611-1621.

WEBER, A., SZASZ, J., DIERICKX, S., ENDLER-SCHUCK, C. & IVERS-TIFFEE, E. 2015. Accelerated Lifetime Tests for SOFCs. *ECS Transactions,* 68**,** 1953-1960.

WEIL, K. S. 2006. The state-of-the-art in sealing technology for solid oxide fuel cells. *The Journal of The Minerals, Metals & Materials Society,* 58**,** 37-44.

WILSON, J. R., CRONIN, J. S., DUONG, A. T., RUKES, S., CHEN, H.-Y., THORNTON, K., MUMM, D. R. & BARNETT, S. 2009. Effect of composition of ($La_{0.8}Sr_{0.2}MnO_3$–Y_2O_3-stabilized ZrO_2) cathodes: Correlating three-dimensional microstructure and polarization resistance. *Journal of Power Sources,* 195**,** 1829-1840.

WINKLER, J., HENDRIKSEN, P. V., BONANOS, N. & MOGENSEN, M. 1998. Geometric Requirements of Solid Electrolyte Cells with a Reference Electrode. *Journal of the Electrochemical Society,* 145**,** 1184-1192.

YAMAMURA, H., YAGI, Y. & KAKINUMA, K. 2007. Dielectric Relaxations of Y-Doped ZrO_2 Single Crystal. *Journal of the Ceramic Society of Japan,* 115**,** 546-550.

YANG, F., ZHAO, X. & XIAO, P. 2010. Electrical properties of YSZ/Al_2O_3 composite and YSZ/Al_2O_3 interface studied by impedance spectroscopy and finite element modelling. *Solid State Ionics,* 181**,** 783-789.

ZHANG, T. S., CHAN, S. H., WANG, W., HBAIEB, K., KONG, L. B. & MA, J. 2009. Effect of Mn addition on the densification, grain growth and ionic conductivity of pure and SiO_2-containing 8YSZ electrolytes. *Solid State Ionics,* 180**,** 82-89.

ZHANG, Y., CHEN, Y. & CHEN, F. 2015. In-situ quantification of solid oxide fuel cell electrode microstructure by electrochemical impedance spectroscopy. *Journal of Power Sources,* 277**,** 277-285.

APPENDIX

A.1 KRAMERS-KRONIG

```
%% Initial setup
% Series R,C and L correction
RsYes=1;
LsYes=1;
CsYes=0;
Lsmanual=0; %if 1 then Ls is defined by the following value:
Lscorrection=5.6E-7;

% Define m, the number of RC elements used initially
m_man=30; %22
m_auto=1; %1 is auto, 0 is manual
if m_auto==1, m=20;%m=20;
else m=m_man;
end

c=0.95; %or 0.5 for SOCs
fit='complex'; %either 'complex','real' or 'imag'
formalism='Z'; %either Z or Y

filename='/Documents/lab/cc_jig/YSZscAu/300oC.z';
fmin=200;
fmax=1E6;
units='Ohm'; %either 'Ohm.cm' or 'Ohm'
[Frequency,ZRe,ZIm]=importZViewfile(filename,fmin,fmax); %see
                                                    %Section A.4

if Lsmanual==1,
    ZIm=ZIm-2.*pi()*Frequency.*Lscorrection;
end

omega=2.*pi.*Frequency;

% Define working variable, X
if strcmp(formalism,'Z')==1,
    XRe=ZRe;
    XIm=ZIm;
elseif strcmp(formalism,'Y')==1,
    ZComplex=ZRe+1i.*ZIm;
    XRe=real(1./ZComplex);
    XIm=imag(1./ZComplex);
end
Xmodulus=sqrt((XRe).^2+(XIm).^2);
weight=1./Xmodulus;

%% Prepare Figure
KK=figure;
KK.Position=[175   45   886   615];

axNyquist=axes;
axBodeRe=axes;
axBodeIm=axes;
axResiduals=axes;

axes(axNyquist)
```

```
ax=gca;
hold on
axis equal
box on
if strcmp(formalism,'Z')==1,ax.YDir='reverse'; end
if strcmp(units,'Ohm.cm')==1 && strcmp(formalism,'Z')==1
xlabel('Z'' (\Omega.cm)')
ylabel('Z" (\Omega.cm)')
elseif strcmp(units,'Ohm.cm')==1 && strcmp(formalism,'Y')==1
xlabel('Y'' (1/\Omega.cm)')
ylabel('Y" (1/\Omega.cm)')
elseif strcmp(units,'Ohm')==1 && strcmp(formalism,'Z')==1
xlabel('Z'' (\Omega)')
ylabel('Z" (\Omega)')
elseif strcmp(units,'Ohm')==1 && strcmp(formalism,'Y')==1
xlabel('Y'' (1/\Omega)')
ylabel('Y" (1/\Omega)')
end
plot(XRe,XIm,'-o')

axes(axBodeRe)
ax=gca;
hold on
ax.XScale='log';
xlabel('Frequency (Hz)');
box on
if strcmp(units,'Ohm.cm')==1
    if strcmp(formalism,'Z')==1
        ylabel('Z'' (\Omega.cm)')
    else
        ylabel('Y'' (1/\Omega.cm)')
    end
else
    if strcmp(formalism,'Z')==1,
        ylabel('Z'' (\Omega)');
    else
        ylabel('Y'' (1/\Omega)');
    end
end
loglog(Frequency,abs(XRe),'-o')
xlim([fmin,fmax])

axes(axBodeIm)
ax=gca;
hold on
ax.XScale='log';
ax.YScale='log';
xlabel('Frequency (Hz)');
box on
if strcmp(units,'Ohm.cm')==1
    if strcmp(formalism,'Z')==1
        ylabel('Z" (\Omega.cm)')
    else
        ylabel('Y" (1/\Omega.cm)')
    end
else
    if strcmp(formalism,'Z')==1,
        ylabel('Z" (\Omega)');
    else
        ylabel('Y" (1/\Omega)');
    end
end
```

```
loglog(Frequency,abs(XIm),'-o')
xlim([fmin,fmax])

axes(axResiduals)
ax=gca;
hold on
ax.XScale='log';
xlabel('Frequency (Hz)');
ylabel('\Delta_R_e, \Delta_I_m (%)');
box on
grid on
xlim([fmin,fmax])
ylim([-1,1])

set(axNyquist,'Posi',[0.6184    0.5482    0.2866    0.3768]);
set(axBodeRe,'Posi',[0.1300    0.7673    0.4    0.1577]);
set(axBodeIm,'Posi',[0.1300    0.51    0.4    0.1577]);
set(axResiduals,'Posi',[0.1300    0.1100    0.7750    0.3]);

%% KK calculation
n=length(Frequency);
mu=1; %starting value
while mu >= c,
    % Define tau for each RC element used
    tau=zeros(m,1);
    tau(1)=1./omega(1); %or customise these values to extend range
    tau(m)=1./omega(n);
    for k=2:m-1;
        tau(k)=tau(1).*exp((k-1)./(m-1).*log(tau(m)./tau(1)));
    end

    % Define matrices A & B
    A=zeros(n,m+2);
    B=zeros(n,m+2);

    if strcmp(formalism,'Z')==1,
        for k=1:m,
            A(:,k)=1./(1+(omega(:).*tau(k)).^2);
            B(:,k)=-1.*(omega(:).*tau(k))./(1+(omega(:).*tau(k)).^2);
        end
        if LsYes==1, B(:,m+2)=omega(:); end
        if CsYes==1, B(:,m+3)=-1./omega(:); end
        var0=0.1.*ones(size(A,2),1);

    elseif strcmp(formalism,'Y')==1,
        for k=1:m,
        A(:,k)=(omega(:)).^2.*tau(k)./(1+(omega(:).*tau(k)).^2);
        B(:,k)=(omega(:))./(1+(omega(:).*tau(k)).^2);
        end
        if LsYes==1, B(:,m+2)=-1./omega(:); end
        if CsYes==1, B(:,m+3)=omega(:); end
        var0=1E-6.*ones(size(A,2),1);
    end

    if RsYes==1, A(:,m+1)=1; end

    % least-squares fitting
    options=optimoptions(@lsqnonlin,'TolFun',1E-15,'TolX',1E-
15,'Display','off');
    LX0=zeros(2,1);
```

```
    if strcmp(fit,'complex')==1,
        fvar=@(var)KKoptfZmod(var,XRe,XIm,weight,A,B);

[var,renorm,residual,exitflag,output]=lsqnonlin(fvar,var0,[],[],optio
ns);
        var(m+3,1)=0;
        A(:,[m+3])=0;
        B(:,[m+3])=0;
    elseif strcmp(fit,'real')==1,
        fvar_Re=@(var)(XRe-A*var).*weight;
        var=lsqnonlin(fR_Re,var0,[],[],options);
        var([m+2,m+3],1)=0;
        if LsYes==1 && CsYes==1, fLX=@(LX)(XIm-(B*var+omega.*LX(1)-
LX(2)./omega)).*weight;
        elseif LsYes==1 && CsYes==0, fLX=@(LX)(XIm-
(B*var+omega.*LX(1))).*weight;
        elseif LsYes==0 && CsYes==1, fLX=@(LX)(XIm-(B*var-
LX(2)./omega)).*weight;
        end
        if LsYes==1 || CsYes==1, LX=lsqnonlin(fLX,LX0,[],[],options);
        else LX=[0;0];
        end
        var([m+2,m+3],1)=[LX(1);LX(2)];

    elseif strcmp(fit,'imag')==1,
        fvar_Im=@(var)(XIm-B*var).*weight;
        var=lsqnonlin(fvar_Im,var0,[],[],options);
        var(m+1,1)=0;
        fRs=@(Rs)(XRe-(A*var+Rs)).*weight;
        Rs0=1;
        Rs=lsqnonlin(fRs,Rs0,[],[],options);
        var(m+1,1)=Rs;
    end
    var_p=var(1:m,1); %parallel only ie/ series variables not
included
    if strcmp(formalism,'Z')==1, Rpfit=var_p; end
    if strcmp(formalism,'Y')==1, Rpfit=tau./var_p; end

    % Calculate mu and increment m
    pos=Rpfit>=0;
    neg=Rpfit<0;
    mu=1-abs(sum(neg.*Rpfit))./abs(sum(pos.*Rpfit));
    if m_auto==0, mu=0; end %end routine if manual value of m is used
    if m>=n, mu=0; end
    if mu>=c, m=m+1; end

 end

if m_auto==0||m>=n, mu=1-abs(sum(neg.*Rpfit))./abs(sum(pos.*Rpfit));
end
if RsYes==0, var(m+1,1)=0; end
if LsYes==0, var(m+2,1)=0; end
if CsYes==0, var(m+3,1)=0; end

%% Results
XRefit=A*var;
XImfit=B*var;
Xmodfit=sqrt((XRefit).^2+(XImfit).^2);
DeltaXRe=100.*(XRe-XRefit)./Xmodulus;
DeltaXIm=100.*(XIm-XImfit)./Xmodulus;

if strcmp(formalism,'Z')==1,
```

```
    Rsfit=var(m+1);
    Lsfit=var(m+2);
    Csfit=1./var(m+3);
    Cpfit=tau./Rpfit;
    ZRefit=XRefit;
    ZImfit=XImfit;

elseif strcmp(formalism,'Y')==1,
    Rsfit=1./var(m+1);
    Lsfit=1./var(m+2);
    Csfit=var(m+3);
    Cpfit=var_p;
    YComplexfit=XRefit+1i.*XImfit;
    ZRefit=real(1./YComplexfit);
    ZImfit=imag(1./YComplexfit);
end

% Plot figures
axes(axNyquist)
plot(XRefit,XImfit,'-o')
legend('expt','fit','Location','SouthEast');
legend('boxoff')

axes(axBodeRe)
semilogx(Frequency,XRefit,'-o')
legend('expt','fit','Location','NorthEast');

axes(axBodeIm)
loglog(Frequency,abs(XImfit),'-o')
legend(axBodeIm,'expt','fit','Location','SouthEast');

axes(axResiduals)
semilogx(Frequency,DeltaXRe,'-o','Color','b')
semilogx(Frequency,DeltaXIm,'-o','Color','r')
legend('\Delta_R_e','\Delta_I_m','Location','NorthWest');
```

A.2 ADIS

```
% Locate data
filename1='/Documents/lab/SOC/EISAi.z';
filename2='/Documents/lab/SOC/EISBi.z';
filename3='/Documents/lab/SOC/EISCi.z';
filename4='/Documents/lab/SOC/EISDi.z';
fmin=0.1;
fmax=1E6;
[Frequency,ZRe,ZIm]=importZViewfile(filename1,fmin,fmax); %see
% Z" Bode plot                                          %Section A.4
figure
ax1=subplot(3,1,1);
semilogx(Frequency0,-ZIm0,'-o')
hold on
xlabel('Frequency (Hz)')
ylabel('-Z" (\Omega)')
box on

% DeltaZ" plot
ax2=subplot(3,1,2);
hold on
ax2.XScale='log';
xlabel('Frequency (Hz)')
ylabel('\DeltaZ" (\Omega)')
box on

% ADIS plot
ax3=subplot(3,1,3);
hold on
ax3.XScale='log';
xlabel('Frequency (Hz)')
ylabel('\DeltadZ''/d(log\itf)')
box on

M=length(Frequency0);
DeltaZRe0=ZRe0(3:M)-ZRe0(1:M-2);
MM=length(DeltaZRe0);

for i=2:length(page),
    %Define filename to be filename(i) in each iteration
    str1=['filename=filename' int2str(i) ';'];
    eval(str1);
    %Import data
    [Frequency,ZRe,ZIm]=importZViewfile(filename,fmin,fmax); %see
    %Plot results                                          %Section A.4
    subplot(3,1,1)
    semilogx(Frequency1,-ZIm1,'-o')
    subplot(3,1,2)
    ADZIm=ZIm1-ZIm0;
     semilogx(Frequency0(1:M),ADZIm,'-o')

    % ADIS calculation
    subplot(3,1,3)
    DeltaZRe1=ZRe1(3:M)-ZRe1(1:M-2);
    dDeltaZRe=(DeltaZRe1(1:MM)-DeltaZRe0(1:MM))./...
          (log(Frequency0(3:M))-log(Frequency0(1:M-2)));
    %plot results
    semilogx(Frequency0(2:M-1),dDeltaZRe,'-o')
end
```

A.3 DRT

```
%% Import data
% initial parameters:
displayfigs=1; %1 (or 0) if plotting multiple DRT graphs on same axes
PointsPerDecade=10;
decadeno=2; % number of frequency decades data is extrapolated over

% Method for determining the Hanning filter size
AutoNfilt=1;   % set to 1 or 0
nfilt=15; % preset value, used if AutoNfilt=0.

% Define graph axes
nyquistgraph=1;
FTZImgraph=2;
FTGgraph=3;
DRTgraph=4;

%Specify parameters
Ls=5.7E-7; %jig inductance
R_L=11;    %jig resistance in parallel with inductor
Rpol=0.78;
fmin=0.1;
fmax=1E5;

% Define data to import
filename='/Documents/lab/SOC/EISAi.z';
[Frequency0,ZRe0,ZIm0]=importZViewfile(filename,fmin,fmax); %see
                                                    %Section A.4

% correct for jig inductance
YtotLpart=1./R_L+1./(1i.*2.*pi.*Frequency0.*Ls);
ZImLR=ZIm-imag(1./YtotLpart);
ZReLR=ZRe-real(1./YtotLpart);

N=length(Frequency0);

% Plot Nyquist graph of data for analysis
if displayfigs==1;
    prepareNyquist(nyquistgraph)
    plot(ZRe0,ZIm0,'-o');
end

%% Extrapolate data
if decadeno~=0,
    % Define extrapolation limits
    minlogf=log10(Frequency0(1));
    maxlogf=log10(Frequency0(end));

    % extrapolate frequency range
    numpoints=round(PointsPerDecade*decadeno);
    nn=(1:(numpoints))'/(numpoints)*decadeno;
    Freq1=10.^(minlogf-flipud(nn));
    Freq2=10.^(maxlogf+nn);
    Frequency=[Freq1; Frequency0; Freq2];
    NN=length(Frequency);

    lgf=log(Frequency0); % nb. log stands for natural log (ln)
    lgZIm=log(-ZIm0);
    % Gradient of ln(-ZIm) vs ln(f) at real values:
    DlgZImDlgf(1:N-1)=(lgZIm(2:N)-lgZIm(1:N-1))./...
```

```
        (lgf(2:N)-lgf(1:N-1));

    % Set gradient values
    grad1Im=(DlgZImDlgf(1)+DlgZImDlgf(2))/2;
    grad2Im=(DlgZImDlgf(end-1)+DlgZImDlgf(end))/2;
    if grad1Im<0, grad1Im=0; end
    if grad2Im>0, grad2Im=0; end

    % Extrapolate ZIm
    lgZIm1=grad1Im*(log(Freq1)-lgf(1))+lgZIm(1);
    lgZIm2=grad2Im*(log(Freq2)-lgf(end))+lgZIm(end);
    lgZImTot=[lgZIm1; lgZIm; lgZIm2];
    ZIm=-exp(lgZImTot);

else % if no extrapolation:
    Frequency=Frequency0;
    ZIm=ZIm0;
    NN=length(Frequency);
end

% Make sure the no. of points is ODD (for Hanning filter):
if rem(NN,2)==0,
    Frequency=Frequency(1:NN-1);
    ZIm=ZIm(1:NN-1);
    NN=length(Frequency);
end

%% Fourier Transforms
mid=(NN+1)/2;
Fmid=Frequency(mid);
x=log(Frequency./Fmid);  %Normalise so that x is 0 at the central
point.
S=sech(x);

% Take Fourier Transforms
Zn=fft(ZIm);
Sn=fft(S);
% Redefine FTs for -L/2 to L/2 (instead of from 0 to L)
Zns=fftshift(Zn);
Sns=fftshift(Sn);

if displayfigs==1;
    figure (FTZImgraph) %-ZIm, its FT: Zns, and Sns, vs a counter (n)
    semilogy((1:NN)-mid,-ZIm)
    hold on
    semilogy((1:NN)-mid,abs(Zns))
    semilogy((1:NN)-mid,abs(Sns))
    legend('-ZIm','Zns','Sns')
end

% Determine Gns (the Fourier transform of G)
T=(1/(N-1))*log(Frequency0(end)/Frequency0(1));%T = sampling interval
Gns=-2/(NN*T*Rpol)*Zns./Sns;

%% Define Hanning filter & calculate DRT

% Determine nfilt
if AutoNfilt==1;
    GnsN=Gns(mid:NN);
    figure
    plot(1:length(GnsN),abs(GnsN))
```

```
    ylabel('Gns')
    xlabel('n-(n_0-1)')
    cutoff=max(abs(GnsN(1:3)));
    var(1:mid)=abs(GnsN(1:mid))>cutoff;
    [~,loc]=max(var); % gives location of 1st non-zero value
    nfilt=loc-2;  % -1 as it starts at 1 not 0, and -1 for avoiding
                                                        % that point
 end

% Define Hanning filter
n0=(NN+1)/2;
ii=n0+(-nfilt:nfilt);
wn=zeros(NN,1);
wn_nz=(1-cos(2*pi*(0:(nfilt*2))'/(nfilt*2)))/2;
wn(ii)=wn_nz;
% Apply filter & inverse FT
Gnw=Gns.*wn;
Gs=ifft(Gnw);
G=ifftshift(Gs);

if displayfigs==1;
    % Figure of raw Gn data & filtered Gn data
    figure (FTGgraph)
    plot(1:NN,abs(Gns),1:NN,abs(Gnw))
    xlabel('n')
    legend('Gns','Gnw')

    % Prepare axes:
    % Bode plot
    figure (DRTgraph)
    subplot(2,1,1)
    hold on
    ax=gca;
    ax.XScale='log';
    xlabel('Frequency (Hz)')
    ylabel('|Z"| (\Omega)')
    box on
    % DRT plot
    subplot(2,1,2)
    hold on
    ax=gca;
    ax.XScale='log';
    xlabel('Frequency (Hz)')
    ylabel('DRT')
    box on
end

% Plot results
subplot(2,1,1)
semilogx(Frequency,abs(ZIm),'-o')
xlim([Frequency0(1) Frequency0(end)])

subplot(2,1,2)
semilogx(Frequency,abs(G),'-o')
xlim([Frequency0(1) Frequency0(end)])
```

A.4 CODE TO IMPORT ZVIEW FILE

```
function [Frequency,ZRe,ZIm]=importZViewfile(filename,fmin,fmax)

% Import data from ZView file
delimiter=',';
startRow=9;
formatSpec='%f%f%f%f%f%f%*s%*s%*s%[^\n\r]';
fileID=fopen(filename,'r');
textscan(fileID,'%[^\n\r]',startRow-1,'ReturnOnError',false);
data=textscan(fileID,formatSpec,'Delimiter',delimiter,...
    'ReturnOnError',false);
Frequency=data{:,1};
ZRe=data{:,5};
ZIm=data{:,6};
fclose(fileID);

% Flip variables to go from low to high frequency
Frequency=flipud(Frequency);
ZRe=flipud(ZRe);
ZIm=flipud(ZIm);

% Adjust data to the frequency range of fmin to fmax
[~,fminloc]=min(abs(Frequency-fmin));
[~,fmaxloc]=min(abs(Frequency-fmax));
Frequency=Frequency(fminloc:fmaxloc);
ZRe=ZRe(fminloc:fmaxloc);
ZIm=ZIm(fminloc:fmaxloc);
```

A.5 EVIDENCE OF A TEXTURED CRYSTAL AND ITS IMPLICATIONS

Transmission Electron Microscopy, courtesy of Ali Mostaed, showed that the "single crystal" sample of 8 mol% YSZ from Chapter 4 exhibited multiple grains with an average size of ~ 10 μm, see Figure A5.1. The orientation of each grain was roughly (100). A more accurate description of the sample is therefore a *textured* crystal of 8 mol% YSZ, orientation (100).

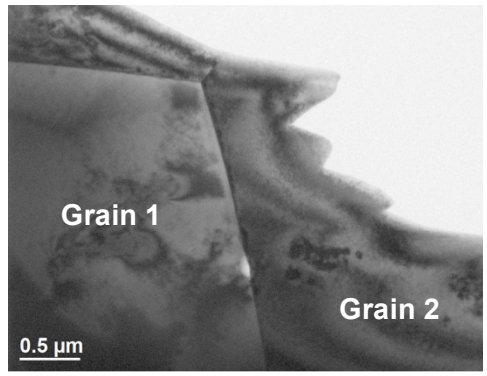

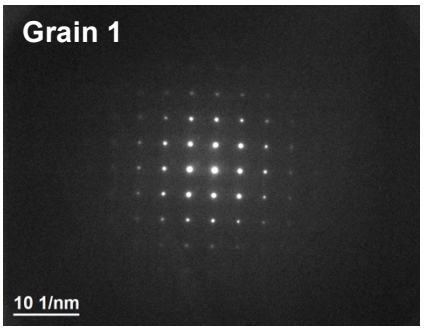

Zone 100
Tilting angles:
X = 0°
Y = 0°

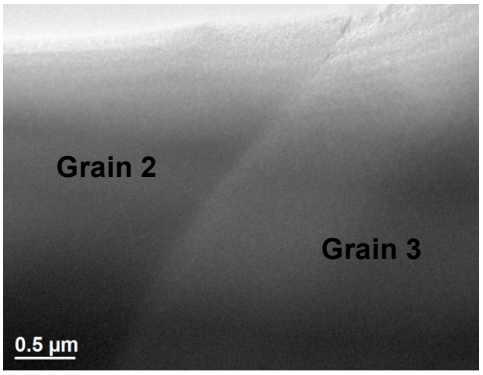

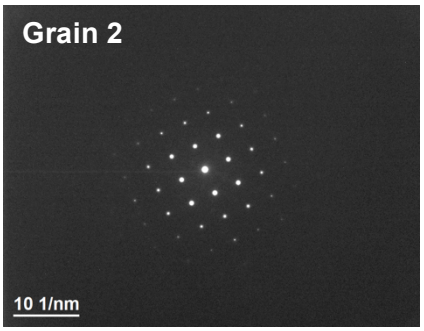

Zone 100
Tilting angles:
X = +10°
Y = -8 °

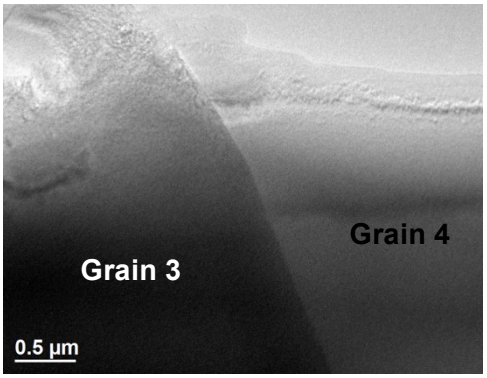

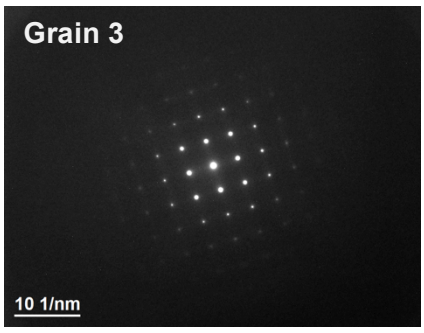

Zone 100
Tilting angles:
X = +10°
Y = -7 °

Grain 4
Zone 100 was not obtained because of tilting limitation (X > 30°)

Figure A5.1: Transmission Electron Spectroscopy of a "single crystal" of 8 mol% YSZ. Images courtesy of Ali Mostaed.

The presence of grain boundaries in the textured crystal is likely to be the source of the immittance response present at mid-frequencies, previously attributed to a charge-transfer effect. The activation energies for the bulk and the mid-frequency response are both around 1.03 ±0.01 eV (see Figure A5.2), which implies that the difference in conductivity is a purely geometrical effect (see Section 5.1.2). The bulk response is visible at lower frequencies for the crystal than for the ceramic pellets investigated in Chapter 5, as there is a greater difference in magnitude between the characteristic frequencies of the high and mid-frequency responses.

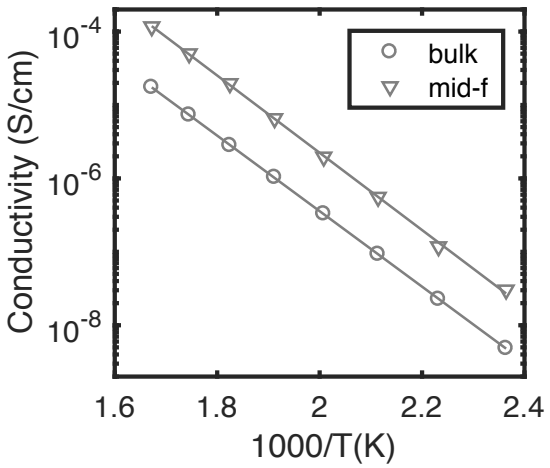

Figure A5.2: Conductivity of the textured crystal: bulk response (o), and mid-frequency response (v).

The absence of grain boundaries in a true single crystal would enable the bulk immittance response of YSZ to be investigated at lower frequency than for a textured crystal. However, the electrode response would still dominate at sufficiently low frequency, as discussed in Section 4.3.

The validity of the results for *bulk* YSZ from Chapter 4 is thought to be unaffected by the extra information discussed in this Appendix.